MULTIWAVELENGTH STUDY OF OLD OPEN CLUSTERS: NGC 188 AND M67

Submitted in partial fulfillment of the requirements for the degree of

Doctor of Philosophy

by

SINDHU. N

VIT®
Vellore Institute of Technology
(Deemed to be University under section 3 of UGC Act, 1956)

August, 2019

DECLARATION

I here by declare that the thesis entitled "Multiwavelength Study of Old Open Clusters: NGC 188 and M67" submitted by me, for the award of the degree of *Doctor of Philosophy* to Vellore Institute of Technology, Vellore is a record of bonafide work carried out by me under the supervision of Dr. C Anu Radha, Associate Professor, Department of Physics, School of Advanced Sciences, Vellore Institute of Technology, Vellore and Dr. Annapurni Subramaniam, Professor, Indian Institute of Astrophysics, Bengaluru.

I further declare that the work reported in this thesis has not been submitted and will not be submitted, either in part or in full, for the award of any other degree or diploma in this institute or any other institute or university.

Place: Vellore

Date: 16/08/2019

Signature of the Candidate

CERTIFICATE

This is to certify that the thesis entitled "Multiwavelength Study of Old Open Clusters: NGC 188 and M67" submitted by Ms. SINDHU. N, Department of Physics, School of Advanced Sciences, Vellore Institute of Technology, Vellore for the award of the degree of *Doctor of Philosophy*, is a record of bonafide work carried out by her under our supervision, as per the VIT code of academic and research ethics.

The contents of this report have not been submitted and will not be submitted either in part or in full, for the award of any other degree or diploma in this institute or any other institute or university. The thesis fulfills the requirements and regulations of the University and in my opinion meets the necessary standards for submission.

Place: Vellore

Date: 16/08/2019

(Dr. C Anu Radha)
(Guide)

(Dr. Annapurni Subramaniam)
(Co-Guide)

Signature of the Guides

ABSTRACT

The thesis focuses on understanding the single and binary stellar evolution in the old open clusters, M67 and NGC 188 using multiwavelength photometric data. We have used images from the Ultra-Violet Imaging Telescope (UVIT) on ASTROSAT, the first Indian space observatory and combined them with other photometric data from 0.14 - 11.5 μm wavelength range and spectra in the ultraviolet (UV) range.

In NGC 188, using the first light data of UVIT, we have discovered a hot companion to a blue straggler star (BSS). The estimated fundamental parameters of the components suggest that the BSS is formed as a result of a recent mass transfer (MT) from a post-AGB/HB star. A deep UV study of the M67 was performed using GALEX images to reveal the presence of a large number of stars with far-UV (FUV) and/or near-UV (NUV) excess. Some of these stars were found to be in binaries and many are single stars. These indicate that a large number of Sun-like stars in this cluster may be chromospherically active. We detect a few main-sequence + white dwarf (MS+WD) binaries in M67, which could be progenitors of Cataclysmic variables. We created multiwavelength spectral energy distributions (SED)s of 45 interesting candidates and estimated their fundamental parameters. We classified BSSs into three groups and suggest that they are formed between 400 Myr - 2 Gyr, more or less continuously. The multi-filter FUV images of M67 from UVIT were used to study 9 bright BSSs. The SEDs of 6 BSSs were found not to fit well with single star spectra, but fitted well with a hot + cool composite spectra, consistent with IUE and HST spectra. The estimated parameters suggest the hot companions to be WDs, and this is the first confirmed detection of WD companions to BSSs in M67.

This study has thus demonstrated the capability of UVIT to detect and characterise binaries with WD companions, particularly to BSSs, with the discovery of 6 BSSs with WD companions in M67 and one BSS with post - AGB/HB companion in NGC 188. The study finds that a good fraction of BSSs are formed through binary MT in M67, apart from other pathways such as triple systems and/or collisions. The BSSs in NGC 188 are likely to be formed by binary MT.

Keywords: *Open Clusters*, *Blue Stragglers Stars*, *Stars:Evolution*.

ACKNOWLEDGEMENT

It has taken a lot of effort, time, and support to be able to complete my Ph.D research work, and I am immensely grateful to everyone who has been with me during this period of my life. I take this opportunity to express my sincere gratitude to all those who have made this Ph.D thesis possible.

I am extremely grateful to Prof. Annapurni Subramaniam at Indian Institute of Astrophysics (IIA) for guiding me for my Ph.D. I would like to thank her for the patient guidance, continuous encouragement and providing her valuable time with her busy schedules. She has been an inspiration to me for her passion, dedication, enthusiasm and commitment to her work. I have been able to learn and unlearn a lot through her guidance. These words are not enough to thank her for being my perfect guide.

I express my sincere gratitude to our respected Chancellor of VIT, Vellore, Dr. G. Viswanathan for providing the platform to pursue my research in VIT. I am grateful to the past and present Dean of SAS and HOD, Department of Physics who have provided me support in several ways throughout my research work. I would like to thank our Research Dean and research office staff for providing their support during my entire Ph.D duration.

I am thankful to the Director of IIA - Dr. P. Sreekumar, Dean - Prof. G C Anupama, Board of Graduate Studies (BGS) and administrative office staff, IIA, Bengaluru for providing me all the support at the institute. I am thankful to Prof. Ram Sagar, Prof. Smitha Subramanian, and Dr. Koshy George for the useful discussions and sharing their knowledge in Astrophysics. I would take this opportunity to thank my doctoral committee members : Prof. Aruna Goswami, IIA, Bengaluru, Prof. K. T Paul, Christ (Deemed to be University), Bengaluru and Prof. Arunai Nambiraj, VIT, Vellore for their advice, useful comments and assessment of my work during the doctoral committee meetings.

I am hugely indebted to the Council of Scientific and Industrial research (CSIR, Govt. of India) for providing me the CSIR- Senior Research Fellowship through grant 3/890(0005)/17 EMR-I, during the course of my Ph.D (2017 - 2019). I am thankful to VIT for providing financial assistance through Teaching- Research Associate and IIA through Visiting Student Internship Programme during 2014 to 2017.

I would like to thank all my fellow-researchers at VIT and IIA for the useful discussion on various subjects and making my PhD days most memorable. I am grateful to Avinash Singh, Chayan Mondal, Vikrant Jhadav and Snehalata Sahu, who spent time to help me with python and other astronomical software packages. It is my pleasure to thank Prasanta Kumar Nayak, Shashanka Gurumath, Rubinur Khatun, Srinivas Prasanna and Raghubar Singh. They have been immensely supportive during the toughest and stressful part of my research days, besides learning astrophysics. Last but not the least, I would say a big thanks to my parents, my siblings, my grandma who are eagerly waiting for me to complete my PhD and finally I am grateful to Mayank for being there for me and thank him for everything.

Place: Vellore

Date: 16/08/2019

SINDHU N

TABLE OF CONTENTS

LIST OF FIGURES

LIST OF TABLES

LIST OF TERMS AND ABBREVIATIONS

AGB Asymptotic Giant Branch

BSS Blue Straggler Star

CCD Charged-Coupled Device

CMD Colour-Magnitude Diagram

FOV Field of View

FSPS Flexible Stellar Population Synthesis

FWHM Full Width Half Maximum

HRD Hertzsprung-Russell Diagram

IRAF Image Reduction and Analysis Facility

$\mathbf{L}_{\odot}$ Solar Luminosity

$\mathbf{M}_{\odot}$ Solar Mass

MS Main-Sequence

MSTO Main-Sequence Turn Off

$\mathbf{R}_{\odot}$ Solar Radius

SED Spectral Energy Distribution

SGB Sub Giant Branch

$\mathbf{T}_{eff}$ Effective Temperature

WD White Dwarf

WOCS WIYN Open Cluster Study

CHAPTER 1

Introduction

1.1 Star Clusters

Stars are born from the fragmentation of the molecular clouds, evolve in the course of their lives and eventually come to a dramatic end. The evolution of a star solely depends on the fusion reaction that occurs inside the star and its interaction with other external objects. Most of the stars are not formed in isolation, but rather in clustered environment presumably formed from the same molecular cloud. Hence the members of the cluster have similar chemical composition, as they originate from the common parent molecular cloud. The stars in the cluster are coeval, co-spatial and are at the same distance from us, held together by mutual gravitational attraction. They also share a common proper motion which can be used to identify the true cluster members, as this motion is not common to other stars that do not belong to the group. As stars in a cluster share similar characteristics except for the difference in their initial mass, they provide invaluable information regarding the details of the process of star formation and stellar evolution.

Over the course of time, the clusters dissolve or are disrupted by the interaction with molecular clouds or tidal stripping by the gravitational field of their parent galaxy. Thus stars formed in clusters may ultimately become part of the field star population. The star clusters are thus among the basic building blocks of galaxies, and hence they are powerful tracers of the structure, formation and the evolutionary history of their host galaxies. The studies of star clusters have a major contribution to the understanding of extragalactic galaxies in the present universe, where resolving individual stars is difficult. In such cases, the integrated properties of the star clusters aid to understand the structure, formation and evolution of these galaxies. The significance of star clusters has been known for decades, but it is during the recent years that major progress for both star clusters in our Galaxy and external galaxies has become possible. This is mainly due to the significant new resources in theory, simulation and an exponential increase in observational data from large surveys of photometry, spectroscopy and astrometry from both ground-and space-based telescopes covering a large wavelength region.

1.2 Star Clusters in Our Galaxy

Our Galaxy, the Milky way is home to several star clusters, which contain some of the youngest to oldest stars. These star clusters are identified by the compactness and the enhanced brightness relative to the field stars. They are located in different parts of our Galaxy: halo, disk, and the central bulge. Based on the observation and characteristics of star clusters in our Galaxy, they are categorized into three basic types: globular clusters, open clusters and stellar associations, a sample images of them are shown in Fig. 1.1. There are about $\sim$ 150 globular clusters, thousands of open clusters or cluster candidates and stellar associations in our Galaxy.

Fig. 1.1 The Colour Composite Images of Star Clusters in Our Galaxy. (Top left:) A Globular Cluster - NGC 2808, (Top right:) An Open Cluster - NGC 7789 and (Bottom:) An OB association - Scorpius-Centaurus. Image Credit: NASA, ESA, G. Piotto (University of Padova) and A. Sarajedini (University of Florida); KPNO, B.J. Mochejska and J. Kaluzny (Warsaw University Observatory); Akira Fujii

1.2.1 Globular Clusters

Globular clusters are massive stellar systems that are located mainly in the halo of our Galaxy. They contain $\sim 10^4$ - 10^6 stars distributed in a nearly spherical shape within a diameter of 50 - 100 pc. The globular clusters of our Galaxy are old, and are presumed to be the relics of the formation of the Galaxy itself. The ages of globular clusters range from 10 billion years to the age of the universe itself. They do not contain gas, dust or young stars and mostly comprise of stars that belong to the Population II class, with metallicity lower than the Sun. These clusters have a bimodal metallicity distribution which can be correlated with their spatial distribution and kinematics. The first group is associated with the stellar halo, which contains about 80% of the clusters, which have little or no rotation and has metallicity $Z < 0.1\ Z_{\odot}$; and remaining 20% of the clusters are associated with the disk and the bulge, which have rapid rotation and $Z > 0.1\ Z_{\odot}$ (Zinn, 1985). The average stellar number density over the entire cluster is typically 0.4 pc^{-3}. The stellar density is extremely high at the center with a gradual decrease in the density of stars in the outer region. As the globular clusters have a high central concentration, three radii are generally estimated for globular clusters: the core radius (r_c), where the surface brightness is reduced to half its central value; the half-light radius (r_h), where the radius contains half of all the luminosity; and the tidal radius (r_t), where the density of the cluster drops to zero. These dense environment result in collision and mergers of stars within the core of the globular clusters, which may often produce single and binary stars from collision (Binney and Merrifield, 1998).

The globular clusters move in highly eccentric orbits around the galactic center and have large spatial velocities up to 300 km s^{-1}. The relaxation times of these clusters are typically 10^8 years. The stellar relaxation will have sufficient time to influence the cluster's structure, as the cluster ages are of the order of 10^{10} years. Though these clusters are relatively stable objects, they suffer from core-collapse. If core-collapse persists, it may increase in stellar collision, which may result in coalescence due to increase in stellar number density. The presence of binaries in the cluster may prevent the core collapse (Heggie, 1975; Hills and Day, 1976; Spitzer and Mathieu, 1980). Recent studies of several globular clusters led to the discovery of multiple stellar populations of main-sequence (MS) stars and giants, which has led to the understanding that these clusters in general, may no longer be defined as single stellar population (Piotto et al., 2005; Piotto et al., 2007; Piotto, 2008).

1.2.2 Open Clusters

Open or galactic clusters are irregular shape grouping of $\sim 10^2$ to 10^3 stars within a diameter of 5 - 10 pc. They are composed of stars that belong to Population I class, and are found in the disk of the Galaxy. Open clusters are excellent laboratories to

understand the physical characteristics of stars in our Galaxy and their evolution. As these clusters are located in the disk, they are part of the recent activities in the Galactic disk. These clusters are often contaminated by field stars, due to the rich stellar number density in the disk. The radial velocity and proper motion measurements of the stars in clusters can be used to decontaminate field stars by computing the membership probability of each star. The typical stellar number density is 0.1-10 pc^3. Though the distribution of the stars vary from cluster to cluster, concentration of stars in the core is not observed, hence it is practically difficult to find the centers of such objects that are not well defined observationally .

The typical open cluster mass ranges from 10^2 to 10^3 $M_\odot$, but it could be the lower limit (Friel, 1995), as the most massive cluster in our Galaxy are found to have cluster masses up to an order of 10^5 $M_\odot$ (Piskunov et al., 2008). These clusters have a small range of metallicity from [Fe/H] = -0.7 to 0.3 and they do not show age-metallicity relationship as seen for disk stars in the Solar neighbourhood. The age of open clusters range from 10^6 to 10^9 years, though most of the clusters dissolve within a short period of their formation, about a few 10 - 100 million years due to several factors. The factors that contribute to the dissolution of an open cluster are: (a) destructive effects of a close encounter of an open cluster from the surrounding giant molecular cloud (Spitzer, 1958), (b) being subjected to strong tidal force by the general galactic field of the host galaxy or (c) dynamical evolution causing low mass stars to acquire enough energy and velocity to be able to escape from the cluster. However, clusters have survived for a long period and have ages of a billion years. They are a small subset of the total open cluster population, and are valuable tools to understand the internal dynamics as well as formation and evolution of the Galactic disk. The global properties of the old open clusters suggest that most of these clusters are found at larger heights from the Galactic plane, in the outer disk region, while very young open clusters are found in the spiral arms of our Galaxy, where there is ongoing star formation. Studies of old clusters often shows a deficiency in the low mass stars, due to dynamical evolution of the cluster, which causes mass segregation and evaporation of low mass stars. This suggests that initial masses of the old open clusters would be in excess of 10^4 $M_\odot$. The typical core radii of old open cluster is 1 - 2 pc and tidal radii of up to 10 to 25 pc (Friel, 1995).

The old open clusters have a significant fraction of binary populations, with estimate of binary fraction ranging from 20 to 50% (Montgomery et al., 1993; Friel, 1995). The binary stars in old open clusters are important proxies to understand binary evolution and to compare with theoretical models and colour-magnitude diagrams (CMDs). Therefore information regarding the binary nature and membership probability of stars are necessary to carry out detailed studies. As single and binary stars evolve through the MS turn-off (MSTO), they yield a wide distribution of colour and luminosity, thus changing the morphology of the MSTO. Only a few old open clusters have radial veloc-

ity and proper motion membership studies, which help in the identification of kinematic members as well as binaries and their orbital parameters.

1.2.3 Stellar Associations

Stellar associations are low density stellar system that span over a large distance and are found in the spiral arms of our Galaxy. As they are located close to the active star formation regions, they are excellent traces of the spiral arms. Stellar associations are loosely bound group consisting of $\sim$ 10-100 stars. Stellar association are identified by the number of stars present in them and by their spectral classification. In our Galaxy, we observe three basic types of associations: OB associations, T-associations and R-associations. Ambartsumian (1947) identified OB and T-associations in our Galaxy.

OB associations or O-associations are stellar aggregates that consist of massive hot stars with spectral types O and B. These stars are spread across a diameter of 30 - 200 pc. They have a short age span of a few million to 10 million years, due to the shorter lifetime of the O and B stars and the loose gravitational binding, which disrupts such system by the tidal pull of the gravitational field of the host Galaxy. They enrich the ISM with heavier elements such as oxygen and iron, through stellar winds and supernova, but destroy the giant molecular clouds during this process. The Ultraviolet (UV) radiation from these stars ionize the interstellar gas, and as result, they are mostly accompanied by HII regions.

T-associations consist of low mass T Tauri type stars, they are young stellar objects which show irregular variability and effective temperature ranging from 3500 to 7000 K. T Tauri stars are found in the nebular regions of the Galaxy where stars are being formed. The stars in T-association span a few light years in diameter. They may be progenitors of stars of spectral type later than O and B, that are still undergoing contraction phase of star formation. These stars produce X-ray emission, due to the magnetic activity at the star's surface (Güdel and Telleschi, 2007). T Tauri stars are low-luminosity stars and their spectra consists of the Balmer, Ca II and Fe I emission lines. The variability in these stars can be correlated to the enormous activity on their stellar surfaces. Sometimes, high-mass young stars are found in T associations, but only within the densest cores of the darkest clouds.

van den Bergh (1966) suggested the associations of stars found in the reflection nebulae be called as R-associations. The existence of these associations was confirmed by obtaining the UBV photometry and MK spectral type (Racine, 1968). These associations are low density stellar aggregates with luminous intermediate-mass stars. As they are found in larger numbers relative to the OB associations, they can be used to map the spiral structure and trace the spiral arms(Racine, 1968; van den Bergh, 1968 Racine and van den Bergh, 1970; Herbst, 1975) of our Galaxy.

1.3 Stellar Evolution

The evolution of a star may be divided into three important phases: pre-MS, MS and post-MS. The pre-MS involves the formation of a star in a molecular cloud, during which the star undergoes gravitational contraction followed by heating, until the time where the hydrogen burning begins. At this stage, the star is born and enters the MS phase and continues to be in this phase, until the hydrogen in its stellar core is exhausted. The star spends more than 90 percent of its lifetime on the MS as indicated by the theoretical studies. The final stage of the star is the post-MS phase, which is relatively shorter but a rapid phase of evolution until the eventual death of the star. The evolutionary history of stars differ according to their initial mass and hence they can be separated into three groups: low-mass ($M < 1.3\ M_{\odot}$), intermediate mass ($1.3\ M_{\odot} < M < 8\ M_{\odot}$) and high mass stars ($M > 8\ M_{\odot}$). The lowest mass star that can burn hydrogen is about $0.08\ M_{\odot}$. We shall briefly discuss the evolution of a single star in the following subsections.

1.3.1 The Pre - Main Sequence Phase: From Protostar to Zero Age Main Sequence

The formation of stars occurs in the giant molecular clouds due to their gravitational collapse and fragmentation processes. The temperature of these molecular clouds are in the range of 10 - 100 K, with a typical mass of $10^6\ M_{\odot}$ across ~ 30 pc in size (de Loore and Doom, 1992). The birth of a protostar begins when it starts to contract due to local instability. The contraction continues until the core region reaches hydrostatic equilibrium, while the collapse continues in the outer layers. During this phase of collapse the evolution proceeds very slowly in Kelvin- Helmholtz time scale and the star occupies the right side of the Hertzsprung-Russell diagram (HRD), and its evolutionary track is called as the Hayashi track. This evolution is for a relatively short period of$\sim 10^{\,7}$ years and even lesser for high mass stars.

In a low-mass star the contraction in the core of the structure causes a rise in the interior temperature, Kramers' opacity κ is reduced as $\kappa \propto T^{-3/5}$. Therefore, the limiting luminosity is increased, and energy transport by radiation becomes dominant. At this stage with continued contraction, the star forms a radiative core, that continues to grow at the expense of the convective envelope (de Loore and Doom, 1992). The effective temperature and luminosity increase with continued contraction, though to a lesser extent. The star now sharply shifts its location towards the left and slight upward on the HRD. Ultimately, radiation dominates in the core, while the convective envelope shrinks to a relatively thin layer. In more massive stars, as electron scattering is predominant, its leftward movement is horizontal, since the luminosity depends mainly on the mass.

The evolutionary path away from the Hayashi track and the development of a radiative core indicates the last stage in the star's advance towards the MS. Typically the time-scale required to reach the MS is relatively much smaller than the life-time of the star on the MS. The star that has reached the MS is considered as a newly born with an age equal to zero. This location of the stars of all masses on the MS is called as zero-age MS (ZAMS).

1.3.2 The Main Sequence

The ZAMS begins with the onset of the hydrogen burning in the core of the star. The temperature at the core of about 2×10^7 K divides stars into two modes of hydrogen burning : pp chain and CNO cycle. The difference in these two modes is primarily due to the temperature dependence of the two nuclear processes. The energy generation rate for many thermonuclear burning stages, within limited temperature range, roughly varies as T^n, where n varies from ~ 3 to 20 depending on the hydrogen burning mode. In the pp chain, the reaction rate is less sensitive with the central temperature varying from $4 \times 10^6 \leq T \leq 2.4 \times 10^7$ K with $6 \geq n \geq 3.5$. Therefore, the radiative transport is dominant for a reasonable temperature gradient. While, in the CNO cycle, the temperature varies from $1.2 \times 10^7 \leq T \leq 5 \times 10^7$ K with $20 \geq n \geq 13$ and therefore the rate of reaction is temperature sensitive (Bowers L and Deeming, 1984). These rates lead to the development of the convective core, as a large core temperature would otherwise lead to a large radiative temperature gradient. In order to reduce the temperature gradient, the core becomes convective. This difference in structure of the two cases is mainly due to the dominance of one mode over the other as a result of its dependency on the central temperature of the star. Though in most cases, both the hydrogen burning channels are active.

As the star proceeds towards the ZAMS, there is a drop in luminosity, which occurs at the same time as the hydrogen begins to burn in the core, as C^{12} that is present in small quantities is converted to form N^{14}. The energy generation rate is $\sim T^{19}$, which leads to the initiation of a convective core. A radiative core would give rise to a greater degree of central condensation, and a less condensed core is typical of a convective core. During the C^{12} burning phase, the star has to adjust the distribution of density from a more to less condensed core, that is, the matter must be moved outwards, against the gravitational pull. As the thermonuclear energy released is spent on doing this work, all the energy released is not available for radiation. At this stage, the gravitational contraction is effectively suspended, with the net reduction in luminosity and effective temperature. The star's evolutionary track moves below and slightly right on the HRD. This phase is short lived, as very little C^{12} is present. The hydrogen burning would then remain as the primary mode of the star's energy source after the exhaustion of

C^{12}. Since the low-mass stars are in favour of the pp chain, which has only a little temperature dependence, the radiative core sets in, with a convective envelope. In the more massive stars, the CNO cycle operates with a convective core as the reaction rate is highly temperature sensitivity, and has a radiative envelope.

The star that has reached the MS evolve slowly in a nuclear time-scale $t_n \sim mc^2/L$, where m is the mass of the star. This evolutionary phase is the longest time scale in the life of a star, which is about 10^{16} times the dynamical time-scale. The star's composition changes with the passage of time due to the thermonuclear processes with four hydrogen fusing into one helium nucleus. The stars, where pp chain dominates i.e. for the masses below 1.3 $M_\odot$, are located at lower part of the MS, while the stars that generates the thermonuclear energy according to the CNO cycle lie on the upper region of the MS.

1.3.2.1 Lower Main Sequence

Stars that reach the lower MS have a radiative core with a convective envelope that extends to the base of the photosphere. The size of the core gradually reduces as we move down the MS. The chemical composition of the core is initially homogeneous. The depletion of the star's energy is supplied by the nuclear reactions. The energy budget is roughly proportional to $\rho X^2 T^n$, where ρ is the density of the star and X is the hydrogen composition, hence as the fuel is consumed, X decreases, which would decrease the energy-generation rate unless, ρ, T or both increase. A consequence of reduction in energy-generation rate would lower the pressure, and hence contract the star and increase X. The amount of potential energy released would partially go into raising the temperature and partly into radiation, by the Virial theorem. Consequently, both ρ and T must increase. This effectively increases the energy output, with a slight increase in the radius of both the envelope and the core. The Luminosity thus increases with a higher energy generation, though the increase in effective temperature is smaller owing to the change in radius. The star thus moves slightly with higher T_{eff} and subsequently higher L on the evolutionary track, which requires about half the MS lifetime.

The star evolves on the MS as the hydrogen in the core burns forming helium. Nearly, 90 percent of the mass is confined within half the radius of the star. The depletion in H, denoted by $X < 1$, occurs within r = 0.3 R and L(r) = L for $r > 0.3$ R (Bowers L and Deeming, 1984). Hydrogen burning occurs entirely within the core of radius (r) of about one-third of the stellar radius (R), equivalent to about 10 percent of the mass. Ultimately the core is dominated by helium, surrounded by a thick hydrogen burning shell. At this point, the zone $r \leq 0.03$R is primarily pure He, and in the region $0.03\ R \leq r \leq 0.3$ R hydrogen burning occurs. The rate of burning is higher causing the He core to be isothermal. A gradual change in composition occurs with the newly formed isother-

mal He core, with the thick H-burning shell moving into the envelope, with the core remaining stable against convection during this evolutionary phase for stars of 1.1 $M_{\odot}$ and less. The end of the MS life of the star occurs with the development of inhomogeneous chemical structure. It now evolves more rapidly with more central condensation, and moves towards lower surface temperature. In the final phase of its evolution away from the MS, the star's shell becomes steadily thinner, with the development of a He core. The core temperature increases with the energy released due to the gravitational contraction of the He core. Thus the excess pressure created during this process, moves the envelope outwards causing the star to expand. Now the luminosity increases which tends to raise T_{eff}, but the increase in the radius, lowers the T_{eff}. The star now traces the path towards the right in the HRD with a small increase in luminosity. This evolutionary time-scale is shorter owing to the rapid energy generation rate in the shell, and is about 12 percent of the entire MS life-time.

1.3.2.2 Upper Main Sequence

A star with a core temperature more than 2×10^7 K proceeds hydrogen burning via the CNO cycle in the convective core. The composition is uniform throughout and a rapid burning takes place within the core than near the outer edge of the region. The Kramer's opacity dominates for stars with intermediate masses, while the electron scattering becomes more important for massive stars. The energy budget for upper main sequence is roughly given by $\rho XZ_{CNO}T^n$, where the mass fraction of C, N and O required for specific reactions is given by Z_{CNO}. The energy generation rate varies in quadratic terms of X in pp-chain and differs significantly from CNO cycle, as the variation being linear in the hydrogen content X and n is typically ~ 18 (Bowers L and Deeming, 1984). Therefore, a decrease in the hydrogen content has a lesser effect on the energy generation rate in stars on the upper MS, and hence it is not necessary for stars in the upper MS to contract as much to maintain their energy output. The increase in the core mass of the star shows a corresponding increase in radius, luminosity, effective temperature and core temperature, but a lower central density. The luminosity and effective temperature has lesser dependency on the mass as the electron scattering dominates. The division between the domination due to Kramer's opacity and electron scattering occurs at about $M \approx 3M_{\odot}$ for Population I stars.

The initial evolution of the upper MS stars proceeds similar to those of the lower MS. The star begins to contract when the rate of energy released is not adequate to support the core and when the nuclear burning has reduced the fraction of hydrogen content to about 0.05. At this point, the star's life on the MS comes to an end. A star more massive than 5 $M_{\odot}$ lack a thick H- burning shell, as seen in stars of 1 $M_{\odot}$, because of convection, which mixes the elements in core thoroughly, reducing the hydrogen

content uniformly. In the absence of the burning shell, the entire star contracts and heats up. During this phase, for a short period the star functions similar to its final phase towards the MS, with a slight increase in its luminosity and more in T_{eff}. The ignition of a H-burning shell surrounding the core, stops the contraction phase. The 5 $M_{\odot}$ star would have lived for nearly 7.2×10^7 years on the MS (Bowers L and Deeming, 1984).

1.3.3 Post - Main Sequence Phase: Onset of Helium Burning in the Core and Beyond

The time scale of the subsequent phases of a star, post its evolution from the MS phase is significantly smaller as compared to its total lifetime. The post-MS stage immediately follows with the He burning in the core, and the development of inhomogeneous composition and corresponding nuclear shell sources as the important constituents. The nuclear shells where the thermonuclear process is releasing energy are referred as active shell sources. A sufficient reduction in the temperature due to an expansion in these shells will cease the release of nuclear energy, and become inactive shell sources. These inactive shell sources may be activated again when the temperature becomes high enough.

The He formed in the core surrounded by the hydrogen envelope during the MS phase has a temperature below its ignition point ($T_c \sim 1.5 \times 10^8$). Therefore, the shell burning continues outward of the stellar core, and is the main source of energy in terms of luminosity. This reaction becomes active when the core mass of the star exceeds the critical value of mass of Schonberg-Chandrashekar (M_{sc}), which occurs when $M_{core} > 0.12\ M_{star}$. As the shell proceeds in converting hydrogen, it correspondingly becomes thinner. The stellar core thus expands and cools at the surface. At this point, the star moves towards the region dominated by convection in the HR diagram completing its sub-giant branch (SGB) phase. As the star is unable to reach a full convective stage, it rapidly increases its radius and luminosity. Therefore an increase in the radius decreases the surface temperature and the star moves to the red giant branch (RGB) phase. The time-scale on this evolutionary phase depends on the initial mass of the star, and for massive stars the core mass is greater than M_{sc} during the end of its MS and hence the duration of the RGB phase is short. The helium core of intermediate mass stars do not exceed the value of critical mass for the core to contract and hence the shell burning proceeds until this condition is satisfied, resulting in a slower RGB phase. The case for the low mass stars is quiet different, where the triple alpha reaction occurs after a very long duration, as the structure remains practically isothermal, while increasing the mass of the core which is only partially degenerate, slowing the nuclear burning process.

In Fig. 1.2 and Fig. 1.3, we have shown the evolution of a lower MS and upper MS star from the ZAMS to the end of post-MS phase respectively. As seen in both

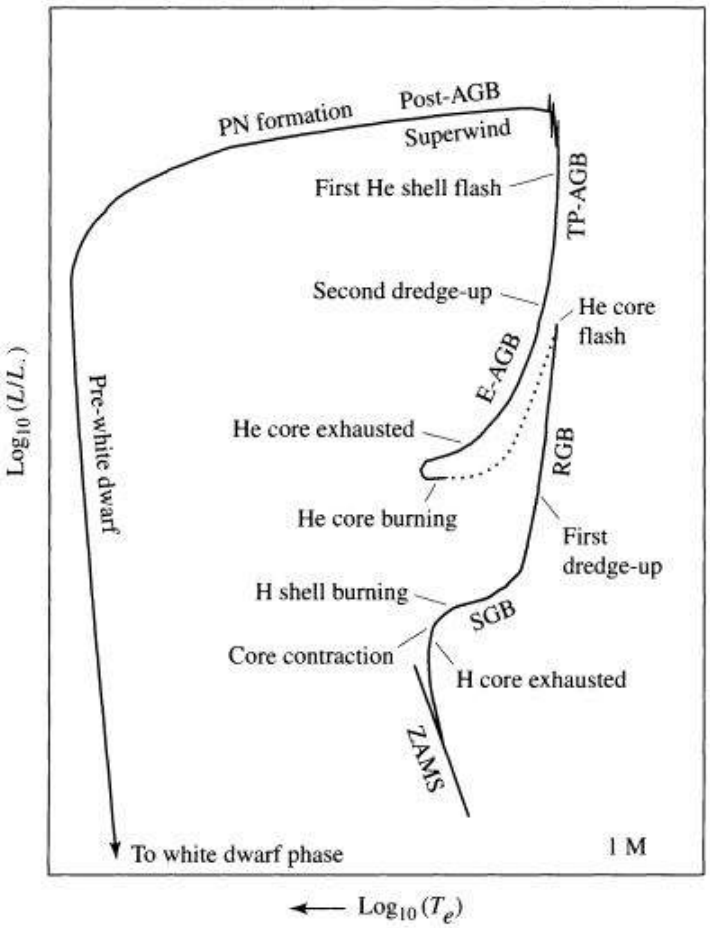

Fig. 1.2 A Diagram of the Evolution of a Lower MS star (1 $M_\odot$) from Zero-Age Main Sequence to the End of its Evolution as a White Dwarf. The Various Phases of Evolution are Labeled. Image Courtesy: Carroll and Ostlie's "An Introduction to Modern Astrophysics, 2nd Ed."

these figures, shortly after the beginning of RGB phase, the ignition of nuclear reaction causes the chemical mixing in the star called the first-dredge up. This results in change in the surface chemical abundance due to convection. A low mass star experiences helium flashes as the helium core reaches a mass of 0.4 to 0.5 $M_\odot$ before the helium in the core is ignited. Therefore as the helium burns under degenerate condition with the rapid energy generation rate being greater than the release of energy outward through conduction, a thermonuclear runaway sets in. As the energy released is almost instantaneous and corresponds to 10^{11} $L_\odot$, this evolutionary phase is termed as flash (Carroll and Ostlie, 2006). The degeneracy is lifted afterwards, and the quiet helium burning phase resumes. The stable helium burning in the core begins at the so called zero age horizontal branch (ZAHB) in the HRD. The evolutionary phase is very short about $\sim 10^6$ years, after the end of the helium flash. The ZAHB is located at a lower luminosity relative to the tip of the RGB on the HRD because of the expansion and relaxation of the core of the star after the He-flash. The location of the star which has reached the

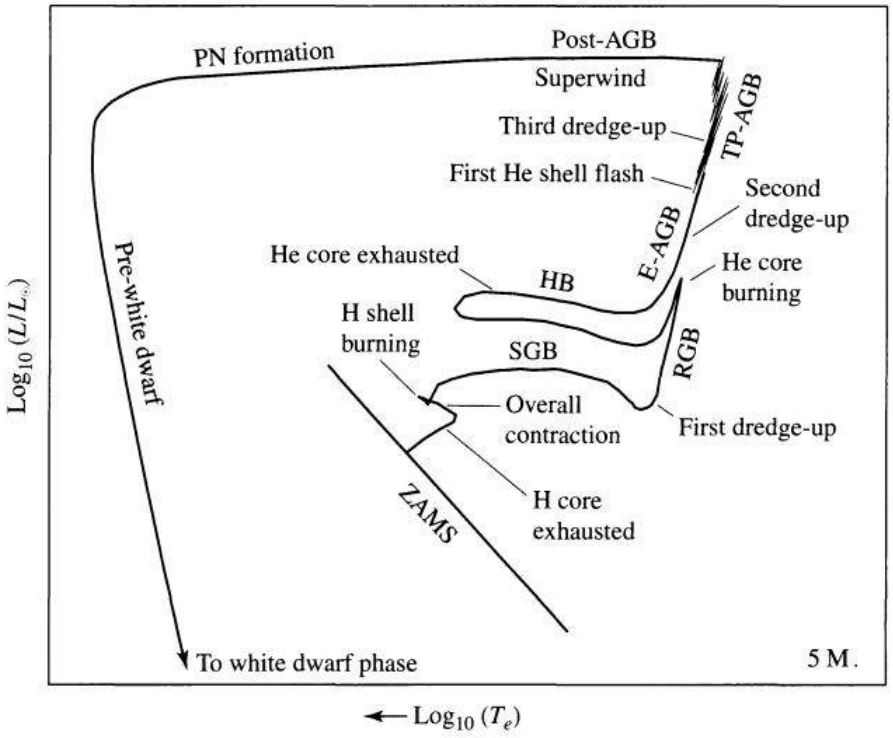

Fig. 1.3 A Diagram of the Evolution of a Upper MS Star (5 $M_{\odot}$) from Zero-Age Main Sequence to the End of its Evolution as a White Dwarf. The Various Phases of Evolution are Labeled. Image Courtesy: Carroll and Ostlie's "An Introduction to Modern Astrophysics, 2nd Ed."

ZAHB on the HRD depends on the ratio of the mass of the core to the total mass. Hence when the luminosity of the shell dominates relative to the emission from the core, the star is positioned at the bluest region of the HRD. After He in the core being exhausted completing the HB phase, the star moves towards the Asymptotic giant branch (AGB).

As the core of the star has exhausted its helium fuel, the star begins to contract to counteract the lack of nuclear energy. In the helium-depleted core, the density increases and the electrons become degenerate. Helium is present in the shell as a product of the previous hydrogen burning, outside the core composed of carbon and oxygen (CO) that is degenerate. The hydrogen shell burning proceeds in a shallow hydrogen layer beyond the helium zones. At the edge of the CO core when the temperature exceeds 10^8 K, the helium shell get ignited. As this region is partially degenerate, its leads to release of large amount of energy and traces the stretch of early AGB (EAGB) on the HRD. During this phase, the hydrogen shell continues to burn forming a helium layer that separates it from the CO core in the process making it degenerate. At this stage, the star has two active shell burning sources: helium burning shell at the boundary of the CO core, and an hydrogen burning shell in the outer layer. The energy is being produced at regular intervals in the helium, but the surplus energy cannot be instantaneously pushed to the

surface due to hydrogen burning shell. Therefore the region between the two shells develops a higher pressure. This translates into the expansion of the inter-shell, pushing the shell of hydrogen to the outer and cool regions, reducing the luminosity, thus the hydrogen burning stops. The helium shell becomes dominant and proceeds to deposit carbon and oxygen in the core making it degenerate. Simultaneously the inter-shell slowly ceases to expand until the hydrogen burning shell becomes dominant.

The high mass stars experience a chemical mixing, as the convection layer penetrate from the outside when the structure expands. If this convection allows to move as deep as the inter-shell layers, the surface elements can be brought which are combustive products of hydrogen. Hence a second dredge-up follows similar to the first. Thermal pulsating AGB (TP-AGB) is the next phase, similar steps continue as in the EAGB phase, and the third dredge-up follows. During this phase, unlike the last two dredge-ups, a change in chemical signatures may be seen due to the mixing of profound regions of the star, with an increase in surface carbon abundance.

During the AGB phase, the envelope of the stars expand and cool relative to other phases and hence formation of layers of molecules and dust becomes possible. These layers are removed through stellar winds due to radiation pressure and therefore suffers from a significant mass loss. The thermal pulses continue until the expansion is sufficient to remove the outermost layers of the CO core which becomes fully degenerate rapidly. This phase, known as the post-AGB, halts the nuclear evolution of the star to lead the star to its last stages. The temperature of the star increases as the star shrinks and crosses the HRD. The remnant of the hot star ionises the matter ejected during the previous phase, a nebulosity appears, called the planetary nebula.

The final stages of the star depends on its initial mass, similar to their evolutionary phases. The stars with mass less than 0.3 $M_\odot$ cools as helium white dwarf (WD). In these stars the nuclear burning halts after the hydrogen in the core is burnt forming a helium core, as they fail to trigger helium burning in the core. The time of their evolution to form helium WD is about 20 Gyr, hence these objects cannot be observed currently. The observation of such objects in the current universe is linked to interaction of the binary stars. The stars with initial mass > 0.3 $M_\odot$ and intermediate stars of mass < 8 $M_\odot$ evolve through the planetary nebula. As the nebula is dispersed into the interstellar medium, a completely degenerate CO core remains. The star moves into the cooling sequence of the WD on the HRD. As these stars cannot obtain energy form thermonuclear reactions, the structure of the WDs are sustained by pressure of degenerate electrons. The critical value of the mass of WD is called the *Chandrashekhar mass* (~ 1.4 $M_\odot$), which is the limit to maintain equilibrium of the structure. When the star exceeds this limit, it collapses to become a neutron star (Carroll and Ostlie, 2006).

1.4 Binary Evolution

The evolution of a star in a binary system does not happen in isolation, if the orbital separation is sufficiently small to cause tidal perturbations due to the companion. Hence, a complex interaction of stars in a binary system would result in a large scale change in their properties which would ultimately result in dramatically different outcome in the evolution in comparison to an isolated star with similar properties. A binary system has two components called the primary and secondary with the masses M_1 and M_2 and the initial more massive star being the primary. The main factors that determine the evolution of close/interacting binaries are the total mass of the system (M= M_1 + M_2), the mass ratio (q=M_1/M_2), the orbital period (P) and the orbital eccentricity (e). In general, about 50% of the stars in the solar neighbourhood are found to be in binary or multiple stellar system (de Loore and Doom, 1992). In this section, we shall focus on the scenario of mass transfer that occurs through Roche Lobe overflow (RLOF) in a binary system. We shall discuss systems containing low and intermediate mass stars, as they are relevant in the case of stars found in the old open clusters.

In order to introduce the concept of Roche lobe, let's consider a simple binary system consisting of two stars of point masses M_1 and M_2 orbiting their centre of gravity in circular orbits of radius *a*. Then the orbital period P is given by

$$P = \frac{2\pi}{\omega} = 2\pi\sqrt{\frac{a^3}{G(M_1 + M_2)}} \tag{1.1}$$

where ω is the angular velocity of the system. Assuming that the rotation is synchronised with the orbital motion, the potential ϕ in this system with the centre of mass at the origin *r* of the binary is given by

$$\phi(r) = -\frac{GM_1}{|r_1 - r|} - \frac{GM_2}{|r_2 - r|} - \frac{1}{2}|\omega * r|^2 \tag{1.2}$$

where r_1 and r_2 are the distance to the star. A cross section of the equipotential surfaces in the orbital plane of the binary system is shown in Fig. 1.4. There are five equilibrium points in the orbital plane where the gradient of the potential is zero, known as Lagrangian points. The L_1 is the inner Lagrangian point, which is the saddle point between the line joining the two masses. The equipotential surfaces containing L_1, around each of the two stars is called Roche lobe. As the star evolves, its radius increases approaching the Roche lobe, which is the maximum radius a star can reach before mass transfer can take place. In a situation, where both the stars in the system are well within the Roche lobe, the system is called detached. Such a system is stable, as there is limited interaction between the two stars. However, if there is an increase in the radius of either one of the star due to stellar evolution, it will fill its Roche lobe taking a peanut

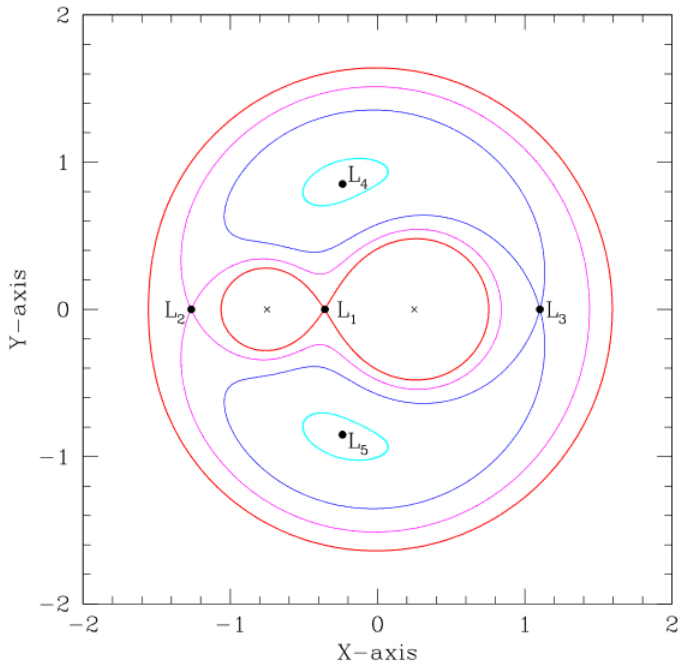

Fig. 1.4 A Cross Section of the Equipotential Surfaces in the Orbital Plane of the Binary System. The Positions of the Two Stars in the System are indicated by Crosses. Image Courtesy: Ecology of Blue straggler Stars

shape. The Roche lobe filling star is likely to lose mass, as the envelope of the star cannot be dynamically stable. Thus mass transfer materializes with the flow of matter to its companion through the inner Lagrangian point L_1. This system is known as semi-detached, and the mass transfer is called RLOF. A contact system is in which both the stars having similar potentials fill their Roche lobe and come in contact at L_1 and therefore may exchange masses (Kopal, 1955). Further, in such systems with an overfilling of the Roche lobe, the stars are surrounded by a common envelope. The star that has reached its maximum Roche limit would experience strong tidal effects. This would cause the star's rotation synchronised with its orbital motion and thus circularizing the orbit in a short timescale.

In general, the Roche lobe is not a sphere; though it may not differ much from a sphere of suitable radius. The critical equipotential, i.e. the Roche lobe can be conveniently defined in terms of effective radius R_L and is the radius of the sphere whose volume equals the volume of the Roche lobe itself. Eggleton (1983) has given one of the approximation for the Roche lobe radius around primary star. By changing q by 1/q in Eqn. 1.3, the Roche lobe radius around secondary is obtained.

$$\frac{R_L}{a} = \frac{0.49q^{\frac{2}{3}}}{0.6q^{\frac{2}{3}} + ln(1+q^{\frac{1}{3}})} \tag{1.3}$$

The R_L/a decrease when mass is transferred from M_1 to M_2. During the mass transfer if the mass ratio $q < 1$, then the Roche radius increases and if $q > 1$ the Roche radius decreases. The final outcome of mass transfer depends on the the initial evolutionary stage and envelope structure of the donor star, type of the accretor and the mass ratio q.

The mass transfer is conventionally classified into three categories based on the evolutionary state of donor, where the star expands and consequently can exceed the Roche volume. Kippenhahn and Weigert (1967) introduced Case A and Case B mass transfer and later Lauterborn (1970) introduced the Case C mass transfer.

Case A mass transfer occurs when the donor is on the MS with hydrogen burning in its core. The initial mass transfer rate is rapid and occurs on a Kelvin-Helmholtz timescale. After a certain duration, the mass ratio is reversed, followed by gradual increase in the mass of the secondary, which occurs on a nuclear timescale. The initial binary separation must be small enough for the RLOF to occur during donor's MS phase. Various factors could lead to a close binary configuration such as magnetic braking, tidal evolution or a perturbation caused by a third companion in a triple system. An interaction of other stellar bodies in a dense environment could lead to formation of a tight binary system or exchange of system to produce a short period binary.

Case B occurs during the end of MS phase of the donor, after the exhaustion of hydrogen in its core and before helium ignition. The donor star is on the Hertzsprung gap and mainly has a radiative envelope. At this stage, the radius of the donor expands its outer envelope filling the Roche volume. As soon as it reaches the critical radius the mass transfer begins. In the case of low mass stars electron degeneracy sets in at the core, when the hydrogen shell decreases. The contraction of the core occurs, therefore the rapid phase of expansion of the envelope does not occur. The increase in temperature is limited and does not ignite Helium. The mass transfer halts after the exhaustion of the H shell.

Case C occurs during the advance stage of evolution, when the core of the donor star has completed helium burning. The binary period in such cases can be expected to be in the range of a few tens to a thousand days, as the donor star is already in a much evolved phase with a large radius. As the radius of the star is large and exceeds the Roche radius RLOF can take place.

The outcome of the binary evolution when the RLOF occurs can be quiet different depending on whether the mass transfer is stable or unstable. The structure of the accretor also changes drastically after mass accretion from the donor occurs. The evolution of the star could be dramatically different and depends on its current evolutionary phase and its mass. Finally some of the exotic systems and phenomenon observed in the universe are the effects of the complexity and interplay of binary systems.

1.5 Exotic Stellar types in Old Open Clusters

The exotic stars in star clusters are attributed to presence of binary or multiple stars in the system, often formed through internal binary evolution or during dynamical interaction between binaries and other stars. Some of the examples of exotic stellar types in open clusters include blue straggler stars (BSSs), yellow straggler stars (YSSs), sub-subgiants (SSGs), cataclysmic variables (CVs), all of which require the presence of binary or multiple stellar systems. The formation and evolution scenario for some of these exotic objects are not well understood, as they do not follow the standard single-star evolution theory.

1.5.1 Blue Straggler Stars

BSSs are cluster members, that are brighter and bluer than the MSTO in the cluster CMD, a region from which most of the stars of same mass and age have evolved. Sandage (1953) discovered these stars in the globular cluster M3. The formation pathways and evolution of these stars are not well understood as they defy standard single stellar evolutionary theory. They seem to be rejuvenated stars, and gained mass as a consequence of some uncommon process. There have been various possible explanation for the BSSs, with three widely accepted mechanism in the literature: (i) stellar collision of two or more stars in dense environment (Hills and Day, 1976), (ii) mass tranfer through RLOF in a binary system (McCrea, 1964) and (iii) mass transfer resulting in a coalescence of the inner binary stars in hierarchical triples (Perets and Fabrycky, 2009; Naoz and Fabrycky, 2014). Though these mechanism have been strongly supported with several evidence, there are some BSSs that cannot be explained by these models (Cannon, 2015).

A large number of BSSs are found in open clusters, about 1887 BSS candidates in 427 open clusters are catalogued (Ahumada and Lapasset, 2007). M67 with its several studies on BSSs has been the primary laboratory (Mathieu and Latham, 1986; Mathys, 1991; Gilliland and Brown, 1992; Landsman et al., 1998; Deng et al., 1999; Liu et al., 2008; Bertelli Motta et al., 2018) while NGC 188 which has 20 BSSs in the cluster has been developed as a new laboratory (Mathieu and Geller, 2009; Geller and Mathieu, 2011; Geller et al., 2013; Mathieu and Geller, 2015; Gosnell et al., 2015) to understand the properties of BSSs found in open clusters. Gosnell et al. (2015) detected WD companions to a BSSs in NGC 188 and indicated that the BSSs in the cluster were possibly formed through mass transfer. The likelihood of a single-single star collision in a less dense environment such as an open cluster is prohibitively small. For a direct collision to occur, a dynamical environment involving encounters of single and or binary systems is essential. The mass transfer could occur through either of the Case A, B or C depending on the evolutionary state of the donor. A WD companion is expected in Case

B mass transfer, whereas CO WD in Case C mass transfer. Case A mass transfer, which generally happens in tight binaries, results in a merged product. The BSSs in such cases may be a product of two MS stars, which might have come in contact through stellar evolutionary processes. In case a stable mass transfer happens, sufficient mass to the secondary could be added to transform it into a BSS or due to the loss of orbital angular momentum via winds could lead to a tight binary system to form a merger product.

Another possible formation of BSSs is through an encounter of a single or a binary star with another binary system. In the case of binary-single encounters, the single star which encounters the binary could break the system, if the separation of the binaries are sufficiently wide. This occurs if the kinetic energy of the incoming star is larger than the binding energy of the binary. These binaries are known as soft, whereas the binaries that are bound tightly are known as hard. The soft binaries break, while the hard binaries become harder. The less massive of three stars is ejected in an exchange encounter. Therefore encounters involving binaries would increase the mass of the stellar objects within the binaries. An encounter can occur if the size of the binary is equal to the distance between the single and the binary system. Similar distance is required for a binary-binary encounters. A typical binary-binary encounter would produce a transient or stable hierarchical triple and single star. As open clusters have lower number densities of stars, collision and followed interaction between binary-binary systems may not dominate.

The theoretical model of BSSs in open cluster environment predicts that they are likely formed through mass transfer or merger. The binary frequency observed among the BSSs in open clusters are high with most of them being spectroscopic binaries (Mathieu and Geller, 2009; Geller et al., 2015). The stellar rotational velocities of the BSSs are higher, in some cases Vsin$i \geq$ 50 km s^{-1}. The observation suggests that a few BSSs in NGC 188 and M67 are rotating more rapidly than the normal MS stars of similar effective temperature. The observational properties of a few BSSs in open clusters have shown that they are 0.2 - 0.8 M$_{\odot}$ more massive than the MSTO. As the BSSs are more massive than the MSTO, they are expected to have experienced mass segregation resulting in a centrally concentrated distribution. The radial distribution of BSSs, are in-fact found to be centrally concentrated in open clusters (Mathieu and Latham, 1986). Though recent studies of a few open clusters have revealed a bi-modal distribution of BSSs, with a central concentration and a few stars in the outer regions of the cluster (Geller et al., 2008). The bi-modal distribution depends on the cluster properties, mainly attributed to the relaxation time of the cluster.

1.5.2 Yellow Straggler Stars

Yellow straggler stars are objects that are located blue-ward of the RGB and above the SGB in the optical CMDs. They are often referred as yellow giants. Mathieu and Latham (1986) studied these stars in M67 and found that most of these were spectroscopic binaries. They are also identified as cluster members based on their proper motion and radial velocity members. Landsman et al. (1997) detected one of the YSS (WOCS 2002) with a WD companion, that has undergone mass transfer, whereas Leiner et al. (2016) conclude that a merger or collision is most likely to have occurred in WOCS 1015 and thus YSSs are likely to be evolved BSSs. Therefore, similar to the BSSs, various mechanism are suggested for the formation of YSSs.

1.5.3 Sub - Subgiants

Sub-sub giants are a new class of stars, which occupy a unique location in the CMD, red ward of the MS and fainter than the SGB where normal single star evolution does not predict stars. They were first discovered in the old open cluster M67 in the ROSAT X-ray studies as X-ray sources (Belloni et al., 1998). Mathieu et al. (2003) presented a detailed description of SSGs and suggested that they may be products of close stellar encounters in cluster environment consisting of binaries. The radial velocity and proper motion studies of these systems confirm them to be members of the cluster. Geller et al. (2017) studied these objects in 16 open and globular clusters to understand their properties and location in the CMD. They found that more than 58% of these objects were X-ray sources with typical luminosities of the order 10^{30} - 10^{31} erg s^{-1}. Leiner et al. (2017) discussed the three possible formation pathways of SSGs which can populate the SSG region in the CMD: mass transfer in a binary system, a dynamical encounter that could lead to stripping of the SG's envelope and the decrease in luminosity due to large star-spots that were produced due to magnetic fields which lower convective efficiency. Their estimation of the formation frequency of SSG systems produced from either of these mechanism find magnetic field hypothesis to generate most of these objects in open clusters.

1.5.4 Cataclysmic Variables

Cataclysmic variables are binary stars, in which one component is a WD and the secondary may be a RG, a dwarf or a WD itself. There are various types of CVs that exist: novae, recurrent novae, dwarf novae, nova-like variables and magnetic accreting stars. These systems exhibit sudden outbursts in which an increase in luminosity becomes visible that are much greater than their normal value. Many of these systems are in close binaries and hence influence the evolution of each star. Nova is the best semi-detached binary system known with very large outburst occurring, that rapidly rises and

falls down slowly. This occurs due to a sudden nuclear fusion reaction of hydrogen in the hot envelope of the degenerate primary star. In the recurrent nova, a similar phenomenon is observed though with a smaller amplitude in comparison to the nova. The separation between successive outbursts is in the range of 10 to 50 years. In a dwarf nova a sudden increase in the luminosity of the accretion disk occur, which is due to large amount of material accreted. They have frequent but small outbursts.

In a standard model of a CV, the secondary is a hydrogen burning star, which is a MS star. The RLOF occurs with the secondary filling its Roche lobe and therefore the material flows towards the WD. In the absence of a magnetic field, an accretion disk around the primary is formed due to inflow of the material. The location where the stream of matter hits the accretion disk is the 'bright/hot spot'. In the presence of a magnetic field, the matter flows towards the magnetic pole of the companion guided by the field lines.

1.6 Motivation and Aim of the Thesis

Star clusters are ideal laboratories to study the stellar population in the host galaxy. The single and binary evolution of stars are easy to study in the star clusters as age, distance and redding are known and hence the fundamental parameters such as effective temperature, luminosity can be estimated. Old open clusters are ideal to study the low mass star evolution which sample all the evolutionary phases such as BSS, sub giant (SG), red giant (RG). As the age of these clusters are of the order of the binary evolution time; these are ideal objects to detect, and study the evolution of various types of binary systems. As we require full membership and kinematic details, we have selected two old open cluster NGC 188 and M67, which are known to have enough stars in the above evolutionary phases. The old open cluster M67 and NGC 188 are well studied clusters that consists of both single and binary stellar population. They also have large number and variety of exotic stellar types. Therefore, these clusters are ideal test-beds to study stellar evolution of stars and understand the properties.

Multiwavelength study of these stars including UV and X-rays help to identify single and binary stars and estimate their properties in these clusters. The UV wavelength is crucial in understanding the hotter population of the cluster, as they emit significant fraction of flux in the UV. The X-ray flux can provide information of accretion from the secondary in a binary system, presence of flares, coronal activity, star spots and chromospheric activity. Detection of UV/X-ray is expected to provide understanding of the active stellar properties of low-mass stars. The multiwavelength study will as well throw light on the evolutionary status of the exotic stellar population known as BSS, YSS that are known to be present in two old open cluster M67 and NGC 188. In Fig. 1.5, we have shown the old open cluster M67 in four different wavelength bands:

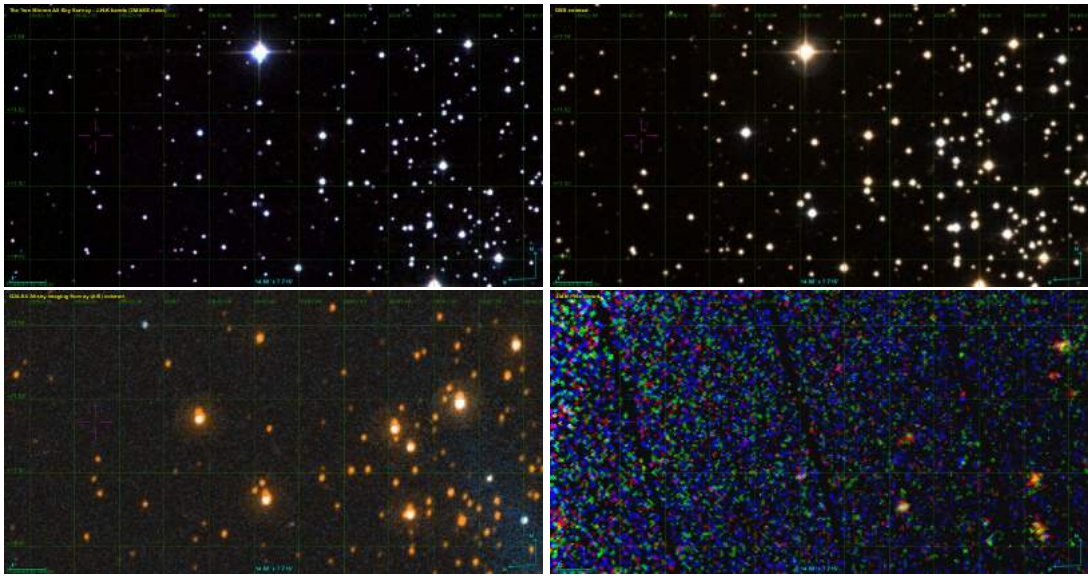

Fig. 1.5 A Multiwavelength Image of a Small Region of M67 in Four Wavelength bands. (Top Panel:) A Colour Composite IR Image in J, H and K Bands from 2MASS and A Colour Composite Optical Image from DSS, (Bottom Panel:) A Colour Composite UV Image in FUV and NUV Bands from GALEX mission and An X-ray Image using PN CCD array of XMM Newton Mission. The FOV of all Images are $\sim 14' \times 7.7'$

Infrared (IR), optical, UV and X-rays. It can be seen from this figure that some stars appear brighter in a particular wavelength, while fainter in other wavelength bands. Therefore, their dominance in particular wavelength depends on the physical properties of the star such as temperature, luminosity. Gosnell et al. (2015) detected 7 WD companions to BSSs in the old open cluster NGC 188 using the far-UV (FUV) images of HST. Motivated by this study we observed the same cluster using Ultra Violet Imaging Telescope (UVIT) on ASTROSAT which has multiple filters in the FUV and near-UV (NUV) wavelength bands. M67 is another cluster that has a large number of BSSs, that has been extensively studied since its first identification in the classical paper by Johnson and Sandage (1955), though there has been no conclusive understanding of their formation and evolution. Hence we study this cluster to estimate their fundamental parameters and understand their formation pathways. Further, M67 is well studied in optical, IR and X-ray but lack a comprehensive deep-study in the UV, hence we study the stellar population in UV and combine it with other wavelength bands.

The aim of this study is to understand the single and binary stellar evolution of stars in old open clusters using multiwavelength data. Several exotic stars in the clusters are formed through uncommon processes. We plot the CMDs in UV and optical. We identify the location of single as well as binary evolutionary products in the CMDs. We also combine the photometry in a wide range of wavelength to construct their spectral energy distribution (SED) to estimate the fundamental parameters such as effective temperature, luminosity and radius of stars which are evolved through single as well as

binary stellar evolutionary processes.

1.7 Structure of the Thesis

The thesis includes eight chapters and an outline of the thesis is given below:

- *Chapter 1* - This chapter introduces star clusters found in our Galaxy. A brief description of single stellar and binary evolution along with exotic stellar types observed in open clusters are given. We describe our motivation of the current work and highlight the importance of using multiwavelength data.

- *Chapter 2* - Details of the multiwavelength data that have been used for the present study are presented.

- *Chapter 3* -We have used various methods in the thesis, a detail description of these methods are presented in this chapter.

- *Chapter 4* - The discovery of a hot companion to a BSS in NGC 188 and the possible formation pathway are presented in this chapter.

- *Chapter 5* - The first comprehensive UV study of M67 using a deep photometric data from Galaxy evolution explorer (GALEX) mission is presented. We have detected UV flux from various types of stars. We present the UV and UV-optical CMDs and have discussed the reasons for their excess UV flux.

- *Chapter 6* - In this chapter, we have examined 45 stars in detail, which have a fairly large amount of flux in the UV. We have estimated the fundamental parameters of these stars by fitting SEDs.

- *Chapter 7* - We have observed the cluster M67 using UVIT, using multiple FUV filters. The flux of 9 BSS detected in the UVIT images are presented. The SED analysis using single and double SED fits of 9 BSS lead to the detection of WD companions to 6 BSS. We discuss the possible formation pathways in this chapter.

- *Chapter 8* - The summary and the outcome of the present work has been summarised in this chapter, with a discussion on future work.

CHAPTER 2

Multiwavelength Data: X-ray to Infrared

2.1 Introduction

In general, observations covering a large wavelength range require more than one instrument, and often, more than one observatory. Also, the observatories in the ground cover only those wavelength which are transmitted by the atmosphere. In order to detect wavelengths which are blocked by the atmosphere, one needs to use space based observatories. In this study we have used X-ray to infrared (IR) part of the electromagnetic spectrum, which thus require a combination of ground and space based observatories.

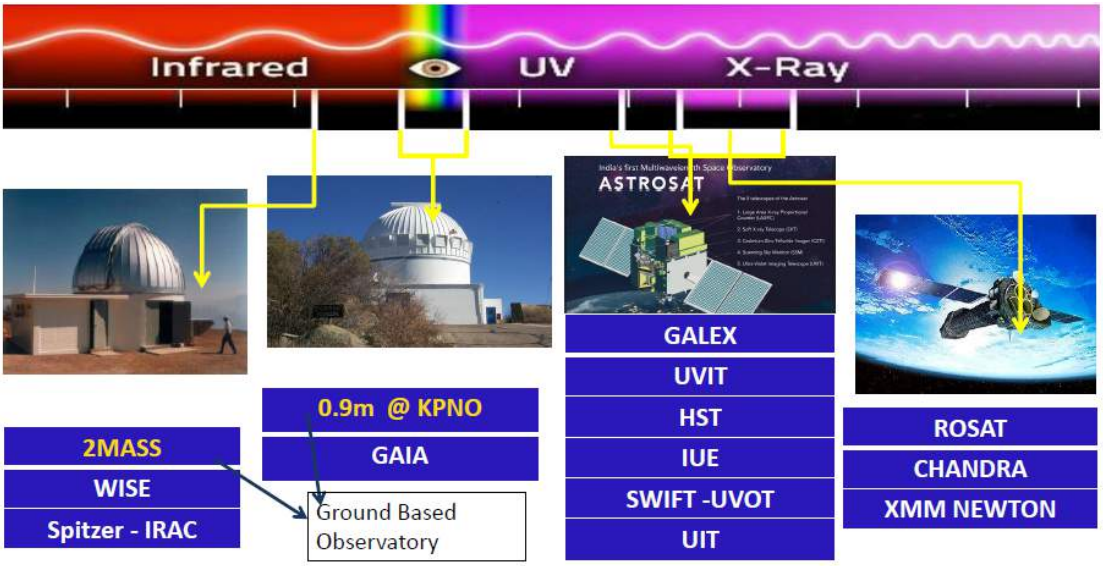

Fig. 2.1 The Multiwavelength Data from IR to X-ray taken from various Observatories Utilized in this Thesis. The Images of a few Telescopes are Shown. (From Left:) Southern 2MASS Observatory at Cerro-Tololo Inter-American Observatory (CTIO), Chile; 0.9 m Telescope at Kitt Peak National Observatory (KPNO); Schematic View of ASTROSAT Multiwavelength Observatory and Chandra X-ray Observatory. Image Credits: 2MASS, KPNO, ISRO, NASA

In this chapter we describe all science instruments/telescopes from which we have obtained the data. We have utilised multiwavelength archival data from both ground and space based observatories, covering a broadband of the electromagnetic spectra from the UV to the IR (0.14 to 11.5 μm) (Fig. 2.1). Apart from the archival data, two clusters were observed using the UVIT on board the ASTROSAT (Fig. 2.2),

which is the first Indian multiwavelength satellite (Subramaniam, 2012). In Fig. 2.3, we have shown the spectral response curve at various wavelength bands of all the filters used in this study. The response curve are taken from the Spanish Virtual Observatory filter profile service (http://svo2.cab.inta-csic.es/theory/fps/).

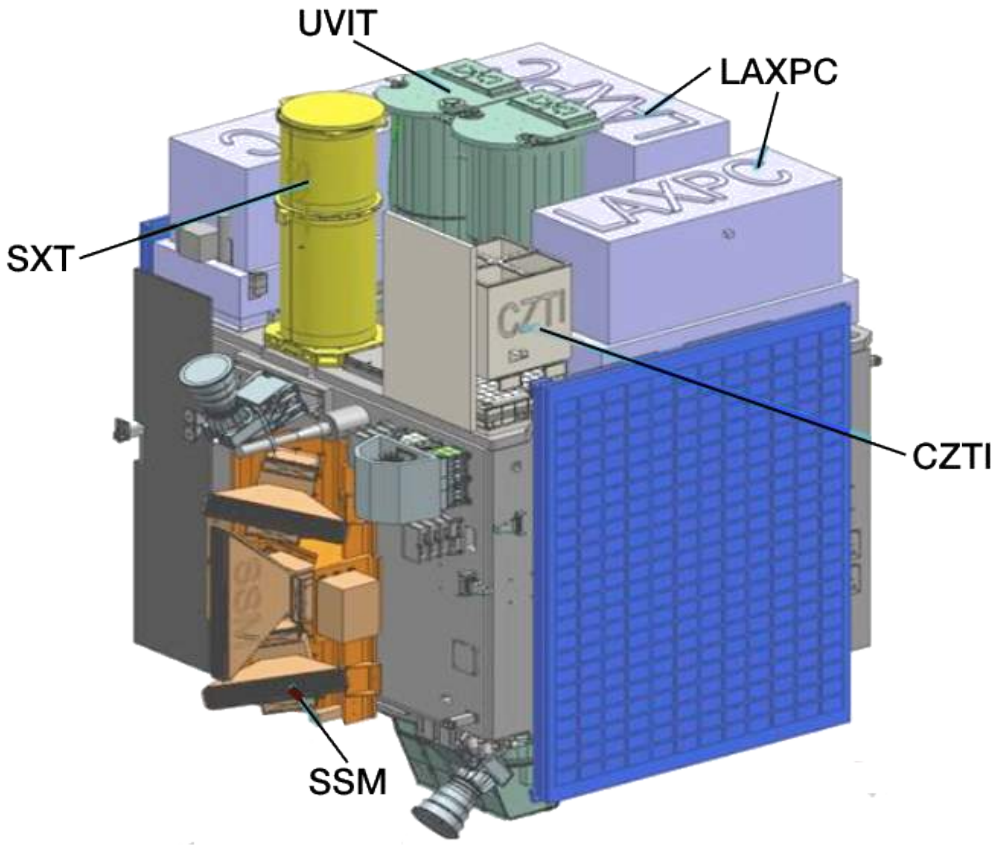

Fig. 2.2 The Multiwavelength ASTROSAT Satellite Consists of Five Payloads viz. Ultra-Violet Imaging Telescopes (UVIT), Large Area Xenon Proportional Counters (LAXPC), Soft X-ray Telescope (SXP), Cadmium-Zinc Telluride Coded-Mask Imager (CZTI) and Scanning Sky Monitor (SSM). Image Courtesy: ASTROSAT Webpage of Inter-Univesity Centre for Astronomy and Astrophysics

2.2 Ultraviolet Data

The UV radiation are classified into different wavelength ranges referred as extreme-UV (EUV) (100 - 912 Å), Lyman-UV (912 - 1150 Å), FUV (1150 -1800 Å), and NUV (1800 -3200 Å). In general, UV telescope is dedicated to one of these wavelength ranges. We have obtained photometric data from UVIT, GALEX, Ultraviolet Imaging Telescope (UIT) and Ultraviolet Optical Telescope (UVOT) and archival spectroscopic data for a few stars from International Ultraviolet Explorer (IUE) and Hubble Space Telescope (HST). The UV telescopes, filters and wavelength region used in this work are listed in Table 2.1.

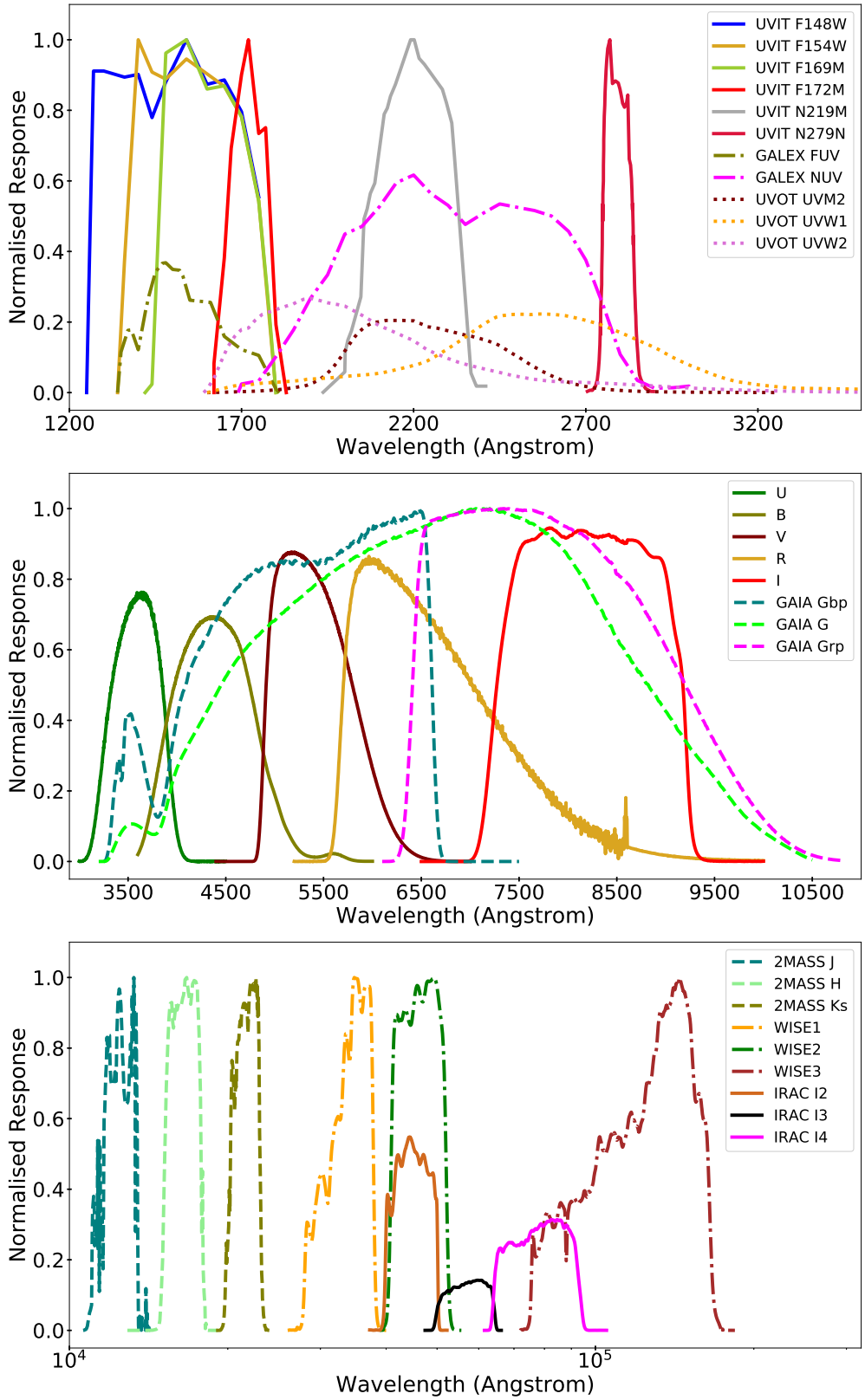

Fig. 2.3 Response Curve of all Filters Utilized in this Study in UV (top), Optical (middle) and IR (bottom) Wavelength Regions

Table 2.1 UV Telescopes, their Operation Dates, Filter Systems used in the present Work, Wavelength band (Å) and References

Telescope	Operation Dates	Filters	Wavelength Band (Å)	Reference
UVIT	2015 -present	F148W, F154W, F169M, F172M, N219M, N272N	1300 - 3000	Tandon et al. (2017)
UVOT	2004 - present	UVM2, UVW1, UVW2	1700 - 3000	Mason et al. (2004)
GALEX	2003-2013	FUV, NUV	1300 - 2800	Morrissey et al. (2007)
HST	1990 - present	G230LB, G430L, G230L, PRISM	1146 - 6000	Kimble et al. (1998)
UIT	1990,1995	B1, B5	1200 - 2200	Stecher et al. (1992)
IUE	1978 -1996	LWP, SWP	1250 - 3000	Boggess et al. (1978)

2.2.1 Ultra-Violet Imaging Telescope (UVIT)

UVIT is one of the payloads on board the ASTROSAT satellite, which was launched on 28^{th} September 2015 by Indian Space Research Organisation (ISRO). UVIT has a twin 38 cm Ritchey-Chretien (RC) configuration telescope with three channels: FUV (1300 - 1800 Å), NUV (2000 - 3000 Å) and visible (3500 - 5500 Å). One of the telescopes carries the FUV channel and the other telescope simultaneously images in both the NUV and visible channels. The incoming light beam is divided by a dichroic beam splitter, where the visible beam is transmitted and the NUV beam is reflected. The visible channel primarily provides the pointing information. UVIT consists of five filters within each channel enabling imaging at different spectral region. Two gratings in the FUV and NUV channels are provided for a low resolution ($\sim$100) slitless spectroscopy. UVIT provides flux calibrated image at a spatial resolution of $\sim$1.5$''$ in FUV and $\sim$1.4$''$ in NUV with a $\sim$28$'$ field of view (FOV). The images are recorded at a frame rate of 29 frames per second on the CMOS imaging detector in photon counting mode (UV channels). Additional details regarding the instruments, on-orbit performance and calibration are described in Hutchings (2014*a*), Hutchings (2014*b*) and Tandon et al. (2017).

2.2.2 Ultraviolet Optical Telescope (UVOT)

The UVOT is one of the three payload on Swift Gamma-ray observatory. It is a 30 cm aperture UV/optical telescope with a modified RC optical design that allows observation in UV or optical wavelength range (1700 - 6500 Å). It consists of seven broad band filters and two low resolution grisms. UVOT has a FOV of 17 $'$ and a spatial resolution of 0.9$''$. The telescope has a micro channel intensified CCD detector that operates in a photon-counting mode. Mason et al. (2004) and Roming et al. (2005) present details of ground calibration, in-orbit calibration and instrument.

2.2.3 Galaxy Evolution Explorer (GALEX)

GALEX mission was aimed at both imaging and spectroscopic surveys simultaneously in two broad bands, FUV (1350$-$1750 Å; λ_{eff} - 1539 Å) and NUV (1750$-$2750 Å; λ_{eff} - 2316 Å). The two channels are separated with a dichroic beam splitter, the FUV is reflected and the NUV transmitted. It has a wide FOV of $\sim 1.2^{\circ}$ and a spatial resolution of 4.2$''$ and 5.3$''$ in FUV and NUV band respectively. Both the bands have an astrometric precision of the order 0.5$''$ rms. GALEX telescope consisted of RC configuration with a 50 cm primary mirror and a focal length of $\sim$300 cm. The incoming light is split into the two detectors simultaneously using a dichroic beam splitter. The individual photons are detected by the two photon-counting micro-channel plate detectors. GALEX performed sky surveys with different depth and coverage; viz. All-sky imaging survey (AIS), medium-depth imaging survey (MIS), deep-imaging sky survey (DIS) and guest investigator survey (GII) (Morrissey et al., 2007; Bianchi, 2009). These surveys had different exposure time, with a minimum of $\sim$100 s for AIS and upto $\sim$30000 s for DIS in selected fields. Martin et al. (2005) and Morrissey et al. (2007) have further described the details of its in-orbit performance and satellite.

2.2.4 Ultraviolet Imaging Telescope (UIT)

UIT was one of the three UV telescopes on the Astro-1/Astro-2 observatory flown twice on two different space shuttles (Stecher et al., 1992). UIT comprised of a 38 cm RC design telescope equipped with FUV and NUV channels covering a wavelength range of 1200 - 3200 Å. It had eleven band pass filters and a grating for imaging and spectroscopy. UIT images were recorded on Kodak IIa-O film and digitized with Perkin-Elmer 1010 m micro-densitometers. It could observe $\sim$ 40 arcmin region of the sky with an image resolution of $\sim$2.5 arcsec. Stecher et al. (1997) have explained in more detail about the instrument and data characteristics.

2.2.5 International Ultraviolet Explorer (IUE)

IUE was the first UV space observatory with 18 years of operation, observing astronomical targets in both FUV and NUV. IUE scientific instruments consisted of a 45 cm RC cassegrain configuration telescope, an off star tracker for fine guidance, an echelle spectrograph (1150 - 1950 Å and 1900 - 3200 Å) and television cameras. Four cameras were used, two for each spectrograph. Long wavelength prime (LWP) and long wavelength redundant (LWR) cameras were used for the long wavelength range and for the short-wavelength spectrograph, only the prime camera (SWP) was used during the mission. Only a handful of images were taken using the redundant (SWR) camera. The FOV of the telescope was $16'$ with an effective image resolution of about $8''$ and could obtain both high resolution (R $\approx$ 12000) and low resolution spectra. Boggess et al. (1978) have given further details of its instruments and in-flight performance.

2.2.6 Hubble Space Telescope (HST)

HST was launched into the low earth orbit in 1990, and is still in orbit providing exponential photometric and spectroscopic data in UV, optical and near infrared IR wavelength region. The telescope was named after the renowned astronomer Edwin Powell Hubble. The telescope has a primary mirror with a diameter of 2.4 m, with an angular resolution of $0.05''$. HST is the first spaced telescope designed to be serviced and upgraded in space by Astronauts. The telescope has a Cassegrain reflector of RC configuration. Space Telescope Imaging Spectrograph (STIS) is an instrument that was installed during the second Hubble servicing mission in 1997. The instrument was in non-operation condition between 2004 to 2009. STIS consists of a 3 detectors of 1024 $\times$ 1024 pixels: CCD, NUV Multi-Anode Microchannel Array (MAMA) and FUV MAMA. The CCD has a FOV of 52 $\times$ 52 arcsecond, that covers a wide wavelength range from $\sim$ 2000 to 10300 Å. The NUV MAMA is a Cs_2Te MAMA with a FOV of 25 $\times$ 25 arcsecond, which is operational in the NUV region from 1600 to 3100 Å. The FUV MAMA is a solar-blind CsI with a FOV of 25 $\times$ 25 arcsecond, covers the FUV wavelength band from 1150 to 1700 Å. The STIS instrument operates in both spectroscopy and imaging mode, with a choice of several filters for each detectors (Kimble et al., 1998).

2.3 Optical Data

The optical or visible radiation corresponds to a wavelength range between 3500 - 8000 Å. We have obtained archival data from the Kitt Peak National Observatory (KPNO) UBVRI filters and photometric data from the Global Astrometric Interferometer for Astrophysics (*Gaia*) data release (DR) 1 and 2 in three passbands, G, G_{bp} and G_{rp}. In

the Table 2.2 we have listed the optical telescopes, filters and wavelength band used in this work.

Table 2.2 Optical Telescopes, Filters and Wavelength Band are listed

Telescope	Operation Dates	Filters	Wavelength Band (Å)	Reference
GAIA	2013 - present	G, Gbp, Grp	3200 -10000	Gaia Collaboration et al. (2016)
Kitt Peak National Observatory (KPNO) (0.9 m)	1960 - present	U, B, V, R, I	3000 - 9300	Montgomery et al. (1993); Sarajedini et al. (1999)

2.3.1 Global Astrometric Interferometer for Astrophysics (Gaia)

Gaia is a space observatory placed at the second Lagragian point (L2) in an orbit around the Sun. The scientific payload comprises of a single integrated instrument that includes three major functions using two common telescopes having a FOV of 0.32 deg^2. *Gaia* mission is dedicated to perform astrometry with an astrometric instrument (ASTRO), photometry in the wavelength region 3200 - 10000 Å using the photometric instrument, and radial velocity and high resolution (R $\approx$ 11500) spectroscopy in the narrow band 8470 - 8740 Å using the radial velocity spectrometer (RVS) on a 0.5 m $\times$ 1.0 m CCD detector array. *Gaia* has three optical photometric band pass: G (3300-10500 Å), G_{bp} (3300-6800 Å) and G_{rp} (6400-10500 Å). *Gaia* performs a continuous sky survey in two simultaneous FOV along great circles.

2.3.2 Kitt Peak National Observatory (KPNO) 0.9 m Telescope

The 0.9 m at KPNO is a Cassegrain telescope with a focal ratio of 7.5 and a wide FOV of 1 degree. A standard set of UBVRI filters were used during the observation. The filter details are listed in https://www.noao.edu/kpno/mosaic/filters/filters.html. We have utilized optical data of the two clusters M67 and NGC 188 from Montgomery et al. (1993) and Sarajedini et al. (1999) and cross identified with other wavelength data. More detailed information regarding observation and photometry are given in these references.

2.4 Infrared Data

The infrared radiation covers the longer wavelength region between 1 - 350 microns. It is usually subdivided into three regions, near-IR (1 - 5 μm), mid-IR (5 - 40 μm)

and far-IR (40 - 350 μm). We have utilised the photometric data from three different IR mission viz. Two Micron All Sky Survey (2MASS), Wide-field Infrared Survey (WISE) and Infrared Array Camera (IRAC) on Spitzer Observatory in our present work. A brief detail of the telescopes, filters and wavelength range are listed in Table 2.3.

Table 2.3 Infrared Telescopes, Filters and Wavelength Band are listed.

Telescope	Operation Dates	Filters	Wavelength Band (μm)	Reference
Two Micron All Sky Survey (2MASS)	1997 - 2001	J, H, K_s	1.0 - 2.31	Cohen et al. (2003)
Infrared Array Camera (IRAC)	2003 - present	I2, I3, I4	3.9 - 9.5	Fazio et al. (2004)
Wide-field Infrared Survey Explorer (WISE)	2009 - 2011	W1, W2, W3	2.7 - 17.2	Wright et al. (2010)

2.4.1 Two Micron All Sky Survey (2MASS)

2MASS survey consisted of two 1.3m equatorial Cassegrain telescopes located at Mount Hopkins in Arizona and at Cerro Tololo Inter-American Observatory (CTIO) in Chile for observing the northern and southern sky respectively. Each telescope was equipped with three filters in the J (1.0 - 1.4 μm), H (1.4 - 1.8 μm) and K_s (1.9 - 2.3 μm) near -IR band, that comprised of three 256 $\times$ 256 array of NICMOS3 (HgCdTe) detectors. Simultaneous imaging was performed in all three bands using two dichroic mirrors within each camera covering a $8'.5 \times 8'.5$ FOV with a plate scale of $2''$ per pixel. The science products from the survey contained a point source catalogue which comprised of over 500 million stars and galaxies along with 1.6 million resolved galaxies in the extended source catalogue (Skrutskie et al., 2006). The 2MASS all sky data were made available for the public in 2003, which imaged nearly 99% of the sky.

2.4.2 Infrared Array Camera (IRAC)

Spitzer space telescope is the first largest IR telescope with a 85 cm aperture and comprises three scientific instruments. IRAC is one of the three instruments with four channels, I1 (3.1 - 3.9 μm), I2 (3.9 - 5.0 μm), I3 (4.8 - 6.5 μm) and I4 (6.2 - 9.5 μm) that acquires broadband images simultaneously on four detector arrays of 256 $\times$ 256 pixels in size with each pixel corresponding to $\sim 1''.2$. Indium Antimony (IdSb) detectors are used for the two shorter wavelength bands and Si:As detectors for the two longer wavelength bands. IRAC has two FOVs of $5'.2 \times 5'.2$ projected from the two

pick-off mirrors that reflect the incoming light beam from the telescope. The dichroic beam-splitters are used to produce adjacent FOV in pairs (3.6 and 5.8 μm; 4.5 and 8.0 μm). The image resolutions are $\sim$1$''$.6, $\sim$1$''$.6, $\sim$1$''$.8, and $\sim$1$''$.9 at 3.6, 4.5, 5.8 and 8.0 μm, respectively. Fazio et al. (2004) have given a comprehensive description of the instrument.

2.4.3 Wide-field Infrared Survey Explorer (WISE)

WISE instrument contains a 40 cm telescope that maps the sky in four channels W1 (2.7 - 3.8 μm), W2 (3.9 - 5.3 μm), W3 (7.4 - 17.2 μm), and W4 (19.5 -27.9 μm) which operates in a single mode in the mid-IR region. The telescope is equipped with four 1024 $\times$ 1024 mercury cadmium telluride (HgCdTe) (for the two mid-wavelength channels) and Si:As detector (for the long wavelength channels) arrays at a pixel scale of 2$''$.75 pixel^{-1}, capable of imaging simultaneously in all four bands with the usage of a dichroic beam splitters. WISE has a wide FOV of 47$'$ $\times$ 47$'$ and a spatial resolution of $\sim$ 6$''$ in the three bands and 12$''$ in W4. A cryostat provides ambient temperature for cooling the payload at a temperature of $<$ 12 K for the telescopes and less than 7.5 K for the Si:As detectors. Wright et al. (2010) present a detailed information of the mission and its initial in - orbit performance. Larsen and Schick (2005) and Mainzer et al. (2005) have given a brief report of the mission payload.

2.5 X-ray Data

In the present work, we have cross-identified the stars of a cluster detected in other wavelength bands with its X-ray counterparts. A few member stars emit in the X-ray as observed in one or more X-ray missions. We have used archival data from three missions Roentgen Satellite (ROSAT), Chandra X-ray observatory (Chandra) and X-ray Multi-mirror Newton mission (XMM- Newton) (Belloni et al., 1993; Belloni et al., 1998; Van den Berg et al., 2004; Mooley and Singh, 2015). Here, we give a brief description of these missions and list the instruments used in this work in Table 2.4

2.5.1 Roentgen Satellite (ROSAT)

ROSAT was an X-ray observatory with two scientific payloads, the X-ray telescope (XRT) was one of the payload comprising of a fourfold concentric Wolter type - I grazing incidence mirror, with its 2.4 m focal-length mirror assembly and a maximum aperture of 85 cm for the soft X-rays (0.1 -2.4 keV). The focal plane instruments consisted of two Position Sensitive Proportional Counters (PSPC) and a high resolution imager for the XRT. The FOV of PSPC was $\sim$ 2° and $\sim$ 40$'$ with the high resolution imager in their focal plane (Briel and Pfeffermann, 1995; Zombeck et al., 1995). The limiting

Table 2.4 Details of X-ray Mission, Scientific Instruments and Energy Band are listed

Telescope	Operation Dates	Instrument	Energy Band (keV)	Reference
Roentgen Satellite (ROSAT)	1990 - 1999	PSPC	0.1 - 2.4	Briel and Pfeffermann (1995)
Chandra X-ray observatory (Chandra)	1999- present	ACIS	0.2 - 10	Weisskopf et al. (2000)
X-ray Multi-Mirror - Newton mission (XMM-Newton)	1999 - present	EPIC MOS, EPIC pn	0.15 - 12	Strüder et al. (2001); Turner et al. (2001)

resolution of PSPC was $25''$ on-axis and due to telescope aberrations could degrade to few arcminute for larger off-axis, while high resolution imager had a better resolution of $3''$. The main science goal of ROSAT's PSPC instrument was to perform all-sky X-ray survey (Aschenbach, 1988).

2.5.2 Chandra X-ray Observatory (Chandra)

The Chandra telescope is a space based observatory detecting objects in the X-ray domain. The telescope was named in honour of the late Nobel laureate in Astrophysics, Subrahmanyan Chandrasekhar. The telescope is a high resolution mirror assembly, which has two sets of four nested mirrors with a FOV $\approx 1^{\circ}$ diameter and angular resolution of $0.5''$. It has two focal plane science instruments, a high resolution camera and Advanced CCD Imaging Spectrometer (ACIS), each of which can perform imaging or spectroscopy and is positioned at the narrow end of the telescope cylinder to converge X-rays. Additionally two other instruments on Chandra are dedicated to high resolution spectroscopy, the high and low energy transmission gratings, which is positioned behind the mirror to perform spectroscopy. The high resolution camera covers the energy range of 0.1 to 10 keV, covering a FOV of 31×31 arcmin and uses micro-channel plates to detect X-ray photons. The ACIS consists of two CCD arrays to obtain simultaneous time-resolved imaging and spectroscopy. These two detectors are covered with alumninized -polyimide optical blocking filter. It covers a spectral range of 0.2 to 10 keV with a wider FOV of $16' \times 16'$ and a smaller ($8' \times 8'$) FOV, when a low energy response is favoured (Weisskopf et al., 2000).

2.5.3 X-ray Multi-Mirror - Newton (XMM- Newton)

The XMM-Newton mission consists of three XRT of Wolter type I and a optical/UV telescope. The XRTs consists of three CCD European Photon Imaging Cameras (EPICs) for imaging and spectrometry, located at the prime focus of each telescope covering a FOV of 30 $'$ in the energy band 0.15 to 12 keV. Two of the EPICs are equipped with metal oxide semi-conductor (MOS) CCD arrays and the third one uses a pn CCD array. The EPIC have an angular resolution of 6$''$, and the CCD operate in photon counting mode. Each EPIC contains four filters: two thin filters, a medium and a thick filters. The EPIC instruments that has MOS CCDs are fitted with the X-ray gratting of reflection grating spectrometer. Strüder et al. (2001) and Turner et al. (2001) present a detailed description about these instruments.

2.6 Summary

A brief description of the instruments and filters are given in this chapter, with information about its spectral coverage, FOV and its resolution. We have mainly emphasized on filters/band pass that are used in the current work and have given only their details in all the tables. The multiwavelength data used in this study are summarised below:

- UVIT - UVIT is a space telescope on ASTROSAT. The telescope has three channels; optical (3200 - 5500 Å), FUV (1300 - 1800 Å) and NUV (2000 - 3000 Å) consisting of 5 filters in each channel. We have observed the two old open clusters NGC 188 and M67 using this telescope. The observation details of the old open clusters are given in the respective chapters 4 and 7.

- UVOT - We have obtained UVOT data from Siegel et al. (2014) and have used in the analysis of a star in NGC 188 in chapter 4.

- UIT - The UIT photometric data from Landsman et al. (1998) are used in the analysis of a star in NGC 188 in chapter 4.

- HST - An archival spectra of a star in M67 is obtained using the STIS instrument on HST. We have used the spectra in our analysis in chapter 7.

- IUE - The telescope has observed a few stars in M67, among these 5 are BSSs and 2 are RGs. We have used these spectra in our analysis in chapter in 6 and 7. We have also obtained the photometric magnitudes at six wavelength bands of IUE from the spectrum.

- GALEX - We have used FUV and NUV photometric data for a star in NGC 188 in chapter 4. M67 is studied using a deep-UV data from GALEX mission in chapter

5 and 6. The photometric magnitude of a few BSSs are obtained from both the UV channels and used in the analysis in chapter 7.

- 0.9 m KPNO Telescope - The optical magnitudes in the UBVRI bands are obtained from Sarajedini et al. (1999) for the cluster NGC 188 and Montgomery et al. (1993) for the cluster M67, which was observed using this telescope. The optical data of the respective clusters are used in chapter 4, 5, 6 and 7.

- GAIA - We have obtained the *Gaia* DR-1 photometric data in G band in our study of M67 in chapter 6 and DR-2 data in G, G_{rp} and G_{bp} bands in chapter 7.

- 2MASS - We have used 2MASS photometric data in 3 wavelength bands - J, H and K_s for a star in NGC 188 in chapter 4, and for a few stars in M67 in chapter 6 and 7.

- IRAC - The IRAC telescope on Spitzer space observatory has 4 channels in the wavelength range 3.5 to 7.6 μm. We have used IRAC photometric data in 3 wavelength bands - I2, I3 and I4 for a star in NGC 188 in chapter 4.

- WISE - The WISE mission has 4 filters covering the wavelength range from 3.3 to 22.1 μm. We have obtained WISE photometric data in 3 wavelength bands - W1, W2 and W3 for a star in NGC 188 in chapter 4, and for a few stars in M67 in chapter 6 and 7. We have not taken the data from W4 as the photometric magnitudes in this filter are not usable as indicated by the photometric quality flag in the source catalogue.

- X-ray Data - The X-ray counterparts for stars in M67 are cross-identified from Belloni et al. (1998) (ROSAT), VandenBerg and Stetson (2004) (Chandra) and Mooley and Singh (2015) (XMM-Newton) and are presented in chapter 5.

CHAPTER 3

Research Methods

3.1 Introduction

In observational astronomy, the first step is to obtain the images/spectra of the celestial objects using a telescope from either ground or space based observatories. Each of these images has all the astronomical information, hence photometric or spectroscopic reductions are initially performed. In this chapter, we give a brief description of the research methods and data calibration that are implemented to infer the underlying physics of the electromagnetic radiation that we receive from the celestial objects. A discussion on the methods are essential, as the results of our analysis are based on these techniques. The most basic information that we receive from all the astronomical sources is the amount of energy, this quantity is described as flux. Photometry is the scientific process of measuring the flux of an astronomical body's electromagnetic radiation, over a broad wavelength bands. To begin with, a concise explanation of photometric reduction is given, followed by flexible stellar population synthesis code to generate isochrones (Conroy et al., 2009; Conroy and Gunn, 2010) and SED, covering the multiwavelength data.

3.2 UVIT Detectors

We have chosen two open clusters for the present study, and they are observed using the space telescope UVIT on board ASTROSAT. We have used a set of filters listed in Table 2.1. The images are recorded on the photon counting detector, which comprise of an image intensifier tube, fiber optic coupling and a micro channel plate based intensified Star250 CMOS image sensor with an aperture of $\sim$ 40 mm diameter as shown in Fig. 3.1. The science targets that are observed by UVIT has to be converted into scientific images to perform photometry, hence we have used CCDLAB which is developed for image reduction and viewing and is an interactive tool as shown in Fig. 3.2 (Postma and Leahy, 2017).

UVIT observes a single target during different orbits and the data is downloaded after each orbit. A level 1 data product is generated for the set of observations of the given target after completion of required exposure time. This level 1 data product

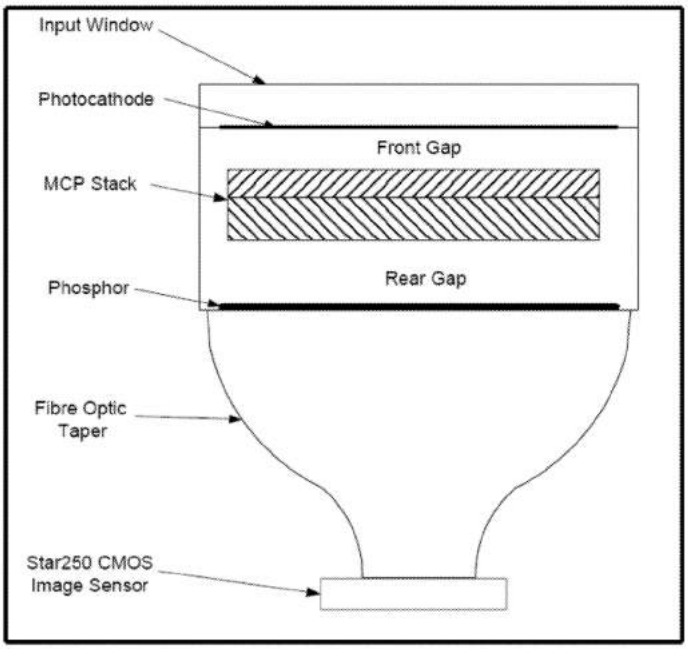

Fig. 3.1 A Diagram of the Photon Couting Detector of UVIT. Image Credit: Hutchings et al. (2007)

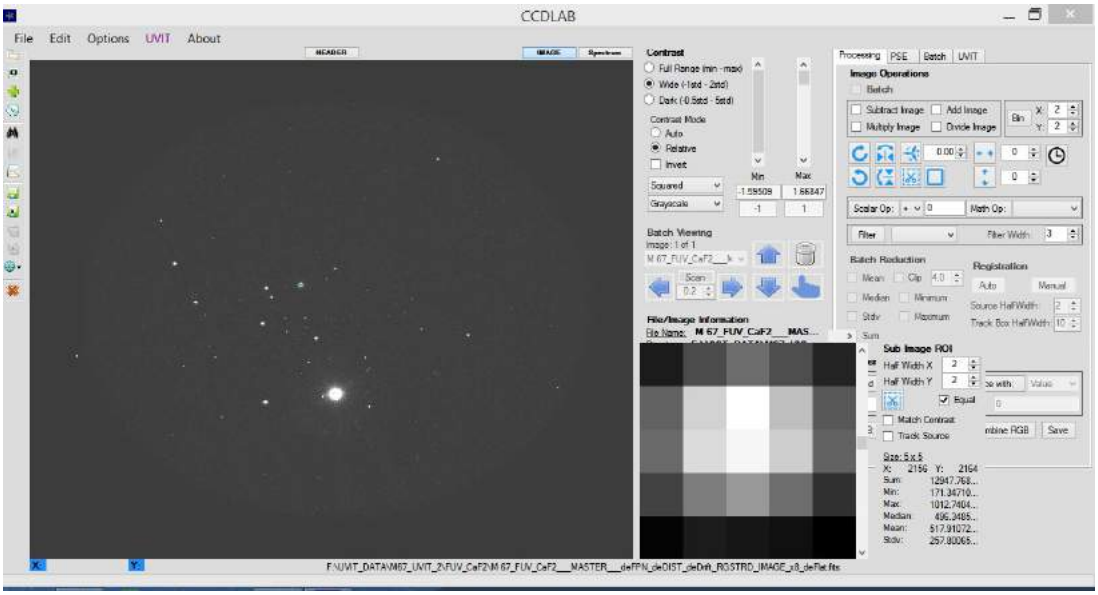

Fig. 3.2 A Screenshot of CCDLAB

is extracted using CCDLAB. This data may contain duplicate data sets, which was replicated partially or completely during different orbit numbers. The entire data sets are searched for, to discard duplication of images in all the filters that the target was observed, ensuring a unique data set.

The first step involves detector corrections, as any photometric reduction must be independent of the detector parameters. The parameters that must be removed from

the UVIT images are as follows:

- Field distortion : The field distortion is likely due to the fiber optic taper, and results in astrometric inaccuracy and this correction must be implemented. This is done by imaging a calibrated grid of holes depicting the distortion of the detectors of UVIT. Girish et al. (2017) have described the detailed procedure to estimate the distortions during ground calibration phase. These are incorporated in CCDLAB and are applied to correct for field distortion

- Centroiding bias: The photon counting mode of the UV detectors allows sub-pixel centroiding of the photon, which improves the source resolution and astrometric accuracy. In order to achieve this, an on-board centroiding algorithm is used, but this is affected by the systematic centroiding bias. The accuracy in estimating the sub-pixel centroid can be affected due to several factors, such as: coarse event sampling, which ultimately causes the centroid to become systematically less accurate as the pixel boundary and event center lie closer; usage of a linear centroiding design to estimate the center of a mostly, a Gaussian signal and a non uniform sensitive distribution of the individual CMOS pixel across its area - certain small regions of the pixel are more sensitive in comparison to other regions (Postma et al., 2011). A photon pulse detected on the CMOS falls on several pixels but within 3 $\times$3 pixels with a FWHM of $\sim$1.5 pixels. The poor profile of the centroiding, would thereby affect the weighted-mean centroid resulting in bias towards the center pixel of the 3 $\times$3 centroiding kernel. Therefore the centroiding bias creates fixed pattern noise, hence must be corrected. Hutchings et al. (2007) and Postma et al. (2011) have described the steps for correcting the centroiding bias. This task is performed with CCDLAB by applying the correction for the fixed pattern noise.

- Flat field: A pixel to pixel variation in detected flux occurs in the detector due to the broad difference between the high and low MCP gains and quantum efficiency of the detector. In general, a science exposure is normally divided by a flat field image to remove these variations. In the case of UVIT, a flat response was obtained using a UV-reflective integrating sphere with the detector window set at the output of the sphere, these flat fields for each detector was measured in the University of Calgary, Canada. A flat field is incorporated in CCDLAB, and the flat field weighing is applied to the centroids in the centroid list (Postma and Leahy, 2017).

The second step is to correct for the drift in the images, as the satellite drifts at a rate of 3×10^{-4} deg/s during the observations. Postma and Leahy (2017) have described the procedure to correct for the drift using CCDLAB. In their Fig. 7 and 8, they show

the image of NGC 2336 before and after drift correction. We have followed this method to correct for drift from our images.

In our present work, we require a deep-field image of the target, therefore stacking of all images observed with a particular filter during different orbits must be done. As the observation is performed in several separate orbits, it is thus subjected to field rotation and translation. Hence the orbit wise, drift corrected images must be aligned before combining all the images. To perform this task, we need to register the images in CCDLAB, and select three or more identical stars in all the different images, a quadratic fitting would thus align, rotate and translate the images with respect to a single image. After this correction is done, we merge all the images of a particular filter to create a master image. The entire procedure is repeated for all the observation done using various filters of UVIT. We also align all the master images of the observed with various filters with a similar task. We can use these final science images to perform photometry to get their magnitudes in the respective filters.

3.3 Photometric Techniques

We have used an astronomical software, Image Reduction and Analysis Facility (IRAF), which is a collection of software packages mainly developed to process astronomical images (Tody, 1986). IRAF contains DAOPHOT II, a revised DAOPHOT software package developed at the Dominion Astrophysical observatory and APPHOT package to perform stellar photometry in crowded and uncrowded fields respectively (Stetson, 1987). An aperture photometry can be performed in a uncrowded or moderately crowded fields, while a point spread function (PSF) photometry is performed in a crowded field. The absolute measurement of a star's brightness is obtained only by aperture photometry, while the psf fitting provides only 'relative' brightness between stars. As both these methods have their own advantages, hence we have used both these methods. The final aim of photometry is to obtain accurate magnitudes of the sources in the images. These magnitudes may be used in several ways such as construction of the CMD or SED. We have used both the photometric methods in the present work and a brief description is given below. Several steps are involved during the entire procedure, while the main task includes the extraction of stellar position and magnitudes from a given image.

The first and foremost step involves the detection of star like objects, which is the initial input to both the DAOPHOT II and APPHOT packages. A star list is generated using a 'daofind' task which automatically searches for point sources in the image with peak intensity above a user defined detection threshold level. In this task, a pixel to pixel search is done to locate the stars and involves the following two steps: 1) Detect and identify small, positive increase in brightness within an image. 2) Differentiate between

the actual stellar profile from those due to random noise peaks in the data, images of galaxies or other extended objects, cosmic rays or any high energy particles and two or more overlapping stellar images which results in a extended objects. The location of the star in a pixel is found by fitting an analytical Gaussian profile to the brightness values in a surrounding sub array of pixels. If this fit is good with central height of the Gaussian profile proportional to the brightness of the star, then the star image is centered at this pixel. The best-fitting Gaussian profile would result in a positive value with high probability of the star image centered at the pixel, while a negative value or zero would imply a empty region of the sky or the wings of a star. The best fitting Gaussian profile is obtained by convolving the image with the analytical Gaussian profile with a user defined full width half maxima (FWHM). The task then computes the magnitudes, approximate centers, and shape statistics for the local maxima and further eliminates the local maxima whose centers are outside the image, and whose shape statistics such as sharpness and roundness are outside the limits set by the user. The final output consists of star list with the X and Y centers of the star image, approximate magnitudes, sharpness and roundness statistics and identity number of the stars.

3.3.1 Aperture Photometry

The main principle of aperture photometry is to measure the flux within a circular aperture centered on the star minus the sky background, for which a fractional pixel integration technique is employed. This is performed using the APPHOT package which contains a set of tasks. The input to the package consists of an image file, object coordinate file that is generated using the 'daofind' task in IRAF, and an optional display terminal. With these initial requirements, and using the task 'phot' generates accurate centers, sky value and magnitudes for the list of objects. As we want to measure all the counts of star within a circular geometric region, taking a larger aperture is a logical choice, but with larger aperture, the sky noise and/or light from the neighbouring object majorly contribute to the light from our target object. This would lead to contamination, while a smaller aperture would gather only a fraction of light. In practical, an aperture of 4 to 10 times the diameter of the typical FWHM is choice to get most of the light. If we consider a faint object, the aperture choice of 4 times the FWHM would contain a lot of noise from the sky signal, as the signal from the faint object is low and would result in low signal to noise ratio (SNR). The SNR could be improved for faint objects if a technique called aperture correction is applied. This can measured using the ratio of light in a small and large aperture for a bright star. The aperture correction defined as in Eqn. 3.1, where the instrumental magnitude mag (1 FWHM) in the small aperture and mag (4 FWHM) in the large aperture is measured. The aperture correction derived for the bright star, is added to the instrumental magnitude mag (1 FWHM) of the faint star

with the small aperture to estimate the total instrumental magnitude in the faint star.

$$\Delta = mag(4FWHM) - mag(1FWHM) \tag{3.1}$$

The final magnitudes and magnitude errors are computed as in Eqn. 3.2 and Eqn.3.3.

$$mag = zmag - 2.5 * log10(sum - area * msky) + 2.5 * log10(t_{exp}) \tag{3.2}$$

$$\begin{aligned} merr = 1.0857 * sqrt((sum - area * msky)/gain + area * stdev^2 \\ + area^2 * stdev^2/nsky)/(sum - area * msky) \end{aligned} \tag{3.3}$$

Here, sum is the total counts (star+sky) in the aperture and area is the aperture area in pixels squared and is approximately equal to $\pi\times$ r^2 and radius of the aperture in pixels is r. The sky value in counts, its standard deviation in counts and the number of pixels used to compute it, are Msky, stdev and nsky respectively. The user has to update the exposure time t$_{exp}$ from the image header file, which is required to estimated the instrumental magnitude scale. The zmag is the zero point magnitude corresponding to a filter (Tandon et al., 2017). The magnitudes must be corrected for saturation and we have used equations from Tandon et al. (2017) to obtain the final magnitudes.

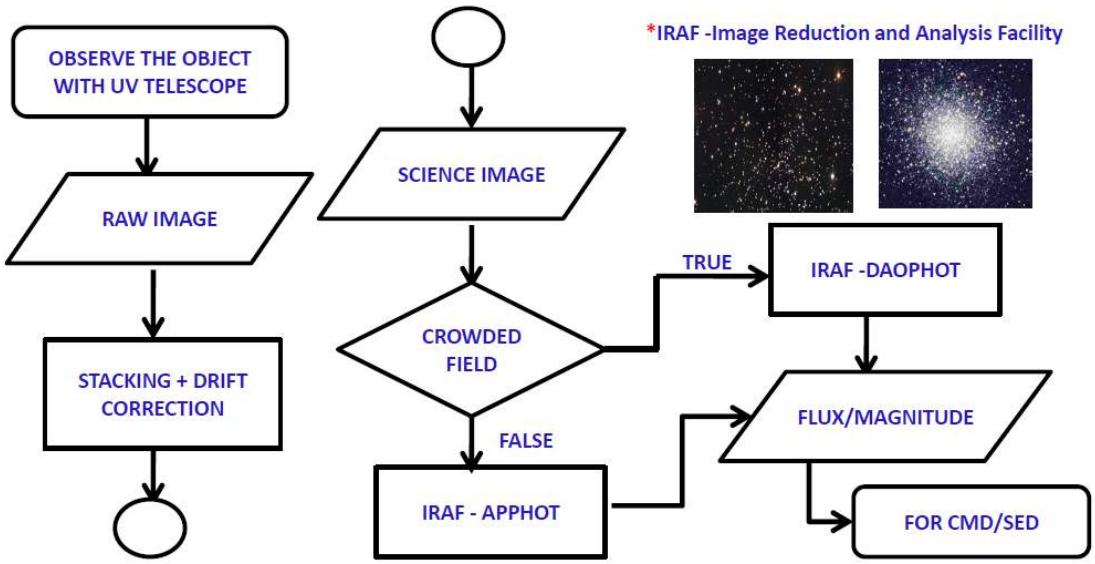

Fig. 3.3 A Flowchart of the Photometric Procedure using IRAF

3.3.2 Point Spread Function Photometry

In a crowded field, using aperture photometry would often result in contamination due to various factors as discussed in the previous section. The flow chart shown above (Fig. 3.3) explains the bifurcation of two types of photometry based on the crowding

of stellar objects in the observed field. PSF is described as the two dimensional brightness distribution of a point source usually an unresolved source such as star. The basic principle that works in PSF photometry, is that all stars in an image can be considered to have the same intrinsic profile shape, which differ only in their brightness or amplitude. Hence a PSF photometry is the most effective method to obtain magnitudes of stars in a crowded field. We use the DAOPHOT II package that contains a set of tasks required to acquire the instrumental magnitudes of stars in a crowded field. An image file, coordinate file and display terminal are the necessary input to the package. The first step involves to find objects that are stars with a certain threshold limit as described in the previous section using the task 'daofind', which creates an output coordinate file. Aperture photometry is performed on the image using the task 'phot', that generates a photometry file that has a rough apparent magnitude estimate and sky background values for all the stars in the coordinate file. A few stars are selected from this photometry file to create PSF model using the 'pstselect' task. During the modelling process, DAOPHOT II provides several choices for the functional form of the analytical component of the PSF model, such as Gaussian, Moffat, Lorentzian, and Penny. The stars selected using the task 'pstselect', must not have any overlapping neighbour stars, or any non-stellar objects or stars affected by cosmetic blemishes. This is done using the 'pexamine' task. Finally the psf model is computed using the input photometry file and the psf star list. An 'addstar' and 'substar' task are available to add and remove stars from an image. The 'substar' task is used to remove any psf star and their neighbour which has systematic pattern in the residual as a function of position, distance from the star or magnitude in the image. Stars not in the input photometry file could be added using the 'daofind' and 'phot' task and the above steps are repeated to include these stars which are bright enough to compute with the psf model. A final good psf model is created after the above steps are concluded, and this model is used for fitting PSF to the rest of the stars in the image to perform photometry.

PSF photometry can be performed using three different tasks: peak, nstar and allstar. The simpler of the three tasks to fit PSF is peak. This task individually fits the PSF model to the stars in the input photometry file. As this task cannot fit stars simultaneously, this is mainly used when the user wants to improve the SNR of faint stars using its optimal weighting scheme or to perform astrometry of a single star. The 'nstar' task fits stars simultaneously in a fixed group. Each group of stars have a physically meaningful association as it is required to perform PSF fitting technique. This grouping is done using 'group' and/or 'grpselect' tasks depending on the size of the group. These groups are combined together and a new group photometry file is created. The 'nstar' and 'substar' task is performed on the grouped photometry file, that simultaneously fits the stars in each group and subtracts the fitted star from the image. This an efficient method, if we want to have explicit control over the grouping process or to fit stars in

a small number of groups that are widely separated. This task is mostly used to fit the PSF model to the PSF stars and their neighbours. The best choice for doing crowded field photometry with DAOPHOT II is using the 'allstar' task. This task groups, fits and subtracts the fitted stars from the input image without user intervention.

All the three techniques return an output photometry file, that have the following quantities: X and Y centers of the best fit position of the star, magnitudes and their respective errors, sky values, number of iterations required to fit the star, sharpness and χ^2 values that define the goodness of the fit and an integer error code and error string which denotes the error encountered during the fit process. The magnitudes that are generated are relative magnitudes, and hence must be calibrated to zero-point magnitudes similar to those in the aperture photometry file. In order to do this, the output from 'allstar' and 'phot' must be cross-identified, and the magnitude difference 'mag(phot)−mag(allstar)' between all these stars versus 'mag(phot)' is plotted. The mean difference is estimated from only the bright stars and ignoring the outliers and larger scatter at the faint end. This mean difference is added to the magnitudes of the output photometry file written by 'allstar' task. These magnitudes are converted to aperture-photometry scale. In order to get the final magnitudes aperture correction must be added to the magnitudes. As the last correction, and not the least, the saturation correction is applied, to the zero-point corrected magnitudes.

3.4 Spectral Energy Distribution: From Far-Ultraviolet to Mid-Infrared Wavelength Region

The development of new observing facilities and large surveys covering a wide wavelength range of the electromagnetic spectrum in the last decade, has made it possible to generate the full SED from FUV to IR region. Easy access to these data within the fingertips through virtual observatory (VO) has further enabled astronomers to study astronomical objects and estimate their physical properties. The construction of SED allows to understand the details of the energy emitted by an astronomical object across the entire broad range of wavelength. Thus a multiwavelength SED of stellar sources can be used to determine the effective temperature, radius (if the distance of the object is known), to identify excess flux in the UV/IR which could be due to various factors such as presence of hot/cool component or non-photospheric contribution such as from chromosphere, disks or dust shells.

In order to create the SED of a few selected stars from UV to IR band, we collected the magnitudes/flux from various filters as listed in chapter 2 using the data from the archives or from VO photometry, while the photometric magnitudes of the UVIT filters are obtained by performing aperture/PSF photometry as discussed in section 3.3. We have then used a virtual observatory tool - VO SED Analyzer (VOSA) (Bayo et al.,

2008) which helps to build a SED for each object based on the magnitude/flux that we have provided. The tool corrects the observed flux for extinction (Fitzpatrick, 1999; Indebetouw et al., 2005) in the respective band using the reddening value provided by the user and fits a SED for the selected object. This tool further computes the synthetic photometry for the required filters based on a variety of model stellar spectra. It also allows the user to perform a χ^2 minimisation test to compare the observed flux to the synthetic flux, to identify the best fitting spectrum of the theoretical model. The parameters of the best fitting spectrum, such as T_{eff} and log g, can be used to estimate the physical parameters of the object.

The synthetic photometry of the theoretical model is calculated using the filter transmission curve. The theoretical spectra is a function $F_i(\lambda)$ with the units of erg/cm^2/s/Å and each filter is represented by a dimensionless response curve $G_f(\lambda)$. Here, if F_i is the spectra obtained when observed with a filter G_f, then the synthetic photometry may be expressed as an integral as,

$$F_{i,j} = \int_{\lambda} F_i(\lambda) N_f(\lambda) d\lambda \tag{3.4}$$

where the normalised filter response function, N_f (λ) is the defined as:

$$N_f(\lambda) = \frac{G_f(\lambda)}{\int G_f(x) dx} \tag{3.5}$$

The user can choose from a vast range of theoretical spectral models and then SED fitting with the model for a selected object is performed. Most of these models include contribution of only stellar photosphere for the analysis of the observed SED. Though for many objects, the observed SED could have contribution from other components as disks or dusts apart from the stellar photosphere. In such cases using the entire SED could be misleading as there would be some excess. This excess may be in the UV/Blue or IR region, so the tool allows the user to ignore these regions, and would not consider these photometric points during the SED analysis while using the stellar photospheric models. A χ^2 test is performed to compare the observed and synthetic photometry and the best fit χ^2/χ^2_r values are calculated using the Eqn. 3.6 for each object. The tool uses the grid of models to compare the observed and theoretical photometry. Therefore, the estimated parameter values (T_{eff}, log g, etc.) are dependent on the model, and hence the best fit value of the parameter can be only the values within the parameter space. Thus, by default, the error estimated in the parameters is half the grid step, around the best fit value, for each parameter.

$$\chi^2_r = \frac{1}{N - n_p} \Sigma_{i=1}^{N} \frac{(Y_{i,o} - M_d Y_{i,m})^2}{\sigma^2_{i,o}}, \tag{3.6}$$

where N is the number of photometric points, n_p is the number of fitted parameters for the selected model, Y_o: and Y_m are the observed and theoretical flux respectively, σ_o is the observational error in the flux and M_d is the proportionality factor which must be multiplied with the model to fit the observation, defined by $M_d = (R/D)^2$, with R and D being the object radius and distance to the object from the observer. The distance to the object is provided by the user or the tool will use the default value of 10 pc. If a certain photometry does not have observational error, in such cases the tool calculates the corresponding error by adding 0.1 to the maximum relative error present in the SED. The measurement of error is important to calculate the reduced χ^2. The tool estimates various fundamental parameters such as: effective temperature (T_{eff}), surface gravity ($\log g$), luminosity ($L/L_\odot$) and stellar radius ($R/R_\odot$) along with the errors for a given fit. Radius is estimated from the scaling factor M_d.

VOSA can produce results for only a single spectral fit. In case, if the star/object has companion, then it cannot fit a composite spectrum. Hence we have developed an algorithm to fit two components, while the secondary is a hotter/cooler companion to the primary object. In this method, we first perform a single spectral fit to the stellar SEDs for the entire wavelength region with VOSA, using the Kurucz model which is updated (Castelli et al., 1997). We compare the observed and model flux and create a residual SED by plotting the fractional difference in flux against the wavelength to find the excess region. If the χ^2 value of the fit is large and/or there is excess flux in the residual in any wavelength region, we modify the analysis. If there exists any excess in the UV/Blue and/or IR region, the tool allows to ignore those photometric points during the fitting process. In Fig. 3.4, we demonstrate the method VOSA utilises to fit a model to the observed SED of a star, before and after UV/Blue excess condition is applied. In the figure, the top panel shows the model fit to the observed SED with all the photometric points considered from UV to IR. In the bottom panel, the UV photometric points are ignored while fitting the model to the observed SED. It can be seen from the bottom panel, that when the UV/Blue excess condition is applied the model fit is consistent with the observed optical to IR photometric points. This step allows us to check for mismatch between the observed and the model SED in the shorter wavelengths and detect excess/decient ux in the UV with respect to the expected flux in the UV region. On the basis of χ^2 value and the residual flux, the user can select the best model to fit the observed SED.

In case we observe a mismatch between the observed and model flux, we perform a single spectral fit again, to get the best fit properties for the primary companion. In order to estimate the parameters of the secondary component, we create a grid of models for synthetic photometry of the combined theoretical flux of the objects. This total synthetic flux for each wavelength corresponding to a filter is estimated by adding individual flux values of each component. The composite model flux is com-

pared with the observed flux using the χ^2 test to obtain the best fit parameters for the object. The flow chart shows the processing chain for single and double component SED fits (Fig.3.5).

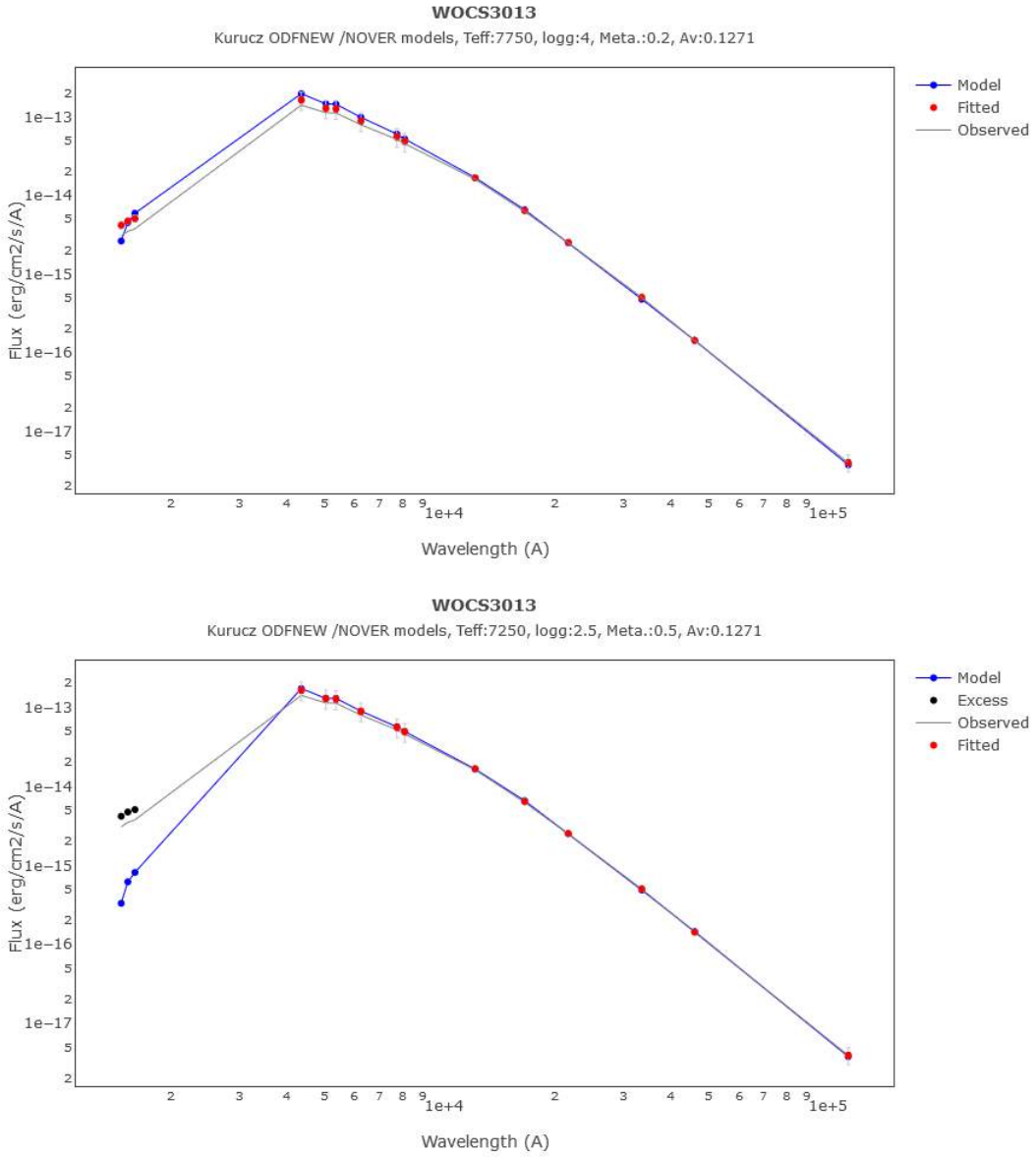

Fig. 3.4 The Figure shows the Demonstration of SED Fitting (top:) Before and (bottom:) After the UV/Blue Excess is Applied in VOSA . Image Credit: VOSA

3.5 Isochrones

The location of stars with same age and having the same metallicity on the theoretical HRD is specified by a theoretical isochrone. These isochrones are generated from the stellar evolutionary calculation of stars for a wide range of mass ($\approx$ 0.1 to 100 M$\odot$). The theoretical isochrone can be used to compare with the observational cluster CMD

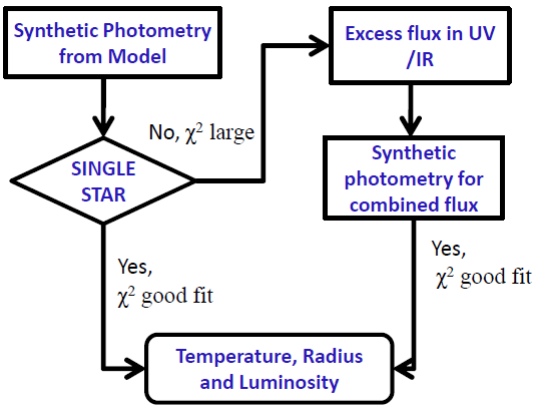

Fig. 3.5 The Flow chart shows the Algorithm for Single and Binary SED Fit

to interpret and estimate the fundamental properties of the star cluster such as age, reddening and distance. In order to make this comparison, the theoretical isochrone must be converted to observational plane by convolving with appropriate filters to produce magnitudes and colours. The MSTO location along the isochrone MS is the bluest point, where hydrogen in the core of stars is exhausted. It is from this location, that the age of the cluster from the isochrone can be determined.

Several isochrone tables are available in the literature. They cover a wide range of ages, chemical composition and cover the most relevant evolutionary phases of stars. Some of the most popular models include the Bag of Stellar Tracks and Isochrones (BaSTI) (Pietrinferni et al., 2004; Cordier et al., 2007), Geneva (Schaller et al., 1992; Meynet and Maeder, 2000), Padova (Girardi et al., 2000; Marigo et al., 2008) and PARSEC (Bressan et al., 2012). While a wide variety of models are available, each of these models are able to handle either high mass stars through their advanced evolutionary phases or very low mass stars and brown dwarf or are focused on the MS, RGB. Hence in our present work we have used Flexible Stellar Population Synthesis (FSPS) model (Conroy et al., 2009; Conroy and Gunn, 2010) that generates isochrones from the models that exists in the literature, with the capability of handling various phases of stellar evolution including the HB stars, BSSs and thermally pulsing-AGB stars along with the standard evolutionary sequences. In Fig. 3.6, we compare a 4 Gyr isochrone generated using the BaSTI model and same model generated using FSPS. It can be seen from this figure, that the BaSTI model generated using FSPS is capable of populating various other stellar evolutionary sequence. The WD sequence is to the left of the MS and BSS model line above the MSTO are shown in Fig. 3.6. The BSS model line is the locus for BSS, assuming them to be MS stars with masses in excess of the turn-off mass, which uniformly populates 0.5 mag above the MSTO to 2.5 mag brighter than the MSTO. The BaSTI models provide isochrones with and without inclusion of convective overshooting computed with scaled Solar and alpha enhanced chemical composition and include

mass loss (Reimers, 1975). The mass loss efficiency parameter η has been fixed for η = 0.2 and η = 0.4. Conroy et al. (2009) have used the non convective overshooting, scaled Solar composition with η=0.4 in their code, with Padova calculations tied to the BaSTI grid for both low and higher masses.

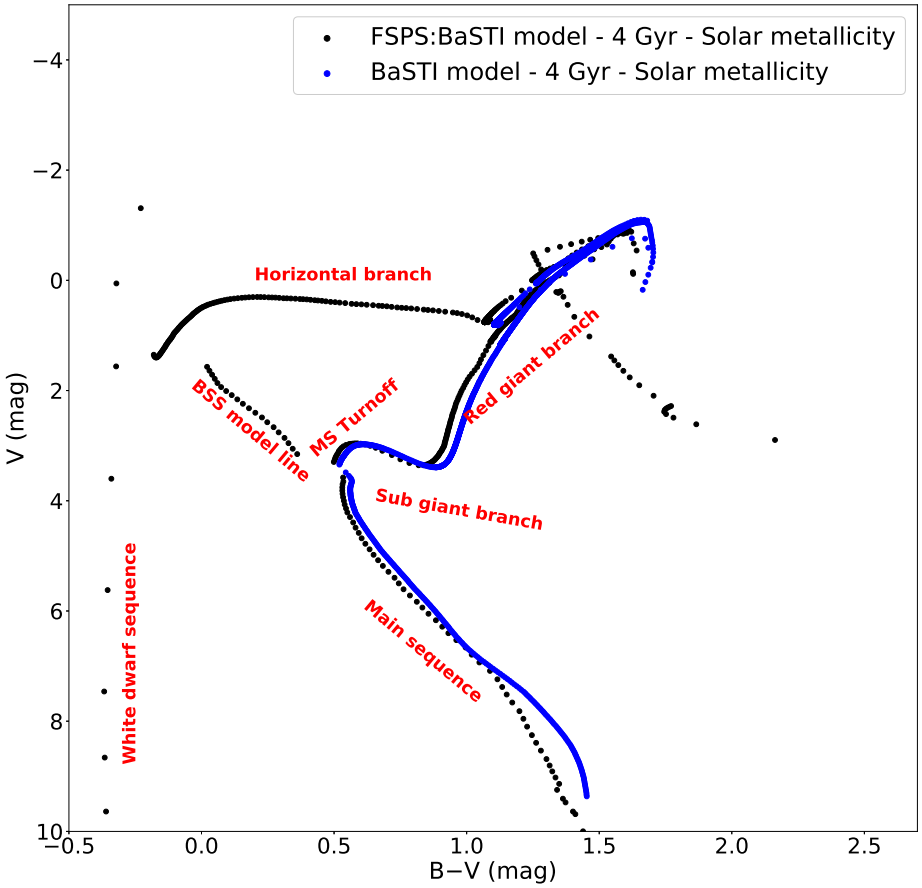

Fig. 3.6 The Figure shows Isochrones of Age 4 Gyr and Solar Metallicity, generated using FSPS Code with BaSTI model. Various Stellar Evolutionary Phases are marked in the Diagram

We have used isochrones generated from FSPS model by running a Fortran code, that combines stellar evolution calculations with stellar spectral libraries. Within the code, we can choose from the various isochrone models that include BaSTI, Padova, MIST and Geneva and the spectral library include BaSeL (Lejeune et al., 1997; Lejeune et al., 1998; Westera et al., 2002) and MILES (Sánchez-Blázquez et al., 2006). The spectral libraries are used to re-calibrate the atmospheric calculation especially for M type stars, as the models do not include the effect of line blanketing due to molecular lines. Further details are given in Conroy et al. (2009) and Conroy and Gunn (2010). All or a set of filters can be chosen to generate the isochrone. A filter can be added to model by including the transmission profile of the filter. The isochrone model selected is convolved with the filter profile to get the magnitudes. One of the module consists of two types of variables: common and parameter. The parameter variables should not be

changed, while the common variables can be changed. A few of the important variables which may be switched on/off include stellar remnants for the calculation stellar mass, magnitude zero point to switch between AB and Vega system, dust type that defines the attenuation curve for the diffuse dust component with the choice of power law, Milky Way extinction law and Calzetti et al. (2000) attenuation curve, the stellar initial mass function type, and the metallicity option based on isochrone selected by the user. A set of isochrone parameters can also be changed such as modifying the weight given to the RGB available only for BaSTI models, to shift bolometric luminosity and effective temperature of the TP-AGB isochrones, specific frequency of BSSs to populate the BSS region, fraction of blue/extended HB stars and weight given to the post - AGB phase. The Fortran code will then produce an theoretical isochrone file that contains magnitudes for all ages in the filters specified.

3.6 Summary

In this chapter we have presented a detailed description of the methods that are implemented in this thesis. We have used these methods in the following chapters to study the two old open clusters NGC 188 and M67.

The two old open clusters NGC 188 and M67 are observed using UVIT (chapter 4 and chapter 7). Hence the raw images obtained from UVIT are corrected for flat and drift correction using CCDLAB developed for UVIT by Postma and Leahy (2017). Further we have used IRAF software to obtain the magnitudes of the stars.

SED fitting method is used to obtain the parameters of stars such as effective temperature, luminosity and radius (using the known distance). Apart from obtaining the parameters of a single star, we can find the possible presence of a binary component provided the primary star is relatively hotter or cooler star in comparison to the secondary. In such cases any excess in the UV or an excess in the IR, we would be able to detect the presence of the binary. This method is utilized in chapter 4 to analyse a star in NGC 188. In chapter 6, we find 45 interesting candidates and hence we have implemented this method to estimate parameters of these stars. In chapter 7 we fit 9 stars in M67 to characterise these stars and analyse the parameters obtained from the fit.

Isochrone defines the location of stars of same age and metallicity. FSPS is able to generate isochrones form various models available in the literature along with the BSS model line and WD cooling sequence. The code also provides isochrones for the user defined filters by convolving the spectra with the filters. The isochrones generated from FSPS are utilized to understand the CMDs of M67 in chapter 5. Using the method we are able to identify stars in their various evolutionary states especially in the UV$-$optical and UV CMDs.

CHAPTER 4

A Hot Companion to a Blue Straggler Star in NGC 188

4.1 Introduction

NGC 188 is an old and rich open cluster, well known for its large binary fraction and BSS population (Mathieu and Geller, 2009). An optical image of the cluster taken from Digitized Sky Survey is shown in Fig. 4.1. This cluster has been extensively studied for several aspects since a long time, with its first photometric observation (S van den Berg, 1956 (unpublished); Sandage, 1962). NGC 188 was once considered to be the oldest galactic cluster with age estimation of 14 -16 Gyr (Sandage, 1962), which has drastically changed over the years with the most recent values between $\sim$ 6 Gyr (Twarog and Anthony-Twarog, 1989; Caputo et al., 1990; Dinescu et al., 1995; Salaris et al., 2004) to $\sim$7-8 Gyr (Sarajedini et al., 1999; VandenBerg and Stetson, 2004; Bonatto et al., 2005; Fornal et al., 2007). Meibom et al. (2009) recently determined the age of 6.2$\pm$0.2 Gyr from the eclipsing binary V 12, which is independent of distance, reddening and colour-temperature transformation, while most of the previous measurements are from isochrone fittings.

The cluster is located in the galactic disk at a distance of $\sim$1700 pc (Twarog and Anthony-Twarog, 1989; Sarajedini et al., 1999; Fornal et al., 2007) and has a reddening of E_{B-V}= 0.09 $\pm$ 0.02 (Sarajedini et al., 1999). The metallicity is close to Solar with measurements from recent studies being [Fe/H]=-0.10 ± 0.09 (Friel et al., 2002), 0.075 ± 0.045 (Worthey and Jowett, 2003), 0.12 ± 0.04 (Friel et al., 2010) and -0.03 ± 0.04 (Jacobson et al., 2011). The member stars are well established with proper motion and radial velocity measurements (Platais et al., 2003; Geller et al., 2008). The proper motion study suggests about $\sim$ 1050 members in the cluster down to a limiting magnitude of V=21. μ_x^{abs}= -2.56 ± 0.2 and μ_y^{abs}= +0.18 ± 0.2 mas yr^{-1} is the absolute proper motion of the cluster (Platais et al., 2003). While the radial velocity study suggests $\sim$ 473 stars to be members from their sample with limiting magnitude to 16.5 within 17 pc in projection. Using only single members of the cluster, they calculated the cluster's average radial velocity to be -42.36 ± 0.04 km s^{-1}. This cluster consists of a rich variety of exotic stars such as: short period variables (Kafka and Honeycutt, 2003; Zhang et al., 2004; Mochejska et al., 2008), close binaries (Zhu et al., 2014), W Uma-type binaries (Liu et al., 2011; Chen et al., 2016), spectroscopic binaries (Geller et al., 2009;

Fig. 4.1 A Colour Composite Optical Image of NGC 188. Image Credit: Digitized Sky Survey 2 (STScI/AURA, Palomar/Caltech, and UKSTU/AAO)

Geller and Mathieu, 2012), sub-dwarfs (Landsman et al., 1998), X-ray sources (Belloni et al., 1998; Gondoin, 2005; Vats et al., 2018), SSGs, red stragglers (Geller et al., 2017; Geller et al., 2008), and BSSs (Mathieu and Geller, 2009; Geller and Mathieu, 2011; Gosnell et al., 2015) and has thus drawn attention of both theoretical and observational astronomers.

NGC 188 contains a rich population of BSSs, Geller et al. (2008) identified 20 BSSs to be confirmed members based on the radial velocity membership probability. These BSSs with effective temperatures ranging from 6000 K to 6500 K are of the spectral type late-F and early-G, which is mainly due to the age and Solar metallicity of the cluster (Mathieu and Geller, 2015). Among the 20 BSSs, only four stars are not detected as spectroscopic binary, with a remarkable high binary frequency of 80%, compared to the Solar-type MS binary frequency of 23% with similar period range. Mathieu and Geller (2009) reported that these BSSs are rotating faster than the normal MS stars with similar surface temperature. They argue that the characteristics properties of most or all BSSs points its origin from a multiple-star systems. Seven of the above mentioned BSSs were detected with the WD companions formed through recent mass transfer (Gosnell et al., 2015). Three BSSs were found to have cool WD companions; four were found to have hotter WDs. Though, no BSS belonging to an open cluster has been found that possesses a post-AGB/HB star as companion.

4.1.1 WOCS 5885

WIYN Open Cluster Study (WOCS)-5885 is located in the inner region of NGC 188 (Table 4.1). This is known to be a single lined spectroscopic binary of uncertain membership (Geller et al., 2008). They found the star to be a rapid rotator and mentioned that they could not establish membership and designated it as an uncertain member due to a lack of measurements. Dinescu et al. (1996) assigned a probability of 80% (D-702, found to be an extended/blended object) and Stetson et al. (2004) found a membership probability of 53% (SMV-8422). It is considered to be a BSS based on its location in the CMD (Fig. 4.2). Landsman et al. (1998) mentioned that this may have a composite spectrum, as suggested by its UV colors, with a possibility of a very hot star and a BSS as components. Siegel et al. (2014) suspected this to be a RG and a pre-WD binary.

Table 4.1 Basic Parameters of WOCS 5885

Parameter		Reference
RA (J2000) (hh:mm:ss)	00:48:19.127	Geller et al. (2008)
Dec (J2000) (dd:mm:ss)	+85:13:27.91	Geller et al. (2008)
V (mag)	14.13	Stetson et al. (2004)
B-V (mag)	0.25	Stetson et al. (2004)
Radial velocity (km/s)	-46.84	Geller et al. (2008)

4.2 Observation and Data

NGC 188 was observed as UVIT's first light object on 2015 November 30. The cluster was observed every month to track the variation in UVIT sensitivity over the first six months of its operation. We present the calibrated flux of WOCS-5885, located near the center of the UVIT field, in four FUV and two NUV pass bands. All data used in the analysis were obtained on 2016 January 26. The star studied here is repeatedly observed, and we have detections within the central 5 arcmin. The variations in the count rates suggest the sensitivity variation to be about 2% - 3%, calibration error of 2% - 3% and the photon noise to be 1% - 2%, with a cumulative effect of about 5%. In the case of the specific filter, N219M, we noticed that the above estimates are almost double, which sets the error to be 10%. Images were corrected for distortion, flat-field illumination, and spacecraft drift using the customized software package CCDLAB (Postma and Leahy, 2017). Aperture photometry was performed on the images to estimate the counts after correcting for the background and saturation effects. We have further obtained flux measurements from GALEX (FUV and NUV), UIT (B1, B5), Swift-UVOT

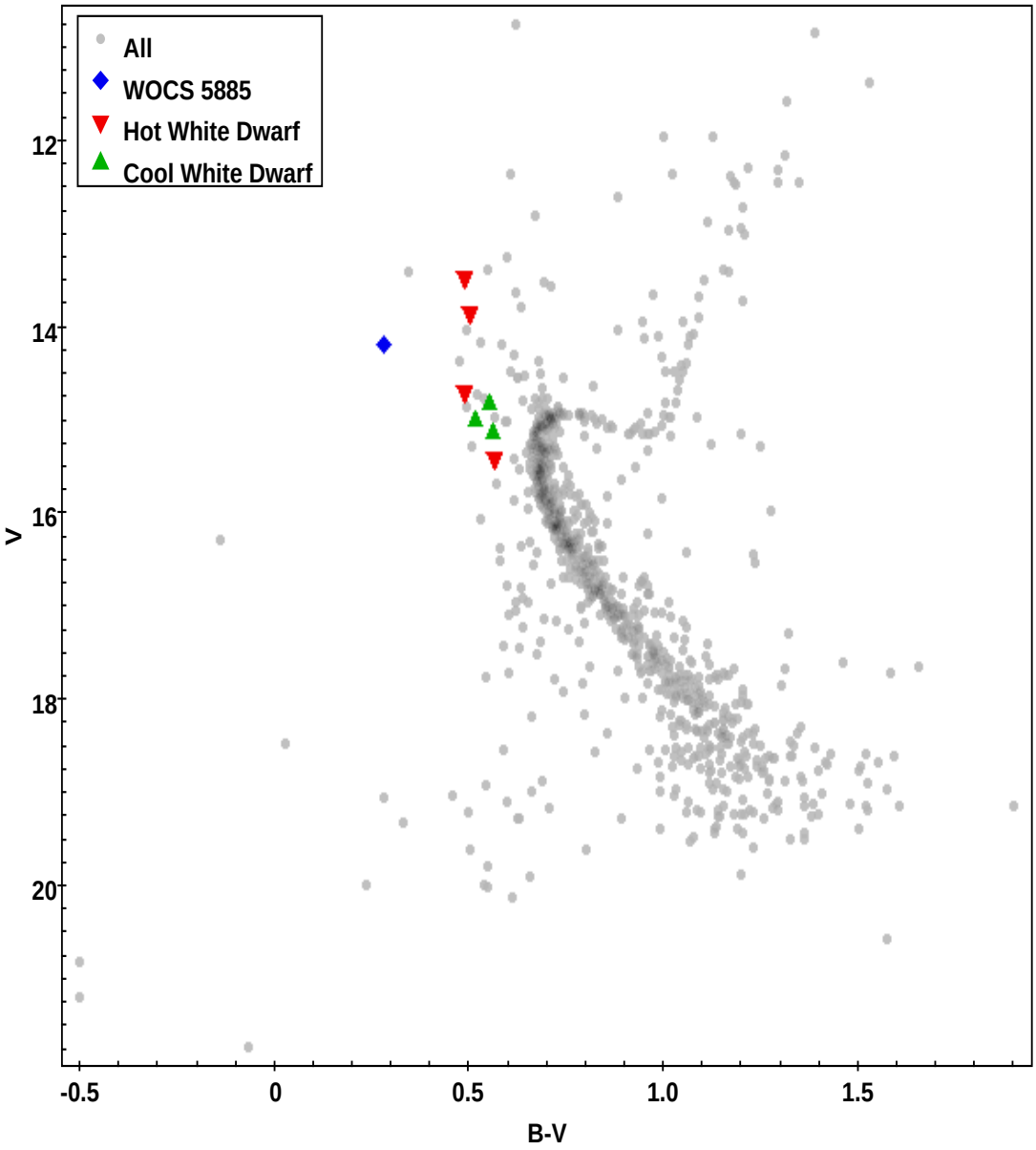

Fig. 4.2 CMD of NGC 188 showing the location of WOCS-5885 and the Seven BSS+WDs Sources Studied by Gosnell et al. (2015). The Members (Proper Motion and Radial Velocity) of the Cluster are shown in the CMD, using the Optical Photometry of Sarajedini et al. (1999)

(UVW2, UVM2, UVW1 ; Siegel et al., 2014), UBVRI (Sarajedini et al., 1999), 2MASS (J, H, K_s), IRAC (I2, I3, I4), and WISE (W1, W2). The filters, their effective wavelength, the unit conversion factor (only for UVIT filters), and estimated fluxes and errors are recorded in Table 4.2. The measured flux is the product of the count rates and unit conversion for each UVIT filter. We have obtained the UVOT magnitude from Siegel et al. (2014), from their Fig. 5. The magnitude in UVW1 as found from the bottom two figures differ by about 0.2 mag; we adopted the mean value. The adopted magnitudes and errors are UVW2=15.0$\pm$0.1, UVM2=15.0$\pm$0.1, and UVW1=15.1$\pm$0.2.

Table 4.2 Flux Measurements for WOCS 5885. The Effective Wavelength of each Filter is given in column 2, with the respective Unit Conversion Factor (Only for UVIT Filters (Tandon et al., 2017)) in Column 3. Column 4 and 5 gives the Measured Flux and its Error

Filter	λ_{eff} (Å)	Unit Conversion	Flux (erg cm^{-2} s^{-1} Å^{-1})	Error (erg cm^{-2} s^{-1} Å^{-1})
F148W	1480.8	0.292E-14	5.09E-14	0.25E-14
F154W	1540.8	0.345E-14	4.73E-14	0.19E-14
F169M	1607.7	0.428E-14	4.09E-14	0.20E-14
F172M	1716.5	0.106E-13	3.51E-14	0.18E-14
N219M	2195.5	0.545E-14	2.06E-14	0.21E-14
N279N	2792.3	0.364E-14	1.19E-14	0.06E-14
FUV	1542.2		7.748E-14	0.97E-15
NUV	2274.3		3.897E-14	0.29E-15
B1	1520.0		8.179E-14	0.92E-14
B5	1620.0		7.225E-14	0.81E-14
UVW2	2030.5		5.243E-14	0.48E-14
UVM2	2228.1		4.499E-14	0.41E-14
UVW1	2589.1		2.462E-14	0.45E-14
U	3570.6		1.3275E-14	0.12E-15
B	4378.1		1.4447E-14	0.15E-15
V	5466.1		1.025E-14	0.94E-16
R	6357.9		6.9317E-15	0.70E-16
I	7829.1		4.293E-15	0.39E-16
J	12350		1.6193E-15	0.84E-16
H	16620		6.263E-16	0.35E-16
K_s	21590		2.506E-16	0.18E-16
I2	44365.8		1.465E-17	0.36E-19
I3	56281.0		6.330E-18	0.51E-19
I4	75891.6		1.839E-18	0.30E-19
W1	33526		7.029E-17	0.15E-17
W2	46028		1.882E-17	0.42E-18

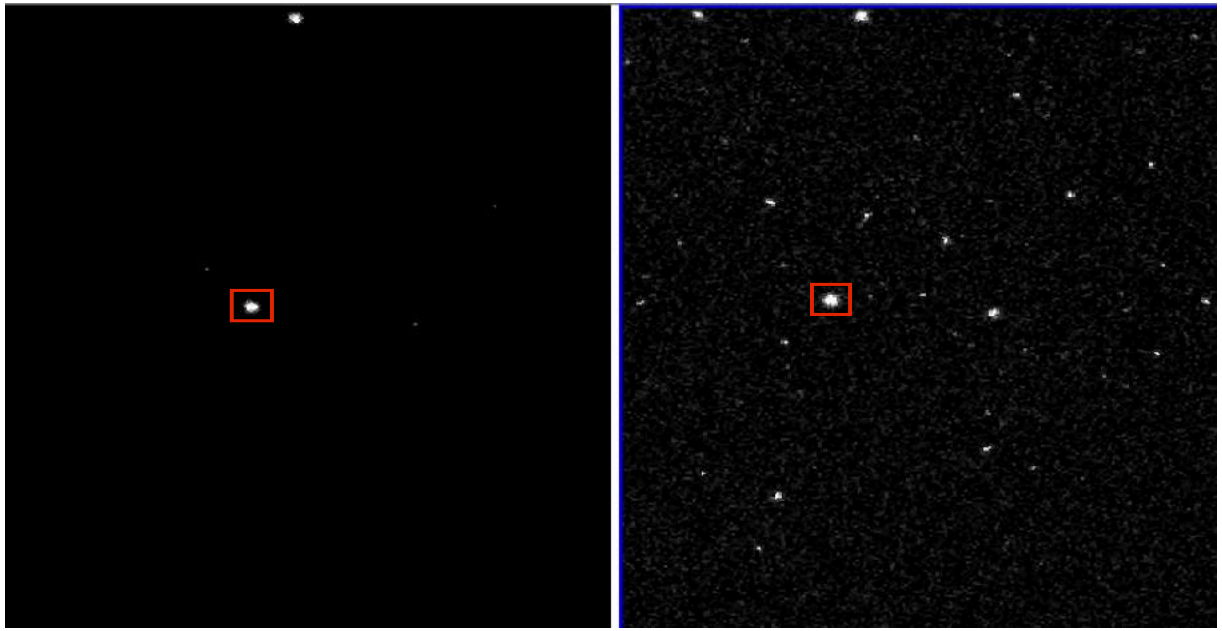

Fig. 4.3 FUV (left) and NUV (right) Images of NGC 188 taken in the F148W and N279N Filters, respectively. WOCS-5885 is marked by the Red Square. The Images Obtained on 2016 February 26 are Aligned with North Up and East toward the Left

4.3 Spectral Energy Distribution of WOCS 5885

In order to characterise the temperature and the evolutionary status of the star, we generated a multiwavelength SED using UVIT data, supplemented by literature data. The final SED consists of 26 data points spanning the wavelength range of 0.15 - 7.80 μm. It can be seen from Fig. 4.4 that the UVIT fluxes are in good agreement with those estimated by UIT, UVOT, and GALEX. We used the virtual observatory tool, VOSA (Bayo et al., 2008), which allows the user to perform a statistical test to compare the observed data with the selected model. We adopted a reddening of E (B$-$V) = 0.09 mag (Sarajedini et al., 1999). To extinction correct the UVIT and UIT fluxes, we used the reddening law (Cardelli et al., 1989). The reduced χ^2 value is estimated using the formula given in Eqn. 3.6. The synthetic flux values of the UVIT filters were computed by us, whereas for other filters, we used the values computed by VOSA, except for the UIT filters. The rise in flux for UV wavelengths can be clearly seen in Fig. 4.4, suggesting the presence of a hot component. In order to fit the SED, we need spectra which have coverage over the UV to IR wavelength range. We used Kurucz models because the spectra need both a large wavelength and temperature coverage (Castelli et al., 1997).

We initially tried to fit the full SED with a single temperature but found this approach to yield unsatisfactory results. The UV part of the SED seems to suggest a relatively hot temperature, whereas the IR part suggests a cooler temperature. Therefore, we created a composite spectrum comprising two components. We fitted the UV range and the optical IR range separately using the VOSA. The temperatures and errors are estimated by the tool. The combination that best fits the observed SED (with the least value) was found to have temperatures of 17,000 $\pm$ 500 K and 6000 $\pm$ 150 K. The reduced χ^2 value using 24 data points are 87 (12), 2698 (1169), and 7582 (868) for composite, cool, and hot components, respectively. The reduced χ^2 values for well-fitting 18 data points, identified by the tool, followed by a visual inspection are shown in the parentheses. In Fig. 4.4, we also show the SED fitted with two spectra, along with a composite spectrum. For comparison, we have also shown a model spectrum of the temperature of 20,000 K. The N279N flux and the U-band flux are lower, whereas the WISE fluxes are higher with respect to the fitted spectrum. The N279N filter is centered on the Mg II spectral line and line absorption could be a possible reason for the reduced flux. Although the temperatures are reliable, the derived log g ($\sim$5.0) are not very accurate since the range of values available in the models is limited. In order to compare with special models, such as helium-rich models for hot stars, we have shown the model LTE spectrum for a temperature of 16,000 K (Jeffery et al., 2001), in Fig. 4.4. The helium rich model shows a reduction in flux in the U band, which may support the observed reduction in the U-band flux. In general, both the models appear comparable.

The high temperature of the hotter component (17,000 $\pm$ 500 K) is clearly re-

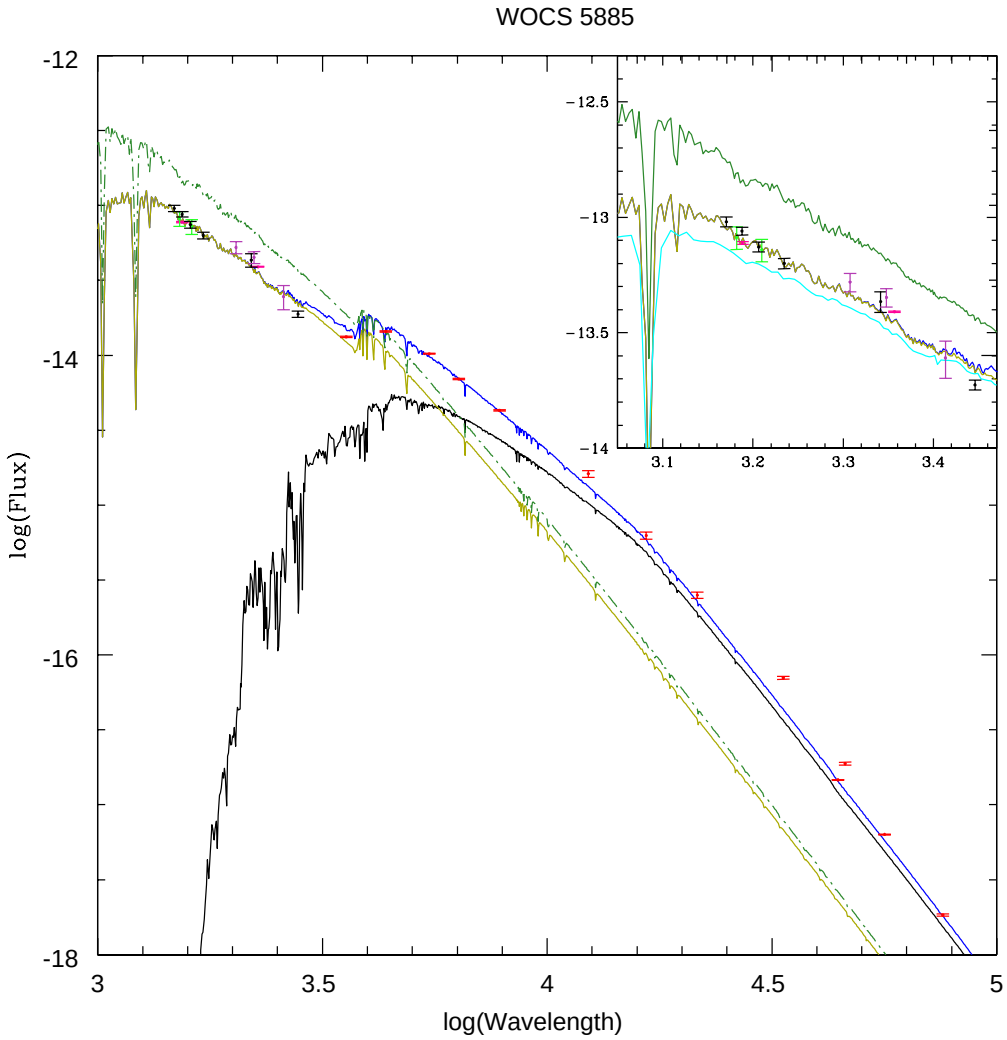

Fig. 4.4 Extinction-Corrected SED of WOCS - 5885. The Black (UVIT), Magenta (GALEX) and Green (UIT), Pink (UVOT) Points Indicate the UV Fluxes (shown in the inset as well); All Other Flux Measurements are shown in Red. Kurucz Model Spectra (Log g= 5.0) for the Separate Components are shown in Gold (17,000 K) and Black (6000 K), with the Composite Spectrum in Blue. For Comparison, We have Shown a Hotter Spectrum of Effective Temperature (20,000 K) in Dark Green. We have also shown the Helium-Rich Model Spectrum for a Temperature of 16,000 K, log g = 4.0, H=0.30, He = 0.70, and CN = 0.00005 from Jeffery et al. (2001) in Cyan. Scaling Factors of 4.45e-22 and 3.1E-23 have been used to Combine the 6000 K and 17,000 K Spectra, respectively. The Unit of Wavelength is Å and flux is erg cm^{-2} s^{-1} Å^{-1}

vealed by the UVIT data, especially in the flux measured using the F148W and F154W filters; the inset in Fig. 4.4 suggests that the UV flux is rising at least until 1481Å. The data also confirm that the temperature of the hot component is not high enough to be classified as a sub-dwarf, as demonstrated by the slope of the FUV part of the SED. The estimated temperature of the cooler component confirms that it is indeed a BSS, as it is similar to the temperature of other BSSs in NGC 188 (Table 1; Gosnell et al., 2015)

and higher than the turn - off temperature of NGC 188 ($\sim$ 5500 K, based on the turn - off color). The optical region of the SED is fitted well by the combined flux from the two components. The Padova models (Marigo et al., 2008) suggest a mass of 1.1 -1.2 $M_{\odot}$ for a star of similar temperature on the MS. This is also similar to the mass of other BSSs in NGC 188 (Perets, 2015).

In obtaining the composite spectrum, the flux of each component is scaled by a factor that is equal to $(R/D)^2$, where R is the radius and D is the distance. We estimated the radii of the component stars, using the relation $R/R_{\odot}=(T_{\odot}/T)^2(L/L_{\odot})^{0.5}$; the luminosity is estimated from the absolute magnitude, bolometric correction, and a distance of $\sim$ 2 kpc. For the BSS, we also estimated the luminosity using the relation given in Table 3 (Eker et al., 2015) and Padova models. The BSS is found to have a radius of $\sim$1.1 - 1.6 $R_{\odot}$, and the luminosity of $\sim$1.4 - 2.8 $L_{\odot}$ whereas the hot component is found to have a radius of $\sim$0.6 $R_{\odot}$, and a luminosity of $\sim$30 $L_{\odot}$. Hence, the hot component is much larger in size than a WD (R $\sim$0.01 - 0.02 $R_{\odot}$; Tremblay et al., 2017 and references therein). The hot star is about three times more luminous than hot B sub-dwarfs (T_{eff} >27,000 K L $\sim$10 $L_{\odot}$) and blue HB stars (L $\sim$ 10 $L_{\odot}$; Heber, 2016). Also, the FUV luminosity is found to be much higher than those of the BSS+WD of similar temperature (e.g., WOCS - 4540, WOCS - 5379; (Gosnell et al., 2015)). These two observations suggest that the hot component cannot be a WD or a sub-dwarf, therefore we speculate that it is a post-AGB star or a post-HB star (depending on the initial mass of the star). Thus, WOCS - 5885 is likely to be an example of the rare class of BSS +post - AGB/HB binary stars. This also suggests that the BSS acquired mass quite recently from the post-AGB/HB star - a scenario that is supported by its rapid rotation, as the BSS can get spun up due to mass transfer (Ivanova, 2015). Mathieu and Geller (2009) found that many NGC 188 BSSs are rotating more rapidly than the MS stars and speculated that the rapid rotation of BSSs may place upper limits on their ages.

As the BSS has a mass of 1.1 - 1.2$M_{\odot}$ and the MSTO mass of NGC 188 is $\sim$1.0$M_{\odot}$, the mass gained by the BSS is at least 0.1 - 0.2$M_{\odot}$. The mass of the progenitor of the post - AGB/HB is likely to be slightly more massive to evolve first. Milliman et al. (2015) recently suggested that mass transfer from AGB stars to be the dominant formation mechanism for BSSs in NGC 188. The evolution of the primary star, once the mass transfer starts, is complicated and is addressed by a few authors for a few specific cases (see reviews by Sills, 2015; Ivanova, 2015). As there are no similar objects observed or modeled, we are unable to compare or comment on the estimated parameters of the hot component. In this study, we have considered the two components to be physically associated. In the direction of NGC 188, approximately one hot star is expected per sq. degree, as per Fig. 10 (Bianchi et al., 2011). As there are at least three hot stars in this cluster field suggesting an over-density, the hot component is likely to be associated with the cluster.

4.4 Summary

We have presented early science results from UVIT that demonstrate its UV imaging capabilities. Observations in four FUV filters and two NUV filters were used. The UVIT flux clearly demonstrates the rising flux of the hot component in the FUV bands; these measurements allow accurate temperature estimates from SED fitting. The UVIT fluxes are in good agreement with those from UIT, GALEX, and UVOT. We therefore demonstrate that accurate flux measurements can be carried out with UVIT in the 0.150 - 0.30 μm wavelength range.

We have combined our UVIT data with flux measurements from other missions, as well as from ground-based optical/IR telescopes, to demonstrate that WOCS-5885 could be a rare BSS+post-AGB/HB binary - the first of its kind to be identified in an open cluster. WOCS-5885 is probably the progenitor of systems composed of a BSS and hot-WD companion. The temperature of the companion rules out the possibility that this has a RG along with a pre-WD (Siegel et al., 2014). Fig. 4.2 shows the location of this star, along with the other BSS+WDs in this cluster, in the cluster CMD. WOCS-5885 is the relatively blue object, while the five BSS+WD binaries are redder in comparison.

Milliman et al. (2015) identified a few BSSs in NGC 6819 to be enhanced in barium, likely to be formed through mass transfer from an AGB star, but none of these stars are found to be binaries. Sivarani et al. (2004) studied a possible field BSSs and found large over abundances of s - process elements, due to accreted material from a companion, formerly an AGB star. Ryan et al. (2002) studied rapidly rotating lithium deficient stars that are possible field BSSs. WOCS-5885 is unique such that this is a BSS where a possible post-AGB star is found as a companion, a target for testing the above findings. This is an interesting target for BSS surface composition studies and possible chemical signatures of recent accretion events. The physical parameters of the components can thus be used to constrain mass transfer models of BSS formation (Chen and Han, 2008).

4.5 Conclusion

The main conclusion of this chapter are as follows:

- Our analysis of UVIT images for the open cluster NGC 188 has allowed us to reach the following conclusions concerning WOCS-5885, a likely BSS and confirmed UV-bright source belonging to the cluster.

- We find the star to be a certain binary and use UVIT to characterize its two components. The cooler component (6000 $\pm$ 150 K) is found to be a BSS, whereas

the hot component (17,000 $\pm$ 500 K) is speculated to be a post-AGB/HB star based on its luminosity and radius.

- We therefore argue that WOCS- 5885 is likely to be a BSS+post-AGB/HB binary.
- The mass of the BSS is estimated to be $\sim$1.1 -1.2$M_{\odot}$. The initial mass of the donor star is estimated to be 1.2$M_{\odot}$.
- This rare system is the first of its kind to be identified in an open cluster and is an ideal candidate to study the chemical composition of the BSSs and constrain the theories of BSSs formation via mass transfer.

CHAPTER 5

UV - Optical Study of the Old Open Cluster M67 (NGC 2682)

5.1 Introduction

M67 (NGC 2682) is a benchmark cluster to study stellar evolution, dynamics and cluster properties due to its proximity, richness, Solar metallicity and exotic stellar populations. This cluster is located at RA = 8h 51m 23.3s and Dec =11° 49′ 02″ (J2000) in the northern constellation of Cancer. The cluster is relatively nearby, with recent distance measurement ranging 800 to 900 pc (Janes, 1985; Nissen et al., 1987; Montgomery et al., 1993; Fan et al., 1996; Percival and Salaris, 2003; Sarajedini et al., 2004; Sarajedini et al., 2009) and has a reddening of E (B−V) = 0.015 to 0.056 mag (Janes and Smith, 1984; Montgomery et al., 1993; Taylor, 2007). Estimation of the cluster age varies between 3 to 5 Gyr (Johnson and Sandage, 1955; Montgomery et al., 1993; Dinescu et al., 1995; Richer et al., 1998; VandenBerg and Stetson, 2004), with the recent findings indicating it to be 3.5 Gyr (Chen et al., 2014; Bonatto et al., 2015). Gonzalez (2016*b*) estimated a gyro-age of 3.7 ± 0.3 Gyr, Gonzalez (2016*a*) revised the estimate to 5.4 ± 0.2 Gyr, whereas Barnes et al. (2016) estimated an age of 4.2 ± 0.2 Gyr, all from the K2 mission data. With the advantage of being one of the closest old cluster with low extinction and providing a large sample of solar type stars, it has been the standard sample to test stellar evolution theory.

The cluster members are well identified by membership studies using both proper motion (Sanders, 1977; Girard et al., 1989; Zhao et al., 1993; Yadav et al., 2008; Krone-Martins et al., 2010) and radial velocity measurements (Mathieu et al., 1986; Mathieu et al., 1990; Milone, 1992; Milone and Latham, 1994; Yadav et al., 2008; Pasquini et al., 2011; Geller et al., 2015; Brucalassi et al., 2017) with various spatial extent and limiting magnitudes. The cluster has evolved phases of both single and binary stellar evolution and 38% of the cluster members are found to be in binaries (Montgomery et al., 1993). The MSTO mass of the cluster is about $\approx 1.25 M_{\odot}$ to $1.3 M_{\odot}$ (Sandquist and Shetrone, 2003*a*; Sandquist, 2004; Gökay et al., 2013). The cluster is exhaustively studied through photometry in the multiwavelength bands (Johnson and Sandage, 1955; Nissen et al., 1987; Montgomery et al., 1993; Fan et al., 1996; Landsman et al., 1998; Belloni et al., 1998; Van den Berg et al., 2004; Sarajedini et al., 2009; Siegel et al.,

2014; Mooley and Singh, 2015). Apart from the standard evolutionary sequence, this cluster has a number of compelling stellar population such as BSSs, SSGs, YSSs, X-ray sources and triple systems whose formation scenario is still not well understood. ROSAT, Chandra and XMM-Newton studies of the cluster detected at least 36 member stars with X-ray emission (Belloni et al., 1993; Belloni et al., 1998; Van den Berg et al., 2004; Mooley and Singh, 2015).

An exceptionally large number of 24 BSSs are detected in M67 as compared to any other old open clusters (Deng et al., 1999). Two SSGs (WOCS 15028 and WOCS 13008) identified in the cluster are also X-ray sources (Belloni et al., 1998; Mathieu et al., 2003). YSSs may represent a population of evolved BSSs (Mathieu et al., 1990; Leiner et al., 2016). Four YSSs (WOCS 2002, WOCS 2008, WOCS 1015 and WOCS 1112) often referred as yellow giants are observed in the cluster CMD (Geller et al., 2015). Landsman et al. (1997) detected one of the YSS (WOCS 2002) with a WD companion, that has undergone a mass transfer, where as Leiner et al. (2016) conclude that a merger or collision is most likely to have occurred in WOCS 1015 and thus YSSs are likely to be evolved BSSs.

Previous UV studies of this cluster has been done by Landsman et al. (1998) and Siegel et al. (2014). Landsman et al. (1998) detected 20 stars in M67 which includes 11 BSSs, 7 WD candidates, a YSS+WD binary (WOCS 2002) and a non member using UIT. They also presented a semi-empirical integrated spectrum of M67 showing a domination of BSSs at wavelengths shorter than 2600 Å. However, UIT images are not deep enough to detect fainter population of stars in the cluster. Recently, Siegel et al. (2014) studied M67 using the UVOT on Swift Gamma-Ray Burst Mission. They detected 10 BSSs along with a number of stars near the WD cooling sequence. They showed that UVOT could easily distinguish stellar population such as BSSs, WDs and young and intermediate age MS stars.

M67 is well studied in the optical and X-ray, though a deep study in the UV is lacking. The UV observations can detect the presence of possible hot companions that are not evident from optical photometry alone. The presence of a hot component to BSSs was detected by FUV observations of NGC 188 by the HST (Gosnell et al., 2015). This provided the necessary observational evidence of mass transfer as one of the formation mechanism of BSSs. In our previous work, we identified a post-AGB/HB companion to a BSS in NGC 188 with the help of FUV and NUV photometry from the UVIT. In the case of M67, a deep UV study will help in identifying similar systems among the BSSs. The FUV and NUV data will help in understanding the UV properties of stars, that do not follow the standard single star evolution as well as those of normal stars.

5.2 Observation and Data

GALEX observed this cluster in several pointings to produce deep images of the cluster. In this study, we use these images to understand the UV stellar population in M67. We present a comprehensive study of this cluster using FUV and NUV data from GALEX. Fig. 5.1 shows the optical and FUV image of M67, one can easily distinguish the reduction in the number of stars observed in the UV as compared to the optical image.

Fig. 5.1 Optical (left) and FUV (right) Image of M67. Image Credit: Palomar Observatory and GALEX

5.2.1 UV data

We obtained the pipeline reduced photometric data of M67 from GR6/GR7 data release. The UV data are mainly obtained from GII and MIS, with a few stars from AIS. Table 5.1 lists GALEX observations of M67. We carefully removed data with multiple measurements as well as artefacts, in the data obtained from the pipeline(Bianchi, 2014). A visual inspection of the images shows that the cluster region is not crowded, and pipeline photometry can be considered reliable. The FUV and NUV magnitudes are corrected for saturation (Camarota and Holberg, 2014). The photometric error in these bands after saturation correction are shown in Fig. 5.2 as a function of magnitude. In this plot, we also show the photometric depth of the UVOT and UIT studies of M67. The photometric depth of UIT (m_{152}) is $\sim$ 19.5 mag (Landsman et al., 1998), and those of UVOT are $\sim$ 21.5 mag (Siegel et al., 2014), whereas the GALEX photometry goes down up to $\sim$ 24.5 mag.

5.2.2 Optical Counterparts

The optical photometric data of M67 are obtained from Montgomery et al. (1993). These stars are cross matched with Yadav et al. (2008) data comprising of stars with a proper motion membership probability $\geq 60\%$ and Geller et al. (2015) data with radial velocity membership probability $\geq 50\%$. Based on both kinematic and radial velocity membership study, we identified 531 cluster members, such that a star is either a proper motion member and/or a radial velocity member. Among these, 164 stars are members based on proper motion membership probability alone. This is due to either the star not studied by Geller et al. (2015), as the limiting magnitude is upto 16.5 mag or the star being a probable member/unknown based on radial velocity measurements. Photometry of additional 152 stars are taken from Geller et al. (2015), that are classified to be members based on radial velocity membership study and are not found in Montgomery et al. (1993). Hence we have selected a total of 683 member stars of the cluster having BV optical photometric data. Their counterparts in the FUV and NUV data are identified with an accuracy of $\leq 3''$ using GalexView (http://galex.stsci.edu/GalexView/). A star with the closest angular separation between optical and UV cross-match is selected in case of multiple detections. Out of 683 cluster members, 92 stars are detected in the FUV and 424 stars in the NUV band, whereas only 67 stars have both FUV and NUV detection. Among the 92 stars detected in FUV, 84 are members based on radial velocity measurement, 4 are based on only proper motion membership probability, 3 are WDs (Landsman et al., 1998) and 1 star (WOCS 1017) with low proper motion and radial velocity membership probabilties. WOCS 1017 is in the location of BSS, it may be interesting to study this object in detail as Landsman et al. (1998) argues that, as a BSS, this star might acquire a peculiar velocity if its formation process is due to stellar interactions (e.g., Leonard, 1996). Of the 424 stars detected in NUV band, 400 are members by radial velocity study, 21 are proper motion members, 2 are WDs (Landsman et al., 1998) and WOCS 1017. The UV photometric data of these stars, along with their already known evolutionary status (classification) taken from literature are tabulated in Table 5.2.

5.3 Method

We have used FSPS (Conroy et al., 2009; Conroy and Gunn, 2010) code to generate both optical and UV isochrones of BaSTI model (Pietrinferni et al., 2004; Cordier et al., 2007) by providing the input parameters of the cluster: distance modulus ($V-M_v$= 9.6 mag), Solar metallicity and reddening of E ($B-V$)= 0.056 mag (Montgomery et al., 1993). The UV isochrones are obtained after convolving the GALEX filters with the BaSTI model. Fig. 5.3 shows the V, ($B-V$) CMD of above mentioned 683 member stars and the stellar population identified based on previous studies. The V and B magnitudes

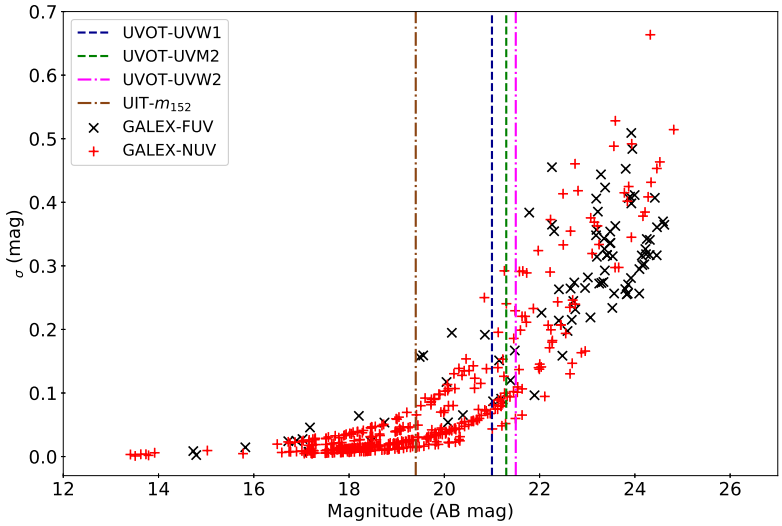

Fig. 5.2 Photometric Error in GALEX FUV and NUV Data vs. their Magnitudes. The Photometric Limit of Other UV Studies of M67 are also Indicated

Table 5.1 Observation Details of M67 by GALEX, which are used in this Study

No. of Stars	Sky Survey	Exposure Time (s).
FUV band detection		
40	GII	5555.20
34	GII	1691.05
11	MIS	455.00
7	AIS	178.05
NUV band detection		
92	GII	5555.20
181	GII	1691.05
20	MIS	1673.30
1	MIS	1594.03
55	MIS	455.00
1	AIS	455.00
5	AIS	217.00
2	AIS	216.00
3	AIS	208.00
1	AIS	192.00
64	AIS	178.05

are converted to AB magnitude system as the GALEX magnitudes are in this system, and the transformation values for Vega to AB magnitude system are taken from Bianchi (2011) Table 1. An isochrone of 3.5 Gyr age is superposed on the optical CMD along with a binary sequence, which is 0.75 mag brighter than the MS as shown in Fig. 5.3. These isochrones are found to match the observed sequence very well. A WD cooling curve to the left of the MS and BSS model line above the MSTO are shown in the Fig.

5.3. All the stars classified in Table 5.2, are shown with different coloured symbols in all the CMDs and discussed in the following sections. We use this optical CMD as the reference CMD to understand the UV CMDs presented in the next section.

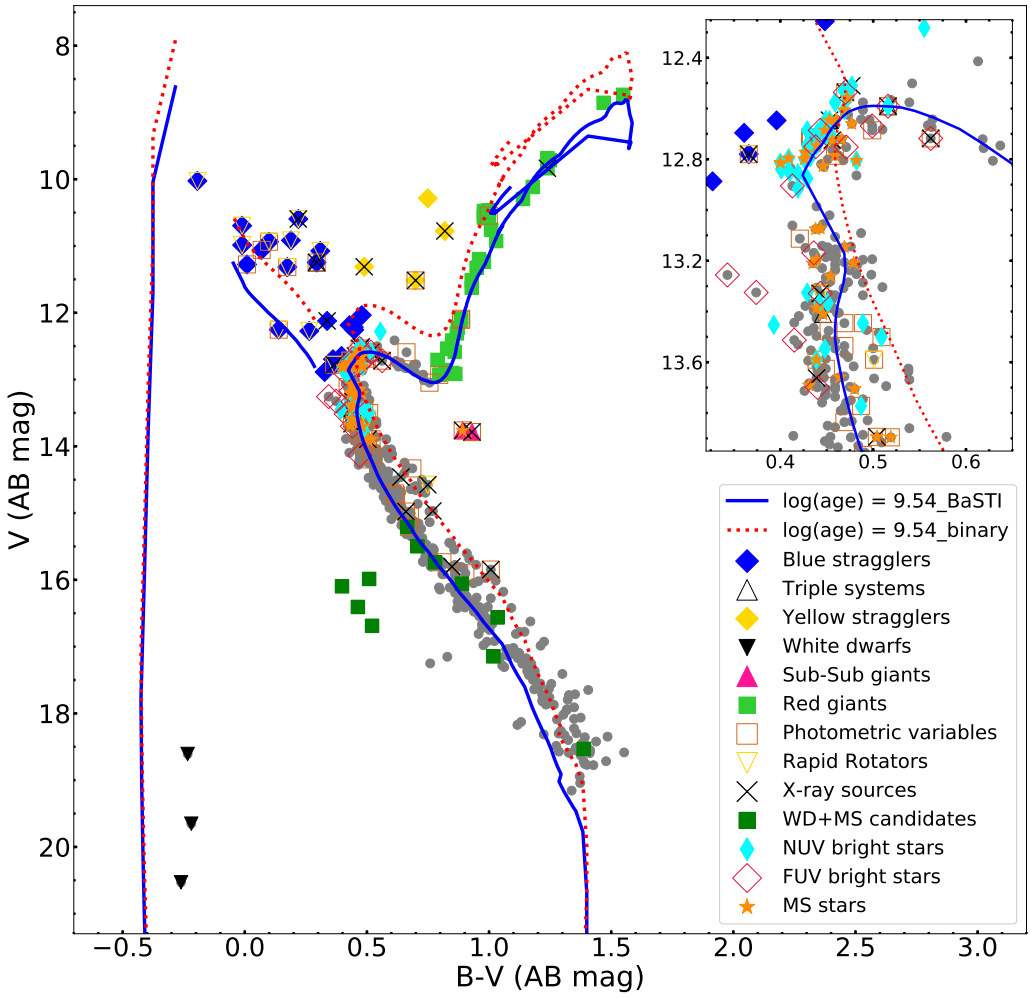

Fig. 5.3 Optical CMD of M67, showing only Member Stars based on Proper Motion and/or Radial Velocity Measurements of the Cluster. A 3.5 Gyr Isochrone is Superposed on the Optical CMD Along with the Equal Mass Binary Sequence. The WD Cooling Sequence is Shown to the Left of the MS and the BSS Model Line is shown above the MSTO

5.4 Data Analysis

We present the UV−optical and UV CMDs of this cluster in this section and discuss the various stellar population that are distinct in these CMDs. We list and discuss the X-ray sources which are detected in GALEX. We also present the UV properties of BSSs in the UV−optical and UV CMDs. UV−optical CMD combines the UV and optical photometry and helps to identify the hot stellar population as well as binaries with hot companions such as WDs. The number of stars detected in FUV and NUV with optical counterparts are 92 and 424 respectively. An (FUV−V) vs. FUV CMD (henceforth

'FUV−V CMD') of M67 is shown in top panel of Fig. 5.4, and the (NUV−V) vs. NUV CMD (henceforth 'NUV−V CMD') is shown in bottom panel of Fig. 5.4. The UV CMDs are shown in the Fig. 5.5. An isochrone of 3.5 Gyr is superposed on all the CMDs along with the binary sequence.

The FUV−V CMD guided by the overlaid isochrone indicates that only stars on and above the tip of the MSTO are detected in the FUV, as the tip of the MS is found at an FUV magnitude of ~ 24. All these are found to be located above and on the MSTO, and upper MS region in the optical CMD. We observe that, 47 stars (orange filled stars and pink open diamonds) appear brighter than the tip of MSTO in this CMD. Among these stars, 3 triple system, 8 X-ray sources, 1 SSG, and 9 photometric variables are identified from the literature. From the radial velocity study (Geller et al., 2015) it is found that 19 of them are binary stars and 28 are single member stars. The binary fraction found in this region is not inconsistent with the cluster binary fraction. Thus a variety of stars are found in this CMD and many have excess flux with respect to their location in the optical CMD. Note that some stars shown in the FUV−V CMD may not appear in the UV CMDs (shown in Fig. 5.5), if they are not detected in the NUV, and vice versa.

In the FUV−V CMD, we identify three regions corresponding to WDs, BSSs and gap stars, as shown in the figure. The location of WDs and BSS are similar to those adapted in the Optical CMDs, whereas the gap region is similar to that found by Knigge et al. (2002), in their FUV−optical CMD. The detected 3 WDs are located in the WD region. We identify 6 stars (filled green squares) in the gap region, which are found to be located in the MS, in the optical CMD. They are found on the bluer side of the FUV−V MS, suggesting that they may be hotter than expected from the optical CMD. The BSS region consists of stars brighter than the MS, along the BSS model line. We see that the BSSs fall in this region. The two YSSs also fall in this region. We notice a number of stars are found along with the bright BSSs, where the model BSS line is also located. The region brighter than the tip of the MS and the fainter end of the BSS model line has three BSSs along with a number of stars. This is an interesting point and we look into this in more detail below.

In the NUV−V vs. V CMD, shown in Fig. 5.4, we notice a very well defined MS well fitted by an isochrone of 3.5 Gyr as well as the adopted reddening. Most of the stars brighter than 16.8 mag in the V band are detected in the NUV band. The stellar evolutionary features of the MS, MSTO, SGB and the RGB stages are clearly delineated in the NUV−V CMD. The MS is found to be a tight sequence, with very little scatter in the (NUV−V) colour. Stars near the MSTO show a spread in magnitude in this CMD when compared to the optical CMD. Similar to the FUV−V CMD, BSSs appear as the brightest sequence in NUV−V CMD.

The SGB is clearly visible in the NUV−V CMD and it is well fitted by the

isochrone (3.5 Gyr age). The RGB stars are detected in the NUV band and show a relatively large scatter. The isochrone more or less fits the bluer RGB stars, while the redder RGB stars tend to be brighter in the NUV and follow the binary isochrone. It is not clear whether the NUV excess detected among some RGB stars is due to binarity. Near the RGB region, 5 brightest stars form a clump in Fig. 5.4. Among these stars, 4 of them are identified as RG clump stars (Sandquist, 2004). Stars which appear in the FUV$-$V, NUV$-$V and the UV CMDs are discussed below. We first discuss the stars that are known from the optical CMD and then stars that are identified from the UV CMDs

5.4.1 Blue Straggler Stars

In the FUV band, 15 members and WOCS 1017 BSSs are detected (listed in Table 5.2). They appear as a bright sequence in the CMDs. The brightest and hottest BSS (WOCS 1010) in the optical CMD is saturated in both the FUV and NUV bands of GALEX, and hence could not be considered further in this study. We observe that BSSs span a range of $\sim$ 3 mag scale on the optical CMD; whereas, in the FUV$-$V CMD, they stretch over a range of $\sim$ 8 mag region above the MSTO, and are easily identified. Among the 16 detected BSSs, 9 are relatively bright (brighter than 19 mag in FUV) and 7 of them are brighter than 17.2 mag. WOCS 1006 and WOCS 1026, which are single lined spectroscopic binaries and rapid rotators are found to be brightest in the FUV ($\sim$ 14.7 mag). They are also among the brightest BSSs observed in the UIT images. In general, the BSSs that are brighter in the FUV are either rapid rotators and/or photometric variable. Three BSSs (WOCS 1020, WOCS 2015 and WOCS 2068) appear fainter than 22.5 mag in the FUV. Among the 16 BSSs detected in the FUV band, 4 (WOCS 1017, WOCS 2009, WOCS 4003 and WOCS 5005) also have X-ray detection. WOCS 2009 is a triple system but also listed as a photometric variable and a double lined spectroscopic binary. WOCS 4003 and WOCS 5005 are relatively faint and are found closer to the base of the BSS model line in the FUV$-$V CMD (Fig. 5.4). We find that 13 BSSs have NUV magnitudes, 8 are bright in the NUV, 5 are relatively fainter and they are located closer to the MSTO. There are 5 stars which are detected in the FUV but do not have the NUV magnitude. On the other hand, 2 stars (WOCS 3009, WOCS 9005) have the NUV detection but are not detected in the FUV band. WOCS 1026 is the brightest BSS observed in the FUV band, but its NUV magnitude could not be determined likely to be due to saturation in the GALEX observation. WOCS 1006 is the brightest in the NUV band. Overall BSSs dominate the UV light in old open clusters.

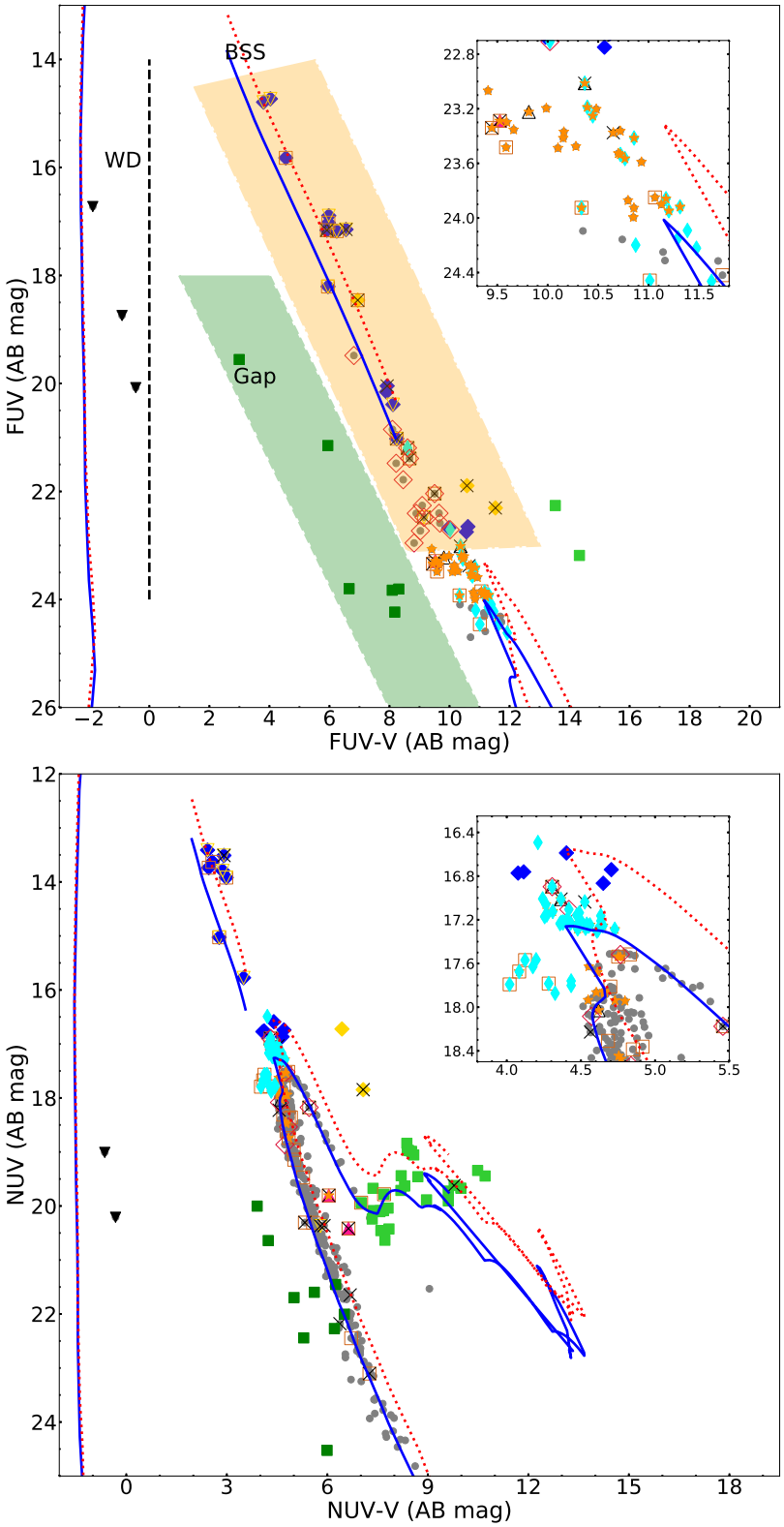

Fig. 5.4 (Top:) FUV, FUV−V CMD, (Bottom:) NUV, NUV−V CMD of M67 are shown. A 3.5 Gyr Isochrone is Superposed on all CMDs along with the Equal Mass Binary Sequence. The WD Cooling Sequence is shown to the left of the MS and a BSS Model Line above the MSTO. The Symbols have the same meaning as those in the Optical CMD. Three Regions (WD, Gap and BSS) are Identified in the FUV, FUV−V CMD

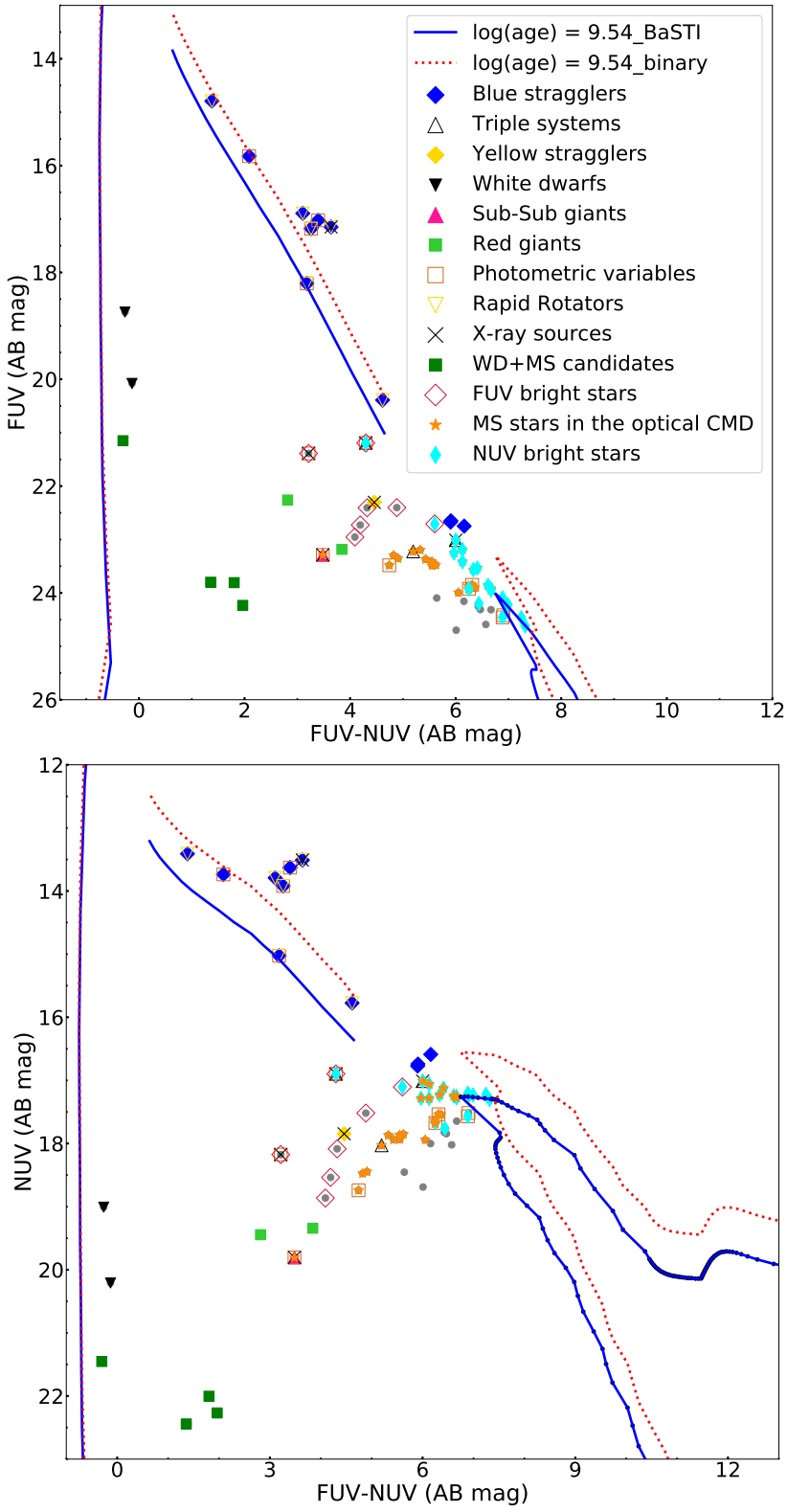

Fig. 5.5 (Top:) FUV, FUV−NUV CMD and (Bottom): NUV, FUV−NUV CMD of M67 are shown. A 3.5 Gyr UV Isochrone is Superposed on all CMDs along with the Equal Mass Binary Sequence. The WD Cooling Sequence is shown to the left of the MS and a BSS Model Line above the MSTO. The Symbols have the same meaning in all the Figures

Table 5.2 List of M67 members detected by GALEX. Column 1 gives the ID from MMJ93, Column 2 gives the WOCS ID of M67. Column 3 and 4 are V and B-V mag from Montgomery et al. (1993). Column 5 and 6 are GALEX FUV and NUV in AB mag, Corrected for Saturation as Mentioned in the text. Column 7 are Magnitude from UIT from Landsman et al. (1998). Chandra, ROSAT and XMM -Newton are the X-ray Counterparts given in Column 8, 9 and 10. The Membership and Type/Class taken from the Radial Velocity Membership Study are shown in Column 11 and 12. In the Comments Section, Details Regarding Their UV Properties are Listed. (The full table is in the appendix)

MMJ	WOCS	V	B-V	FUV	NUV	m_{152}	CX	X	NX	Memb.	Type/Class	Comments
6490	1006	10.99	0.11	14.79	13.41	12.10	...	...	...	(BL)M	BSS, SB1, RR	
6504	1007	10.94	0.22	17.18	13.92	14.47	...	...	...	BM	BSS, SB1, RR,EX Cnc	
6511	1017	10.6	0.34	17.15	13.51	14.32	109	...	...	(S)N	BSS, RR	
5191	1020	12.7	0.48	22.67	16.77	...	...	...	...	SM	BSS	
6006	1025	12.28	0.39	20.39	15.77	...	...	...	...	BM	BSS,SB1, RR	
6510	1026	10.7	0.11	14.73	...	12.06	...	...	...	(BL)M	BSS, SB1, RR	
5699	2007	12.26	0.57	20.16	...	...	...	...	...	SM	BSS	
6479	2011	11.28	0.13	15.82	13.74	13.15	...	...	...	SM	BSS, PV	
...	2013	10.92	0.31	16.89	13.79	14.20	...	...	...	BM	BSS, SB1, RR	
6477	2015	12.04	0.60	22.65	16.74	...	...	...	...	SM	BSS	

SM - Single Member, SN-Single Non-member, BM- Binary member, BLM- Binary Likely Member, U-unknown with RV measurements.

5.4.2 Yellow Straggler Stars

Three of the 4 known YSSs are detected in the FUV (WOCS 2002, WOCS 1015 and WOCS 2008), they are also single lined spectroscopic binaries stars (Geller et al., 2015). WOCS 2002 is relatively bright in the FUV, whereas the other two are relatively faint and have redder (FUV−V) colours. 2 YSSs are detected in the NUV band and are found to be located brighter than the SGB in the NUV−V CMD. The brightest YSS, detected in the FUV which was identified in the BSS location, on the other hand, does not have NUV detection. All 3 stars have X-ray emission (ROSAT, Chandra and XMM-Newton). Two of these YSSs (WOCS 2002, WOCS 1015) are believed to have undergone mass transfer (Landsman et al., 1997; Leiner et al., 2016). WOCS 2002 is found to have a hot WD companion with a low mass of 0.23 $M_{\odot}$ (Landsman et al., 1997). A recent study showed that WOCS 1015 has a normal MS or a BSS companion (Leiner et al., 2016). They suggested that it is likely to be an evolved BSS.

5.4.3 Red Giants

Two RGs (WOCS 1036, WOCS 1075) are detected in the FUV which are bright with redder colour in the optical CMD (Table 5.2). The detection of these RGs, particularly in the FUV band, is quite intriguing since their (FUV−NUV) colour is $\lessapprox$ 4 mag and is bluer in the UV CMDs as seen in Fig. 5.5 (bottom panel). The FUV brightness as well as the blue UV colour are suggestive of extra flux in the UV when compared to the prediction based on the optical CMD.

5.4.3.1 Sub-Sub Giants

Some of the previous studies has often termed SSGs as red stragglers. Geller et al. (2017) in a recent study, clearly delineated them by giving their demographics in the optical CMD, so as to separate SSGs and red stragglers. Two SSGs are known in M67, both have high proper motion and radial velocity membership probability. Among two SSGs, only WOCS 15028 is detected in the FUV, which also has X-ray detection. The fact that this star, which is quite sub-luminous in the optical CMD, is detected in the FUV warrants attention. Both the stars are detected in the NUV band. They are fainter than the SGB but bluer than the RGB stars. One SSG is relatively brighter and bluer in the NUV−V CMD, whereas both occupy the same location in the optical CMD.

5.4.4 Triple Systems

Four triple systems are detected in the FUV band (Table 5.2) and 3 in the NUV band. WOCS 2009 is a BSS and double lined spectroscopic binary as discussed earlier and has the brightest FUV mag among the triple systems, and is not detected in the NUV

band. WOCS 3012, WOCS 7008 and WOCS 4030 are the other three triple systems with FUV detection.WOCS 7008 and WOCS 4030 are identified at the FUV detection limit of GALEX.

5.4.5 White Dwarfs

There are 3 WD candidates (refer Table 5.2) detected in the GALEX FUV, and 2 in the NUV which were earlier identified in UIT data (Landsman et al., 1998). They occupy the WD region in both the FUV−V and NUV−V CMDs. Fleming et al. (1997) derived the effective temperature of the 2 WDs; MMJ 5670 is the brightest WD candidate and is known as a hot DA WD with T_{eff}=68,230 $\pm$ 3200 K and MMJ 5973 to be a DB WD with T_{eff}=17,150 $\pm$ 150 K. MMJ 6061 is relatively fainter in the FUV.

5.4.6 FUV Bright Stars

We identify 15 stars located in the same BSS region outlined in Fig. 5.4 along with the 16 BSSs, which are located on or below the MSTO, including the SGB in the optical CMD. Thus, we classify these 15 stars as FUV bright stars (pink open diamonds) and are listed in Table 5.2. These stars have FUV magnitude in the range 19.5 - 23.0, whereas the MSTO is at $\sim$ 24 mag. Among these 15, 6 are significantly FUV bright (WOCS 2012, WOCS 11005, WOCS 3012, WOCS 6008, WOCS 3001 and WOCS 11006) based on the FUV−V CMD (Fig. 5.4). These 6 stars are located close to the BSS model line as shown in the FUV−V CMD, with FUV $<$22 mag, at least 2 magnitude brighter than the MSTO. Among the 6 stars, 5 stars have high membership probability based on both proper motion and radial velocity measurements. WOCS 11006 is a member based on proper motion study. WOCS 2012 is the brightest among these 6 stars and lie close to the BSS model line (Fig. 5.4), though it lies on the SGB in the optical CMD. WOCS 6008 and WOCS 11005 are SGB stars in the optical CMD. Among these 15, 9 stars are in the FUV magnitude range of 22.0 - 23.0, fainter than the above 6, but brighter than the MSTO. These are identified close to the 3 FUV faint BSSs ($\sim$ 22.7 mag). Among these 9 stars, Sandquist (2004) suggested that WOCS 8004 and WOCS 6006 are likely BSS candidates. In the UV CMDs, the FUV bright stars shift to a bluer region in the CMD, when compared to their location in the FUV−V CMD, suggesting they are brighter and probably hotter in the FUV. It can also be seen that in the NUV−FUV vs NUV CMD, they occupy a region fainter than the MSTO, suggesting that they are not bright in the NUV. A detailed spectral energy analysis using multiwavelength observation data of all these FUV bright stars are presented in chapter 6.

5.4.7 White Dwarf + Main Sequence Binaries

Apart from the 3 WD candidates, in the FUV−V CMD (Fig. 5.4), we identify 6 possible WD+MS binaries (6 green filled squares in the gap region of Fig. 5.4). These stars are identified based on the fact that they occupy MS location in the optical CMD, well below the MSTO (more than 2 magnitude fainter than MSTO), whereas they are brighter and bluer than the MSTO stars in the UV CMD, in a region between the MS and WD cooling sequence. These are similar to WD+MS binaries shown by Parsons et al. (2016) in their figure 1 and 2. The UV excess could be possibly due to a WD companion to the low mass GK type MS stars, similar to the population of FGK type stars with WD companions (Parsons et al., 2016). Knigge et al. (2002), while studying the FUV observations of 47 Tuc, suggested a cataclysmic variable (CV) zone in their FUV-optical CMD. The other stellar types which could occupy this region, other than CVs, are MS+WD binaries and He WDs. This region is similar to the location of gap stars in UV study of M15, M80 and NGC 6397 (Haurberg et al., 2010; Dieball et al., 2010; Dieball et al., 2017). They suggested the region between WD and MS in the FUV−NUV CMD belong to gap stars, which could be a combination of CVs, detached WD+MS binaries and He WDs. Hurley et al. (2005) based on the N-body model of M67, expected to find 226 single WDs, 60 double WD binaries and 145 WD in non-WD companion near the cluster center. They also expected to find another 33 WDs in other binaries, some with low mass MS, which could appear near the WD sequence and suggest that the observation of WDs in M67 is incomplete. Similar to the 6 stars which lie to the bluer side of FUV−V CMD, we observe another 5 stars which are significantly ($\sim$ 1 magnitude) bluer than the MS stars but are redder than the WD in the NUV−V CMD, they are listed in Table 5.2. Further analysis of these objects are presented in the next chapter 6.

5.4.8 Anomalous Stars in the NUV−V CMD

An inspection of the NUV−V CMD reveals a group of stars (cyan filled diamonds in Fig. 5.4 (bottom panel)) in the NUV magnitude range of 16.5 to 17.3. This group consisting of 31 stars are located between the MSTO of the single and binary star isochrone, and we refer to them as NUV bright stars. These stars occupy the MSTO in the optical CMD in the Fig. 5.3, thus they show a moderate excess in the NUV flux (the excess is up to 0.5 mag, whereas the photometric error is less than 0.1 mag). Among these, 2 stars belong to the FUV bright stars which show large excess (WOCS 3012, WOCS 3015) and a few stars have less FUV excess (orange filled star) in Fig. 5.4 (upperpanel). From the radial velocity estimation, 23 stars are classified to be single members and 8 stars are binary members. Of the 8 binary stars; 3 (WOCS 4004, WOCS 3023, WOCS 4051) are known single lined spectroscopic binaries while 5 (WOCS 3012, WOCS 7008, WOCS

6010, WOCS 3015, WOCS 3006) are known double lined spectroscopic binaries stars. In short, these NUV bright stars appear to be populated by various types of stars. Some show only NUV excess, whereas some show FUV excess as well. Five of the NUV bright stars are classified as MSTO gap stars (Sandquist, 2004). They suggest that these stars are likely to be categorised as BSSs.

In Fig. 5.4, we identify another 9 stars (cyan filled diamonds) which are found on the bluer side of the MSTO. They are also NUV bright stars, but in the optical CMD, they are located below the MSTO. All of them have radial velocity membership probability $> 90\%$, but only 7 stars have proper motion membership probability $> 99\%$. Among these stars, 5 are single and 4 are binary members. WOCS 5035 is a photometric variable and classified as a MSTO gap star (Sandquist, 2004). WOCS 8007, WOCS 11022 and WOCS 2016 are single lined spectroscopic binaries, while WOCS 4016 is a double lined spectroscopic binary star. Sandquist (2004) suggested that WOCS 7044 and WOCS 7015 could be tentatively classified as BSSs based on their V-I CMD. In the optical CMD, these stars are found at least 1 magnitude below the MSTO.

In the NUV$-$V CMD, we identify a star (WOCS 2083) which has a radial velocity membership of 97%, and is located below the RGs and redder than the MS in Fig. 5.4 (bottom panel). This star is not shown in the optical CMD since the MMJ93 does not provide B magnitude. Taking the value of B = 13.52 from Sanders (1977) and V =12.49 from MMJ93, the star will lie on the SGB region in the optical CMD. We suggest that it could be an SSG candidate.

5.4.9 X-ray Counterparts

There are 36 optical member stars with X-ray observation in at least one of the three missions mentioned earlier. We have cross identified GALEX UV sources with their X-ray counterparts. In Table 5.2 we have listed 25 stars which have both UV and X-ray detection. Among them, 15 sources are detected in the FUV, 16 in the NUV and 6 in both the filters. Among these stars, 20 are binary members, 2 are single stars, 3 are unknown and WOCS 1017 of the cluster based on the radial velocity study.

Four BSSs are detected in both X-ray and GALEX, WOCS 1017 is a rapid rotator, and is also brightest among the four BSSs with X-ray detection, as seen in the FUV$-$V CMD. WOCS 2009 is a triple system, with an X-ray luminosity of the order 10^{30} ergs/s. Landsman et al. (1998) suggested that this system could be an Algol type mass transfer due to its X-ray emission and presence of a hot sub-luminous companion. They also eliminate the possibility of the hot secondary being a WD, due to the NaI D and OI absorption lines being present. Van den Berg et al. (2001) derived the period of this star and argued that the X-ray emission could be due to magnetic activity in the rapidly rotating SG. WOCS 4003 is a semi-detached system with rapid rotation. Yakut

et al. (2009) determined the period of this star and suggested the X-ray emission was perhaps due to the chromospheric activity induced by rapid rotation. The X-ray detection of the fourth BSS, WOCS 5005 detected in Chandra is not clearly understood. WOCS 4011 is an RGB star with an X-ray luminosity of the order of 10^{30} ergs/s and is detected only in the NUV. This star is a single member of the cluster from the radial velocity study. It is recently found to host a Jupiter-mass exoplanet (Brucalassi et al., 2014). Two SSGs were detected in ROSAT (Belloni et al., 1998), and both have X-ray luminosity of 7.3×10^{30} ergs/s. Mooley and Singh (2015) studied the X-ray spectrum and variability of one SSG (WOCS 13008) and suggested that the X-ray emission is from its corona. Leiner et al. (2017) studied both these stars and stated that the X-rays are from the hot corona, due to strong magnetic field. A recent study suggested a few formation pathways for these stars (Geller et al., 2017).

Three stars (WOCS 2009, WOCS 3012 and WOCS 7008) are in triple systems and are found to be RS CVn systems. All three stars are bright in the FUV, WOCS 2009 is a BSS as discussed above and has the brightest FUV magnitude among the triple systems. WOCS 3012 is one of the FUV bright star based on the UV CMD, and is detected in all three X-ray observation with the luminosity of the order 10^{30} ergs/sec. WOCS 6010 lies on the MS in the optical CMD and is also located in the NUV bright star region in the NUV$-$V CMD. The star is detected only in Chandra and has an X-ray luminosity of 4.2×10^{28} ergs/sec, though Van den Berg et al. (2004) stated that the X-ray and optical position are uncertain due to relatively large offset. WOCS 10025 could be a possible CV based on the X-ray spectrum suggested by Belloni et al. (1998), though Mooley and Singh (2015) contradict this possibility. This star is detected only in the NUV and is located on the MS, close to the binary sequence in the NUV$-$V CMD.

Three YSSs have X-ray detections in all the three missions. WOCS 2008 and WOCS 1015 are redder than the MS in the FUV$-$V CMD. Mooley and Singh (2015) indicated that tidal interaction cannot explain the X-ray emission of both these stars due to their wide separation. In the NUV$-$V CMD, only 1 (WOCS 1015) YSS with X-ray counterpart is detected. Four contact binaries, which are all W Uma type are detected in the UV (Mooley and Singh, 2015). Among these 4 contact binaries, 2 are detected only in the FUV and 2 only in the NUV.

5.5 Summary

M67 is a very well studied cluster and these studies have revealed the presence of a large number of stars in non-standard stellar evolutionary phases. Some of them being, BSSs, YSSs, SSGs, W Uma systems, triple systems etc. Many single stars are also found to be photometric variables or rapid rotators. Therefore M67 serves as a test-bed to study these stars in detail and understand their properties, origin and evolution. There have

been extensive studies of this cluster in the optical and X-ray, but a detailed study in the UV pass band is not attempted so far. In this study, we use the deep photometric data of GALEX in the NUV and FUV pass bands to study the behaviour of M67 member stars. Here we present the UV− optical and UV CMDs of the member stars.

We combined all the observations of M67 made by GALEX to obtain the FUV and NUV magnitudes of 449 stars. We used the optical CMD as the reference to deduce the evolutionary phases of the stars and compare their location in the UV CMDs to understand their behaviour. We detect 92 stars in the FUV, which include BSSs and WDs. Most of the FUV detected BSSs are bright and located 3 - 8 magnitudes above the MSTO in the UV CMDs. As the BSS region in UV CMDs extend to about 8 mag above the MSTO, these CMDs are ideal to study BSSs (Sindhu et al., 2015; Siegel et al., 2014). The CMDs shown in the Fig. 5.4 and Fig.5.5 are a first of its kind for this cluster and it reveals a lot of interesting properties of various types of stars. The sequences which are identified in the UV CMDs suggest that there are a good number of stars with FUV and/or NUV excess.

We empirically identified regions in the FUV−V CMD belonging to WDs, gap stars and BSSs. In the BSS region, it was noticed that 15 MS stars were co-located along with the BSSs. The BSSs are in general identified in the optical CMD as stars located above the MS. Now, if we apply the same criteria in the UV CMD, we find a lot more stars in the BSS region. There may be FUV/NUV non-photospheric emission resulting in a UV excess occurring in these stars appearing brighter than the MSTO. The 15 FUV bright stars with excess UV flux could harbour hot companions or have active chromospheres. Detection of a large number of stars with FUV and/or NUV excess in this cluster suggests that these stars could be active stars resulting in the production of excess UV flux. This is supported by the fact that many stars are detected in X-rays as well. We present the catalog of UV detections, along with their WOCS and MMJ identification numbers and X-ray detections in Appendix.

The cluster sequence is clearly delineated in the NUV−V CMD. The MS, SG and RGB are clearly seen, where we notice a very tight SGB and a fairly spread out RGB. The SGB is well fitted by a 3.5 Gyr. It would be interesting to find the origin of spread among these RGB stars in the NUV. We detect two RGs in the FUV and are brighter in the NUV as well. These stars could be chromospherically active stars or stars with coronal emission.

A number of stars near and below the MSTO in the optical CMD are found to have NUV excess flux. All MS stars in the F-M spectral types are observed to have varying amounts of chromospheric activity (Linsky, 2017). Reiners and Giampapa (2009) studied 15 solar-type stars and concluded that high activity in these stars that exceeds the Solar levels is likely to be due to rapid rotation. This study thus clearly brings out the need to probe cluster stars in the UV wavelength.

5.6 Conclusion

The main conclusion of this chapter are as follows:

- The first comprehensive UV properties of member stars of the old open cluster M67 are presented in this chapter. We have compiled the UV magnitudes of 449 stars (92 in the FUV and 424 in the NUV). We have listed the FUV and NUV magnitudes, and classification of the detected member stars in the catalog, which can be found in the appendix.

- Sixteen BSSs, 3 WDs, 3 YSSs, 1 SSG, 2 RGs, 3 triple system in the FUV and 13 BSSs, 2 WDs, 2 YSSs, 2 SSGs, and 1 triple system in the NUV are detected.

- We detect a few lower MS stars to have large UV excess, suggesting that they could be MS + WD binaries. We identified 11 such systems, which are new identifications, with 7 showing FUV excess.

- We also detect stars near the MSTO and SGB to have excess flux in the FUV and/or NUV. This excess flux could be due to chromospheric activity.

CHAPTER 6

A Multiwavelength Study of the UV Bright Stars in M67 (NGC 2682)

6.1 Introduction

The star cluster evolution is dictated by the complex interaction between stellar dynamics and single and binary stellar evolution (Heggie, 1975; Hurley et al., 2001; Hurley et al., 2005) and hence the production of exotic stars is possible in M67, as the cluster is dynamically active (Glebbeek and Pols, 2008). Previous photometric studies from X-ray to IR have revealed that exotic stars such as BSSs, YSSs, SSG, and X-ray sources are found in the old open cluster M67 (Nissen et al., 1987; Montgomery et al., 1993; Belloni et al., 1993; Latham and Milone, 1996; Landsman et al., 1997; Landsman et al., 1998; Belloni et al., 1998; Deng et al., 1999; Van den Berg et al., 2001; Mathieu et al., 2003; Van den Berg et al., 2004; Geller et al., 2015; Mooley and Singh, 2015; Geller et al., 2017). These studies revealed that, these stars are cluster members that do not fall along standard single evolutionary tracks. The BSSs populate the region above the MSTO and are bluer than the MSTO, these stars should have evolved to post-MS phases. Similarly the location of YSSs and SSGs on the observational CMD cannot be explained with single stellar evolutionary models.

In the previous chapter, we examined this cluster in the UV and optical bands, which showed that a few stars in the the UV CMD are exceptionally bright. Some of these stars are the well known BSSs, but apart from these stars we also observed a few stars that occupy the gap region in the FUV$-$V CMD, which we have newly identified, and are suggested to be MS $+$ WD binaries. Two RGs are detected in the FUV, which is quite compelling. We also observed a few stars which lie on and below the MSTO in the optical CMD to have an excess flux in FUV, as seen from Fig. 5.4. Hence we probe further to understand the nature of all the stars with UV excess. M67 is a well studied cluster in all wavelength bands, as mentioned earlier, though a multiwavelength band investigation covering the full extent of stellar flux distribution has not been attempted so far. We devised a multiwavelength approach to study these stars, and used existing photometric data from the UV to IR to obtain their fundamental properties.

6.2 Data and Observation

In the present work we analyse 45 stars of M67 that are found to have excess flux in the FUV band of GALEX. We have used the existing photometric data from UV (GALEX (FUV, NUV)), optical (Montgomery et al., 1993 (U, B, V, R, I), GAIA (G)), near-infrared (2MASS (J, H, K_s)) to mid-infrared (WISE (W_1, W_2, W_3)). The pipeline reduced photometry data of GALEX is obtained from GR6/GR7 data release and GAIA is obtained from DR1 release. GAIA, 2MASS and WISE data are obtained directly from VO photometry. The cross-match is found within a spatial search radius of $3''$. The input file to obtain the photometry of stars consists of stellar parameters such as RA, Dec, and the distance to the objects. We have tabulated the photometry magnitudes for the 45 stars in all the filters that these stars were detected. The photometric magnitudes of 15 FUV bright stars are tabulated in Table 6.1, 11 WD+MS candidate binaries and 2 RG in Table 6.2 and 17 BSS in Table 6.3.

We have also obtained the spectra of two RGs and 5 BSSs from IUE archival spectra. The two RGs: WOCS 1036 (NGC2682 4202/ M67 IV-202) was observed on 28/10/1984 for an exposure time of 24.6 ks and WOCS 1075 (NGC2682 S1553) was observed on 14/03/1987 for an exposure time of 14.7 ks in the NUV region. The 4 BSSs (WOCS 1006,WOCS 1007,WOCS 1026 and WOCS 2011) detected in the GALEX FUV along with the UV bright BSSs WOCS 1010 have IUE spectra in both FUV and NUV region. The five BSSs: WOCS 1010 (Cl*NGC2682 CI 1) was observed on 18/03/1986 for an exposure time of 270 s in the NUV region and 660 s in the FUV region, WOCS 1006 (Cl*NGC2682 FBC3674) was observed on 18/03/1986 for an exposure time of 1.2 ks in the NUV and 4.5 ks in the FUV region, WOCS 1026 (BD+12 1930) was observed on 18/03/1986 for an exposure time of 840 s in the NUV region and 4.5 ks in the FUV region on 19/03/1986, WOCS 2011 (Cl*NGC2682 FBC 3649) was observed on 19/03/1986 for an exposure time of 1.8 ks in the NUV and 7.267 ks in the FUV region and WOCS 1007 (V*EX Cnc) was observed on 20/03/1986 for an exposure time of 2.1 ks in the NUV region and 3.6 ks in the FUV region on 15/12/1987.

6.3 Data Analysis

The BSSs are found to have a large range in FUV flux, in comparison to the optical flux. It is therefore essential to identify the parameters of BSSs which makes them more sensitive in the FUV. Also the FUV bright stars are interestingly found to be co-located with the known BSSs and will be good to compare their properties. The fundamental properties, which can be estimated and compared are the total Luminosity ($L/L_{\odot}$), the radius ($R/R_{\odot}$) and the effective temperature (T_{eff}).

Table 6.1 The Photometric Magnitudes of 15 FUV Bright Stars with Excess UV Flux. GALEX - FUV and NUV in AB Mag are taken from GR6/GR7 Data Release and Corrected for Saturation. The Optical Magnitude U, B, V, R and I are in Vega Magnitudes and taken from Montgomery et al. (1993). 2MASS, WISE and GAIA are taken from their respective Source Catalogue through VO Photometry

WOCS ID	FUV	NUV	U	B	V	R	I	W1	W2	W3	J	H	Ks	G
2003	22.04	—	13.20	13.13	12.54	12.18	11.84	10.94	11.02	11.09	11.43	11.15	11.12	12.32
2012	19.48	—	13.45	13.29	12.67	—	11.95	11.09	11.10	10.49	11.49	11.22	11.19	12.44
3001	21.48	—	13.7	13.72	13.26	12.98	12.67	12.06	12.03	12.04	12.36	12.16	12.08	13.10
3015	22.71	17.1	13.3	13.25	12.69	—	12.02	11.24	11.27	11.39	11.60	11.36	11.28	12.50
3024	22.73	18.54	14.30	14.26	13.7	—	13.03	12.07	12.11	11.99	12.58	12.34	12.26	13.46
5030	22.41	18.08	14.01	14.06	13.52	—	—	12.04	12.09	12.04	12.40	12.14	12.10	13.29
6006	22.59	—	13.42	13.44	12.91	—	12.24	11.49	11.52	11.71	11.80	11.57	11.52	12.65
6008	21.39	18.18	13.54	13.4	12.72	12.33	11.92	10.92	10.98	11.06	11.38	11.08	11	12.43
7009	22.48	—	13.97	13.89	13.33	—	12.63	12.03	12.05	12.17	12.39	12.15	12.09	13.18
7010	22.4	17.52	—	13.35	12.76	—	12.07	11.27	11.30	11.53	11.67	11.38	11.34	12.54
8004	22.26	—	13.81	13.73	13.17	12.85	12.52	11.77	11.79	11.87	12.13	11.91	11.85	12.98
11005	20.85		13.34	13.32	12.76	—	12.07	10.76	10.85	10.75	11.28	10.90	10.82	12.47
11006	21.78		13.74	13.83	13.33	—	12.69	10.94	11.00	10.88	11.50	11.09	11.02	12.71
17028	22.95	18.86	14.75	14.73	14.14	—	13.4	12.51	12.58	11.95	13.02	12.72	12.67	13.93

Table 6.2 The Photometric Magnitudes of 11 WD+ MS Candidate Stars and 2 RG stars. GALEX - FUV and NUV are in AB Mag are taken from GR6/GR7 Data Release and Corrected for Saturation. The Optical Magnitude U, B, V, R and I are in Vega Magnitudes and taken from Montgomery et al. (1993). 2MASS, WISE and GAIA are taken from their respective Point Source Catalogue through VO photometry

WOCS ID	FUV	NUV	U	B	V	R	I	W1	W2	W3	J	H	Ks	G
17029	23.83	—	—	16.64	15.74	—	—	13.47	13.56	—	14.09	13.63	13.51	15.38
19032	24.23	22.27	17.77	17.07	16.06	—	14.9	13.27	13.37	—	14.07	13.58	13.43	15.60
19045	—	21.6	—	16.62	15.99	—	—	14.33	14.36	—	14.76	14.50	14.36	15.76
21027	—	20.64	16.95	16.99	16.41	—	15.66	14.88	14.86	—	15.21	14.97	14.76	16.16
23028	23.81	22.00	16.8	16.33	15.5	—	15.5	13.42	13.53	—	13.98	13.59	13.51	15.16
24022	21.15	21.45	16.31	16.0	15.21	—	14.34	13.32	13.37	—	13.81	13.44	13.34	14.93
36035	—	20.00	—	16.62	16.1	—	15.46	14.8	14.8	—	15.08	14.81	14.71	15.88
6427*	23.8	22.44	19.08	18.29	17.15	—	15.78	14.03	14.15	—	14.82	14.22	14.05	16.45
5658*	19.56	—	18.75	17.73	16.57	15.88	15.19	13.36	13.37	—	14.33	13.79	13.56	16.01
6398*	—	21.7	17.35	17.33	16.69	—	15.91	14.88	14.88	—	15.46	15.13	15.11	16.46
6409*	—	24.53	—	20.05	18.54	—	16.69	14.57	14.74	—	15.59	14.82	14.63	—
1036	23.18	19.34	—	10.45	8.86	—	—	4.99	4.93	4.99	6.01	5.26	5.02	8.10
1075	22.26	19.45	—	10.41	8.74	—	6.68	4.22	3.84	4.26	5.39	4.69	4.36	7.81

Table 6.3 The Photometric Magnitudes of 17 BSSs are listed. GALEX - FUV and NUV in AB Mag are taken from GR6/GR7 Data Release and Corrected for Saturation. The Optical Magnitude U, B, V, R and I are in Vega Magnitudes and taken from Montgomery et al. (1993). 2MASS, WISE and GAIA are taken from their respective Source Catalogue through VO Photometry

WOCS ID	FUV	NUV	U	B	V	R	I	W1	W2	W3	J	H	Ks	G
1006	14.79	13.41	—	11.10	10.99	—	10.86	10.62	10.67	10.77	10.75	10.73	10.70	10.93
1007	17.18	13.91	—	11.16	10.94	—	10.62	10.22	10.24	10.34	10.43	10.32	10.27	10.86
1017	17.15	13.51	—	10.94	10.60	—	10.32	9.96	10.00	10.01	10.10	10.05	9.98	10.51
1020	22.67	16.77	13.16	13.18	12.70	—	12.07	11.42	11.47	11.49	11.75	11.53	11.46	12.53
1025	20.39	15.77	12.63	12.66	12.28	—	11.77	11.27	11.30	11.29	11.55	11.41	11.34	12.18
1026	14.73	—	—	10.81	10.70	—	10.70	10.34	10.37	10.37	10.41	10.43	10.41	—
2007	20.15	—	12.90	12.83	12.26	11.90	11.55	10.60	10.71	10.86	11.14	10.89	10.84	12.05
2011	15.82	13.73	—	11.41	11.28	–	11.01	10.97	10.99	11.07	11.02	11.01	10.99	11.24
2013	16.89	13.79	—	11.23	10.92	—	—	10.36	10.39	10.37	10.49	10.43	10.40	10.85
2015	22.65	16.74	—	12.64	12.04	—	11.37	10.47	10.52	10.57	10.85	10.59	10.52	11.76
2068	22.74	16.58	—	12.74	12.19	—	—	10.79	10.84	10.88	11.16	10.93	10.86	12.10
3005	17.02	13.63	—	11.25	11.06	—	10.80	10.50	10.54	10.57	10.65	10.54	10.53	11.01
3009	—	16.86	12.87	12.79	12.22	—	11.56	10.81	10.84	10.84	11.18	10.91	10.84	12.04
4003	21.02	—	13.26	13.28	12.78	—	12.18	11.44	11.44	11.33	11.80	11.51	11.45	12.62
4006	18.21	15.02	12.54	12.52	12.26	12.12	11.92	11.52	11.55	11.02	11.73	11.66	11.62	12.15
5005	20.04	—	12.58	12.58	12.13	11.85	11.56	10.85	10.87	10.93	11.21	11.02	10.99	11.97
9005	—	16.76	13.21	13.17	12.65	12.35	12.04	10.93	10.99	11.34	11.49	11.09	11.01	12.49

We derive these parameters for the BSSs as well as the FUV bright stars using SED. We further compare the properties of the FUV bright stars and BSSs using the HRD and $L/L_{\odot}$ vs $R/R_{\odot}$ diagram. We have also constructed the SED of the 11 WD+MS candidates and 2 RGs.

6.3.1 Spectral Energy Distribution of UV Bright Stars

SEDs are constructed with the observed photometric data from UV-to-IR and fitted with Kurucz models (Castelli et al., 1997). The SED fitting is done as described in section 3.4. Stellar mass is determined using the Seiss theoretical isochrones and evolutionary tracks (Siess et al., 2000), after obtaining the T_{eff} and $L/L_{\odot}$ values from the fit. The evolutionary tracks underestimate the mass of the BSSs by 15%, as seen in two BSSs in NGC 188 (Mathieu and Geller, 2009; Geller and Mathieu, 2011). We estimate the mass only to compare the mass range for BSSs and FUV bright stars.

We fitted SEDs for 18 BSSs (those detected in GALEX), of which we present the results of 17 BSSs. We have excluded the BSS (WOCS 2009), which is in a triple system. The estimated parameters T_{eff}, $R/R_{\odot}$, $L/L_{\odot}$, and $M/M_{\odot}$ along with the errors of 17 BSSs are tabulated in Table 6.4. These are the values corresponding to the best fitting Kurucz model spectrum. Though we estimated log g values, we do not tabulate our estimations, as SED is not the ideal method to estimate log g. In general, the estimated values of log g range between 3-5 dex. The estimated temperatures are compared with previous measurements (SED fitting method) as listed in the Table 6.4 (Deng et al., 1999; Liu et al., 2008). We have shown the SED fit of three BSSs - WOCS 2015, WOCS 2011 and WOCS 3005 in Fig. 6.1 to demonstrate our fitting. An inspection of the table reveals that the BSSs have a large range in both T_{eff} ($\sim$ 6000 - 9000 K) and $L/L_{\odot}$ ($\sim$ 5-30), and a small range in $R/R_{\odot}$ ($\sim$ 1.5 - 3.0). The estimated temperatures compare well with those from the earlier studies.

Gilliland and Brown (1992) determined the parameters of two stars (WOCS 4006 and WOCS 1007) as $L/L_{\odot}$= 26.7, $M/M_{\odot}$=2.13, $R/R_{\odot}$= 2.8 and T_{eff}=7900 K for WOCS 1007 and $L/L_{\odot}$= 8.32, $M/M_{\odot}$= 1.65, $R/R_{\odot}$= 1.52 and T_{eff}=7706 K for WOCS 4006. Bruntt et al. (2007) analysed these two variable stars and estimated the mass and temperature using theoretical pulsation models. From their estimation the mass range for WOCS 4006 was found to be 1.7 - 2.0 $M_{\odot}$ for T_{eff} 7930 - 8210 K and for WOCS 1007, it is found to be 1.8 - 2.3 $M_{\odot}$ for T_{eff} 7450-7740 K. Our estimated values of mass and temperature for these stars using SED fitting are comparable with the estimations of Bruntt et al. (2007) and Gilliland and Brown (1992), though we derive slightly lower luminosities for these stars.

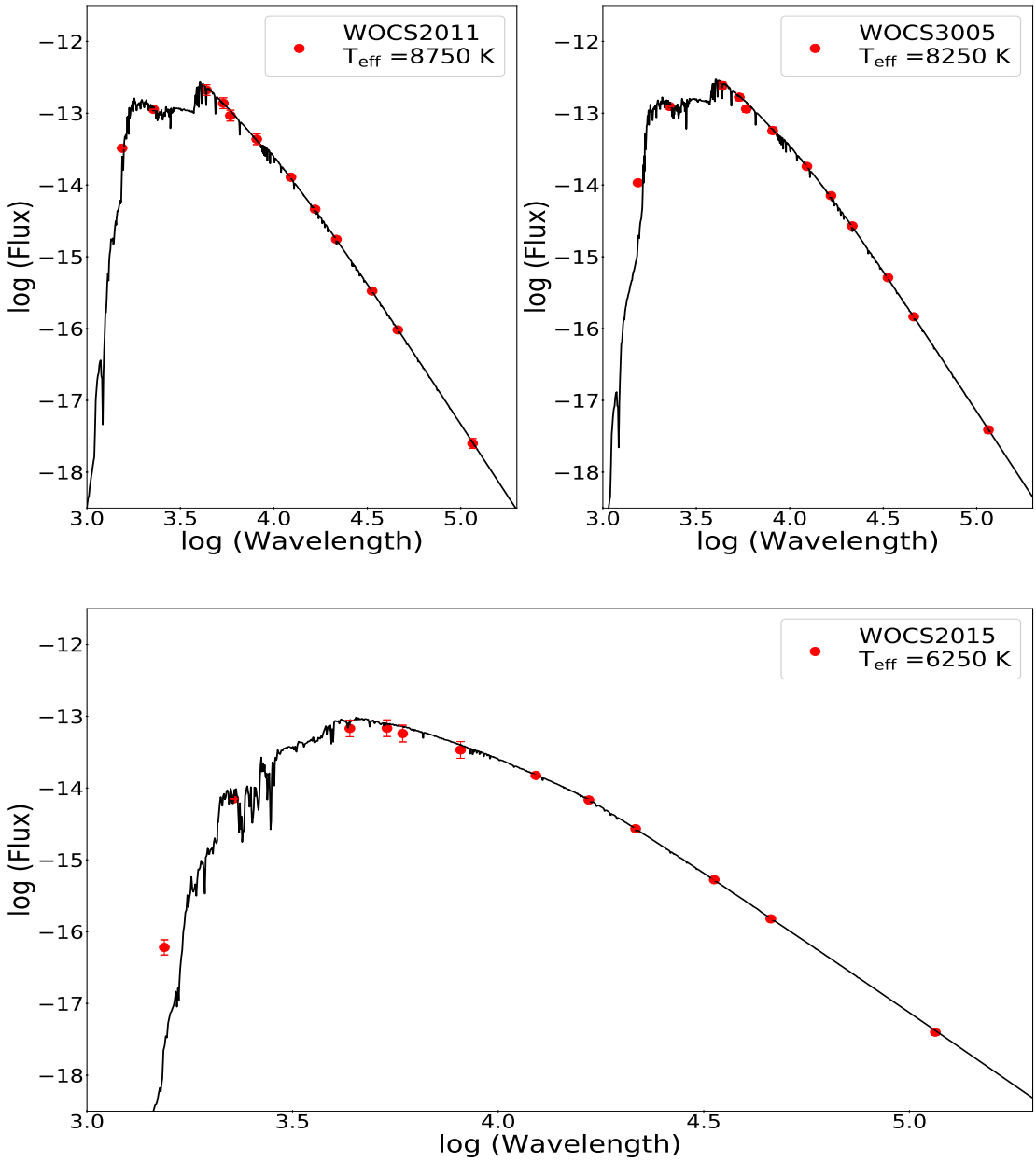

Fig. 6.1 The SEDs (Extinction Corrected) of WOCS 2011, WOCS 3005 and WOCS 2015 with Photometric Flux from UV to IR. Best Fitting Kurucz Model Spectrum is Overplotted and the Corresponding Temperature is Listed in each Panel. The Unit of Wavelength is Å and Flux is ergs cm^{-2} s^{-1} $Å^{-1}$

Table 6.4 The Parameters of BSSs from the SEDs. Column 1 gives ID from Montgomery et al. (1993), Column 2 gives the WOCS ID of M67, Column 3 gives the Temperature Derived from SED Fitting, Column 4 and 5 give the Temperature from Literature (Deng et al., 1999, Liu et al., 2011). Column 6, 7 and 8 give the Radius, Mass and Luminosity in Solar Units

MMJ	WOCS	T_{eff} (K)	T^{a}_{eff} (K)	T^{b}_{eff} (K)	Radius (R$\odot$)	Mass(M$\odot$)	Luminosity (L$\odot$)
6490	1006	9000 ± 125	8000	8950	2.11 ± 0.028	2.20	27.60 ± 0.74
6504	1007	7750 ± 125	6750	7900	2.88 ± 0.038	2.00	22.29 ± 0.79
6511	1017	8000 ± 125			2.93 ± 0.04	2.19	29.52 ± 0.78
5191	1020	6750 ± 125	6250	6500	1.75 ± 0.023	1.55	4.96 ± 0.14
6006	1025	7250 ± 125	6500	7050	1.84 ± 0.024	1.60	6.63 ± 0.18
6510	1026	8750 ± 125	8000	8500	2.54 ± 0.035	2.20	34.67 ± 1.44
5699	2007	6000 ± 125	6000	6200	2.66 ± 0.035	1.66	8.20 ± 0.23
6479	2011	8750 ± 125	8000	8450	1.94 ± 0.026	2.14	19.72 ± 0.54
	2013	8000 ± 125	7250	8100	2.78 ± 0.037	2.00	22.56 ± 0.71
6477	2015	6250 ± 125	6000	6150	2.88 ± 0.038	1.58	10.42 ± 0.29
	2068	6500 ± 125	6000	6450	2.39 ± 0.032	1.60	8.05 ± 0.23
6501	3005	8250 ± 125	7000	8050	2.45 ± 0.032	2.01	20.89 ± 0.56
6047	3009	6250 ± 125	6000	6950	2.45 ± 0.032	1.62	8.08 ± 0.22
5833	4003	6750 ± 125	6250	6500	1.75 ± 0.023	1.52	4.84 ± 0.16
5940	4006	8000 ± 125	6750	7800	1.50 ± 0.020	1.77	6.74 ± 0.18
5667	5005	6500 ± 125	6250	6600	2.37 ± 0.031	1.60	8.42 ± 0.30
5571	9005	6500 ± 125	6250	6100	1.87 ± 0.025	1.48	5.37 ± 0.16

[a] Deng et al. (1999), the temperature is taken from their Kurucz model fit.

[b] Liu et al. (2008). the temperature is taken from their Bluered model fit.

We also constructed SEDs for 15 FUV bright stars which are shown in Fig. 6.2, Fig. 6.3 and Fig. 6.4. The spectral fit to the SEDs reveal that we are able to fit with one spectrum for all the candidates, except WOCS 3012, which is known to be a triple system. From the figures, it is clear that all of these stars show certain amount of excess flux in the FUV, similar to that noticed in the SED of WOCS 2015. In the case of WOCS 2012 and WOCS 6008, we notice relatively large excess in the FUV flux, where the observed flux is about two orders more than the expected flux. The SEDs are used to estimate their T_{eff}, $R/R_{\odot}$, $L/L_{\odot}$, and $M/M_{\odot}$, which are listed along with the error in Table 6.5. Yakut et al. (2009) estimated the parameters ($L/L_{\odot}$= 2.78, $R/R_{\odot}$= 1.40, $M/M_{\odot}$= 1.47 and T_{eff} = 6300 K) of WOCS 7009 in their Table 13, which is an AH Cnc, a contact binary. Peng et al. (2016) also estimated radius ($R/R_{\odot}$= 1.33) and mass ($M/M_{\odot}$= 1.18) for WOCS 7009. Our estimation of $L/L_{\odot}$, $R/R_{\odot}$ and T_{eff} are in good agreement with the estimates using other methods. When we compare the properties of the BSSs with these FUV bright stars, we find these span a smaller range in following three parameters; T_{eff} ($\sim$ 5750 - 6750 K); $R/R_{\odot}$ ($\sim$ 1.0 - 2.5) and $L/L_{\odot}$ ($\sim$ 1.5 - 6.3). The FUV bright stars have the lower end of the parameter range of the BSSs.

We also created SEDs for the two RGs which show FUV excess, which are shown in the upper panels of Fig. 6.5. Both stars show excess flux in the NUV and FUV, with respect to the fitted spectrum. This is suggestive of the presence of excess UV flux in these RGs, which explains them having detected in the FUV band. The SED fit suggests a temperature of $\sim$ 4000K for the RGs. The FUV flux detection is close to the detection limit of GALEX. The origin of the UV excess flux could be due to chromospheric activity or the presence of a hotter component. IUE observations of some of the M67 RGs were done to detect and characterise their chromospheric emissions. An archival search finds that both these RGs have IUE spectra. These two spectra are shown in the bottom panel of Fig. 6.5. Both the spectra show the presence of Mg II $h + k$ lines in emission, which are marked in the figure. As these are low resolution spectra, the two Mg II $h + k$ lines are not separated. IUE spectra of 5 more RGs are also available and an inspection of their Mg II $h + k$ line suggests that mild emission is detected in WOCS 1008 and WOCS 1045, whereas no emission is found in WOCS 1005, WOCS 1054 and WOCS 2059. The presence of Mg II $h + k$ lines in emission is suggestive of chromospheric activity. Pérez Martínez et al. (2011) studied 177 cool G, K and M giants and supergiants using IUE spectra and measured their Mg II $h + k$ line strength. They argue that these emission represent the chromospheric radiative energy losses presumably related to basal heating by the dissipation of acoustic waves, plus a highly variable contribution due to magnetic activity. The detection of the Mg II $h + k$ emission lines along with the presence of excess continuum UV flux suggests that the FUV detected RGs have more chromospheric activity, in comparison to the other RGs in the cluster.

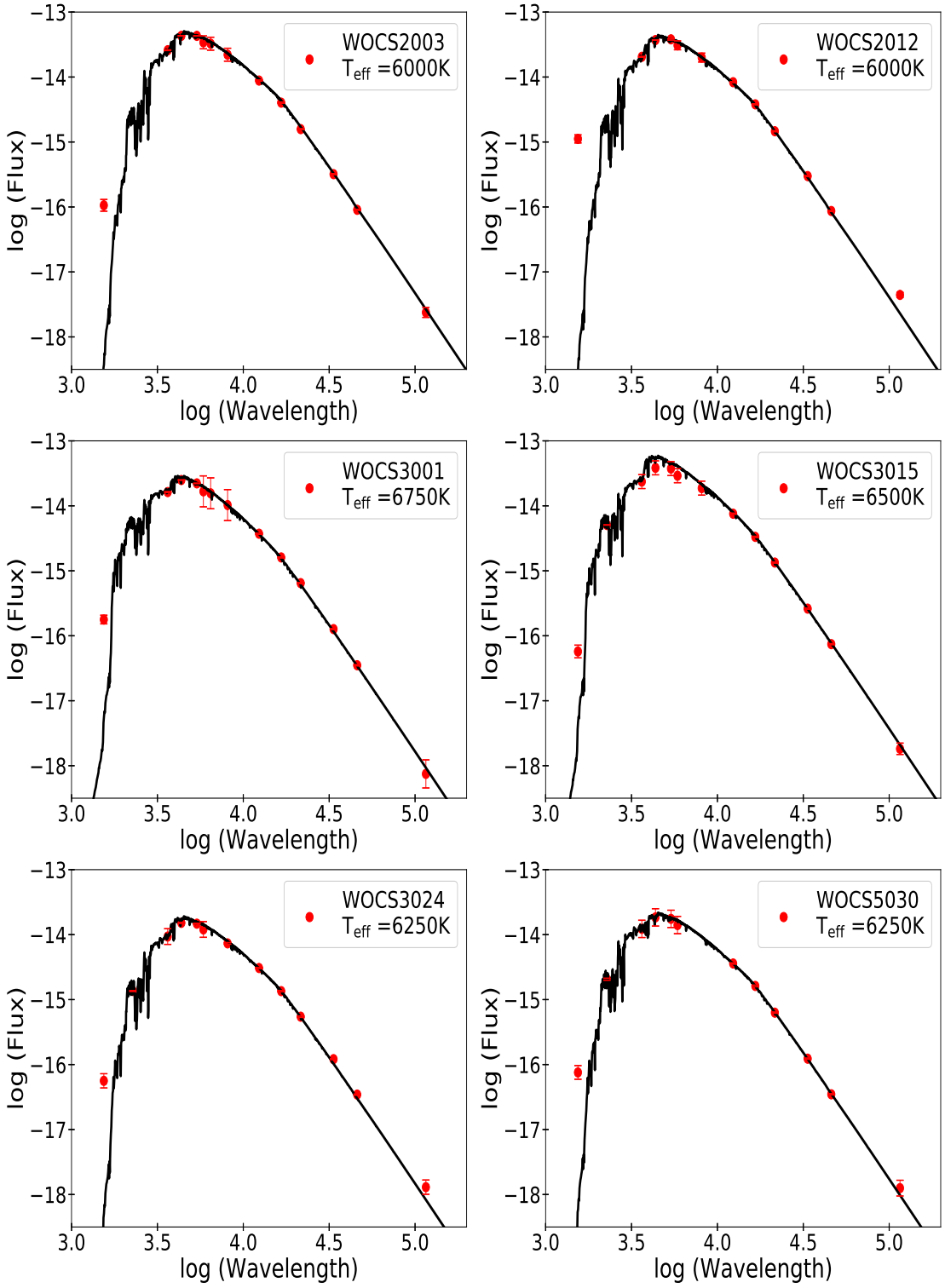

Fig. 6.2 The SEDs (Extinction Corrected) of 6 FUV Bright Stars (WOCS 2003, WOCS 2012, WOCS 3001, WOCS 3015, WOCS 3024, WOCS 5030) with Photometric Flux from UV to IR. Best Fitting Kurucz Model Spectrum is Overplotted and the Corresponding Temperature is Listed in Each Panel. The Unit of Wavelength is Å and Flux is ergs cm^{-2} s^{-1} $Å^{-1}$

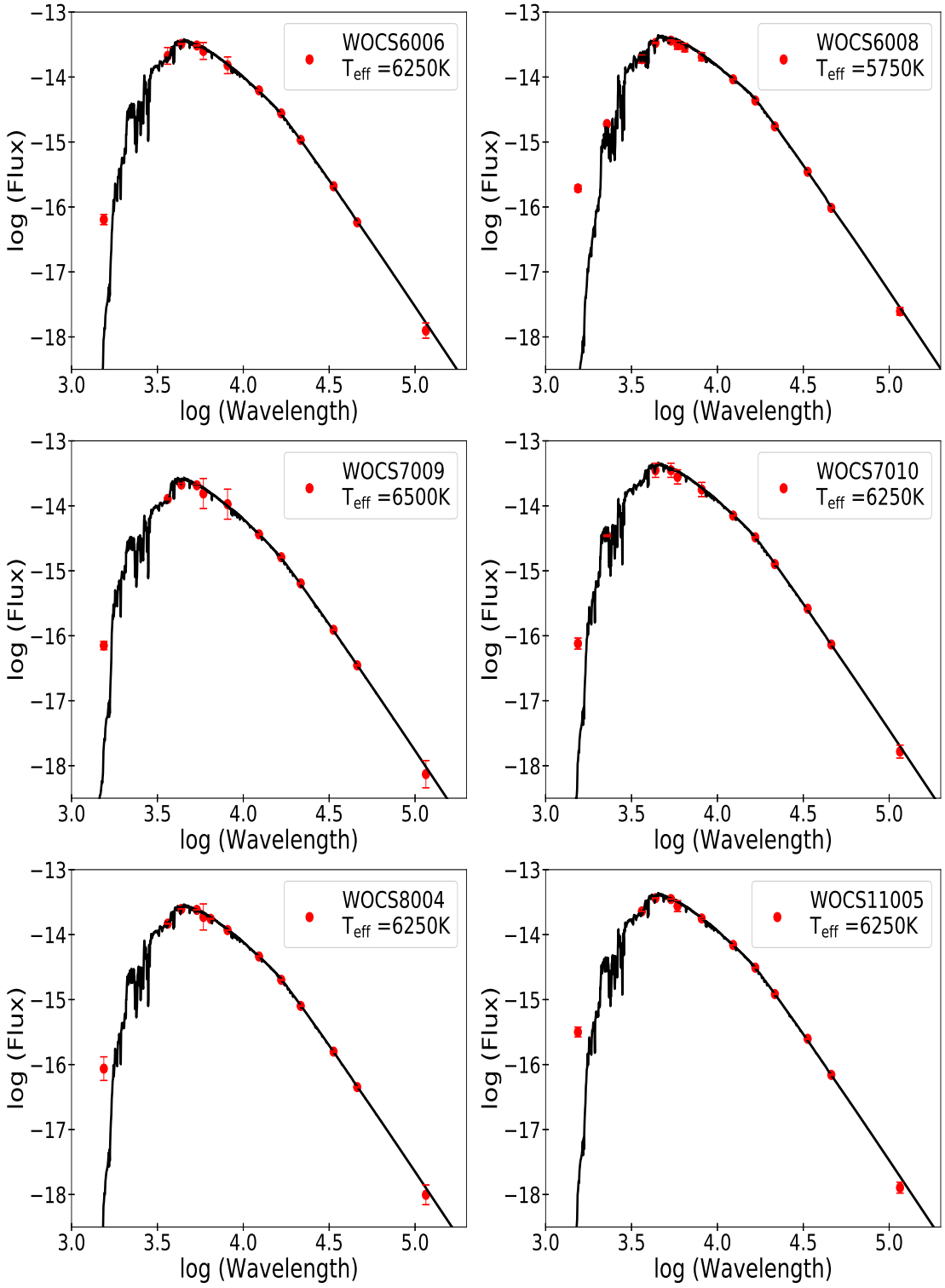

Fig. 6.3 The SEDs (Extinction Corrected) of 6 FUV Bright Stars (WOCS 6006, WOCS 6008, WOCS 7009, WOCS 7010, WOCS 8004, WOCS 11005) with Photometric Flux from UV to IR. Best Fitting Kurucz Model Spectrum is Overplotted and the Corresponding Temperature is Listed in Each Panel. The Unit of Wavelength is Å and Flux is ergs cm^{-2} s^{-1} $Å^{-1}$

Table 6.5 The Parameters of FUV Bright Stars from the SEDs. Column 1 gives ID from Montgomery et al. (1993), Column 2 gives the WOCS ID of M67, Column 3 gives the Temperature Derived from SED Fitting, Column 4, 5 and 6 give the Radius, Mass and Luminosity in Solar Units

MMJ	WOCS	T_{eff}	Radius (R⊙)	Mass(M⊙)	Luminosity (L⊙)
5654	2003	6000 ± 125	2.34 ± 0.032	1.40	6.32 ± 0.24
5388	2012	6000 ± 125	2.18 ± 0.030	1.51	5.61 ± 0.17
5741	3001	6750 ± 125	1.31 ± 0.018		2.96 ± 0.10
5451	3012	6500 ± 125	1.90 ± 0.026	1.50	6.22 ± 0.18
6076	3015	6500 ± 125	2.00 ± 0.028	1.47	5.30 ± 0.16
5249	3024	6250 ± 125	1.28 ± 0.018		2.16 ± 0.06
6467	5030	6250 ± 125	1.39 ± 0.019	1.30	2.63 ± 0.09
5969	6006	6250 ± 125	1.81 ± 0.025	1.40	4.46 ± 0.15
5993	6008	5750 ± 125	2.47 ± 0.034	1.69	5.93 ± 0.17
6027	7009	6500 ± 125	1.35 ± 0.019	1.39	2.74 ± 0.09
5825	7010	6250 ± 125	1.99 ± 0.027	1.41	5.11 ± 0.16
5603	8004	6250 ± 125	1.58 ± 0.022	1.30	3.35 ± 0.11
5675	11005	6250 ± 125	1.94 ± 0.027	1.40	5.01 ± 0.16
5871	11006	6500 ± 125	1.39 ± 0.019	1.40	2.98 ± 0.09
5426	17028	6250 ± 125	1.08 ± 0.015		1.46 ± 0.04

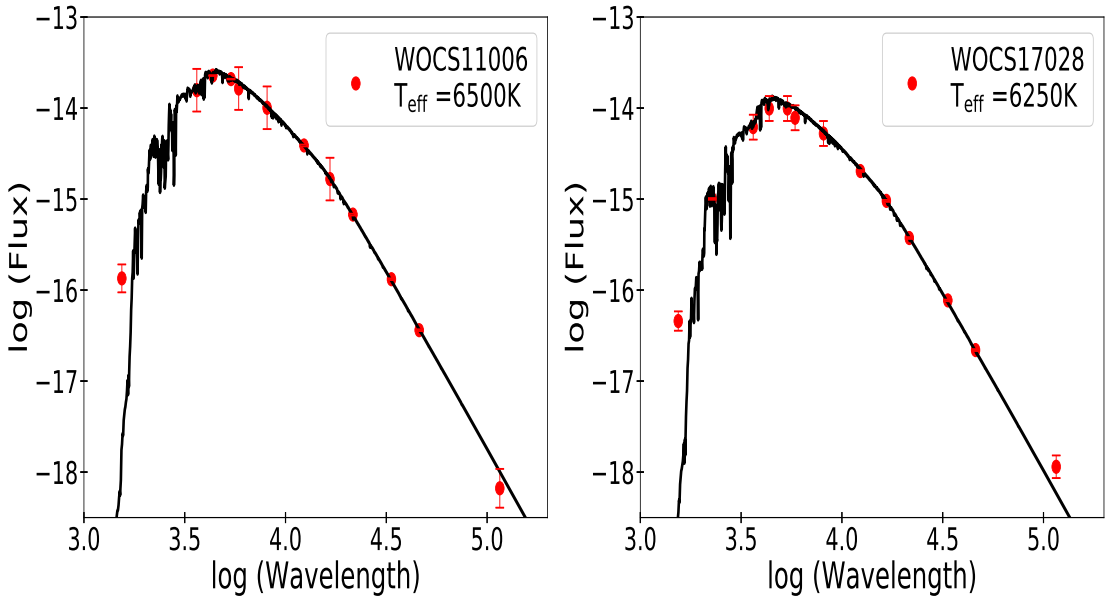

Fig. 6.4 The SEDs (Extinction Corrected) of 2 FUV Bright Stars (WOCS 11006, WOCS 17028) with Photometric Flux from UV to IR. Best Fitting Kurucz Model Spectrum is Overplotted and the Corresponding Temperature is Listed in Each Panel. The Unit of Wavelength is Å and Flux is ergs cm^{-2} s^{-1} $Å^{-1}$

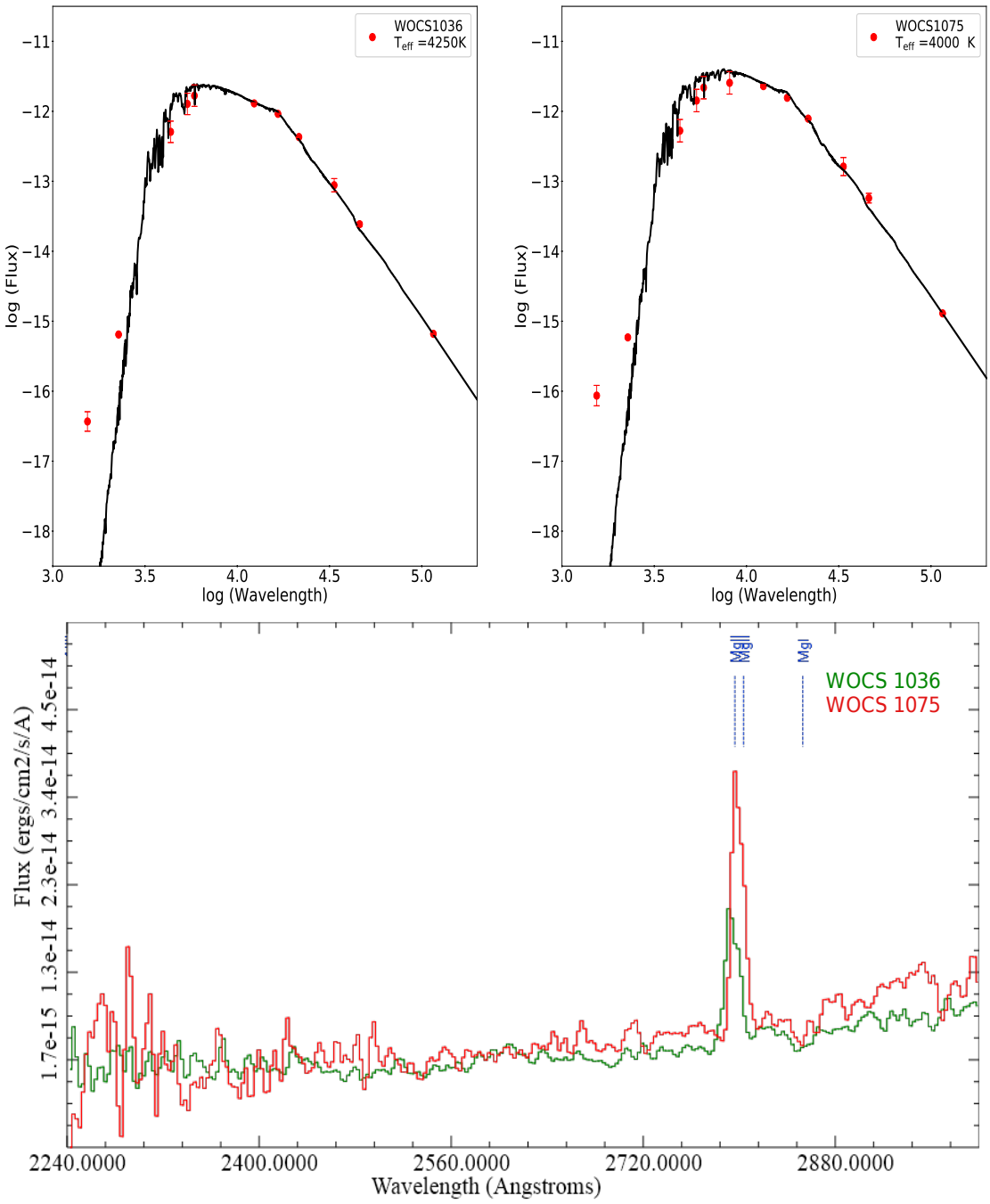

Fig. 6.5 (Top:) SEDs (Extinction Corrected) of RGs (WOCS 1036 and WOCS 1075 - Detected in the FUV band) with Photometric Flux from UV to IR. The Fitted Spectra suggest that there could be Excess in Both NUV and FUV for these Two RGs. Best Fitting Kurucz Model Spectrum is Overplotted and the Corresponding Temperature is Listed in Each Panel. The Unit of Wavelength is Å and Flux is ergs cm^{-2} s^{-1} $Å^{-1}$. (Bottom:) IUE Spectra of These RGs in the NUV Region having the Mg II $h + k$ Lines in Emission

We also constructed SEDs for the MS+WD candidates (Fig. 6.6 and 6.7). We detect excess flux in the UV for 7 of the 11 stars. We observe a range in the excess FUV flux detected in these stars. Thus the UV excess found in 7, suggests that, these could be potential MS+WD binaries. The rest of the 4 sources (WOCS 19045 and WOCS 21027 in Fig. 6.6 and WOCS 36035 and WOCS MMJ6398 in Fig. 6.7) do not have FUV flux and are also not found to have any excess in the NUV flux, with respect to the fitted SED. The slope of the flux in the UV, is suggestive of a range in temperature for the WD companions. The temperature of the MS stars are found to be in the range 4000 K - 6250 K. The 4 stars which are not found to have any UV excess are located to the left of the MS in the optical CMD (Fig. 5.3). It is interesting to note that the estimated temperatures of these stars are at least 1000 K higher than the MS stars at the same luminosity. The fact that these stars are bluer with respect to the MS in optical and NUV$-$V CMDs due to their inherent hotter temperature might warrant a closer look at the nature of these stars.

6.3.2 Hertzprung - Russell and L/L$_\odot$vs R/R$_\odot$ Diagrams

We used the HRD (L/L$_\odot$ vs T$_{eff}$) and L/L$_\odot$vs R/R$_\odot$ diagram to compare the properties of the BSSs and the FUV bright stars. In Fig. 6.8, the L/L$_\odot$ vs T$_{eff}$ plot is shown, where the BSSs, 2 YSSs and the FUV bright stars are shown with different symbols along with their identification numbers. These stars are also colour coded according to their radius. The BSSs and YSSs are labelled in black and the FUV bright stars are labelled in red. We calculated L/L$_\odot$ of 2 YSS with the values of R/R$_\odot$ and T$_{eff}$ taken from Leiner et al. (2016) and Landsman et al. (1997). In this figure, we over plotted the isochrones of various ages, and BSS model lines for 3.5 Gyr and 4 Gyr population of BaSTI model generated by FSPS.

In Fig. 6.8, we notice that the 7 BSSs are indeed quite luminous and are well separated from the other BSSs. All these are bright in the FUV and are the brightest 7 among the BSSs. The rest of the 10 BSSs are located between the BSS model line and the isochrone, with relatively low luminosity. We notice that all the BSSs are either hotter or luminous than the 3.5 Gyr isochrone. We can possibly group the BSSs into 3 groups: (a) the luminous and hot BSSs (WOCS (1006, 1007, 1017, 1026, 2011, 2013 and 3005)), (b) hot and less luminous BSSs (WOCS (4006, 4003, 1025,1020 and 9005)) and (c) moderately luminous and cooler BSSs (WOCS (3009, 5005, 2068, 2015 and 2007)). The group (a) BSSs are found to be located in the isochrones with the age range of 400 Myr - 1 Gyr. Their younger age is consistent with their higher temperature, luminosity and mass. This probably is why group (a) BSSs are FUV bright. Thus the group (a) BSSs are likely to be youngest among the BSS population. WOCS 1007 is a group (a) BSS with a relatively large radius suggestive of it being more evolved. This

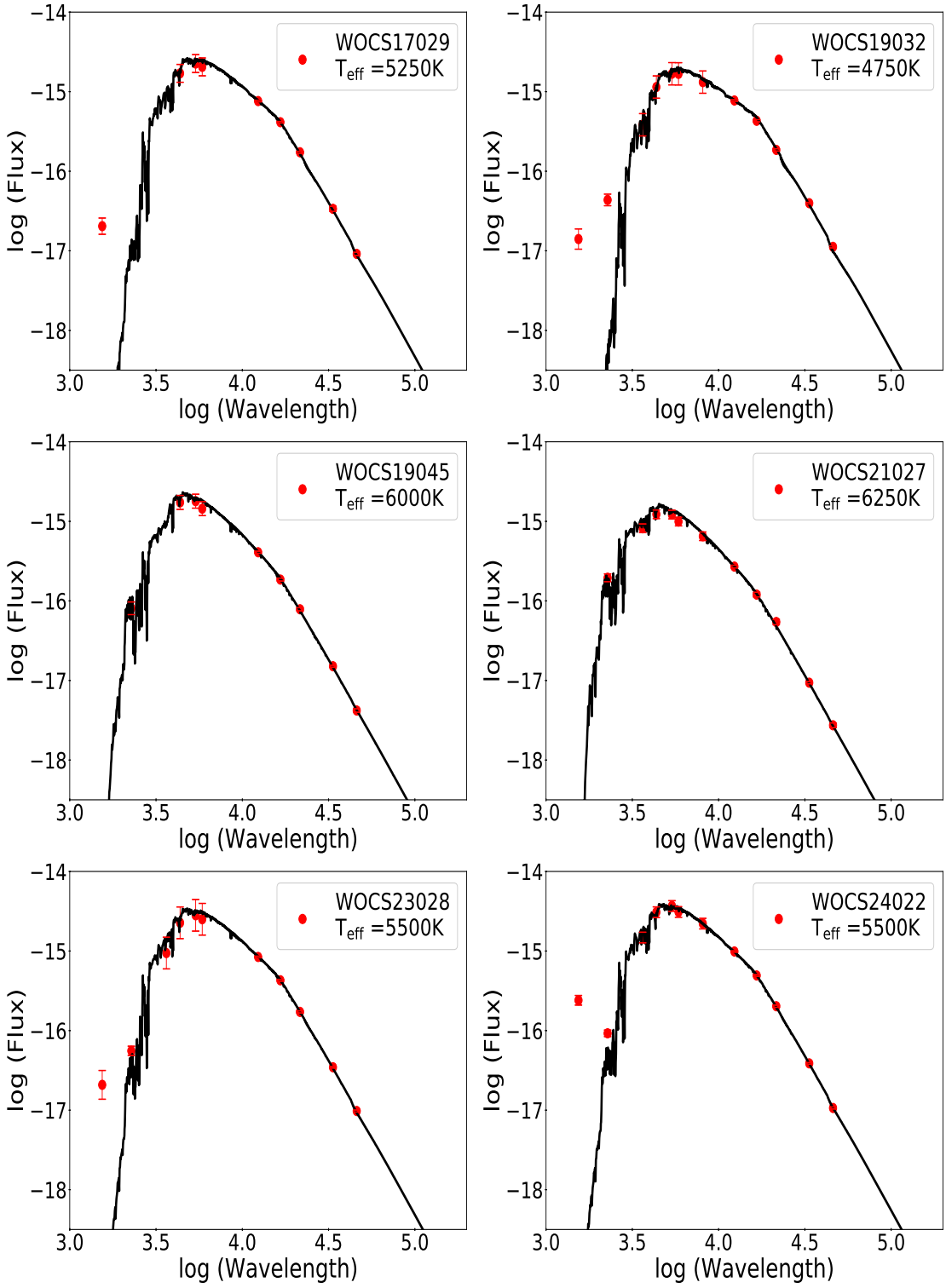

Fig. 6.6 SEDs (Extinction Corrected) of 6 WD+MS Candidates (WOCS 17029, WOCS 19032, WOCS 19045, WOCS 21027, WOCS 23028, WOCS 24022) with Photometric Flux from UV to IR. Best Fitting Kurucz Model Spectrum is Overplotted and the Corresponding Temperature is Listed in Each Panel. The Unit of Wavelength is Å and Flux is ergs cm^{-2} s^{-1} $Å^{-1}$

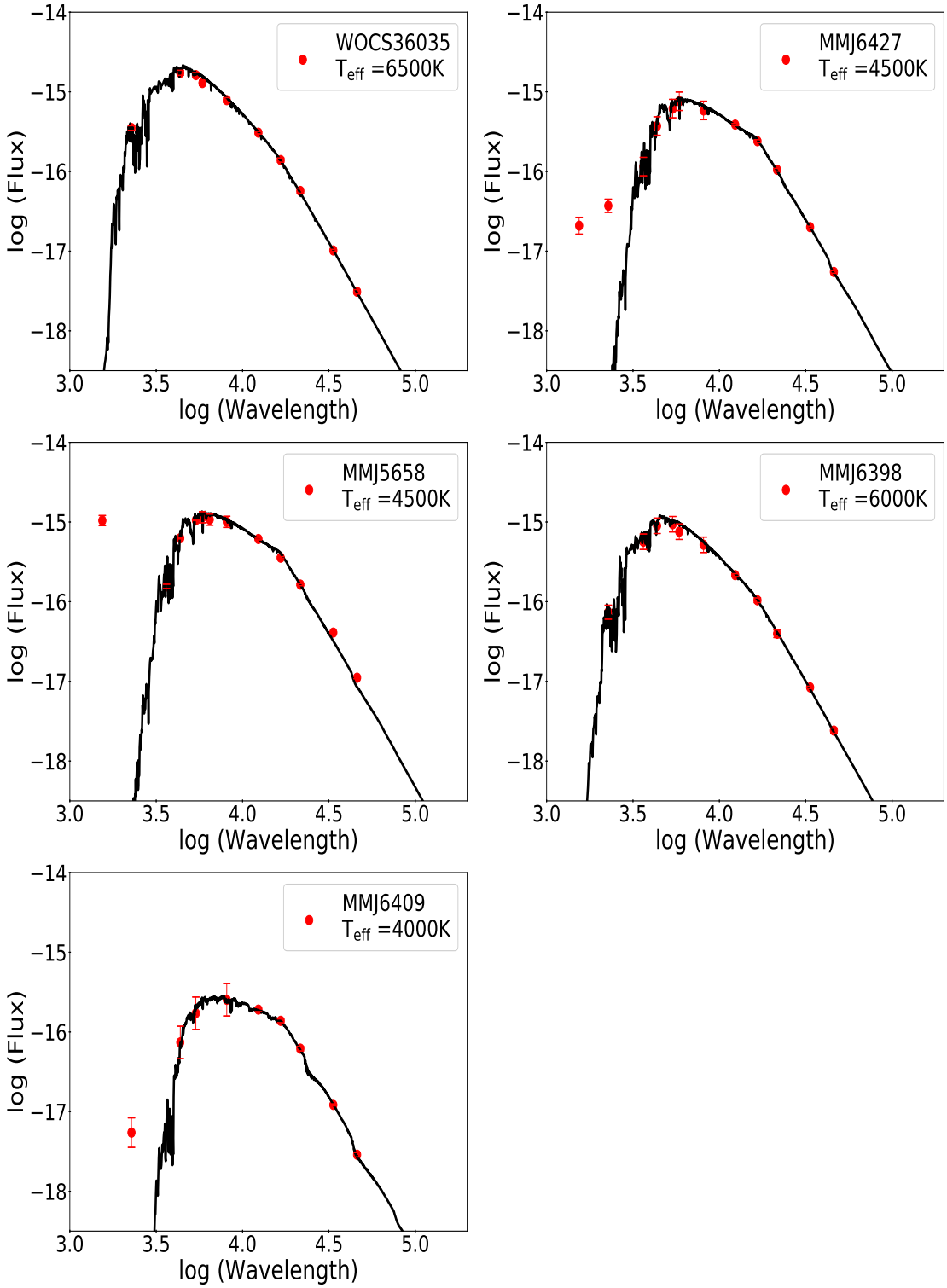

Fig. 6.7 SEDs (Extinction Corrected) of 5 WD+MS Candidates (WOCS 36035, MMJ6427, MMJ5658, MMJ6398, MMJ6409) with Photometric Flux from UV to IR. Best Fitting Kurucz Model Spectrum is Overplotted and the Corresponding Temperature is Listed in Each Panel. The Unit of Wavelength is Å and Flux is ergs cm^{-2} s^{-1} $Å^{-1}$

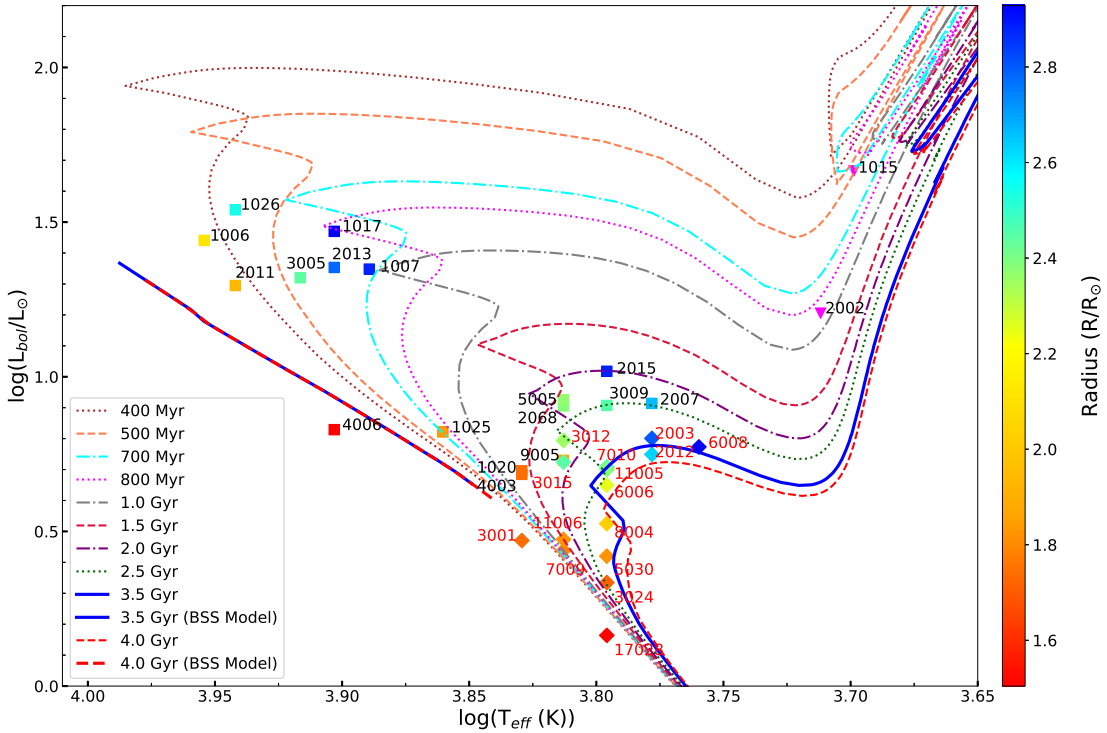

Fig. 6.8 Luminosity vs. Effective Temperature, H-R Diagram of the BSSs and FUV Bright Stars. The Points are Colour Coded Based on the Radius of the Stars, shown on the right. 2 YSSs (Pink Triangles) are also shown in the Plot. The BSSs are Labelled in Black and FUV Bright Stars in Red. Isochrones Generated using FSPS for Various Ages are shown with Different Colours. The BSS Model Line for 3.5 and 4 Gyr are also shown in the Figure

is a δ-Scuti star (Gilliland and Brown, 1992) and they suggested that this star could be evolving from the MS to the SG phase. The YSS (WOCS 1015) is found to be located near the isochrone of the range 500 Myr - 700 Myr. Leiner et al. (2016) estimated the age of a YSS (WOCS 1015) to be in the range of 450 -$\sim$ 750 Myr, consistent with our estimation. We also find that WOCS 2002 has an age of 800 Myr - 1 Gyr. Landsman et al. (1997) suggested a possible evolutionary sequence for this binary, with $\sim$ 765 Myr as the period of stable mass transfer for the formation of the BSS progenitor, and a further 75 Myr for its post-BSS evolution. This is consistent with our age estimation. We suggest that the two YSSs could also belong to the group (a) BSSs.

Among the group (b) BSS, WOCS 4006 is known to be a δ-scuti star (Gilliland and Brown, 1992). We estimate the star to be slightly under luminous, with respect to the previous estimates. The remaining stars in the group are located in and around the plotted isochrones, with moderate radii. As these stars are located close to the MS and as well as BSS model line, we are unable to estimate their age range. This suggests that the group (b) BSSs do not show any evidence of evolution beyond the MS. The group (c) BSSs, on the other hand, are located on the SGB of the plotted isochrones with an age range 2-2.5 Gyr. These BSSs are relatively cooler and have larger radii, which are

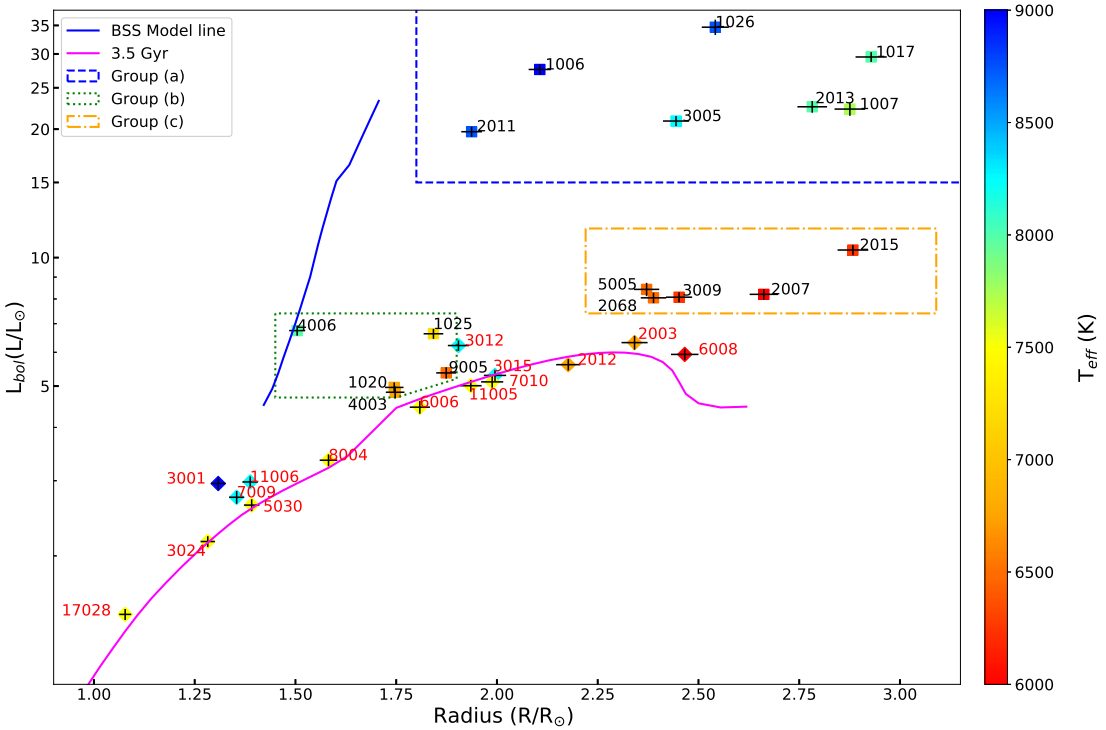

Fig. 6.9 A Plot of Luminosity vs. Radius for BSS and FUV Bright Stars. The Stars are Colour Coded Based on the Effective Temperature shown on the Right Side of the Figure. The BSS are Labelled in Black and FUV Bright Stars in Red

consistent with their location on the isochrones. Thus, group (c) may be an evolved group of old BSSs with an age range of 2-2.5 Gyr.

We notice that all of the FUV bright stars are located near the older isochrones. Among them, WOCS 3001, WOCS 11006, WOCS 7009 and WOCS 17028 are located close to the MS of the isochrones, though WOCS 3001 and WOCS 17028 are marginally under-luminous. We could consider them to be similar to the group (b) BSSs. Therefore, there is a possibility that the FUV bright stars could actually be BSS like stars. In Fig. 6.9, we present $L/L_{\odot}$ vs $R/R_{\odot}$ plot for the BSSs and the FUV bright stars, where the stars are colour coded based on T_{eff}. We have marked the regions occupied by these three groups in the figure. In this figure also, the group (a) BSSs are located separately, whereas the group (b) and (c) show a similar trend, with group (c) stars located towards the right extreme. It is interesting to note that the FUV bright stars, and group (b) and (c) stars have similar location in this diagram. The δ-scuti star (WOCS 4006) is found to be located away from the sequence, suggesting that it probably has lesser radius (as it is already found to be under luminous). From this figure, we can only infer that the following FUV bright stars share the same location as the BSSs; WOCS (6008, 2003, 2012, 3012, 3015, 11005, 6006 and 7010).

6.4 Summary and Discussion

In the BSS region, it was noticed that 15 stars were co-located along with the BSS. There may be FUV/NUV non-photospheric emission resulting in a UV excess occurring in these stars appearing brighter than the MSTO. Also, it is better to identify BSSs based on their total luminosity, rather than their brightness in a particular pass band. Thus, we make use of the HRD to understand the properties of BSS as well as FUV bright stars. We detect 15 stars to have similar UV flux as the BSSs. We estimated $L/L_{\odot}$, $R/R_{\odot}$ and T_{eff} for the GALEX detected BSSs and the FUV bright stars using SEDs. The Fig. 6.8 and Fig. 6.9 suggest that the BSSs in M67 have a wide range of properties. We use these figures to group the BSSs into 3. The location of BSSs in the HRD is interpreted with the help of overlaid isochrones. The BSSs are found to be located in isochrones of a large age range (400 Myr to 2.5 Gyr). The group (a) BSSs are found to be hotter, luminous and the youngest with an age range of 400 Myr - 1 Gyr, whereas the group (c) stars are as old as 2.5 Gyr. The group (a) BSS are found to be brighter up to 10 magnitudes in the FUV. We suggest that the large range of FUV magnitude of BSSs is likely due to their range in their temperature and luminosity. As we find the BSSs to be more or less evenly distributed across the large age range, the BSSs is M67 is likely to be forming fairly continuously in the 400 Myr - 2.5 Gyr duration.

The Fig. 6.9 gives a different perspective of the BSSs, with respect to the expected location of BSSs. The group (b) and (c) mostly follow the 3.5 Gyr isochrone values for their $L/L_{\odot}$, $R/R_{\odot}$, with only one star following the BSS model line. All the group (a) BSSs are found to have relatively larger radii. If we consider only the 6 FUV bright stars which lie very close to the BSS model line in the FUV$-$V CMD (See Fig. 5.4) to check whether any of these could be BSSs, we see that, these stars have T_{eff} very similar to the co-located BSSs. Among these WOCS 3012 lies within the group (b) location, and is a potential BSS candidate. The star WOCS 6008 has a large radii and is located below the group (c) location, whereas WOCS 3001 and WOCS 11006 are found to be hotter than the MS, suggesting that these 3 stars could also be BSS candidates. On the other hand, WOCS 11005 and WOCS 2012 are located on the MS and hence are unlikely to be BSSs. Thus, 4 among the FUV bright stars could be BSS candidates. The fainter stars in the FUV$-$V CMD, located in the BSS region could be FUV bright due to a variety of reasons. We also detect YSSs, wheres the RGs are located just outside this region. It is likely that this group might comprise of a wide variety of stars which show UV excess due to non-photospheric emission, as well as BSS.

The BSSs in M67 spans a very large range in T_{eff}, unlike those in NGC 188 (Gosnell et al., 2015). This is one of the reasons for a large range in their FUV magnitude. The SEDs of a few of the BSSs including WOCS 2015 have FUV excess and it is important to understand the origin of this excess. Some of the BSSs in NGC 188

are identified to have a hot companion, resulting in FUV excess (Gosnell et al., 2015; Subramaniam et al., 2016). Thus, it will be interesting to probe whether these BSSs also have any hot companion. We searched the IUE archive for spectra of bright BSSs and we could trace low resolution spectra of 4 BSSs. These 4 BSSs (WOCS (1006, 1007, 1026 and 2011)) along with the UV bright BSSs WOCS 1010 have FUV as well as NUV spectra. The FUV spectra of these 5 BSSs are shown in Fig. 6.10 (top panel). The FUV spectrum of WOCS 1010 is scaled down by 0.1 to place it along with the other spectra, which is suggestive of its large UV flux. This spectrum has very well defined absorption lines and is also suggestive of a relatively hotter temperature relative to the other BSSs. The spectra of BSSs WOCS 1006, WOCS 1007 and WOCS 1026 appear very similar with respect to the continuum as well as absorption lines, and all of which belong to group (a). Some absorption lines can be identified in all the spectra. The spectrum of WOCS 2011 has relatively low signal and is scaled up by 1.5. This spectrum does not show any clear absorption lines. In the bottom panel, the NUV spectra are shown. All the 5 BSSs show the presence of Mg II h +k line in absorption. This is a clear indicator of absence or very low chromospheric activity for these BSSs. Thus, if there is any excess in the UV emission present in these BSSs, it may not be due to chromospheric activity, unlike the RGs.

We also find some of the FUV bright stars to have excess UV flux. These could harbour hot companions or have active chromospheres. The SED analysis of the MS+WD candidates also suggest hot companion. As the GALEX FUV gives one data point in the FUV region of the SED, it is hard to characterise the hot component based on a single data point, even though the excess is much larger in a few cases. Subramaniam et al. (2016) demonstrated that UVIT observations with its filters in the FUV and NUV can provide a good profile of the UV continuum of stars with UV excess. Thus UVIT observations of M67 will help in detecting the WDs if they are present. These observations could also help in placing limits on the flux contribution in the FUV due to chromospheric activity and the temperature range of chromospheres of stars in M67.

Detection of a large number of stars with FUV and/or NUV excess in this cluster suggests that these stars could be chromospherically active. We detect 2 RGs with FUV excess in concurrence with the presence of Mg II h +k emission lines from the archival IUE spectra, suggestive of significant chromospheric activity. Stello et al. (2016) recently found these two giants to have very low frequency oscillations, whereas some other giants in this cluster were found to be oscillating with relatively large frequency. Connecting this to the dispersion in the location of RGs in the (NUV$-$V) CMD, we speculate that some RGs in this cluster are chromospherically active resulting in excess flux in the NUV. The physical processes operating in the cool giants with active chromospheres are still being understood (Pérez Martínez et al., 2011). The excess emission

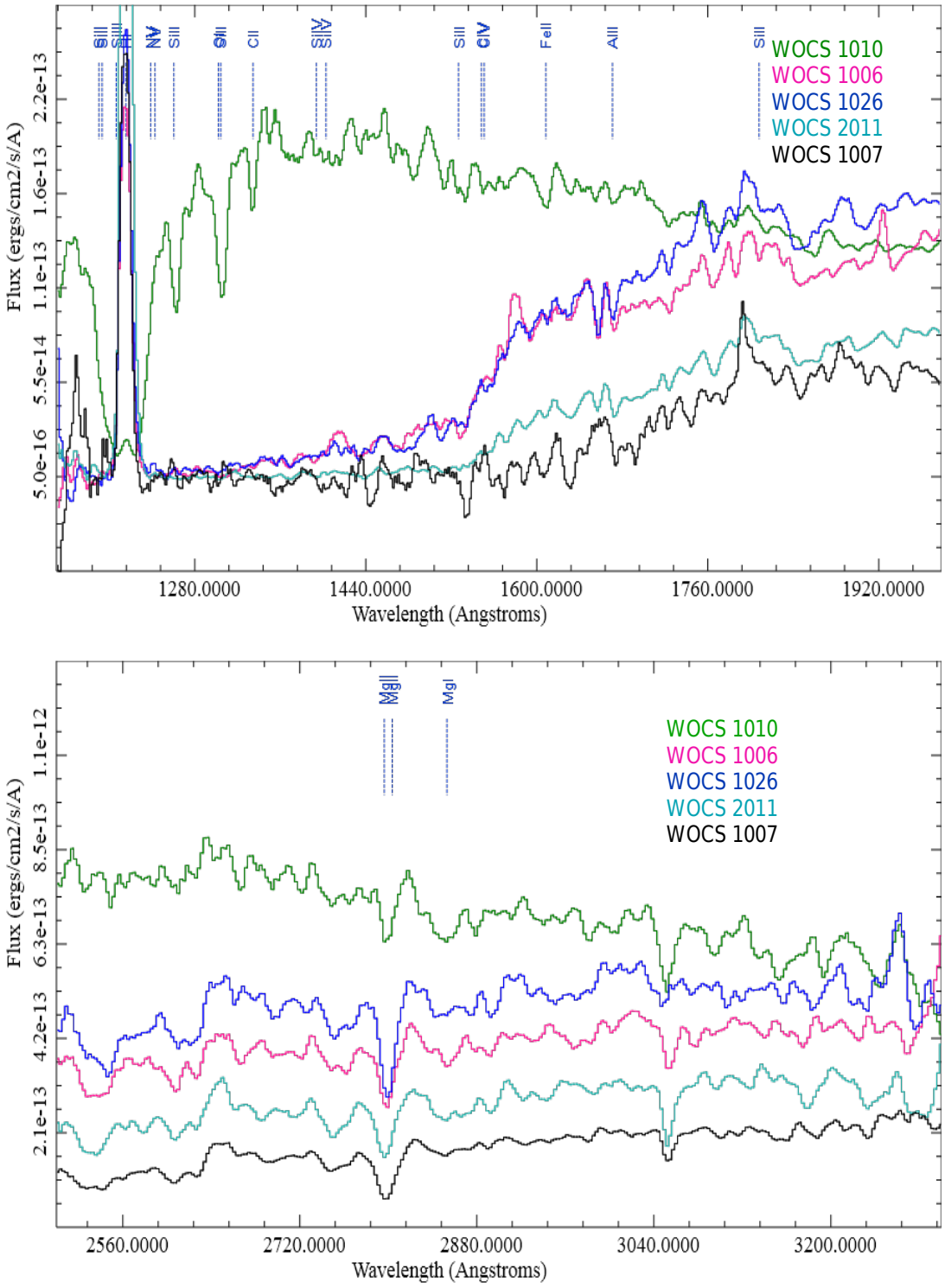

Fig. 6.10 Upper Panel: IUE Spectra in the FUV for 5 BSSs. The WOCS 1010 Spectrum is Scaled Down by 0.1 to Plot Along with the Other Spectra. The WOCS 2011 is Scaled up by 1.5 as well. The Spectra of WOCS 1006, WOCS 1007 and WOCS 1026 are shown Without Any Scaling. Some of the Spectral Lines are Marked. Lower panel: The Spectra of 5 BSSs in the NUV Range. The Spectra are Scaled to Bring Out the Absorption Profile of the Mg II *h* +*k* Line, which is Present in All the Spectra

seen could be due to the dissipation of purely mechanical energy in the turbulent chromosphere or magnetic activity. As one expects minimal magnetic activity in the giants, the heating and emission from the chromosphere of these RGs can be mostly attributed to the dissipation of mechanical energy. It may be possible that the low frequency waves seen in the active RGs, effectively contribute to the heating of chromosphere. Dziembowski et al. (2001) describes on possible modes of oscillations and energy dissipation rate in red giants.

6.5 Conclusion

The main conclusion of this chapter are as follows:

- The BSS in M67 span a large range in T_{eff} and $L/L_{\odot}$, which is found to correlate well with the large range of FUV magnitude (14 - 23 mag). The FUV bright BSSs are found to be the hotter, luminous, and probably younger. We have grouped the BSSs in M67 into 3 groups - (a), (b) and (c)

- The isochrones overlaid on the HRD suggest that the group (a) including the two YSSs is very young (400 Myr - 1 Gyr). WOCS 2011 and WOCS 1006 could be the most recently formed BSS, good candidates to probe the BSS formation mechanism. The group (c) stars are likely to be the oldest among the BSS in M67. We suggest that the BSS in M67 are formed in the last 2.5 Gyr - 400 Myr, more or less continuously.

- We detect two RGs to have UV continuum excess as well as emission in the Mg II h + k lines from the IUE archival spectra. Along with the scatter of the RG stars in the NUV$-$V CMD, and the detection of stars with UV excess, we speculate that the RGs as well as a good fraction of stars in M67 could be chromospherically active.

- The bright BSSs stars are not found to be chromospherically active.

CHAPTER 7

Detection of Probable White Dwarf Companions to Blue Stragglers in M67

7.1 Introduction

Stars evolve from the main sequence (MS) to the red giant (RG) phase after they exhaust hydrogen burning in their core. In a star cluster, blue straggler stars (BSSs) are found to be bluer and brighter than stars that are close to the end of MS lifetime, suggesting that these stars have continued to stay on the MS, defying further evolution. BSSs are believed to have gained mass by some process and hence have a rejuvenated lifetime on the MS. The process by which BSSs gains mass, resulting in a rejuvenation, is not well understood. Three processes are suggested in the literature: (1) stellar collision of two or more stars to produce a single massive star (Hills and Day, 1976; Geller et al., 2013) (2) transfer of material through Roche Lobe from a close companion in a binary system (McCrea, 1964; Tian et al., 2006) and (3) a triple system where the doublet becomes a close binary, and merges to form a massive star (Perets and Fabrycky, 2009; Naoz and Fabrycky, 2014). The first mechanism is preferred in crowded fields like globular clusters, whereas the second mechanism is preferred in uncrowded fields like that of open clusters. Gosnell et al. (2015) found the observational evidence for the second mechanism, by detecting white dwarf (WD) companions to 7 BSSs in the old open cluster, NGC 188. Subramaniam et al. (2016) similarly detected a post-AGB/HB companion to a BSS in the same cluster.

M67 is a benchmark cluster to study stellar evolution, dynamics and cluster properties due to its proximity, richness, Solar metallicity and presence of exotic stellar populations. The cluster is also very rich in BSSs, where 14 are confirmed as bona-fide members (Geller et al., 2015). There have been several attempts previously, to detect hot companions to these BSSs, particularly from spectroscopic study using the IUE and UV photometry from the UIT. Landsman et al. (1998) in their seminal study used UIT images to detect 11 BSSs in M67. Among these, they suspect that WOCS 3010 (S975) and WOCS 2009 (S1082) have hot sub-luminous companions. As there is a 0.5 mag uncertainty in the predicted UIT flux and an uncertainty of 0.14 mag in the measured UIT flux, a strong evidence for a UV excess only for the above two BSSs was found (Landsman et al., 1998). They noted that while the hot companion of WOCS 2009 is

probably not a WD, the nature of the hot companion of WOCS 3010 is unknown. They also concluded that the IUE spectra do not provide any evidence for the presence of a sub-luminous companion for 4 BSS, for which IUE spectra are available, where 3 are common in our study (WOCS 1006, WOCS 1007 and WOCS 2011). In particular, the absence of detection of a hot companion to WOCS 1007 was surprising as this is a spectroscopic binary with a 4.2 day period and suspected to be currently undergoing mass transfer (Milone and Latham, 1992). They estimated the companion mass of WOCS 1007 to be 0.19 $M_{\odot}$, and was suggested as a BSS+WD by Shetrone and Sandquist (2000), due to the estimated mass of the companion. Shetrone and Sandquist (2000) suggest the companion of WOCS 3010 to be possibly a low-luminosity WD, based on its flux contribution to the visible part of the composite spectrum. On the other hand, Landsman et al. (1997) detected a WD companion to a YSS in M67 using HST GHRS observations. In summary, there has been no confirmed detection of WD companions to any of the BSSs in M67, except for a couple of suggestions.

Several attempts to study the chemical signatures of mass transfer in the BSSs, also rendered no evidence as the chemical composition of BSSs were found to be similar to that of stars near the MSTO (Bertelli Motta et al., 2018; Shetrone and Sandquist, 2000). These suggest that the preferred mechanism for the formation of BSSs in M67 may be collision. This is also supported by the fact that many of the BSSs are found to be in binaries with eccentric orbits (Mathieu et al., 1990; Sandquist and Shetrone, 2003*b*), which can result due to binary-binary and binary-single interactions (Leonard, 1996). Only a couple of BSSs are found to have either an almost circular orbit or very short periods, which favour mass-transfer scenario for its formation. Binary evolution alone cannot explain the full range of BSSs observed in M67, in particular, the short-period eccentric binaries as well as the so-called super-BSSs, which are more massive and twice that of the cluster MSTO mass (Leonard, 1996). The evolution and properties of two-thirds of the BSSs, including all those found in binaries, have been altered by cluster dynamics as seen from N-body simulations of M67, since nearly half of these system would not have formed at all outside the cluster environment (Hurley et al., 2001; Hurley et al., 2005). Their successful model produced 20 BSSs with one BSS+WD binary. They were able to produce single as well as binary BSSs with a range of periods and eccentricities. The simulations and the observations matched well so far, as no WD companions were detected for any of the BSSs, with only one or two suspected cases. In this study, we present the detection of WD companions to 6 BSSs, which drastically changes the nature of BSSs and their formation pathways in M67.

The UVIT on board the Indian space observatory, ASTROSAT, has been producing FUV and NUV images of superior resolution (George et al., 2018; Mondal et al., 2018). The first science paper from this mission presented the detection of a post-AGB/HB companion to a BSS in NGC 188 (Subramaniam et al., 2016). Motivated by

this study, we observed M67 using the UVIT and here, we present the near-simultaneous FUV observations of 9 BSSs in M67 in 3 filters of UVIT. We combine the UVIT magnitudes with other estimations in the UV, optical and near-IR from space as well as ground observations to create multiwavelength SED. The SEDs are analyzed with the help of theoretical spectra to detect and characterise the BSSs as well as a hot components, if it is present.

7.2 Observation and Reduction

M67 was observed during G07 cycle of ASTROSAT and observations were performed on 23 April 2017. We obtained the FUV data in three filters, viz. F148W, F154W and F169M filters, all observed on the same day. We were unable to get the NUV data due to some payload related issue. UVIT data were corrected for distortion, flat fielding and spacecraft drift using the CCDLAB software package (Postma and Leahy, 2017). The science ready images were used for further analysis. In Fig. 7.1, we show the color-composite image of M67, created using F148W (red), F154W (green) and F169M (blue) filter images.

Fig. 7.1 The Colour Composite FUV Image of M67 created using F148W (red), F154W(green) and F169M(blue) Filter Images

PSF photometry was performed on the images to estimate the magnitudes in three filters. The standard IRAF routines were followed to obtain the magnitudes in all the filters, which are also corrected for aperture and saturation (Tandon et al., 2017). The observation details of UVIT along with already available observations, which are used in this study are listed in Table 7.1. As we may be dealing with potential binary systems, it is important to note the date of observations as well, which are also provided in the table.

Table 7.1 Details of All Observations Used in This Study. The First Column Provides the Date of Observation (Based on the Availability). The Filter Details and Exposure Time are given in the Second and Third Columns. 4th Column gives the Zero Point Magnitude

Date of Observation	Filter	Exposure Time (s)	m_{zp}
2017 April 23	UVIT F148W	2290	18.016
2017 April 23	UVIT F154W	2428	17.778
2017 April 23	UVIT F169M	2428	17.455
2006 Jan 21	GALEX FUV	5555.2	18.82
2006 Jan 21	GALEX NUV	5555.2	20.08
1986 March 18	IUE FUV	4500	
1986 March 19	IUE FUV	7267	
1987 Dec 12	IUE FUV	3600	
1990 Feb 15-18	KPNO U	900	
1990 Feb 15-18	KPNO B	480	
1990 Feb 15-18	KPNO V	240	
1990 Feb 15-18	KPNO R		
1990 Feb 15-18	KPNO I	240	
	GAIA2 Gbp		25.3806
	GAIA2 G		25.7934
	GAIA2 Grp		25.1161
1997 Nov 16	2MASS J	403	21.039
1997 Nov 16	2MASS H	403	20.696
1997 Nov 16	2MASS K	403	20.05
2010 April 29	WISE W1		20.5
2010 April 29	WISE W2		19.5
2010 April 28	WISE W3		18.0

7.3 Analysis

The main aim of this study is to check for the presence of hot companions to BSSs. Hence we restrict our sample to the confirmed 14 BSSs based on radial velocity measurements (Geller et al., 2015). Among these 14 stars, we detected 10 stars in UVIT images. We cross identified these stars with their optical counterparts (Montgomery et al., 1993) and 9 BSSs are listed in Table 7.2 along with their magnitudes in all three UVIT filters. WOCS 2009 is known to be a triple system and hence we do not consider this star for further analysis (Van den Berg et al., 2001; Sandquist et al., 2003). In Fig. 7.2, we have shown the images of the 9BSSs detected in the FUV F148W filter of UVIT. The spatial plot of the cluster is shown in Fig. 7.3 along with the location on 9 BSSs. Mathieu and Latham (1986) showed that BSSs and the spectroscopic binaries in M67 are centrally concentrated relative to the single stars. Davenport and Sandquist (2010) estimated the core radius of M67 to be $4'.12$ using 2MASS data and a larger core radius of $8'.24$, when fainter stars from the SDSS sample was considered. In our sample of 9 BSSs, we find that 5 stars are within $4'$, while WOCS 2011, WOCS 2013, WOCS 3010 and WOCS 3013 are within $6'.5$, and therefore all the 9 BSSs are within the larger core radius of the cluster. We need to first check whether the detected FUV flux is same as that expected for the BSSs corresponding to its T_{eff}, which in turn requires accurate estimation of BSS properties. We use the SED analysis to compare the expected flux to the detected FUV flux, as detailed in the following section.

7.3.1 Spectral Energy Distribution of Blue Straggler Stars

SEDs for the 9 BSSs are constructed by combining multiwavelength photometric flux from UV to IR, spanning a wavelength range of 0.12 - 11.5 μm. The fluxes obtained from UVIT (F148W, F154W and F169M) are combined with fluxes from GALEX (Martin et al. (2005) FUV and NUV, for 6 BSSs), IUE (Boggess et al. (1978) 1250 Å, 1450Å, 1675Å, 2150 Å, 2395 Å, 2900 Å for 3 BSSs), UBVRI (Montgomery et al., 1993), *Gaia* (Gaia Collaboration et al. (2016) G_{bp}, G, G_{rp}), 2MASS (Cohen et al. (2003) J, H, Ks) and WISE (Wright et al. (2010) W1,W2 and W3). The multiwavelength SED covers a maximum of 25 data points, and is corrected for extinction in the respective bands (Fitzpatrick, 1999; Indebetouw et al., 2005). We adopted a reddening of E (B$-$V) = 0.041 mag (Taylor, 2007), a distance modulus V$-M_v$ = 9.6 mag and Solar metallicity.

We used VOSA to fit the SEDs and the details of fitting are given in chapter 3. We find spectral fits to be satisfactory in the optical - IR region, whereas an excess flux in the UV region was detected for some stars. The estimated χ^2_{red} values for these single spectral fits were found to be large as shown in column 5 of Table 7.3. Seven of these stars also show significant UV excess in their residual SEDs, suggesting the presence of a hot component for the BSSs.

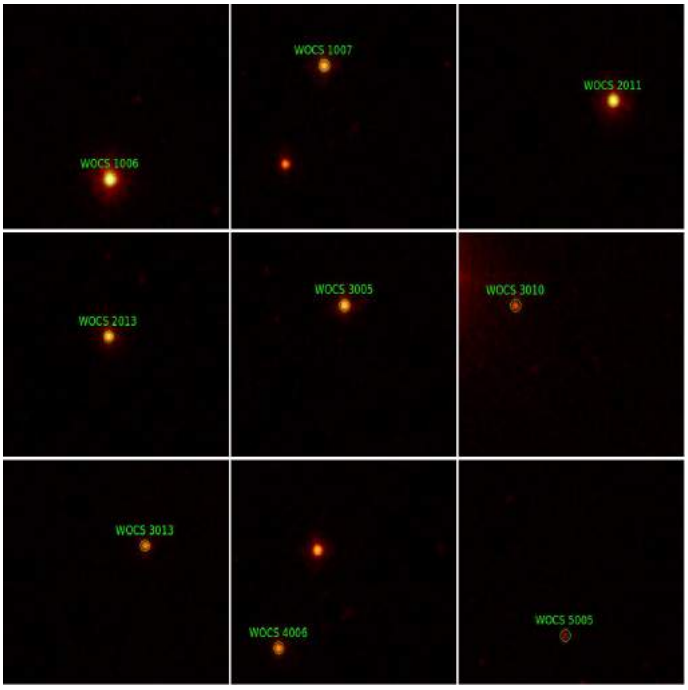

Fig. 7.2 The Image of all 9 BSSs taken from F148W Filter Image. These Stamp Images of Size $0.83'$ show that the BSS are Fairly Isolated and There are no Close Neighbour Stars, Contaminating the UV flux

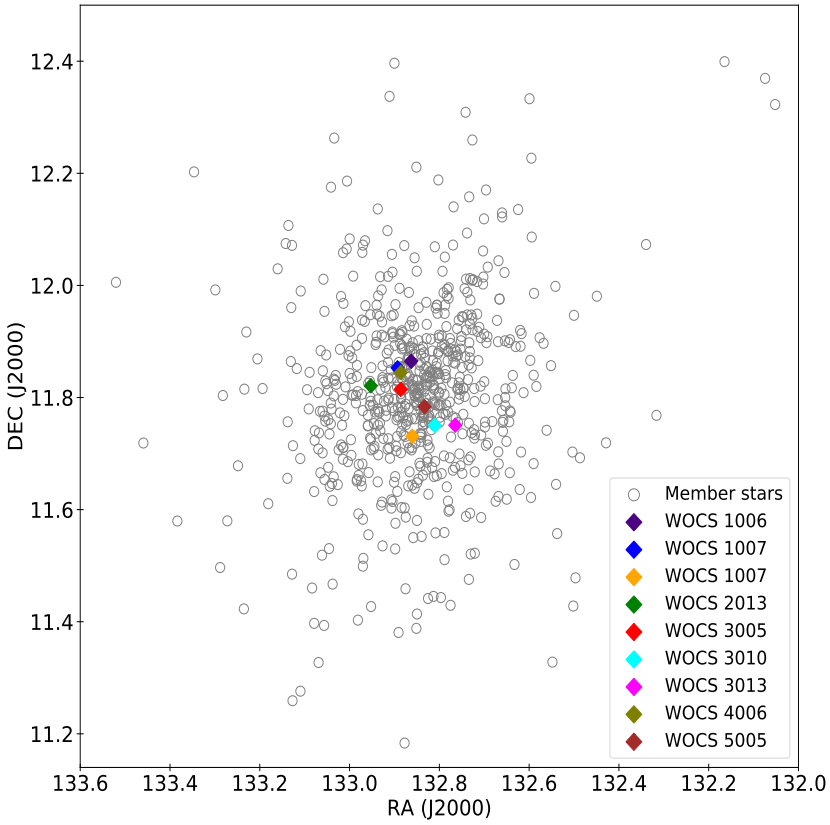

Fig. 7.3 Spatial Image of M67 showing the Member Stars of the Cluster with the 9 BSSs in Different Coloured Symbols

Table 7.2 The Magnitudes of the 9 BSSs Detected in the Three FUV Filters of UVIT are Listed Along with their RA and DEC and Optical Magnitudes taken from Montgomery et al. (1993)

WOCS ID	RA (deg)	DEC (deg)	V (mag)	B-V (mag)	F148W (AB mag)	F154W (AB mag)	F169M (AB mag)
1006	132.8627	11.86472	10.99	0.11	14.999±0.004	14.839±0.016	14.679±0.017
1007	132.8931	11.85302	10.94	0.22	17.036±0.018	16.72±0.016	16.638±0.019
2011	132.8601	11.73097	11.28	0.13	15.838±0.017	15.643±0.011	15.439±0.007
2013	132.9527	11.82116	10.92	0.31	16.726±0.017	16.567±0.016	16.354±0.014
3005	132.8859	11.81464	11.063	0.19	16.945±0.024	16.737±0.016	16.588±0.019
3010	132.8099	11.75033	11.078	0.43	18.765±0.048	18.590±0.038	18.354±0.038
3013	132.7647	11.75095	11.32	0.295	18.017±0.043	17.794±0.026	17.619±0.036
4006	132.8859	11.84477	12.257	0.26	17.881±0.031	17.811±0.028	17.612±0.035
5005	132.8331	11.78362	12.126	0.458	20.078±0.060	19.833±0.084	19.560±0.059

The SEDs of the 9 BSSs are shown in Fig. 7.5 to 7.13, where the UV observed flux are in gold (IUE), cyan (UVIT) and green (GALEX) and the blue dots represent the optical to IR observed fluxes and the synthetic flux are in red dots, after scaling. The insets show the close-up view of the UV region, where the presence of excess flux can be inferred from the observed photometric points extending significantly to the FUV region, when compared to the continuum shown in grey. The bottom panel in each of the SEDs shows the residual, where the square dots connected by gray dash line show the residual due to single spectral fit and rhombus dots connected by olive line show the residual of a composite fit. Error in the residual is also shown in the bottom panel. The residual SEDs establish clearly that 7 BSSs have significant UV excess suggestive of the presence of a hot companion. The flux level in the UV part of the SED also shows that the companion is a sub-luminous object (in comparison to UV luminous SED of the post-AGB/HB+BSS in NGC 188 - Fig. 2 of Subramaniam et al., 2016). The SEDs of stars WOCS 1006 and WOCS 2011 do not show an excess in the UV, as we can see from the residuals.The residuals are calculated as

$$Residual = (Flux_{Obs} - Flux_{Model})/Flux_{Obs} \tag{7.1}$$

In order to fit the hot component that may be present in the SEDs of 7 BSSs, we use Koester spectral models (Koester, 2010; Tremblay and Bergeron, 2009). As the hot component is sub-luminous and suspected to be a WD, we used log g = 7.75, though the broad band fluxes used in the SED are quite insensitive to the value of log g, which is in agreement with the findings of Kepler et al. (2012) where most of the WDs are found to have log $g \sim 8$. For completeness sake, we also consider log g value of 9. As the flux of the hot component as well as that of the BSS will get added up at all wavelengths, we created composite SEDs in order to fit the observed full SED. Though the parameters (Radius and Temperature) of the hot component spectra are mainly varied for the χ^2 minimisation, minor modification of the BSS parameters were also done to obtain the overall good fit over the entire wavelength range.

The best fitting composite theoretical spectra (olive) and the WD spectra (green) along with the composite flux (red dots) are shown in Fig. 7.5 to 7.13. The residual SEDs estimated from the composite model SED are shown in rhombus shape dots connected with olive line (lower panel of the figure), which suggest satisfactory double component fits for the 6 BSSs. WOCS 3005 does show an excess flux in the UV, though we are unable to fit a Koester model to the SED and obtain the parameters. Details of the estimated parameters from the double fit can be found in Table. 7.3. The χ^2_{red} values for the double fit are much lower than the single fit, except for WOCS 3010. We discuss each of the BSS, the SED fit and its implications below.

In Fig. 7.4 (top) we show a single fit for WOCS 5005, to demonstrate the pres-

ence of strong UV excess. As discussed in chapter 3, we use the condition of UV excess (Fig. 7.4) (bottom) to obtain the best fitting parameters of the primary companion. As we observe a strong UV excess flux, we construct a double fit as shown in Fig. 7.13. This method is followed for every single star, to check for the presence of a binary companion. The χ^2 values are tabulated in Table. 7.3 for all the 6 BSSs for a single fit and for the double fit. The large χ^2 values and the residual flux more than 50% in the UV, suggest the possible presence of a hotter companion.

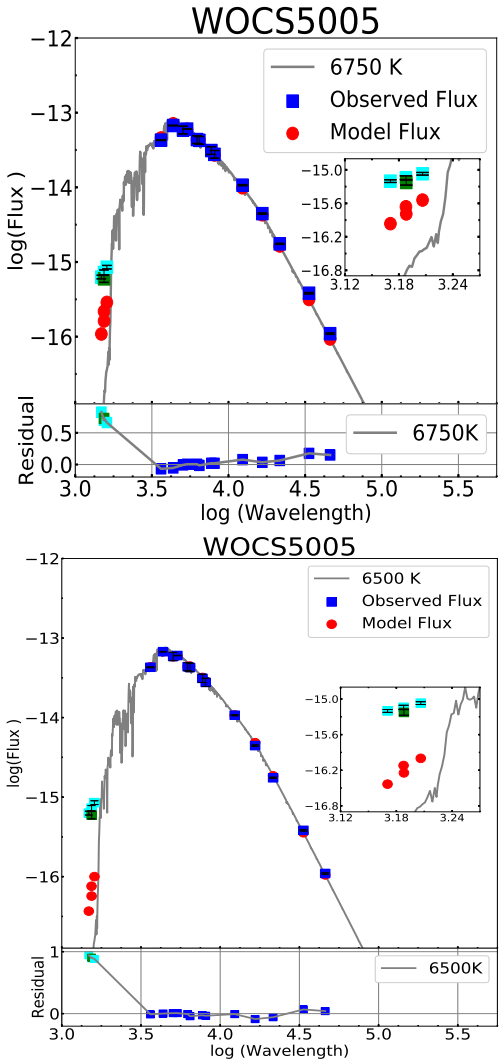

Fig. 7.4 Extinction Corrected SED of WOCS 5005 for a Single SED Fit Before (Top) and After (Bottom) UV Excess Condition is Applied. The Cyan (UVIT) and Green (GALEX) Points Indicate the UV Fluxes (shown in the inset as well); All Other Flux Measurements are shown in Blue. The Model Fluxes are Obtained from Convolving with Respective Filter bands, shown in Red Points. Kurucz Model Spectra for the Cooler Component is shown in Gray. The Unit of Wavelength is Å and Flux is ergs cm^{-2} s^{-1} $Å^{-1}$.The Bottom Panel Shows the Residual in the Respective Bands, where the Square Points Connected by Grey Line is the Residual for Single Spectral Fit

Table 7.3 Fundamental Parameters of the BSS and WD Companion are Listed. The First Column gives the WOCS Number, The Second and Third Column Lists The T_{eff} and Log g Estimated for BSS (Top) and WD (Bottom) Companion Respectively, Fourth Column gives The Luminosity of BSS (Top) and WD (Bottom), Radius of BSS (Top) and WD (Bottom) are given in 5th Column , χ^2_{red} with a Single Temperature Fit and A Composite Fit is given in Top and Bottom of 6th Column

WOCS ID	T_{eff} (K)	log g	$L/L_\odot$	$R/R_\odot$	χ^2_{red}
1006	8750±125	3.0	26.75±0.72	2.31±0.03	42.2
	—	—	—	—	—
	—	—	—	—	—
1007	7500±125	3.5	24.82±1.10	2.94±0.04	36.1
	13250±125	7.75	0.24±0.01	0.094±0.001	2.49
	13750±125	9.0	0.28±0.01	0.094±0.001	2.43
2011	8500±125	4.0	19.76±0.78	2.10±0.03	37.7
	—	—	—	—	—
	—	—	—	—	—
2013	7750±125	3.5	24.84±1.42	2.74±0.04	57.8
	15000±125	7.75	0.210±0.008	0.0680±0.0008	4.30
	18250±125	9.0	0.175±0.007	0.0421±0.0005	4.42
3005	7750±125	3.0	21.62±1.06	2.58 ±0.03	28.5
	—	—	—	—	—
	—	—	—	—	—
3010	6750±125	4.5	22.99±1.16	3.50±0.05	53.9
	13750±125	7.75	0.068±0.003	0.0466±0.0006	38.4
	16500±125	9.0	0.056±0.002	0.0293±0.0004	38.4
3013	7250±125	3.0	17.04±0.85	2.60±0.03	15.5
	17500±125	7.75	0.097±0.004	0.0344±0.0004	0.86
	20000±500	9.0	0.083±0.008	0.0247±0.0003	0.85
4006	7500±125	3.5	7.36±0.36	1.60±0.06	38.2
	21000±500	7.75	0.11±0.01	0.0258±0.0003	2.27
	24000±500	9.0	0.096±0.008	0.0188±0.0002	2.29
5005	6500±125	4.0	8.58±0.26	2.33±0.03	55.2
	11500±125	7.75	0.053±0.003	0.0583±0.0008	4.21
	12750±1250	9.0	0.043±0.002	0.0436±0.0006	4.14

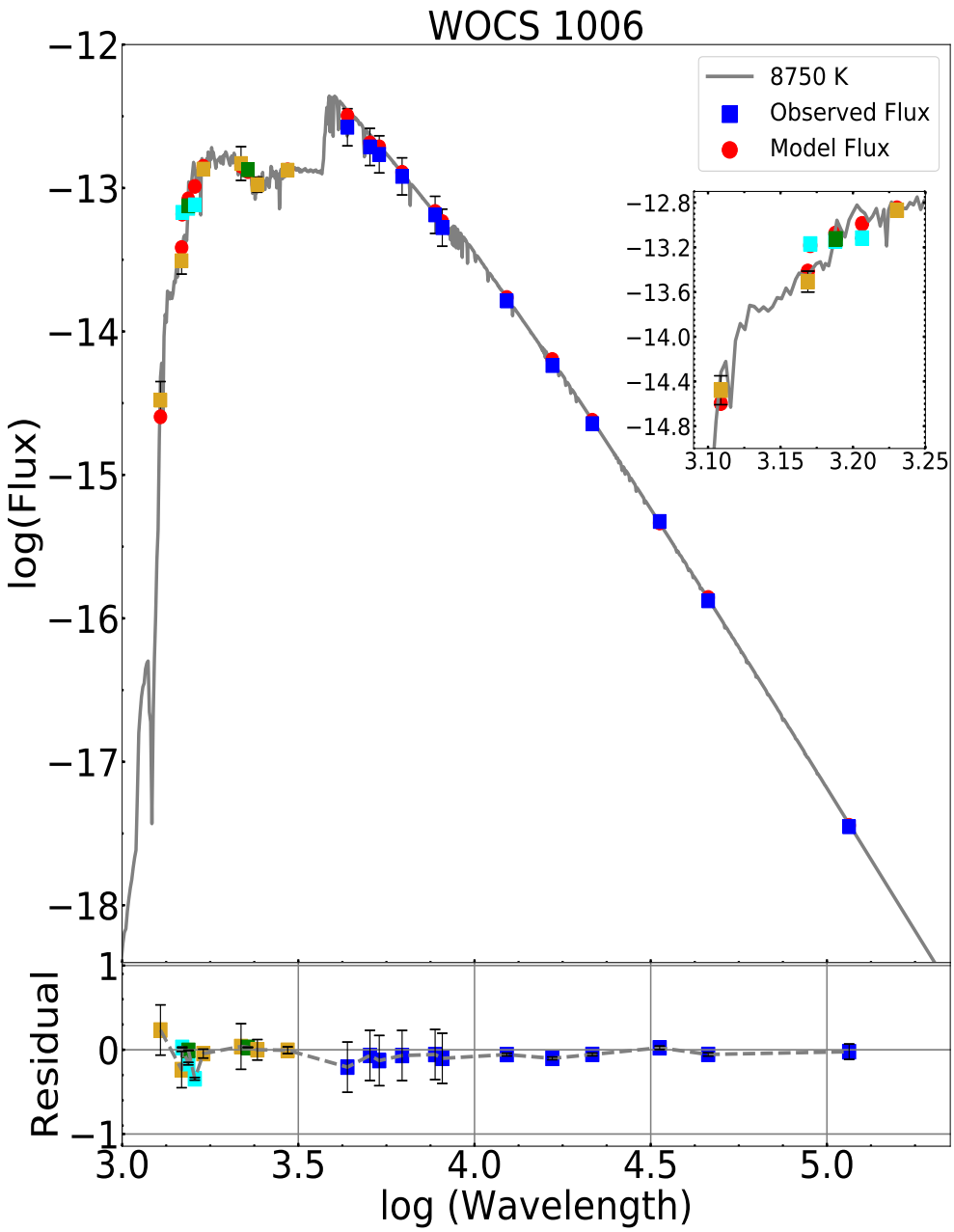

Fig. 7.5 Extinction Corrected SED of WOCS 1006. The Gold (IUE), Cyan (UVIT) and Green (GALEX) Points Indicate the UV Fluxes (shown in the inset as well); All Other Flux Measurements are shown in Blue. The Model Fluxes are Obtained from Convolving with Respective Filter bands, shown in Red Points. Kurucz Model Spectra is shown in Gray (8750 K). The Unit of Wavelength is Å and Flux is ergs cm^{-2} s^{-1} $Å^{-1}$. The Bottom Panel Shows the Residual in the Respective Bands, where the Square Points Connected by Grey Dash Line is the Residual for Single Spectral Fit

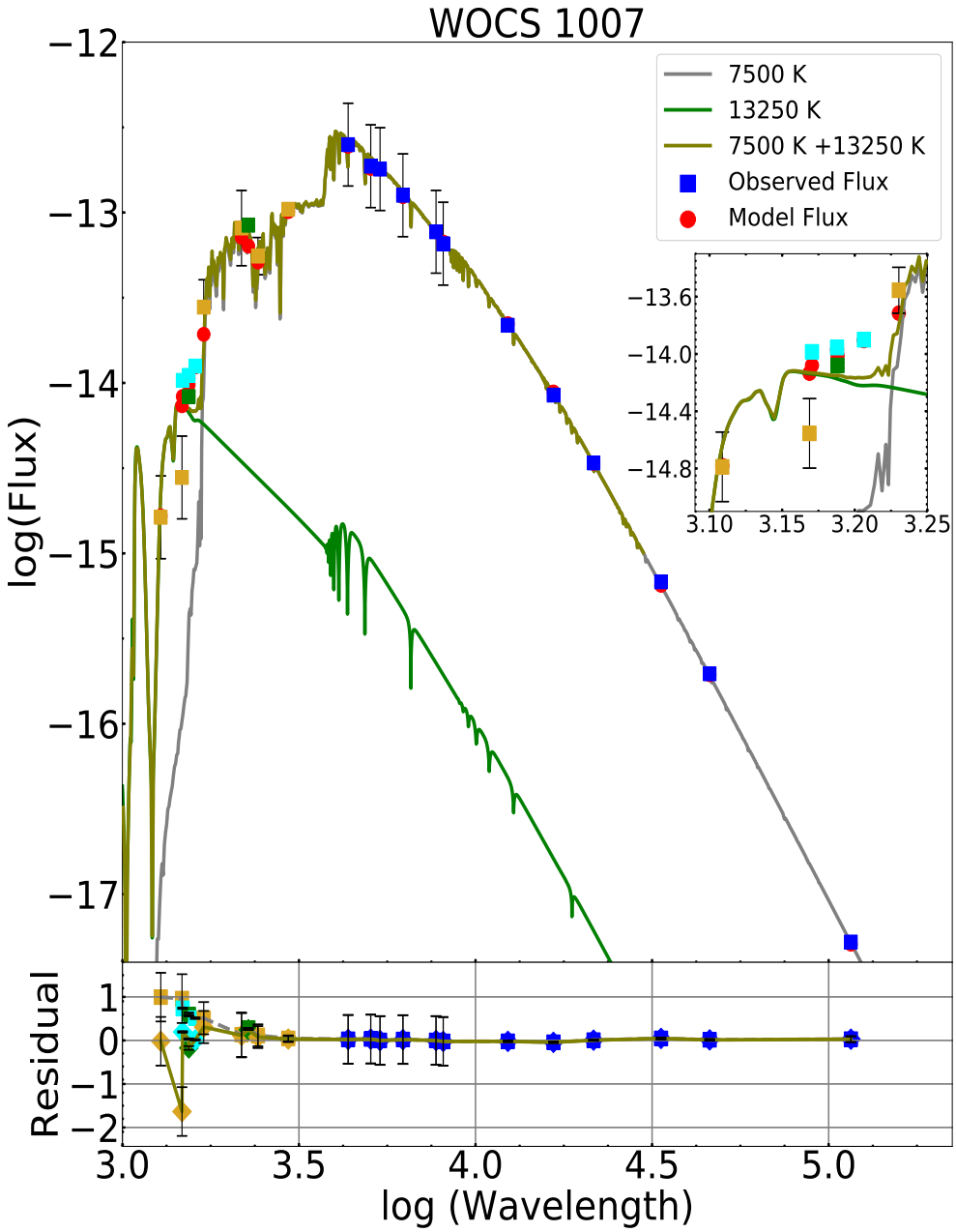

Fig. 7.6 Extinction Corrected SED of WOCS 1007. The Gold (IUE), Cyan (UVIT) and Green (GALEX) Points Indicate the UV Fluxes (shown in the inset as well); All Other Flux Measurements are shown in Blue. The Model Composite Fluxes are Obtained from Convolving with Respective Filter bands, shown in Red Points. Kurucz Model Spectra for the Cooler Component is shown in Gray (7500 K), The Koester Model Spectra (log g =7.75) for the Hotter Component is Shown in Olive (13250 K) and the Composite Spectra is in Green. The Unit of Wavelength is Å and Flux is ergs cm^{-2} s^{-1} Å^{-1}. The Bottom Panel Shows the Residual in the Respective Bands, where the Square Points Connected by Grey Dash Line is the Residual for Single Spectral Fit and Rhombus Points Connected by Olive Line is the Residual for Composite Spectral Fit

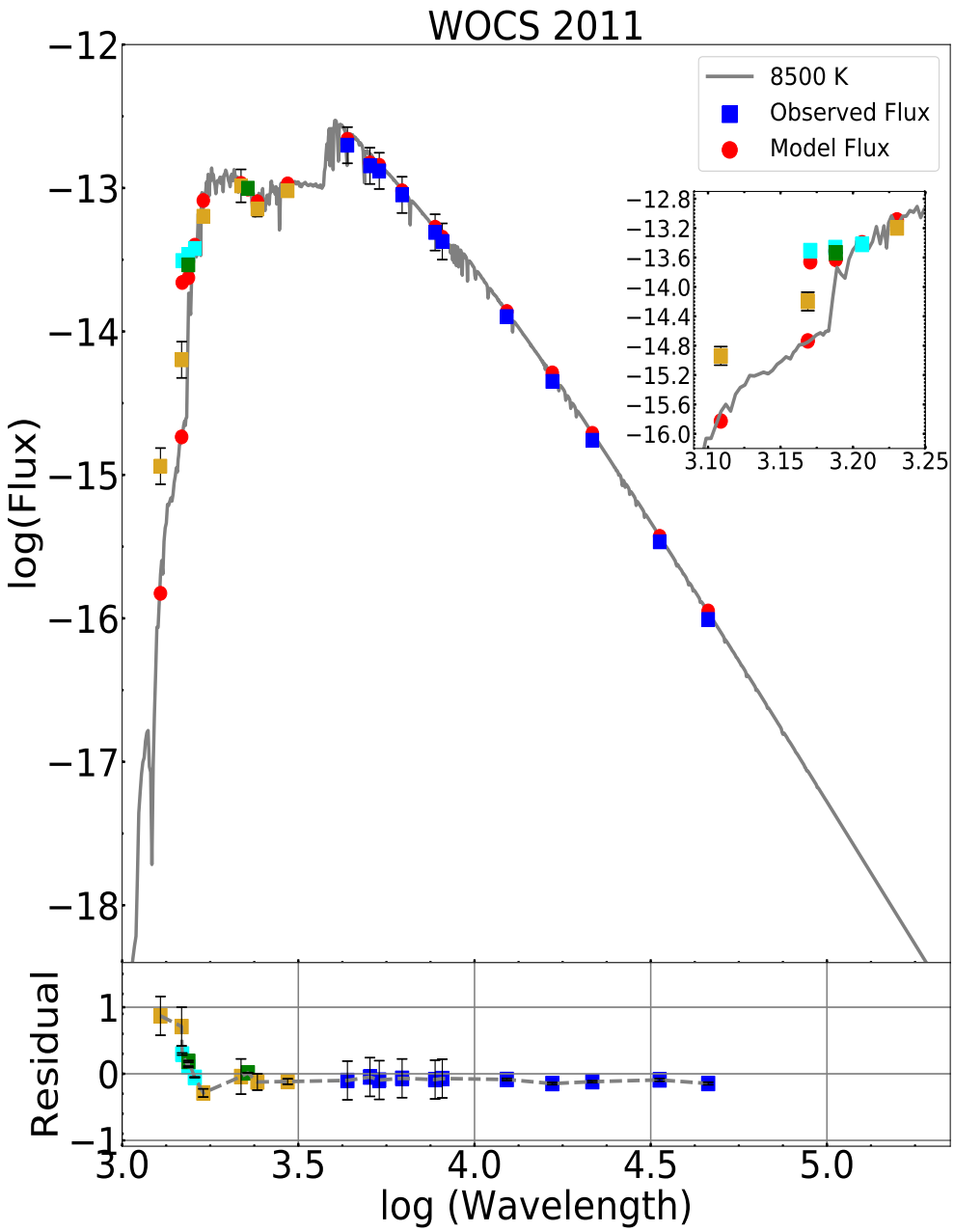

Fig. 7.7 Extinction Corrected SED of WOCS 2011. The Gold (IUE), Cyan (UVIT) and Green (GALEX) Points Indicate the UV Fluxes (shown in the inset as well); All Other Flux Measurements are shown in Blue. The Model Fluxes are Obtained From Convolving with Respective Filter bands, shown in Red Points. Kurucz Model Spectra is Shown in Gray (8500 K). The Unit of Wavelength is Å and Flux is ergs cm^{-2} s^{-1} $Å^{-1}$. The Bottom Panel Shows the Residual in the Respective Bands, where the Square Points Connected by Grey Dash Line is the Residual for Single Spectral Fit

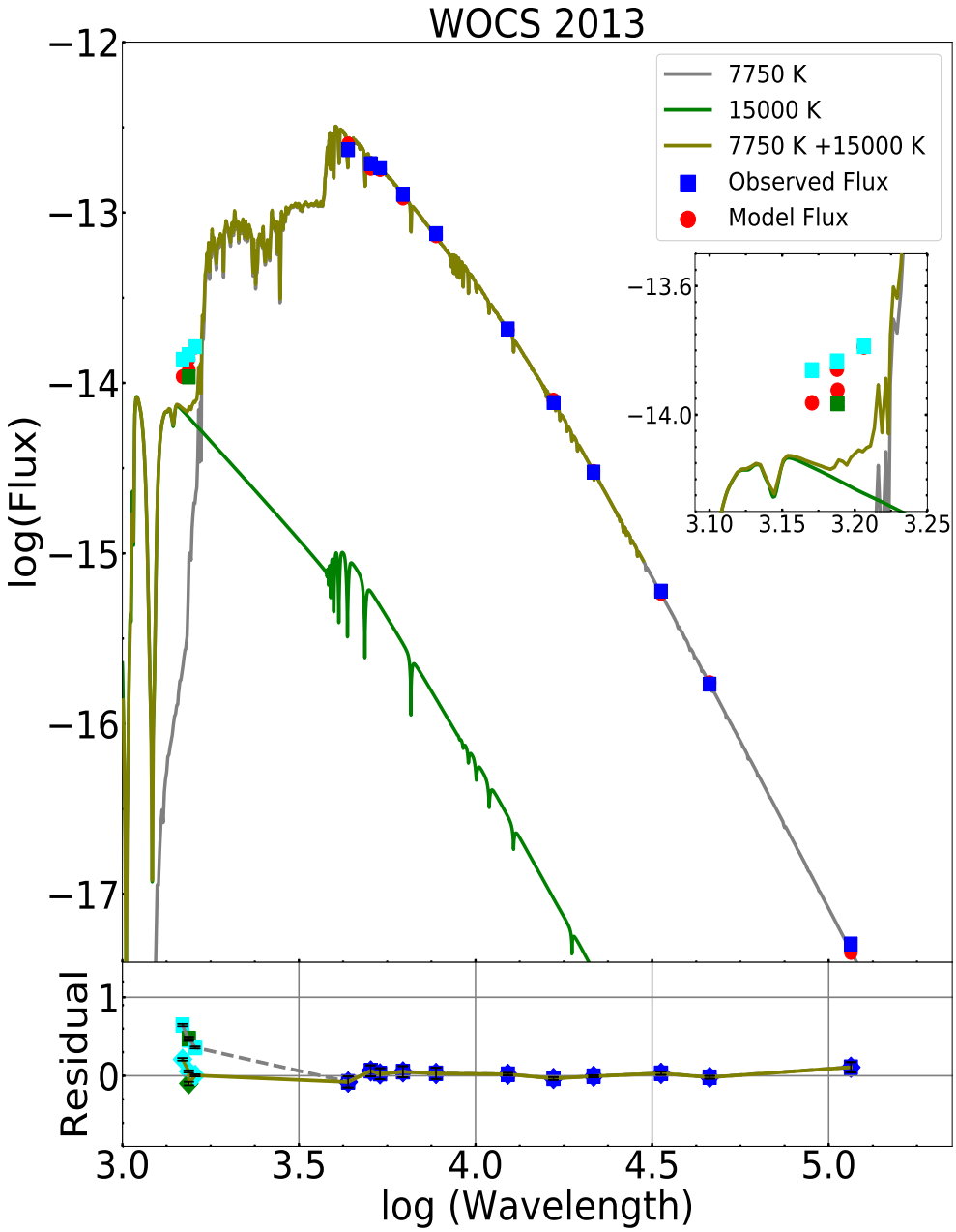

Fig. 7.8 Extinction Corrected SED of WOCS 2013. The Cyan (UVIT) and Green (GALEX) Points Indicate the UV Fluxes (shown in the inset as well); All Other Flux Measurements are shown in Blue. The Model Composite Fluxes are Obtained from Convolving with Respective Filter bands, shown in Red Points. Kurucz Model Spectra for the Cooler Component is shown in Gray (7750 K), The Koester Model Spectra (log g = 7.75) for the Hotter Component is Shown in Olive (15000 K) and the Composite Spectra is in Green. The Unit of Wavelength is Å and Flux is ergs cm^{-2} s^{-1} Å^{-1}. The Bottom Panel Shows the Residual in the Respective Bands, where the Square Points Connected by Grey Dash Line is the Residual for Single Spectral Fit and Rhombus Points Connected by Olive Line is the Residual for Composite Spectral Fit

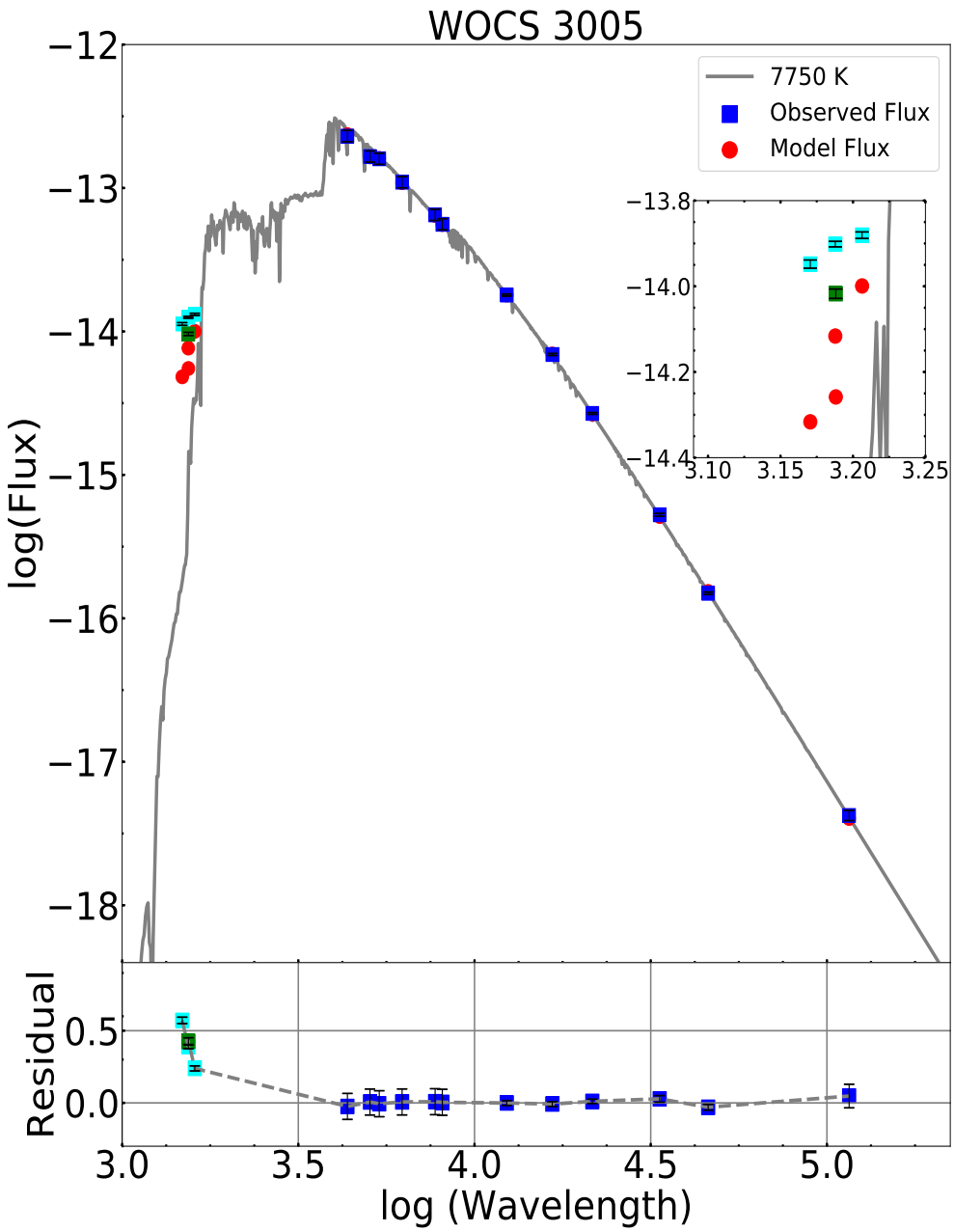

Fig. 7.9 Extinction Corrected SED of WOCS 3005. The Cyan (UVIT) and Green (GALEX) Points Indicate the UV Fluxes (shown in the inset as well); All Other Flux Measurements are shown in Blue. The Model Fluxes are Obtained from Convolving with Respective Filter bands, shown in Red Points. Kurucz Model Spectra for the Cooler Component is shown in Gray (7750 K). The Unit of Wavelength is Å and Flux is ergs cm^{-2} s^{-1} $Å^{-1}$. The Bottom Panel Shows the Residual in the Respective Bands, where the Square Points Connected by Grey Dash Line is the Residual for Single Spectral Fit

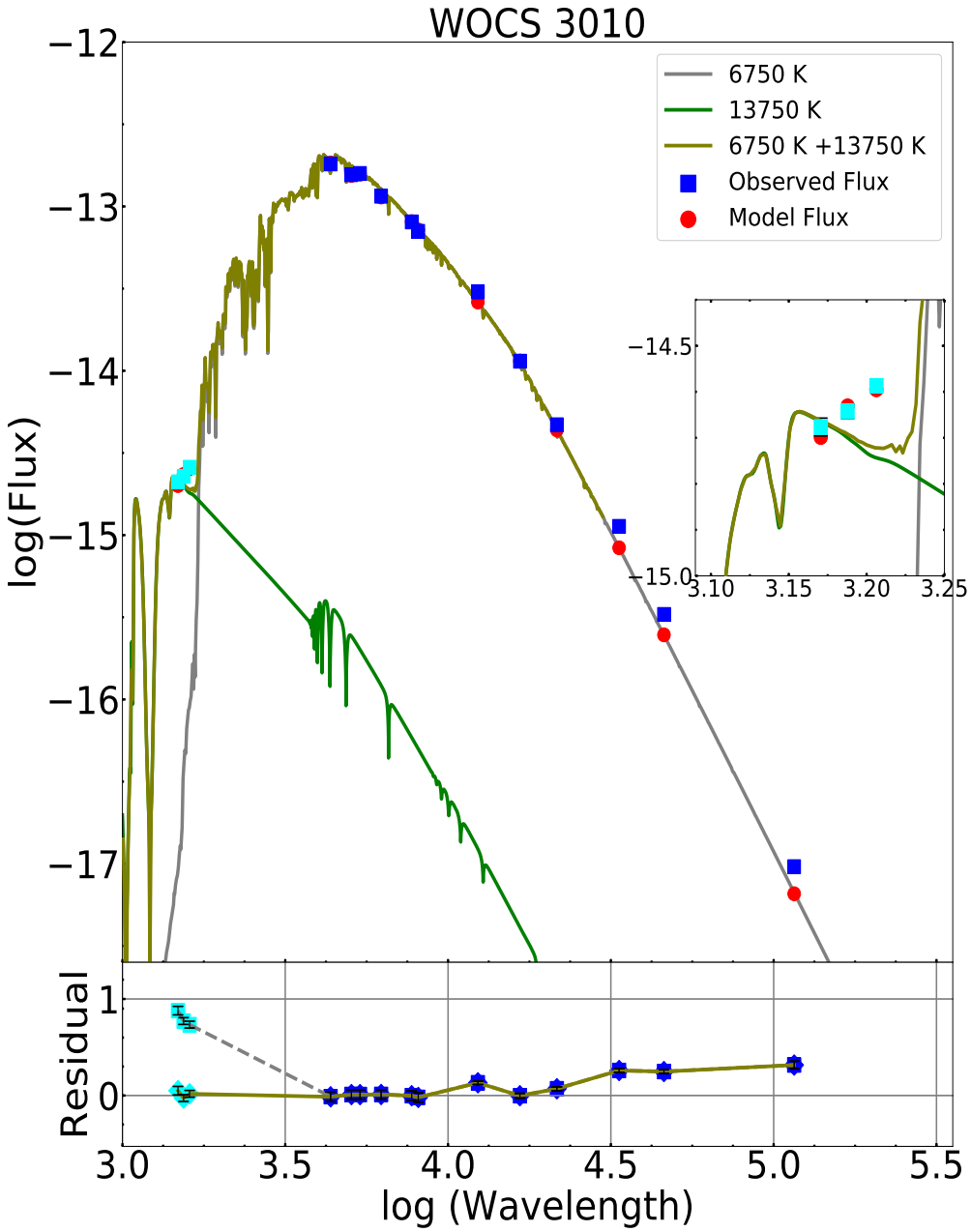

Fig. 7.10 Extinction Corrected SED of WOCS 3010. The Cyan (UVIT) Points Indicate the UV Fluxes (shown in the inset as well); All Other Flux Measurements are shown in Blue.The Model Composite Fluxes are Obtained from Convolving with Respective Filter bands, shown in Red Points. Kurucz Model Spectra for the Cooler Component is shown in Gray (6750 K), The Koester Model Spectra (log g =7.75) for the Hotter Component is Shown in Olive (13750 K) and the Composite Spectra is in Green.The Unit of Wavelength is Å and Flux is ergs cm^{-2} s^{-1} Å^{-1}. The Bottom Panel Shows the Residual in the Respective Bands, where the Square Points Connected by Grey Dash Line is the Residual for Single Spectral Fit and Rhombus Points Connected by Olive Line is the Residual for Composite Spectral Fit

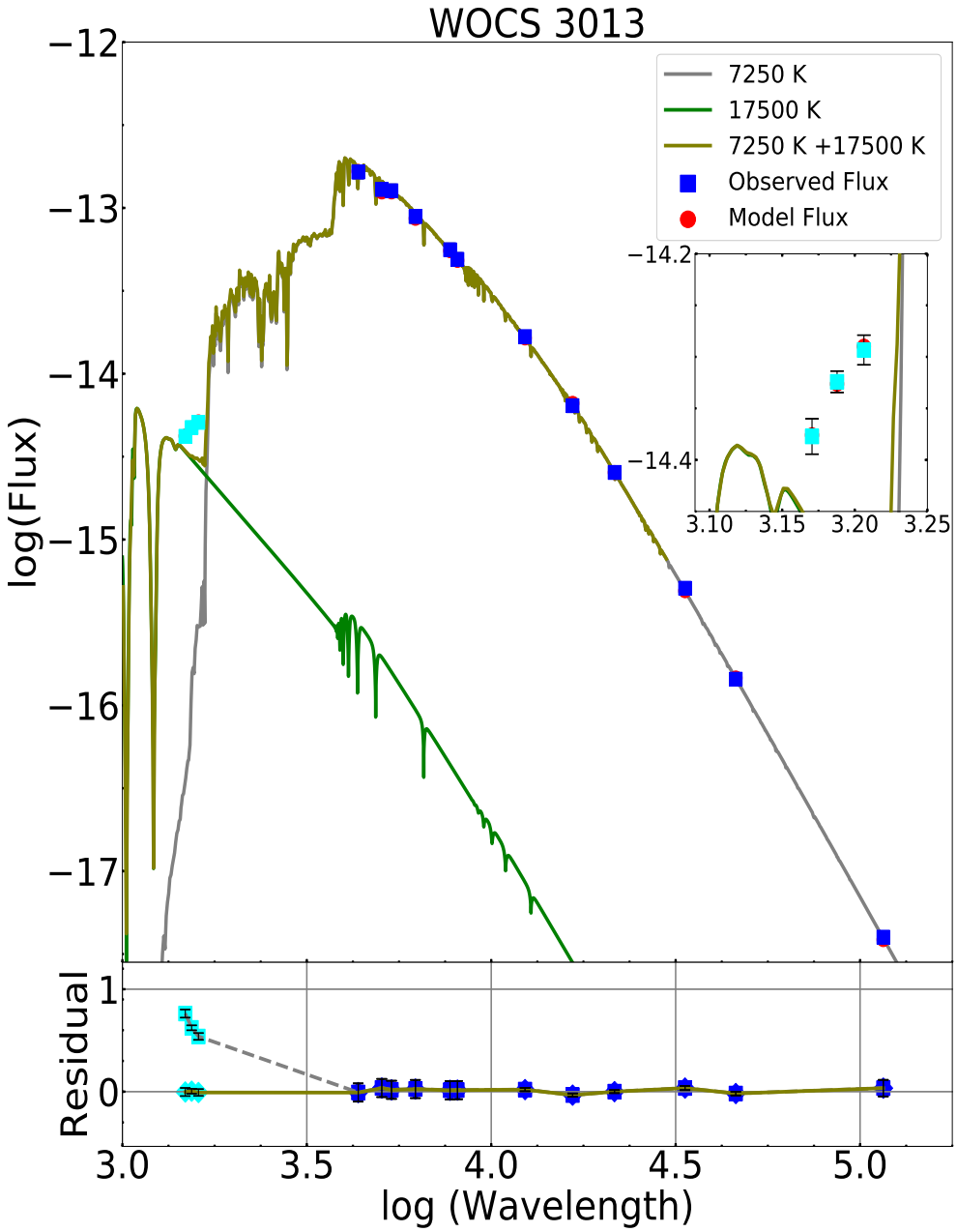

Fig. 7.11 Extinction Corrected SED of WOCS 3013. The Cyan (UVIT) Points Indicate the UV Fluxes (shown in the inset as well); All Other Flux Measurements are shown in Blue. The Model Composite Fluxes are Obtained from Convolving with Respective Filter bands, shown in Red Points. Kurucz Model Spectra for the Cooler Component is shown in Gray (7250 K), The Koester Model Spectra (log g =7.75) for the Hotter Component is Shown in Olive (17500 K) and the Composite Spectra is in Green. The Unit of Wavelength is Å and Flux is ergs cm^{-2} s^{-1} Å^{-1}. The Bottom Panel Shows the Residual in the Respective Bands, where the Square Points Connected by Grey Dash Line is the Residual for Single Spectral Fit and Rhombus Points Connected by Olive Line is the Residual for Composite Spectral Fit

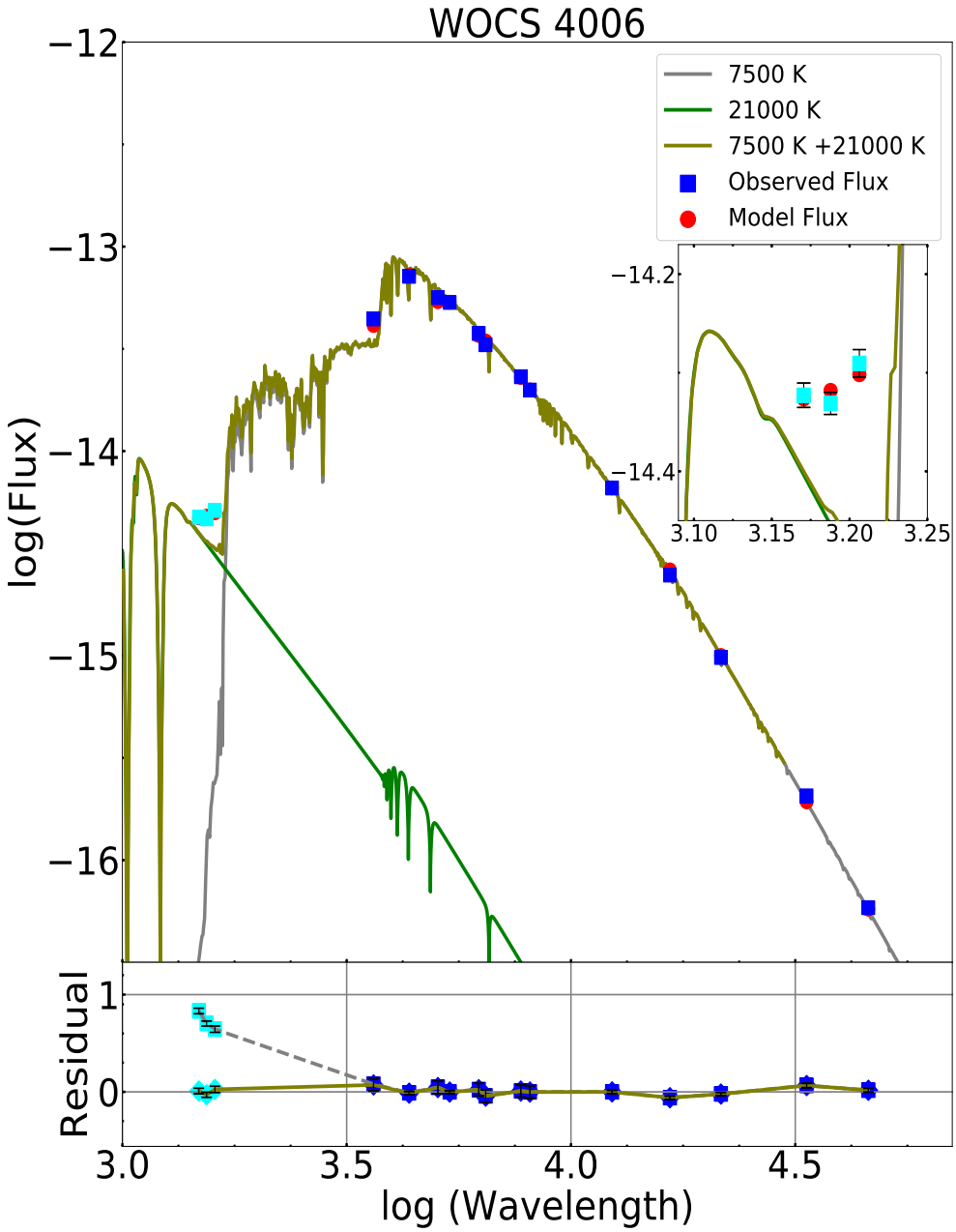

Fig. 7.12 Extinction Corrected SED of WOCS 4006. The Cyan (UVIT) Points Indicate the UV Fluxes (shown in the inset as well); All Other Flux Measurements are shown in Blue. The Model Fluxes are Obtained from Convolving with Respective Filter bands, shown in Red Points. Kurucz Model Spectra for the Cooler Component is shown in Gray (7500 K), The Koester Model Spectra (log$g$ =7.75) for the Hotter Component is Shown in Olive (21000 K) and the Composite Spectra is in Green.The Unit of Wavelength is Å and Flux is ergs cm^{-2} s^{-1} Å^{-1}. The Bottom Panel Shows the Residual in the Respective Bands, where the Square Points Connected by Grey Dash Line is the Residual for Single Spectral Fit and Rhombus Points Connected by Olive Line is the Residual for Composite Spectral Fit

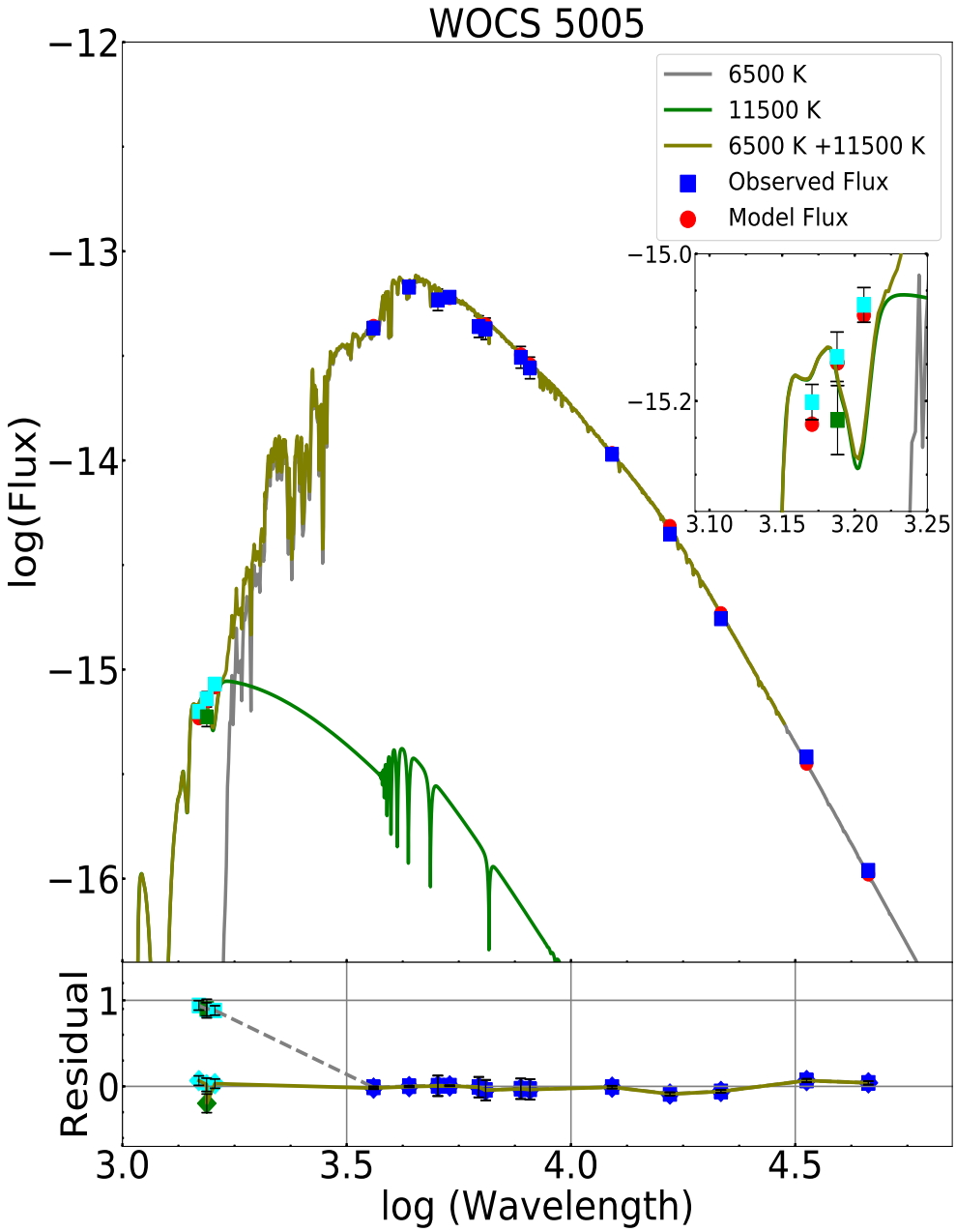

Fig. 7.13 Extinction Corrected SED of WOCS 5005. The Cyan (UVIT) and Green (GALEX) Points Indicate the UV Fluxes (shown in the inset as well); All Other Flux Measurements are shown in Blue. The Model Composite Fluxes are Obtained from Convolving with Respective Filter bands, shown in Red Points. Kurucz Model Spectra for the Cooler Component is shown in Gray (6500 K), The Koester Model Spectra (log g =7.75) for the Hotter Component is Shown in Olive (11500 K) and the Composite Spectra is in Green.The Unit of Wavelength is Å and Flux is ergs cm^{-2} s^{-1} $Å^{-1}$. The Bottom Panel Shows the Residual in the Respective Bands, where the Square Points Connected by Grey Dash Line is the Residual for Single Spectral Fit and Rhombus Points Connected by Olive Line is the Residual for Composite Spectral Fit

Table 7.4 The Kinematic Details and Ages of the 9 BSSs are Listed, Along with Mass of the BSS and WD Companion. The Formation Pathway is listed in the last column, where MT indicates Mass Transfer

WOCS No.	P days	e	Vsin$i$ Kms^{-1}	Age(WD) Myr	Mass(BSS) M/M$_\odot$	Mass(WD) M/M$_\odot$	Formation Pathway
Group(a)							
1006	-	-	100		2.15	-	
1007	4.18^a	0.266^a	65, 79.45		2.08	$<$0.2	WD, MT
2011	-	-	0				
2013	846^b	0.47^b	59, 60.90		2.05	$<$0.2	WD, MT
3005	-	-	20, 26		1.99	-	
3010	1221^b	0.088^b	50	190	2.11	$<$0.2	WD, MT
3013	1003^b	0.32^b	70, 76.26	40	1.90	0.2-0.3	WD, MT
Group(b)							
4006	-	-	80	74	1.69	0.3	WD, MT
Group(c)							
5005	4913^b	0.342^b	20		1.60	$<$ 0.2	WD, MT

period and eccentricity are taken from: ^{a} - Latham et al. (1992); ^{b} - Latham and Milone (1996)
Vsin$i$ is taken from: Latham and Milone (1996), Bertelli Motta et al. (2018)

7.4 Detection of UV Excess and Possible White Dwarfs

The results of the SED fits are discussed in this section. The HRD for the 9 BSSs, along with the isochrones are shown in Fig. 7.14. The bright BSSs, which are classified as group (a) BSS in the previous chapter, span a range in T_{eff}. We note that WOCS 3010 and WOCS 3013 also belong to this group, which were not studied in the previous chapter. The HRD for the WD candidates are also shown in Fig. 7.15. The isochrones shown in this figure are taken from Holberg and Bergeron (2006) and Tremblay, P.-E. et al. (2011) for C-core and DA compositions and the He-core composition models are taken from Panei et al. (2007). Orbital properties as well as projected rotational velocity, Vsin$i$ of several BSSs are available in literature (Latham et al., 1992; Milone et al., 1992; Milone and Latham, 1992, updated values in Sandquist and Shetrone, 2003*b*; see table 4, Bertelli Motta et al., 2018). These parameters as well as the estimated age and mass of the BSSs and the WD companions are tabulated in Table. 7.4. SED fits of individual BSSs are discussed below.

7.4.1 WOCS 1006 (S1066)

This BSS is best fitted with a T_{eff} = 8750 K, which makes it one of the hottest BSS in M67. The value of T_{eff} derived here is in agreement with the value estimated by Sindhu et al. (2018), tabulated in last chapter. By including the UVIT and IUE data points, the $R/R_{\odot}$ and $L/L_{\odot}$ of the BSSs are re-estimated. The SEDs found to fit the entire wavelength from UV to mid-IR with one spectrum as shown by the residual plot. The large value for χ^2_{red} for the single fit is arising out of very small flux errors and not due to excess of flux.This is again checked by plotting the photometric points, the extinction corrected IUE spectra and the model in Fig. 7.16. The figure shows the IUE spectra in the FUV and NUV, photometric data points and the fitted spectrum up to 6000 Å. The model is found to fit the UV region very well. This demonstrates that the UVIT photometry consistently traces the flux distribution found in the IUE spectra.

7.4.2 WOCS 1007 (S1284)

This BSS is fitted with a two component model, as excess UV flux is detected in the single fit. In the SED, the UVIT data points are consistent with the GALEX FUV data as well as the IUE photometric data points (though these have relatively large errors). The excess flux found in the UV region is found to rise gradually up to the FUV region, as there are a good number of NUV data points as well. The double fit with a cool (T_{eff} = 7500 K) and a hot component (T_{eff} =13250 K) fits the excess flux very well, thereby reducing the χ^2_{red} value from 36.1 to 2.4. The BSS is found to have a T_{eff} = 7500 K, is in agreement with the value estimated by Sindhu et al. (2018), within errors.

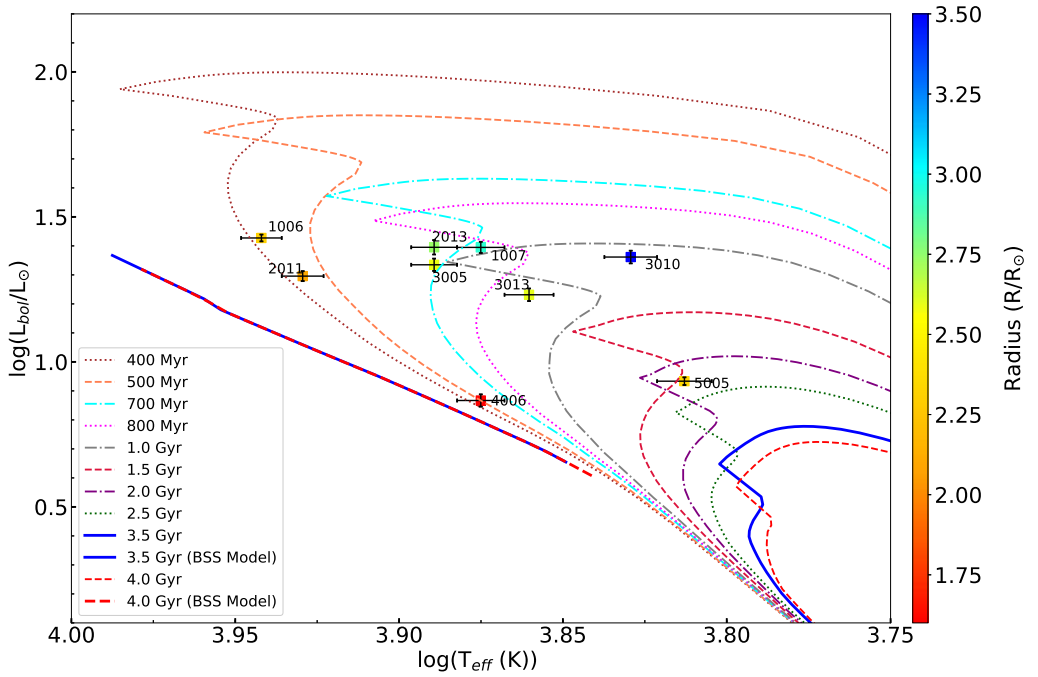

Fig. 7.14 The HRD of the BSSs. The Isochrones for Various Ages are Plotted, along with the BSS Model Line for 3.5 and 4.0 Gyr Generated using FSPS Code with BaSTI model are shown with Different Colours. The Points are Colour Coded Based on the Radius of the Stars

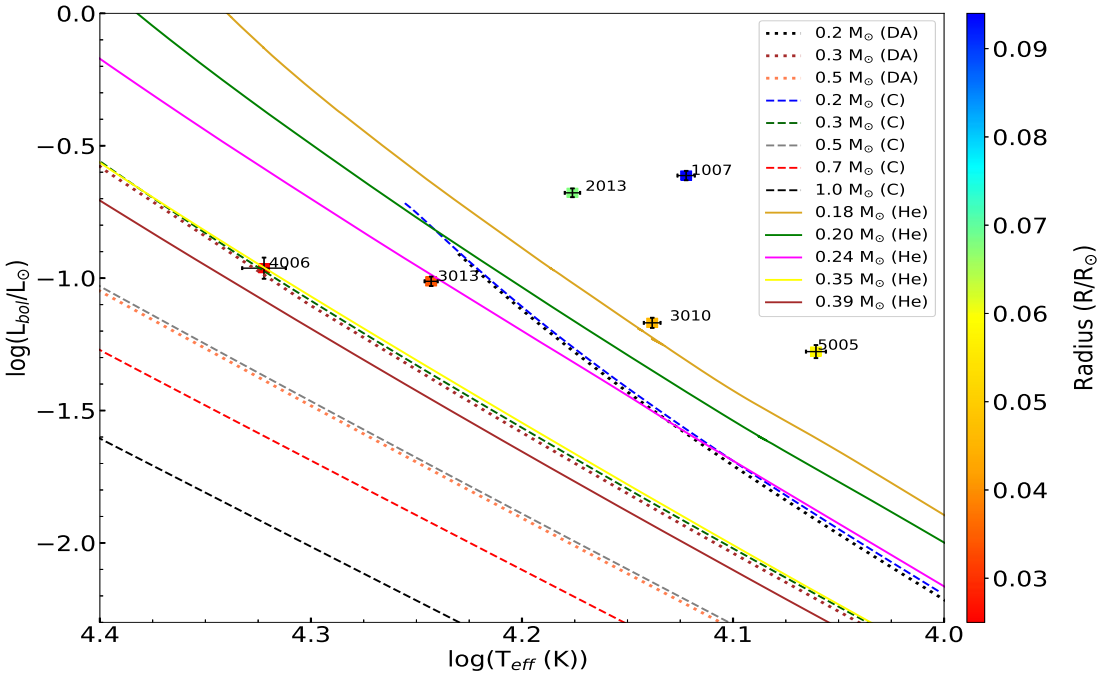

Fig. 7.15 The HRD of the 6 Probable WD Companions of the BSSs are shown. The WD evolutionary tracks of C-Core and DA Compositions are taken from Holberg and Bergeron (2006), Tremblay, P.-E. et al. (2011) and He-Core Composition are taken from Panei et al. (2007)

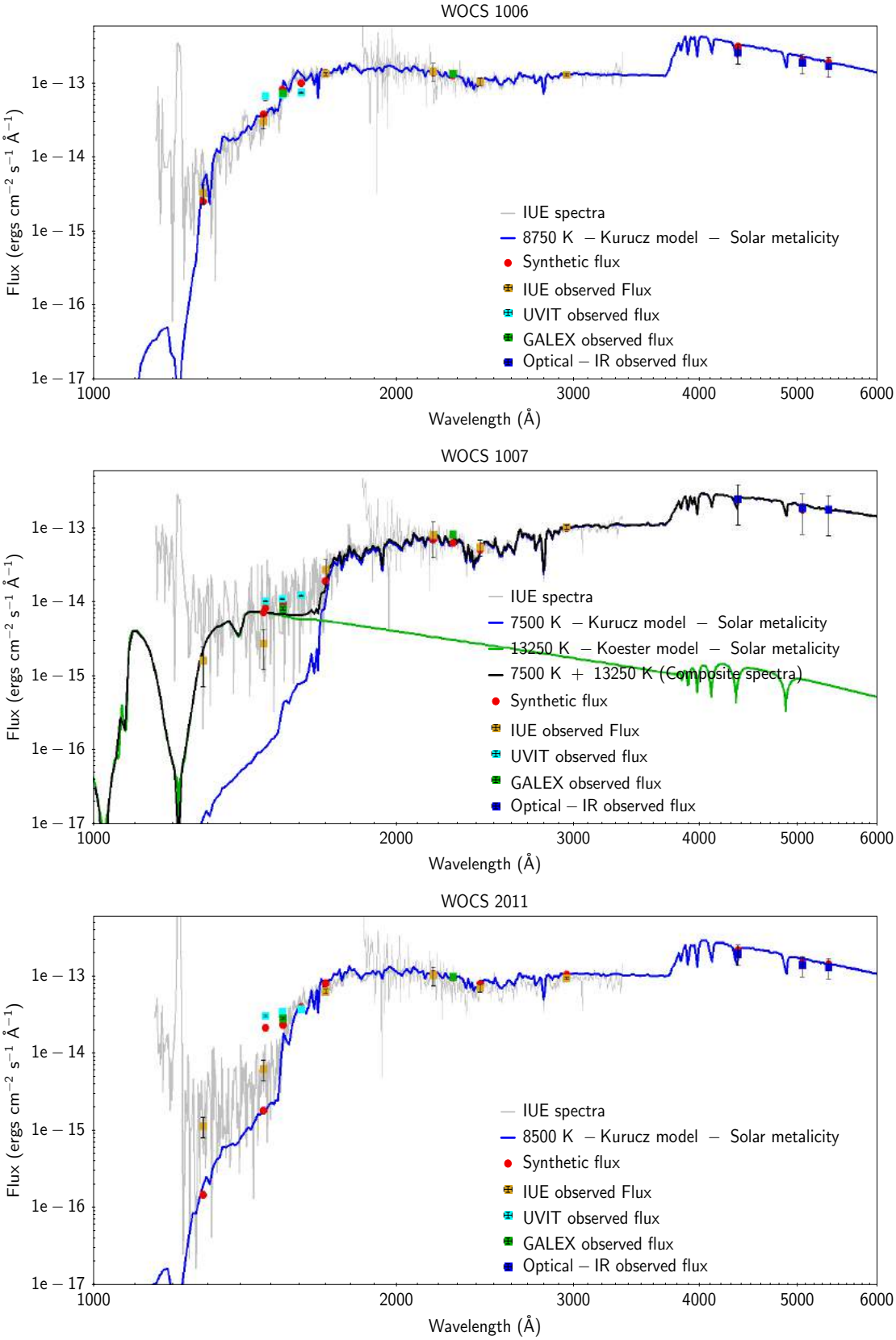

Fig. 7.16 The Extinction Corrected IUE Spectra of W0CS 1006, WOCS 1007 and WOCS 2011 are shown in Gray, Along with the Observed Fluxes shown as Square Points and the Single (WOCS 1006, WOCS 2011)/Composite (WOCS 1007) Synthetic Flux Points are shown as Red Circles. The Theoretical Spectra of Kurucz Model is plotted in Blue Line in All Three Figures. The Composite Spectra for WOCS 1007 is Show in Black and Theoretical Spectra of Koester Model (log g = 7.75) is Shown in Green

The hot component is found to have a T_{eff} = 13250 - 13750 K, depending on the value of log g. The IUE spectra shown in Fig. 7.16, along with the UVIT observations suggest a very good agreement between the above two. The hot component spectrum, with a temperature of 13250 K is found to fit the IUE spectrum in the FUV very well, supporting the presence of a hot component for this BSS. Thus, we detect the elusive hot component to this BSS and estimate its parameters. The hot component is found to have a $L/L_{\odot}$ = 0.28 and a $R/R_{\odot}$ = 0.094, which suggest the object to be a sub-luminous small object, candidate for a WD. The kinematic estimation suggests a mass of 0.21 - 0.19$M_{\odot}$, which makes this a candidate low mass WD. This BSS has rapid rotation, and (Milone and Latham, 1992) argued that this rapid rotation is sustained by a slow mass transfer. In Fig. 7.15, where the WDs along with the models are shown, the WD for WOCS 1007 is found to be located away from the models. A relatively large radius could be the reason for a relatively large luminosity, shifting its location above the isochrones.

7.4.3 WOCS 2011 (S968)

SED of this star is fitted with a single spectrum of T_{eff} = 8500 K. There is a marginal excess flux in the FUV, as found by UVIT and IUE photometric points, when compared to the expected flux from the above spectrum. The comparison with IUE spectra, as shown in the bottom panel of Fig. 7.16, also shows a marginal excess in FUV, along with an overall good fit between the SED, spectra and the photometric data points. A comparison of this BSS with the above two BSSs suggests that this BSS is a single star, unlike WOCS 1007, but certainly has a marginal amount of FUV excess flux, unlike WOCS 1006. This star is known to be a Am star and the excess UV flux could be due to the magnetic activity.

7.4.4 WOCS 2013 (S1267)

The SED of this BSS is fitted with a single spectrum to reveal an excess flux in the FUV, which is significant in all the UVIT filters as well as in GALEX FUV. We used a double fit by including a hot component. The expected flux from a combination of two spectra with T_{eff} = 7750 K and 15000 K fits the observed flux in GALEX FUV band, UVIT F154W (within errors) and F169M, though we still detect a mild excess in F148W. We obtain a fit for a T_{eff} of 15000 - 18250 K, depending on the value of log$g$. The values of the $L/L_{\odot}$ and $R/R_{\odot}$ are also relatively small, suggesting the object could be a WD. The χ^2_{red} for the double fit is much smaller than that for the single fit, but slightly higher than that for the double fit of WOCS 1007. We find that a WD like component fits the excess UV flux which suggests that there is a possible WD companion to this star. This BSS is known to be a single lined spectroscopic binary, with a period of 846 days

and eccentricity of 0.47 (Latham and Milone, 1996). Thus the hot sub-luminous WD component could be the binary component. The location of the WD in Fig. 7.15 suggest that this is also likely to be a low mass WD with mass < 0.2 $M_{\odot}$. Similar to the WD found in WOCS 1007, this WD is also more luminous, probably due to a slightly large radius.

7.4.5 WOCS 3005 (S1263)

The SED of this BSS is fitted with a single spectrum of T_{eff} = 7750 K, to detect a UV excess which is significant. The observed flux is much higher when compared to the expected flux for the above temperature in all three filters of the UVIT and the GALEX FUV filter. The slope of the residual is very steep and we are unable to fit the excess UV flux. This star is known to be single star from radial velocity studies by Geller et al. (2015).

7.4.6 WOCS 3010 (S975)

The SED of this BSS is fitted with a single spectrum of T_{eff} = 6750 K, to detect a UV excess which is quite significant. The UV excess can be successfully fitted by a hot component, thereby reducing the χ^2_{red} values from 53.9 to 38.4. We note the presence of IR excess in the residual, which is likely to be due to a faint nearby star. The double SED fits suggest the hot component to have a T_{eff} = 13750 - 16500 K, with a $R/R_{\odot}$ of 0.047 - 0.029 and is very sub-luminous. The parameters suggest the hot companion to be a WD. This BSS is known to be a single lined spectroscopic binary, with a period of 1221 days and an eccentricity of 0.088 (Latham and Milone, 1996) and we detect the predicted sub-luminous component for this BSS and confirm it to be a WD. The location of this WD in Fig. 7.15 shows that the WD is located near the isochrones, and the mass is ~ 0.18 $M_{\odot}$. This again is a low mass WD, similar to those found in WOCS 1007 and WOCS 2013.

7.4.7 WOCS 3013 (S752)

The SED of the WOCS 3013 is fitted well with a double fit, where the BSS is found to have a T_{eff} = 7250 K and the hot component with a T_{eff} = 17500 - 20000 K. The χ^2_{red} reduces from 15.5 to 0.8 suggesting that the double component shows an excellent fit to the full SED. The $R/R_{\odot}$ of the hot component is 0.02 - 0.03 and sub-luminous, suggesting it to be a WD. This BSS is also known to be a single lined spectroscopic binary and the detected hot, sub-luminous WD may be the binary component. The period of this BSS is 1003 days with an eccentricity of 0.32 Latham and Milone (1996). The location of the WD in Fig. 7.15 shows that it is located within the grids of He WD isochrones, with a mass of 0.24 $M_{\odot}$.

7.4.8 WOCS 4006 (S1280)

The SED of this BSS is well fitted by a double SED, where the BSS is fitted with a T_{eff} = 7500 K and the hot component for the excess UV flux. The double fit brings down the χ^2_{red} value from 38.2 to 2.2. The hot component is found to have T_{eff} = 21000 - 24000 K and a radius of $\sim$ 0.02$R_\odot$. This is suggestive of a relatively hot WD. This BSS is known to be a binary star, but the orbital parameters are not known. Hence the detected hot WD could be the binary component. The WD is located near the model lines for DA as well as C-core WD models and the mass is estimated to be 0.3 $M_\odot$. Therefore this is also likely to be a low mass WD.

7.4.9 WOCS 5005 (S997)

The SED of this BSS is well fitted by a double SED, where the BSS is fitted with a T_{eff} = 6500 K and the hot component for the excess UV flux, which is found to be significant. The double fit brings down the χ^2_{red} value from 55.2 to 4.2. The hot component is found to have T_{eff} = 11500 - 12750 K and a radius of $\sim$ 0.04 - 0.06 $R_\odot$. This star is observed by the HST and the extinction corrected HST spectrum is plotted along with the photometric data points as well as the model spectra, in Fig.7.17. The FUV part of the spectrum is not fitted by the 6500 K spectrum (shown in blue), suggestive of FUV excess. The hot component model spectrum of T_{eff} = 11500 K (shown in green) and the composite spectrum (shown in black) fits the spectrum well. Therefore, the FUV excess flux is confirmed by the HST spectrum. This BSS is known to be a single lined spectroscopic binary, with a period of 4913 days and an eccentricity of 0.342. The location of the WD in Fig. 7.15, finds the WD to be slightly over-luminous with a mass $< 0.2M_\odot$. Hence we suggest that the relatively cool WD is the binary component of this BSS.

7.5 Rotation of Blue Straggler Stars

We note that WOCS 1006 is a fast rotator with a V$\sin i$ = 100kms^{-1}, closely followed by WOCS 4006 and WOCS 1007 ($\sim$ 80 kms^{-1}). WOCS 2011, WOCS 5005 and WOCS 3005 are the slow rotators. Bertelli Motta et al. (2018) also estimated V$\sin i$ for MSTO stars and their figure 11 suggests that MSTO stars have V$\sin i$ $<$ 20 kms^{-1}. Thus, a good fraction of the BSSs studied here are fast rotators. Among the slow rotators, WOCS 2011 is known to be an AM star, and could have slowed down due to magnetic breaking (Mathys, 1991). Mass transfer is one of the reasons suggested for the presence of fast rotation. Mass transfer also transports angular momentum, which results in spin-up of the mass-accreting star (Packet, 1981; de Mink et al., 2013; Matrozis et al., 2017). Similarly, mergers and stellar collisions are expected to yield rapidly rotating stars (Sills

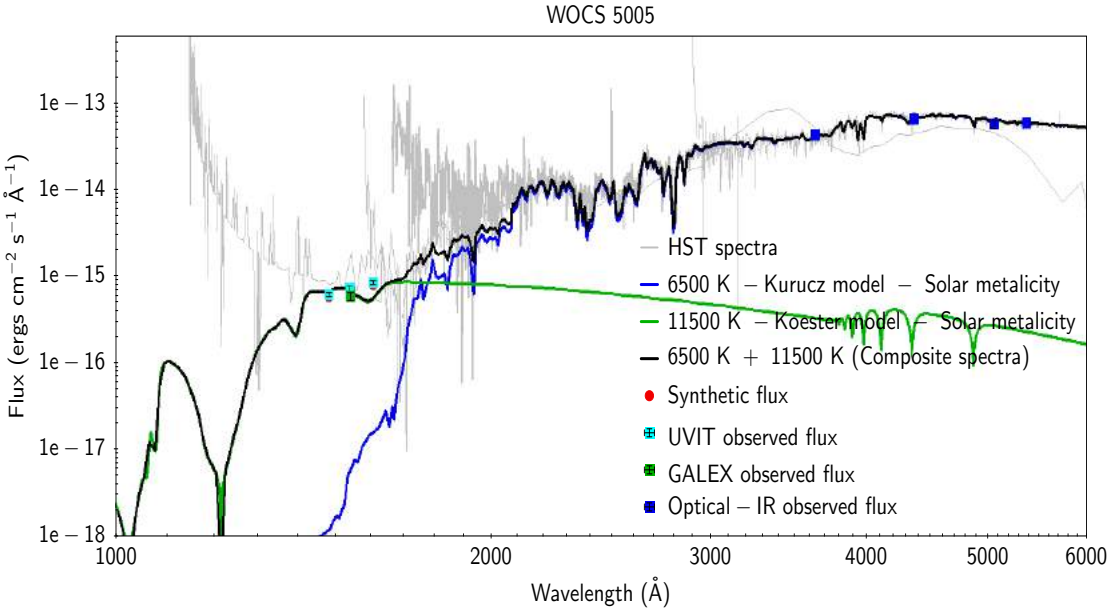

Fig. 7.17 The Extinction Corrected HST Spectra of WOCS 5005 Are Shown in Gray, Along with the Observed Fluxes shown as Square Points and Composite Flux Points are shown as Red Circles. The Theoretical Spectra of Kurucz Model is plotted in Blue. The Composite Spectra for WOCS 5005 is shown in Black and Theoretical Koester Spectra (log g = 7.75) is shown in Green

et al., 2001; Sills et al., 2005). Recently Leiner et al. (2018) demonstrated that post-mass transfer systems have rapid rotation rates soon after formation. They then spin down as they age, similar to the spin down of Solar-type MS stars. The large rotation of WOCS 1006 could be due to a merger, whereas the fast rotation of WOCS 1007, WOCS 2013, WOCS 3010, WOCS 3013 and WOCS 4006 could be due to a recent mass transfer. In fact, if we associate the T_{eff} of the WD as a proxy to the cooling age, we could expect a correlation between T_{eff} and Vsin$i$. We do find a good correlation such that, the BSS with the hottest WD, WOCS 4006 is the fastest rotator, whereas the slowest rotation is found for the BSS with the coolest WD (WOCS 5005) as seen from Fig. 7.18. The cooling age estimates suggest that the WDs of WOCS 4006 and WOCS 3013 are formed recently (40 - 70 Myr). Thus, we detect a good correlation here as well, which is suggestive of the spin of the BSS due to mass transfer.

Among the 6 BSSs with detected WD, only WOCS 1007 is a short period binary. The other BSSs have long periods ($\geq$ 1000 days) and non-circular orbits. WOCS 2013 has an orbit of 850 days and an eccentricity of 0.47, whereas WOCS 5005 has an orbit of 5153 days with an eccentricity of 0.357. Milone et al. (1991) found that WOCS 1007, WOCS 2013, WOCS 3010, WOCS 3013 and WOCS 5005 show radial velocity variations, where WOCS 2013 shows relatively less variations. They also showed that WOCS 3005 and WOCS 2011 do not show radial velocity variation. They also note that the velocity variations of WOCS 3010 and WOCS 5005 look like they are due to orbits with periods $>$ 1000 days, and with semi-amplitudes under 10 km s^{-1}. They

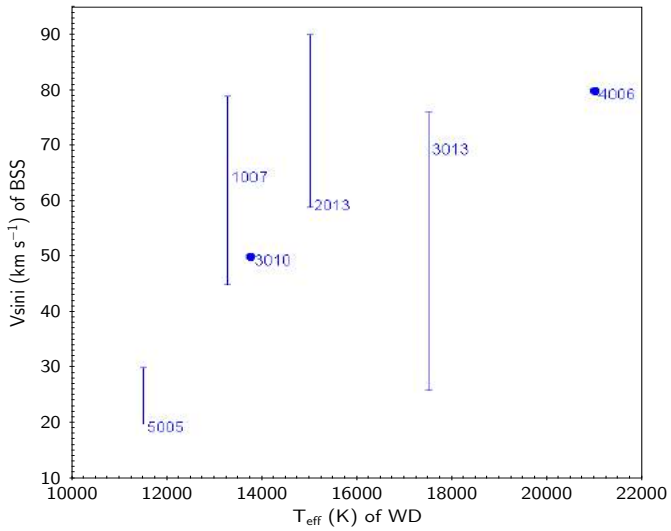

Fig. 7.18 A Plot of Rotation of the BSS vs. Effective Temperature of the WD companions are shown. The Lower and Upper Values of the vsin$i$ Available from the Literature (Table 7.4) are shown as the Error bars for Rotation.

suggest that these may be in the final slow stages of mass transfer. The results obtained in this study are in excellent agreement with the above findings. We detect possible WD companions to WOCS 1007, WOCS 2013, WOCS 3010, WOCS 3013 and WOCS 5005, whereas no such companions were detected for WOCS 2011 and WOCS3005.

7.5.1 Discussion

The summary of the finding can be found in the Table. 7.4. The last column in the table shows whether a candidate WD is detected. It can be seen that among the 7 group (a) BSSs, four are suspected to have WD companions. One is a short period binary, whereas two are $\sim$ 1000 day binaries. These systems are likely to have undergone mass transfer, resulting in the formation of the BSSs. We do not detect hot companions to the rest of the three BSSs. Thus, 57% of the group (a) BSS are suggested to be formed by mass tranfer. WOCS 4006 belongs to group (b) BSSs and its origin could be mass transfer. WOCS 5005 belongs to group (c), for which we detect a possible WD. Overall, we detect possible WD companion to 6 BSSs among the 9 studied (66.7%).

The mass of the WDs detected are < 0.4 M$_{\odot}$, suggesting that these are all low mass WDs. It is generally accepted that most low-mass He-core WDs are the result of binary star evolution (Panei et al., 2007), since an isolated star with low mass would take more than a Hubble time to evolve into a WD configuration. He-WDs would be the result of mass transfer episodes in close binary systems (Iben and Webbink, 1989; Iben and Webbink, 1989). Thus, the presence of low mass WDs in 6 BSSs directly implies that these are post-mass transfer systems. Thus 66.7% of BSSs in M67 are likely to have formed via mass transfer. This is a large fraction and therefore, mass transfer is

an important pathway to the formation of BSSs in M67. The rest could be formed due to mergers. We speculate that the BSS, WOCS 1006 (a rapid rotator), WOCS 2011 and WOCS 3005 are single stars, where the WD could have merged with the BSS to form a single star. In future, we plan to study the possible evolutionary pathways for the formation of these BSSs.

Lu et al. (2010) studied the formation BSSs via mass transfer in close binaries in M67. Detailed close binary evolutionary models were calculated, including both Cases A and B. They followed the evolution of a binary of 1.4 $M_{\odot}$ + 0.9 $M_{\odot}$ and compare the evolutionary behaviour of both cases. The end product of this close binary pair was found to be a 2.04 $M_{\odot}$ BSS with a 0.26 $M_{\odot}$ WD companion. This configuration is very similar to the group (a) BSSs as shown in Table 7.4. Thus, the group (a) BSSs, which are the luminous BSSs in M67 show a close resemblance and hence could originate from similar close binaries. They also argue that Case B is as important as Case A in forming BSSs. Also, BSSs formed through Case B are generally bluer and even more luminous than those produced by Case A. Their simulations suggest that among the luminous BSSs in M67, five BSSs could be formed through mass transfer, whereas another three by dynamical merger processes. This amounts to a fraction of 62.5% BSSs formation via mass transfer, which agrees very well with our detection of 66.7% of BSSs formed through mass transfer. Thus, we find an excellent agreement between our estimates and the simulations by Lu et al. (2010) to suggest that mass transfer through Case A/Case B is a major pathway for the formation of BSSs in M67.

7.6 Conclusion

Our analysis of the UVIT imaging for the open cluster M67 has allowed us to reach the following conclusion concerning the companions to 6 BSSs in this cluster. The old open cluster M67, well known for the presence of several BSSs, has been put to detailed tests to understand BSS formation pathways. Currently, there are three accepted formation channels: mass transfer due to RLOF in binary systems, and stellar mergers, either through coalescence of close binaries or due to dynamical collisions. So far, there has not been any confirmed detection of a WD companion to any of the BSSs in this cluster. Here, we present the first detection of possible WD companions to 6 bright BSSs in M67, imaged using FUV images from the UVIT. The multiwavelength SEDs covering 0.14 - 11.5 μm range, were found to require binary spectral fits to 6 BSSs, consisting of a cool (BSS) and a hot companion. The parameters (Luminosity,Temperature, Radius and Mass) of the hot companion suggest them to be low mass WDs, which are formed only in close binaries. This study suggests that at least 66.7% of the BSSs in M67 are formed due to mass transfer. We suggest that mass transfer is a significant pathway to the formation of BSSs in M67.

CHAPTER 8

Summary and Conclusion

8.1 Summary

Open clusters are excellent laboratories to study the single and binary evolution of stars as their parameters such as age, distance and reddening are known and hence their fundamental parameters such as temperature, luminosity can be estimated. In this thesis we have selected two open clusters NGC 188 and M67 as the stars in these clusters are well identified through proper motion and radial velocity membership studies. Both the clusters have higher binary fraction, exotic stellar types and are well studied in optical, IR, wavelength bands as well as a few studies in the X-ray. We have used images from UVIT on ASTROSAT, the first Indian space observatory along with other photometric data from 0.14 -11.5 m wavelength range for this study.

NGC 188 has a rich population of BSSs, with 20 BSSs to be confirmed members based on the radial velocity membership probability (Geller et al., 2008), Among these stars 7 BSSs were detected with WD companions formed through recent mass transfer; four BSS with hotter WD and three with cool WD companions. NGC 188 was observed as the first light object of UVIT on 2015 November 30. The data used in our analysis were obtained on 2016 January 26, observed in 4 FUV and 2 NUV filters of UVIT. The images were corrected for distortion, flat-field illumination and drift with a customized software package CCDLAB (Postma and Leahy, 2017). We corrected the images for background and saturation effects and performed aperture photometry.

We have detected WOCS 5885 star in the UVIT images, and is located at the inner region of the cluster NGC 188. This star is known be a single lined spectroscopic binary, and a rapid rotator. The location of the star in the optical CMD suggests it to be a BSS. A multi-wavelength SED of the star is constructed from 26 data points covering the wavelength range of 0.15 to 7.8 μm to characterise the temperature and evolutionary status. The cooler component is found to be a BSS with a temperature of 6000$\pm$ 150 K, whereas the hot component with a temperature estimate of 17000 $\pm$ 500 K is suggested to be a post-AGB/HB star based on its luminosity and radius. The parameters estimated from the SED suggest that the BSS is by a recent mass transfer from a post-AGB/HB star. This is a rare system with an hot post-AGB/HB star as a binary companion to a BSS to be identified in an open cluster.

The old open cluster M67 is an ideal laboratory to study single and binary stellar evolution due to its relative proximity, age, solar metallicity and the presence of rich single and binary member stars. The members of the cluster are well identified through numerous proper motion and radial velocity measurements of various spatial extent and limiting magnitudes (Sanders, 1977; Mathieu et al., 1986; Girard et al., 1989; Milone and Latham, 1994; Zhao et al., 1993; Yadav et al., 2008; Krone-Martins et al., 2010; Pasquini et al., 2011; Geller et al., 2015; Brucalassi et al., 2017). The cluster is well studied through photometry in several wavelength bands covering from the X-rays to the IR regions (Belloni et al., 1993; Belloni et al., 1998; Van den Berg et al., 2004; Landsman et al., 1997; Siegel et al., 2014; Mathieu and Latham, 1986; Sarajedini et al., 2009 and reference therein), and also a few stars are studied through spectroscopy (Mathieu et al., 1990; Shetrone and Sandquist, 2000; Bertelli Motta et al., 2018). The cluster has a rich population of exotic stellar types, that do not follow the standard single stellar evolutionary theory.

In the present study, we use GALEX photometric data in the FUV and NUV bands, as a deep study of the cluster in the UV region is lacking. We have cross-identified the member stars detected in both the bands with its optical counterparts from Montgomery et al. (1993). We have combined all the observations made by GALEX to obtain the UV magnitudes of 449 member stars of the cluster, with 92 stars in FUV and 424 stars in the NUV band. The CMDs shown in Fig. 5.4 and Fig.5.5 are first of its kind for this cluster and has been able to reveal interesting properties of various types of stars. A good fraction of the stars in the cluster seem to have excess flux in the UV as identified from theses CMDs. We have detected 16 BSSs in the FUV and 13 BSSs in the NUV band. Most of the FUV detected BSSs are bright and located 3-8 mag above the MSTO of the UV CMD. Apart from the BSSs, we have detected 3 WDs, 3 YSSs, 1 SSG, 2RGs, 3 triple system in the FUV and 2 WDs, 2 YSSs, 2 SSG and 1 triple system in the NUV. The detection of the RGs, particularly in the FUV band is intriguing, suggestive of an excess flux relative to the expected flux from the optical CMD. A comprehensive catalogue consisting of identification number, optical and UV magnitudes, X-ray detections along with known classification and comments for M67 is provided in the appendix.

We notice at least 15 stars (FUV bright stars) in the FUV-V CMD to be as bright as some of the BSSs itself. These stars are located on the MSTO in the optical CMD. An excess flux in the UV for these stars could be due to the FUV/NUV non-photospheric emission. We detect a few lower MS stars to have larger UV flux and they are located in the gap region of the FUV-V CMD. Therefore suggesting that they could be MS+WD binaries. We have identified 11 such systems, which are new identifications. The cluster sequence is clearly delineated in the NUV-V CMD. The MS, SG and RGB are clearly seen, where a very tight SG branch and a spread in the RGB are noticed. A number of

stars near and below the MSTO in the optical CMD are found to have excess flux in the NUV. As many of the stars are found to have excess UV flux, we study them further to understand the nature of these stars.

We analysed 45 interesting stars that were found to have excess flux in the UV. These include 17 BSSs, 15 FUV bright stars, 11 possible WD + MS binaries and 2 RGs. Multiwavelength SEDs are constructed for these stars with the observed flux from UV to IR region, and fitted with Kurucz models (Castelli et al., 1997). The fundamental parameters: T_{eff}, $L/L_{\odot}$ and $R/R_{\odot}$ are estimated for these stars. The BSSs have a large range in both T_{eff} ($\sim$ 6000 - 9000 K) and $L/L_{\odot}$ ($\sim$ 5 - 30) which are found to correlate well with the large range of FUV magnitudes, and they have small range in $R/R_{\odot}$ ($\sim$ 1.5 - 3.0). The estimated temperature compare well with those from the earlier studies. The FUV bright stars clearly show a certain amount of excess flux in the FUV as seen by fitting the SEDs. Our estimation of the fundamental parameters compare well those estimated with other methods for some of these FUV bright stars (Yakut et al., 2009; Peng et al., 2016). The FUV bright stars span a smaller range in the three parameters: T_{eff} ($\sim$ 5750 - 6750 K), $R/R_{\odot}$ ($\sim$ 1.0 - 2.5), and $L/L_{\odot}$ ($\sim$ 1.5 - 6.3), when compared to the BSSs.

In order understand the properties of BSSs as well as the FUV bright stars, we make use of the HRD and $L/L_{\odot}$ vs $R/R_{\odot}$ diagram. We use these diagrams to categorise the BSSs into three groups. The location of the BSSs are interpreted with the help of the isochrones overlaid on the HRD. The BSSs in M67 belong to a wide age range (400 Myr to 2.5 Gyr) based on the isochrones. The group (a) BSSs are found to be hotter, luminous and the youngest with an age range of 400 Myr - 1 Gyr, group (b) consists of BSSs that are hot though less luminous, whereas the group (c) BSSs are moderately luminous and relatively cooler and are as old as 2.5 Gyr. Therefore, the BSSs in M67 are more likely to be forming continuously in the 400 Myr - 2.5 Gyr duration. We used archival IUE spectra for five BSSs, which have FUV as well as NUV spectra. All these BSSs showed the Mg II *h*+*k* line in absorption. This is a clear indicator of absence or very low chromospheric activity for these stars. Thus, the excess UV emission in these is unlikely due to chromospheric activity. Among the FUV bright stars, based on the location on the HRD and $L/L_{\odot}$ vs $R/R_{\odot}$ diagram, four could be probable BSSs candidates. The excess flux in the FUV bright stars may be due to active chromosphere or a possible hot binary component.

The SED fits for the 11 possible WD+MS binaries detected excess flux in 7 of the stars. Therefore, these seven stars could be potential WD+MS binaries and progenitors of CVs. The temperature range of these MS stars are found to be in the range of 4000 - 5500 K. As the GALEX FUV band gives one data point in the FUV region of the SED, it is hard to characterize the hot component based on a single data point, even though the excess is very significant in a few cases. We also created SEDs for the

2 RGs which show excess FUV and NUV flux. The estimated temperature from the SED fit is $\sim$ 4000 K for the RGs. We found archival IUE spectra for these two RGs in the NUV region, which show the presence of Mg II *h*+*k* line in emission, a proxy to chromospheric activity (Pérez Martínez et al., 2011). Hence the excess flux in the UV is likely to be active chromosphere in these RGs.

The BSSs are very well known to be M67 cluster members, though the formation pathways of these stars are not well understood. Gosnell et al. (2015) detected 7 WD companions to the BSSs in NGC 188 using HST FUV data to provide the first direct evidence for mass transfer as the formation channel to these BSSs in the cluster. Theoretical models suggest several pathways for their formation, with two processes favoured in an open cluster environment: (i) mass transfer through RLOF in close binaries and (ii) merger of a close binary in a hierarchical triple system. M67 has a rich population of BSSs, with 14 BSSs as confirmed members through radial velocity measurements (Geller et al., 2015). Several attempts to study the formation pathways via chemical signatures of mass transfer on the BSSs have rendered no evidence. We observed the cluster using UVIT on ASTROSAT in three FUV filters, and we have detected 10 of 14 BSSs. We have analysed 9 BSSs in our study, as one of the star WOCS 2009 is well know to be a triple system (Van den Berg et al., 2001; Sandquist et al., 2003).

The SEDs for the 9 BSSs are constructed using multiwavelength photometric data from UV to IR region by including the data from UVIT, GALEX and IUE (for 3 BSSs). Seven of these stars show significant UV excess in their residual SEDs, suggesting a presence of a hot component for the BSSs. Therefore, a binary SED fit for the 7 BSSs is attempted using Koester WD models for the hot component and Kurucz model for the cool BSSs. A statistical test using χ^2 minimisation gives us the best binary fit for 6 BSSs. The estimated parameters of the hot component suggest them to be low mass WDs with T_{eff} in the range of 11000 - 24000 K and mass estimate of 0.2 - 0.3 $M_{\odot}$ from the HRD of the WDs. This is the first detection of the probable WD companions to BSSs in the cluster, apart from a few previous suggestions (Landsman et al., 1998; Shetrone and Sandquist, 2000; Milone and Latham, 1992).

The presence of a low mass-WD companions suggest that the formation of the 6 BSSs is likely due to mass transfer, as an isolated low-mass WD would take more than a Hubble time to evolve into a WD phase. Thus 66.7% of BSSs in M67 are likely to be formed via binary mass transfer, implying that it is an important pathway for the formation of BSSs in M67.

8.2 Conclusion

The main conclusion of this thesis are:
This study has made use of multiwavelength data to study the properties and evolution of stars in two old open clusters: NGC 188 and M67. We have observed these clusters using UVIT and combined with the photometric data from 0.14 to 11.5 μm taken from several ground and space based observatories.

1. The study demonstrates the capability of UVIT to detect and characterise binaries with hot companions, particularly the BSSs, with the discovery of one BSS with post-AGB/HB companion in NGC 188 and detection of 6 BSSs with possible WD companions in M67.

2. The BSS in NGC 188 is formed as a result of recent mass transfer from a post-AGB/HB star suggested from the estimated parameters. This is a rare system and is first of its kind to be identified in an open cluster.

3. A deep-UV study of M67 was performed to reveal the presence of a large number of stars to have excess flux in the FUV and NUV, which could be due to their active chromosphere. Thus we suggest that a large number of Sun-like stars in the cluster are chromospherically active.

4. We have detected a few lower MS stars in M67 to have a large UV excess, suggesting them to be WD+MS binaries. Seven of the eleven systems identified are found to have FUV excess. These stars could be potential progenitors of CVs. We also suggest that there could be many such WDs locked up in binaries in M67.

5. We detect 2 RGs with excess flux in the UV as well as Mg II h+k emission line in the IUE spectra. A few other RG stars are found to have Mg II h+k emission line. Therefore, we conclude that good fraction of RGs in M67 could be chromospherically active.

6. We have created multiwavelength SEDs of 45 interesting stars in M67 and estimated their fundamental parameters. Based on the Luminosity and Temperature, the BSS are divided into three groups in M67.

7. We detected 6 BSSs in M67 to have WD companions. These BSSs are formed via mass transfer episodes, as the WD companions are of very low mass. Therefore, mass transfer is a significant pathway for the formation of BSSs in M67, as 66.7% of BSS are detected to have low mass WD companions. .

8.3 Future Work

In this study, we are able to detect the hot companions to BSSs using the UVIT. These detections suggested mass transfer as the important pathway for the formation of BSSs in the two studied open clusters. Some of the future studies planned are listed below:

1. We plan to study BSSs in other open clusters to understand their formation pathway. We have already observed up to 10 open clusters which are older than 1 Gyr with UVIT. Apart from the BSSs, we shall study their UV and UV−optical CMDs of these open clusters, identify interesting stars with excess UV flux, followed by studies using multiwavelength SED analysis.

2. The hot companion to the BSS in NGC 188 studied here, is suggested as post-AGB/HB star. We plan to study the spectrum of the star in FUV, obtained by Far Ultraviolet Spectroscopic Explorer (FUSE) to check its evolutionary state. We also plan to study the optical/IR high resolution spectra of this star for signatures of chemical enrichment.

3. We plan to obtain high resolution spectra of the 6 BSSs with WD companions, to study their chemical compositions. We also plan to obtain the UV spectra of these stars using the UVIT.

4. We have performed a deeper observation of M67 using UVIT in multiple FUV filters. We plan to detect WD+MS binary stars with these observations and characterise them. Single WD members of M67 will also be studied using these images.

5. Many stars in M67 show FUV/NUV excess as well as X-ray emission. As we know the evolutionary stage of these stars, we plan to perform an X-ray vs UV flux/Luminosity correlation study to understand the emission mechanisms in these stars.

REFERENCES

Ahumada, J. A. and Lapasset, E. (2007), 'New catalogue of blue stragglers in open clusters', *Astronomy and Astrophysics* **463**, 789–797.

Ambartsumian, V. A. (1947), ' In Stellar Evolution and Astrophysics,', *Armenian Acad. of Sci.* .

Aschenbach, B. (1988), 'Design, construction, and performance of the Rosat high-resolution X-ray mirror assembly', *Applied Optics* **27**, 1404–1413.

Barnes, S. A., Weingrill, J., Fritzewski, D., Strassmeier, K. G. and Platais, I. (2016), 'Rotation periods for cool stars in the 4 Gyr old open cluster M67, The Solar-stellar connection, and the applicability of gyrochronology to at least Solar age', *Astrophysical Journal* **823**, 16–31.

Bayo, A., Rodrigo, C., Barrado Y Navascués, D., Solano, E., Gutiérrez, R., Morales-Calderón, M. and Allard, F. (2008), 'VOSA: virtual observatory SED analyzer. An application to the Collinder 69 open cluster', *Astronomy and Astrophysics* **492**, 277–287.

Belloni, T., Verbunt, F. and Mathieu, R. D. (1998), 'X-rays from old open clusters: M 67 and NGC 188', *Astronomy and Astrophysics* **339**, 431–439.

Belloni, T., Verbunt, F. and Schmitt, J. H. M. M. (1993), 'ROSAT detection of stellar X-ray sources in the old open cluster M 67', *Astronomy and Astrophysics* **269**, 175–180.

Bertelli Motta, C., Pasquali, A., Caffau, E. and Grebel, E. K. (2018), 'A chemical study of M67 candidate blue stragglers and evolved blue stragglers observed with APOGEE DR14', *Monthly Notices of the Royal Astronomical Society* **480**, 4314–4326.

Bianchi, L. (2009), 'The Ultraviolet sky surveys: filling the gap in our view of the Universe', *Astrophysics and Space Science* **320**, 11–19.

Bianchi, L. (2011), 'GALEX and star formation', *Astrophysics and Space Science* **335**, 51–60.

Bianchi, L. (2014), 'The Galaxy Evolution Explorer (GALEX). Its legacy of UV surveys, and science highlights', *Astrophysics and Space Science* **354**, 103–112.

Bianchi, L., Efremova, B., Herald, J., Girardi, L., Zabot, A., Marigo, P. and Martin, C. (2011), 'Catalogues of hot white dwarfs in the Milky Way from GALEX's ultraviolet sky surveys: constraining stellar evolution', *Monthly Notices of the Royal Astronomical Society* **411**, 2770–2791.

Binney, J. and Merrifield, M. (1998), *Galactic Astronomy*.

Boggess, A., Carr, F. A., Evans, D. C., Fischel, D., Freeman, H. R., Fuechsel, C. F., Klinglesmith, D. A., Krueger, V. L., Longanecker, G. W. and Moore, J. V. (1978), 'The IUE spacecraft and instrumentation', *Nature* **275**, 372–377.

Bonatto, C., Bica, E. and Santos, Jr., J. F. C. (2005), 'Spatial dependence of 2MASS luminosity and mass functions in the old open cluster NGC 188', *Astronomy and Astrophysics* **433**, 917–929.

Bonatto, C., Campos, F., Kepler, S. O. and Bica, E. (2015), 'Extracting parameters from colour - magnitude diagrams', *Monthly Notices of the Royal Astronomical Society* **450**(3), 2500–2505.

Bowers L, R. and Deeming, T. (1984), *Astrophysics 1:Stars*.

Bressan, A., Marigo, P., Girardi, L., Salasnich, B., Dal Cero, C., Rubele, S. and Nanni, A. (2012), 'PARSEC: stellar tracks and isochrones with the PAdova and TRieste Stellar Evolution Code', *Monthly Notices of the Royal Astronomical Society* **427**, 127–145.

Briel, U. G. and Pfeffermann, E. (1995), ROSAT position-sensitive proportional counter and its in-orbit performance, *in* 'Proceedings of the Society of Photo-Optical Instrumentation Engineers', pp. 120–131.

Brucalassi, A., Koppenhoefer, J., Saglia, R., Pasquini, L., Ruiz, M. T., Bonifacio, P., Bedin, L. R., Libralato, M., Biazzo, K., Melo, C., Lovis, C. and Randich, S. (2017), 'Search for giant planets in M 67. IV. Survey results', *Astronomy and Astrophysics* **603**, A85–100.

Brucalassi, A., Pasquini, L., Saglia, R., Ruiz, M. T., Bonifacio, P., Bedin, L. R., Biazzo, K., Melo, C., Lovis, C. and Randich, S. (2014), 'Three planetary companions around M 67 stars', *Astronomy and Astrophysics* **561**, L9– L15.

Bruntt, H., Stello, D., Suárez, J. C., Arentoft, T., Bedding, T. R., Bouzid, M. Y., Csubry, Z., Dall, T. H., Dind, Z. E., Frandsen, S., Gilliland, R. L., Jacob, A. P., Jensen, H. R., Kang, Y. B., Kim, S.-L., Kiss, L. L., Kjeldsen, H., Koo, J.-R., Lee, J.-A., Lee, C.-U., Nuspl, J., Sterken, C. and Szabó, R. (2007), 'Multisite campaign on the open cluster M67 - III. δ Scuti pulsations in the blue stragglers', *Monthly Notices of the Royal Astronomical Society* **378**, 1371–1384.

Calzetti, D., Armus, L., Bohlin, R. C., Kinney, A. L., Koornneef, J. and Storchi-Bergmann, T. (2000), 'The dust content and opacity of actively star-forming galaxies', *Astrophysical Journal* **533**, 682–695.

Camarota, L. and Holberg, J. B. (2014), 'White-dwarf-based evaluation of the GALEX absolute calibration', *Monthly Notices of the Royal Astronomical Society* **438**, 3111–3118.

Cannon, R. D. (2015), *Ecology of Blue Straggler Stars*, Springer Publications.

Caputo, F., Chieffi, A., Castellani, V., Collados, M., Martinez Roger, C. and Paez, E. (1990), 'CCD photometry of stars in the old open cluster NGC 188', *Astronomical Journal* **99**, 261–272.

Cardelli, J. A., Clayton, G. C. and Mathis, J. S. (1989), 'The relationship between infrared, optical, and ultraviolet extinction', *Astrophysical Journal* **345**, 245–256.

Carroll, B. W. and Ostlie, D. A. (2006), *An introduction to modern astrophysics and cosmology*.

Castelli, F., Gratton, R. G. and Kurucz, R. L. (1997), 'Notes on the convection in the ATLAS9 model atmospheres', *Astronomy and Astrophysics* **318**, 841–869.

Chen, X., Deng, L., de Grijs, R., Zhang, X., Xin, Y., Wang, K., Luo, C., Yan, Z., Tian, J., Sun, J., Liu, Q., Zhou, Q. and Luo, Z. (2016), 'Physical parameter study of eight W Ursae Majoris-type contact binaries in NGC 188', *Astronomical Journal* **152**, 129–141.

Chen, X. and Han, Z. (2008), Blue stragglers from primordial binary evolution, *in* 'IAU Symposium -252', pp. 417–418.

Chen, Y., Girardi, L., Bressan, A., Marigo, P., Barbieri, M. and Kong, X. (2014), 'Improving parsec models for very low mass stars', *Monthly Notices of the Royal Astronomical Society* **444**(3), 2525–2543.

Cohen, M., Wheaton, W. A. and Megeath, S. T. (2003), 'Spectral irradiance calibration in the infrared. XIV. The absolute calibration of 2MASS', *Astronomical Journal* **126**, 1090–1096.

Conroy, C. and Gunn, J. E. (2010), 'The propagation of uncertainties in stellar population synthesis modeling. III. Model calibration, comparison, and evaluation', *Astrophysical Journal* **712**, 833–857.

Conroy, C., Gunn, J. E. and White, M. (2009), 'The propagation of uncertainties in stellar population synthesis modeling. I. The relevance of uncertain aspects of stellar

evolution and the initial mass function to the derived physical properties of galaxies', *Astrophysical Journal* **699**, 486–506.

Cordier, D., Pietrinferni, A., Cassisi, S. and Salaris, M. (2007), 'A large stellar evolution database for population synthesis studies. III. Inclusion of the full asymptotic giant branch phase and web tools for stellar population analyses', *Astronomical Journal* **133**, 468–478.

Davenport, J. R. A. and Sandquist, E. L. (2010), 'Death of a cluster: The destruction of m67 as seen by the sloan digital sky survey', *Astrophysical Journal* **711**(2), 559 –572.

de Loore, C. and Doom, C. (1992), *Structure and Evolution of Single and Binary Stars*.

de Mink, S. E., Langer, N., Izzard, R. G., Sana, H. and de Koter, A. (2013), 'The Rotation Rates of Massive Stars: The Role of Binary Interaction through Tides, Mass Transfer, and Mergers', *Astrophysical Journal* **764**, 166–182.

Deng, L., Chen, R., Liu, X. S. and Chen, J. S. (1999), 'The blue stragglers in M67 and single-population synthesis', *Astrophysical Journal* **524**, 824–830.

Dieball, A., Long, K. S., Knigge, C., Thomson, G. S. and Zurek, D. R. (2010), 'A far-ultraviolet survey of m80: X-ray source counterparts, strange blue stragglers, and the recovery of nova tsco', *Astrophysical Journal* **710**(1), 332 –345.

Dieball, A., Rasekh, A., Knigge, C., Shara, M. and Zurek, D. (2017), 'Far-ultraviolet observation of the globular cluster ngc 6397', *Monthly Notices of the Royal Astronomical Society* **469**(1), 267–277.

Dinescu, D. I., Demarque, P., Guenther, D. B. and Pinsonneault, M. H. (1995), 'The ages of the disk clusters NGC 188, M67, and NGC 752, using improved opacities and cluster membership data', *Astronomical Journal* **109**, 2090–2095.

Dinescu, D. I., Girard, T. M., van Altena, W. F., Yang, T.-G. and Lee, Y.-W. (1996), 'A proper-motion membership study of the old open cluster NGC 188', *Astronomical Journal* **111**, 1205 –1219.

Dziembowski, W. A., Gough, D. O., Houdek, G. and Sienkiewicz, R. (2001), 'Oscillations of α UMa and other red giants', *Monthly Notices of the Royal Astronomical Society* **328**, 601–610.

Eggleton, P. P. (1983), 'Approximations to the radii of Roche lobes', *Astrophysical Journal* **268**, 368–369.

Eker, Z., Soydugan, F., Soydugan, E., Bilir, S., Yaz Gökçe, E., Steer, I., Tüysüz, M., Şenyüz, T. and Demircan, O. (2015), 'Main-sequence effective temperatures from a revised mass-luminosity relation based on accurate properties', *Astronomical Journal* **149**, 131–143.

Fan, X., Burstein, D., Chen, J.-S., Zhu, J., Jiang, Z., Wu, H., Yan, H., Zheng, Z., Zhou, X., Fang, L.-Z., Chen, F., Deng, Z., Chu, Y., Hester, J. J., Windhorst, R. A., Li, Y., Lu, P., Sun, W.-H., Chen, W.-P., Tsay, W.-S., Chiueh, T.-H., Chou, C.-K., Ko, C.-M., Lin, T.-C., Guo, H.-J. and Byun, Y.-I. (1996), 'Deep wide-field spectrophotometry of the open cluster M67', *Astronomical Journal* **112**, 628– 648.

Fazio, G. G., Hora, J. L., Allen, L. E., Ashby, M. L. N., Barmby, P., Deutsch, L. K., Huang, J.-S., Kleiner, S., Marengo, M., Megeath, S. T., Melnick, G. J., Pahre, M. A., Patten, B. M., Polizotti, J., Smith, H. A., Taylor, R. S., Wang, Z., Willner, S. P., Hoffmann, W. F., Pipher, J. L., Forrest, W. J., McMurty, C. W., McCreight, C. R., McKelvey, M. E., McMurray, R. E., Koch, D. G., Moseley, S. H., Arendt, R. G., Mentzell, J. E., Marx, C. T., Losch, P., Mayman, P., Eichhorn, W., Krebs, D., Jhabvala, M., Gezari, D. Y., Fixsen, D. J., Flores, J., Shakoorzadeh, K., Jungo, R., Hakun, C., Workman, L., Karpati, G., Kichak, R., Whitley, R., Mann, S., Tollestrup, E. V., Eisenhardt, P., Stern, D., Gorjian, V., Bhattacharya, B., Carey, S., Nelson, B. O., Glaccum, W. J., Lacy, M., Lowrance, P. J., Laine, S., Reach, W. T., Stauffer, J. A., Surace, J. A., Wilson, G., Wright, E. L., Hoffman, A., Domingo, G. and Cohen, M. (2004), 'The Infrared Array Camera (IRAC) for the Spitzer Space Telescope', *Astrophysical Journal Supplement* **154**, 10–17.

Fitzpatrick, E. L. (1999), 'Correcting for the effects of interstellar extinction', *Publications of the Astronomical Society of the Pacific* **111**, 63–75.

Fleming, T. A., Liebert, J., Bergeron, P. and Beauchamp, A. (1997), White dwarfs in M67, *in* 'Astrophysics and Space Science Library', pp. 91–96.

Fornal, B., Tucker, D. L., Smith, J. A., Allam, S. S., Rider, C. J. and Sung, H. (2007), 'A Survey of open Clusters in the u'g'r'i'z' filter system. III. Results for the cluster NGC 188', *Astronomical Journal* **133**, 1409–1420.

Friel, E. D. (1995), 'The old open clusters of The milky way', *Annual Review of Astronomy and Astrophysics* **33**, 381–414.

Friel, E. D., Jacobson, H. R. and Pilachowski, C. A. (2010), 'Abundances of red giants in old open clusters. V. Be 31, Be 32, Be 39, M 67, NGC 188, and NGC 1193', *Astronomical Journal* **139**, 1942–1967.

Friel, E. D., Janes, K. A., Tavarez, M., Scott, J., Katsanis, R., Lotz, J., Hong, L. and Miller, N. (2002), 'Metallicities of old open clusters', *Astronomical Journal* **124**, 2693–2720.

Gaia Collaboration, Brown, A. G. A., Vallenari, A., Prusti, T., de Bruijne, J. H.J., Mignard, F., Drimmel, R., Babusiaux, C., Bailer-Jones, C. A.L., Bastian, U., Biermann, M., Evans, D. W., Eyer, L., Jansen, F., Jordi, C., Katz, D., Klioner, S. A., Lammers, U., Lindegren, L., Luri, X., O´Mullane, W., Panem, C., Pourbaix, D., Randich, S., Sartoretti, P., Siddiqui, H. I., Soubiran, C., Valette, V., van Leeuwen, F., Walton, N. A., Aerts, C., Arenou, F., Cropper, M., Høg, E., Lattanzi, M. G., Grebel, E. K., Holland, A. D., Huc, C., Passot, X., Perryman, M., Bramante, L., Cacciari, C., Castañeda, J., Chaoul, L., Cheek, N., De Angeli, F., Fabricius, C., Guerra, R., Hernández, J., Jean-Antoine-Piccolo, A., Masana, E., Messineo, R., Mowlavi, N., Nienartowicz, K., Ordóñez-Blanco, D., Panuzzo, P., Portell, J., Richards, P. J., Riello, M., Seabroke, G. M., Tanga, P., Thévenin, F., Torra, J., Els, S. G., Gracia-Abril, G., Comoretto, G., Garcia-Reinaldos, M., Lock, T., Mercier, E., Altmann, M., Andrae, R., Astraatmadja, T. L., Bellas-Velidis, I., Benson, K., Berthier, J., Blomme, R., Busso, G., Carry, B., Cellino, A., Clementini, G., Cowell, S., Creevey, O., Cuypers, J., Davidson, M., De Ridder, J., de Torres, A., Delchambre, L., Dell´Oro, A., Ducourant, C., Frémat, Y., García-Torres, M., Gosset, E., Halbwachs, J.-L., Hambly, N. C., Harrison, D. L., Hauser, M., Hestroffer, D., Hodgkin, S. T., Huckle, H. E., Hutton, A., Jasniewicz, G., Jordan, S., Kontizas, M., Korn, A. J., Lanzafame, A. C., Manteiga, M., Moitinho, A., Muinonen, K., Osinde, J., Pancino, E., Pauwels, T., Petit, J.-M., Recio-Blanco, A., Robin, A. C., Sarro, L. M., Siopis, C., Smith, M., Smith, K. W., Sozzetti, A., Thuillot, W., van Reeven, W., Viala, Y., Abbas, U., Abreu Aramburu, A., Accart, S., Aguado, J. J., Allan, P. M., Allasia, W., Altavilla, G., Álvarez, M. A., Alves, J., Anderson, R. I., Andrei, A. H., Anglada Varela, E., Antiche, E., Antoja, T., Antón, S., Arcay, B., Bach, N., Baker, S. G., Balaguer-Núñez, L., Barache, C., Barata, C., Barbier, A., Barblan, F., Barrado y Navascués, D., Barros, M., Barstow, M. A., Becciani, U., Bellazzini, M., Bello García, A., Belokurov, V., Bendjoya, P., Berihuete, A., Bianchi, L., Bienaymé, O., Billebaud, F., Blagorodnova, N., Blanco-Cuaresma, S., Boch, T., Bombrun, A., Borrachero, R., Bouquillon, S., Bourda, G., Bouy, H., Bragaglia, A., Breddels, M. A., Brouillet, N., Brüsemeister, T., Bucciarelli, B., Burgess, P., Burgon, R., Burlacu, A., Busonero, D., Buzzi, R., Caffau, E., Cambras, J., Campbell, H., Cancelliere, R., Cantat-Gaudin, T., Carlucci, T., Carrasco, J. M., Castellani, M., Charlot, P., Charnas, J., Chiavassa, A., Clotet, M., Cocozza, G., Collins, R. S., Costigan, G., Crifo, F., Cross, N. J.G., Crosta, M., Crowley, C., Dafonte, C., Damerdji, Y., Dapergolas, A., David, P., David, M., De Cat, P., de Felice, F., de Laverny, P., De Luise, F., De March, R., de Martino, D., de Souza, R., Debosscher, J., del Pozo, E., Delbo, M., Delgado, A.,

Delgado, H. E., Di Matteo, P., Diakite, S., Distefano, E., Dolding, C., Dos Anjos, S., Drazinos, P., Duran, J., Dzigan, Y., Edvardsson, B., Enke, H., Evans, N. W., Eynard Bontemps, G., Fabre, C., Fabrizio, M., Faigler, S., Falcão, A. J., Farràs Casas, M., Federici, L., Fedorets, G., Fernández-Hernández, J., Fernique, P., Fienga, A., Figueras, F., Filippi, F., Findeisen, K., Fonti, A., Fouesneau, M., Fraile, E., Fraser, M., Fuchs, J., Gai, M., Galleti, S., Galluccio, L., Garabato, D., García-Sedano, F., Garofalo, A., Garralda, N., Gavras, P., Gerssen, J., Geyer, R., Gilmore, G., Girona, S., Giuffrida, G., Gomes, M., González-Marcos, A., González-Núñez, J., González-Vidal, J. J., Granvik, M., Guerrier, A., Guillout, P., Guiraud, J., Gúrpide, A., Gutiérrez-Sánchez, R., Guy, L. P., Haigron, R., Hatzidimitriou, D., Haywood, M., Heiter, U., Helmi, A., Hobbs, D., Hofmann, W., Holl, B., Holland, G., Hunt, J. A.S., Hypki, A., Icardi, V., Irwin, M., Jevardat de Fombelle, G., Jofré, P., Jonker, P. G., Jorissen, A., Julbe, F., Karampelas, A., Kochoska, A., Kohley, R., Kolenberg, K., Kontizas, E., Koposov, S. E., Kordopatis, G., Koubsky, P., Krone-Martins, A., Kudryashova, M., Kull, I., Bachchan, R. K., Lacoste-Seris, F., Lanza, A. F., Lavigne, J.-B., Le Poncin-Lafitte, C., Lebreton, Y., Lebzelter, T., Leccia, S., Leclerc, N., Lecoeur-Taibi, I., Lemaitre, V., Lenhardt, H., Leroux, F., Liao, S., Licata, E., Lindstrøm, H. E.P., Lister, T. A., Livanou, E., Lobel, A., Löffler, W., López, M., Lorenz, D., MacDonald, I., Magalhães Fernandes, T., Managau, S., Mann, R. G., Mantelet, G., Marchal, O., Marchant, J. M., Marconi, M., Marinoni, S., Marrese, P. M., Marschalkó, G., Marshall, D. J., Martín-Fleitas, J. M., Martino, M., Mary, N., Matijevic, G., Mazeh, T., McMillan, P. J., Messina, S., Michalik, D., Millar, N. R., Miranda, B. M. H., Molina, D., Molinaro, R., Molinaro, M., Molnár, L., Moniez, M., Montegriffo, P., Mor, R., Mora, A., Morbidelli, R., Morel, T., Morgenthaler, S., Morris, D., Mulone, A. F., Muraveva, T., Musella, I., Narbonne, J., Nelemans, G., Nicastro, L., Noval, L., Ordénovic, C., Ordieres-Meré, J., Osborne, P., Pagani, C., Pagano, I., Pailler, F., Palacin, H., Palaversa, L., Parsons, P., Pecoraro, M., Pedrosa, R., Pentikäinen, H., Pichon, B., Piersimoni, A. M., Pineau, F.-X., Plachy, E., Plum, G., Poujoulet, E., Prsa, A., Pulone, L., Ragaini, S., Rago, S., Rambaux, N., Ramos-Lerate, M., Ranalli, P., Rauw, G., Read, A., Regibo, S., Reylé, C., Ribeiro, R. A., Rimoldini, L., Ripepi, V., Riva, A., Rixon, G., Roelens, M., Romero-Gómez, M., Rowell, N., Royer, F., Ruiz-Dern, L., Sadowski, G., Sagristà Sellés, T., Sahlmann, J., Salgado, J., Salguero, E., Sarasso, M., Savietto, H., Schultheis, M., Sciacca, E., Segol, M., Segovia, J. C., Segransan, D., Shih, I.-C., Smareglia, R., Smart, R. L., Solano, E., Solitro, F., Sordo, R., Soria Nieto, S., Souchay, J., Spagna, A., Spoto, F., Stampa, U., Steele, I. A., Steidelmüller, H., Stephenson, C. A., Stoev, H., Suess, F. F., Süveges, M., Surdej, J., Szabados, L., Szegedi-Elek, E., Tapiador, D., Taris, F., Tauran, G., Taylor, M. B., Teixeira, R., Terrett, D., Tingley, B., Trager, S. C., Turon, C., Ulla, A., Utrilla, E., Valentini, G., van Elteren, A., Van Hemelryck, E., van Leeuwen, M., Varadi, M., Vecchiato, A., Veljanoski, J., Via, T., Vicente, D., Vogt, S., Voss, H., Votruba, V., Voutsinas, S., Walmsley, G.,

Weiler, M., Weingrill, K., Wevers, T., Wyrzykowski, L., Yoldas, A., Zerjal, M., Zucker, S., Zurbach, C., Zwitter, T., Alecu, A., Allen, M., Allende Prieto, C., Amorim, A., Anglada-Escudé, G., Arsenijevic, V., Azaz, S., Balm, P., Beck, M., Bernstein, H.-H., Bigot, L., Bijaoui, A., Blasco, C., Bonfigli, M., Bono, G., Boudreault, S., Bressan, A., Brown, S., Brunet, P.-M., Bunclark, P., Buonanno, R., Butkevich, A. G., Carret, C., Carrion, C., Chemin, L., Chéreau, F., Corcione, L., Darmigny, E., de Boer, K. S., de Teodoro, P., de Zeeuw, P. T., Delle Luche, C., Domingues, C. D., Dubath, P., Fodor, F., Frézouls, B., Fries, A., Fustes, D., Fyfe, D., Gallardo, E., Gallegos, J., Gardiol, D., Gebran, M., Gomboc, A., Gómez, A., Grux, E., Gueguen, A., Heyrovsky, A., Hoar, J., Iannicola, G., Isasi Parache, Y., Janotto, A.-M., Joliet, E., Jonckheere, A., Keil, R., Kim, D.-W., Klagyivik, P., Klar, J., Knude, J., Kochukhov, O., Kolka, I., Kos, J., Kutka, A., Lainey, V., LeBouquin, D., Liu, C., Loreggia, D., Makarov, V. V., Marseille, M. G., Martayan, C., Martinez-Rubi, O., Massart, B., Meynadier, F., Mignot, S., Munari, U., Nguyen, A.-T., Nordlander, T., Ocvirk, P., O´Flaherty, K. S., Olias Sanz, A., Ortiz, P., Osorio, J., Oszkiewicz, D., Ouzounis, A., Palmer, M., Park, P., Pasquato, E., Peltzer, C., Peralta, J., Péturaud, F., Pieniluoma, T., Pigozzi, E., Poels, J., Prat, G., Prod´homme, T., Raison, F., Rebordao, J. M., Risquez, D., Rocca-Volmerange, B., Rosen, S., Ruiz-Fuertes, M. I., Russo, F., Sembay, S., Serraller Vizcaino, I., Short, A., Siebert, A., Silva, H., Sinachopoulos, D., Slezak, E., Soffel, M., Sosnowska, D., Straizys, V., ter Linden, M., Terrell, D., Theil, S., Tiede, C., Troisi, L., Tsalmantza, P., Tur, D., Vaccari, M., Vachier, F., Valles, P., Van Hamme, W., Veltz, L., Virtanen, J., Wallut, J.-M., Wichmann, R., Wilkinson, M. I., Ziaeepour, H. and Zschocke, S. (2016), 'Gaia data release 1 - summary of the astrometric, photometric, and survey properties', *Astronomy and Astrophysics* **595**, A2–24.

Geller, A. M., Hurley, J. R. and Mathieu, R. D. (2013), 'Direct N-body modeling of the old open cluster NGC 188: A detailed comparison of theoretical and observed binary star and blue straggler populations', *Astronomical Journal* **145**, 8–29.

Geller, A. M., Latham, D. W. and Mathieu, R. D. (2015), 'Stellar Radial Velocities in the Old Open Cluster M67 (NGC 2682). I. Memberships, Binaries, and Kinematics', *Astronomical Journal* **150**, 97–114.

Geller, A. M., Leiner, E. M., Bellini, A., Gleisinger, R., Haggard, D., Kamann, S., Leigh, N. W. C., Mathieu, R. D., Sills, A., Watkins, L. L. and Zurek, D. (2017), 'On the origin of sub-subgiant stars. I. Demographics', *Astrophysical Journal* **840**, 66.

Geller, A. M. and Mathieu, R. D. (2011), 'A mass transfer origin for blue stragglers in NGC 188 as revealed by half-solar-mass companions', *Nature* **478**, 356–359.

Geller, A. M. and Mathieu, R. D. (2012), 'WIYN open cluster study. XLVIII. The hard-binary population of NGC 188', *Astronomical Journal* **144**, 54–73.

Geller, A. M., Mathieu, R. D., Harris, H. C. and McClure, R. D. (2008), 'WIYN open cluster study. XXXII. Stellar radial velocities in the old open cluster NGC 188', *Astronomical Journal* **135**, 2264–2278.

Geller, A. M., Mathieu, R. D., Harris, H. C. and McClure, R. D. (2009), 'WIYN open cluster study. XXXVI. Spectroscopic binary orbits in NGC 188', *Astronomical Journal* **137**, 3743–3760.

George, K., Joseph, P., Mondal, C., Devaraj, A., Subramaniam, A., Stalin, C. S., Côté, P., Ghosh, S. K., Hutchings, J. B., Mohan, R., Postma, J., Sankarasubramanian, K., Sreekumar, P. and Tandon, S. N. (2018), 'UVIT observations of the star-forming ring in NGC 7252: Evidence of possible AGN feedback suppressing central star formation', *Astronomy and Astrophysics* **613**, L9–13.

Gilliland, R. L. and Brown, T. M. (1992), 'The oscillating blue stragglers in the open cluster M67', *Astronomical Journal* **103**, 1945–1954.

Girard, T. M., Grundy, W. M., Lopez, C. E. and van Altena, W. F. (1989), 'Relative proper motions and the stellar velocity dispersion of the open cluster M67', *Astronomical Journal* **98**, 227–243.

Girardi, L., Bressan, A., Bertelli, G. and Chiosi, C. (2000), 'Evolutionary tracks and isochrones for low- and intermediate-mass stars: From 0.15 to 7 M_{sun}, and from Z=0.0004 to 0.03', *Astronomy and Astrophysics Supplement Series* **141**, 371–383.

Girish, V., Tandon, S. N., Sriram, S., Kumar, A. and Postma, J. (2017), 'Mapping distortion of detectors in UVIT onboard AstroSat observatory', *Experimental Astronomy* **43**, 59–74.

Glebbeek, E. and Pols, O. R. (2008), 'Evolution of stellar collision products in open clusters. II. A grid of low-mass collisions', *Astronomy and Astrophysics* **488**, 1017–1025.

Gökay, G., Gürol, B. and Derman, E. (2013), 'Multiband photometric and spectroscopic analysis of HV Cnc', *Astronomical Journal* **146**, 123–130.

Gondoin, P. (2005), 'X-ray observations of the old open stellar cluster NGC 188', *Astronomy and Astrophysics* **438**, 291–300.

Gonzalez, G. (2016*a*), 'A revised gyro-age for M67 from Kepler/K2-Campaign-5 light curves', *Monthly Notices of the Royal Astronomical Society* **463**, 3513–3519.

Gonzalez, G. (2016*b*), 'Variability among stars in the M 67 field from Kepler/K2-Campaign-5 light curves', *Monthly Notices of the Royal Astronomical Society* **459**, 1060–1068.

Gosnell, N. M., Mathieu, R. D., Geller, A. M., Sills, A., Leigh, N. and Knigge, C. (2015), 'Implications for the formation of blue straggler stars from HST ultraviolet observations of NGC 188', *Astrophysical Journal* **814**, 163–174.

Güdel, M. and Telleschi, A. (2007), 'The X-ray soft excess in classical T Tauri stars', *Astronomy and Astrophysics* **474**, L25–L28.

Haurberg, N. C., Lubell, G. M. G., Cohn, H. N., Lugger, P. M., Anderson, J., Cool, A. M. and Serenelli, A. M. (2010), 'Ultraviolet-bright stellar populations and their evolutionary implications in the collapsed-core cluster M15', *Astrophysical Journal* **722**, 158–177.

Heber, U. (2016), 'Hot subluminous stars', *Publications of the Astronomical Society of the Pacific* **128**(8), 082001–082086.

Heggie, D. C. (1975), 'Binary evolution in stellar dynamics', *Monthly Notices of the Royal Astronomical Society* **173**, 729–787.

Herbst, W. (1975), 'R associations. I - UBV photometry and MK spectroscopy of stars in southern reflection nebulae', *Astronomical Journal* **80**, 212–226.

Hills, J. G. and Day, C. A. (1976), 'Stellar collisions in globular clusters', *Astrophysics Letters.* **17**, 87–93.

Holberg, J. B. and Bergeron, P. (2006), 'Calibration of Synthetic Photometry Using DA White Dwarfs', *Astronomical Journal* **132**, 1221–1233.

Hurley, J. R., Pols, O. R., Aarseth, S. J. and Tout, C. A. (2005), 'A complete N-body model of the old open cluster M67', *Monthly Notices of the Royal Astronomical Society* **363**, 293–314.

Hurley, J. R., Tout, C. A., Aarseth, S. J. and Pols, O. R. (2001), 'Direct N-body modelling of stellar populations: blue stragglers in M67', *Monthly Notices of the Royal Astronomical Society* **323**, 630–650.

Hutchings, J. B. (2014*a*), The UVIT telescopes on board the ISRO Astrosat Observatory, *in* 'Space Telescopes and Instrumentation 2014: Ultraviolet to Gamma Ray', Vol. 9144 of *Proceedings of the Society of Photo-Optical Instrumentation Engineers*, pp. 914407–914412.

Hutchings, J. B. (2014*b*), 'The UVIT telescopes on the Astrosat observatory', *Astrophysics and Space Science* **354**, 143–146.

Hutchings, J. B., Postma, J., Asquin, D. and Leahy, D. (2007), 'Photon event centroiding with UV photon-counting detectors', *Publications of the Astronomical Society of the Pacific* **119**, 1152–1162.

Iben, I. and Webbink, R. F. (1989), On the Formation of Close Binary White Dwarfs, *in* G. Wegner, ed., 'IAU Colloq. 114: White Dwarfs', Vol. 328 of *Lecture Notes in Physics, Berlin Springer Verlag*, pp. 477–478.

Indebetouw, R., Mathis, J. S., Babler, B. L., Meade, M. R., Watson, C., Whitney, B. A., Wolff, M. J., Wolfire, M. G., Cohen, M., Bania, T. M., Benjamin, R. A., Clemens, D. P., Dickey, J. M., Jackson, J. M., Kobulnicky, H. A., Marston, A. P., Mercer, E. P., Stauffer, J. R., Stolovy, S. R. and Churchwell, E. (2005), 'The wavelength dependence of interstellar extinction from 1.25 to 8.0 μm using GLIMPSE data', *Astrophysical Journal* **619**, 931–938.

Ivanova, N. (2015), *Ecology of Blue Straggler Stars*, Springer Publications.

Jacobson, H. R., Pilachowski, C. A. and Friel, E. D. (2011), 'A chemical abundance study of 10 open clusters based on WIYN-Hydra spectroscopy', *Astronomical Journal* **142**, 59–89.

Janes, K. (1985), The open cluster M67 as a fundamental standard of reference for stellar properties, Vol. 111 of *in 'IAU Symposium'*, pp. 361–363.

Janes, K. A. and Smith, G. H. (1984), 'The giant branch of the old open cluster M67', *Astronomical Journal* **89**, 487–495.

Jeffery, C. S., Woolf, V. M. and Pollacco, D. L. (2001), 'Time-resolved spectral analysis of the pulsating helium star V652 Her', *Astronomy and Astrophysics* **376**, 497–517.

Johnson, H. L. and Sandage, A. R. (1955), 'The galactic cluster M67 and its significance for stellar evolution', *Astrophysical Journal* **121**, 616–627.

Kafka, S. and Honeycutt, R. K. (2003), 'WIYN open cluster study. XV. Photometric monitoring of open clusters: New variables in NGC 188', *Astronomical Journal* **126**, 276–285.

Kepler, S. O., Pelisoli, I., Peçanha, V., Costa, J. E. S., Fraga, L., Hermes, J. J., Winget, D. E., Castanheira, B., Córsico, A. H., Romero, A. D., Althaus, L., Kleinman, S. J., Nitta, A., Koester, D., Külebi, B., Jordan, S. and Kanaan, A. (2012), 'Seismology of a Massive Pulsating Hydrogen Atmosphere White Dwarf', *Astrophysical Journal* **757**, 177–183.

Kimble, R. A., Woodgate, B. E., Bowers, C. W., Kraemer, S. B., Kaiser, M. E., Gull, T. R., Heap, S. R., Danks, A. C., Boggess, A., Green, R. F., Hutchings, J. B., Jenkins, E. B., Joseph, C. L., Linsky, J. L., Maran, S. P., Moos, H. W., Roesler, F., Timothy, J. G., Weistrop, D. E., Grady, J. F., Loiacono, J. J., Brown, L. W., Brumfield, M. D., Content, D. A., Feinberg, L. D., Isaacs, M. N., Krebs, C. A., Krueger, V. L., Melcher, R. W., Rebar, F. J., Vitagliano, H. D., Yagelowich, J. J., Meyer, W. W., Hood, D. F., Argabright, V. S., Becker, S. I., Bottema, M., Breyer, R. R., Bybee, R. L., Christon, P. R., Delamere, A. W., Dorn, D. A., Downey, S., Driggers, P. A., Ebbets, D. C., Gallegos, J. S., Garner, H., Hetlinger, J. C., Lettieri, R. L., Ludtke, C. W., Michika, D., Nyquist, R., Rose, D. M., Stocker, R. B., Sullivan, J. F., Houten, C. N. V., Woodruff, R. A., Baum, S. A., Hartig, G. F., Balzano, V., Biagetti, C., Blades, J. C., Bohlin, R. C., Clampin, M., Doxsey, R., Ferguson, H. C., Goudfrooij, P., Hulbert, S. J., Kutina, R., McGrath, M., Lindler, D. J., Beck, T. L., Feggans, J. K., Plait, P. C., Sandoval, J. L., Hill, R. S., Collins, N. R., Cornett, R. H., Fowler, W. B., Hill, R. J., Landsman, W. B., Malumuth, E. M., Standley, C., Blouke, M., Grusczak, A., Reed, R., Robinson, R. D., Valenti, J. A. and Wolfe, T. (1998), 'The on-orbit performance of the space telescope imaging spectrograph', *The Astrophysical Journal* **492**(2), L83–L93.

Kippenhahn, R. and Weigert, A. (1967), 'Entwicklung in engen Doppelsternsystemen I. Massenaustausch vor und nach Beendigung des zentralen Wasserstoff-Brennens', *Zeitschrift fuer Astrophysik* **65**, 251–273.

Knigge, C., Zurek, D. R., Shara, M. M. and Long, K. S. (2002), 'A far-ultraviolet survey of 47 Tucanae. I. Imaging', *Astrophysical Journal* **579**, 752–759.

Koester, D. (2010), 'White dwarf spectra and atmosphere models ', *Memoire della Societa Astronomica Italiana* **81**, 921–931.

Kopal, Z. (1955), 'The classification of close binary systems', *Annales d'Astrophysique* **18**, 379–430.

Krone-Martins, A., Soubiran, C., Ducourant, C., Teixeira, R. and Le Campion, J. F. (2010), 'Kinematic parameters and membership probabilities of open clusters in the Bordeaux PM2000 catalogue', *Astronomy and Astrophysics* **516**, A3–A17.

Landsman, W., Aparicio, J., Bergeron, P., Di Stefano, R. and Stecher, T. P. (1997), 'S1040 in M67: A post–mass transfer binary with a helium core white dwarf', *Astrophysical Journal Letters* **481**, L93–L96.

Landsman, W., Bohlin, R. C., Neff, S. G., O'Connell, R. W., Roberts, M. S., Smith, A. M. and Stecher, T. P. (1998), 'The hot stars of old open clusters: M67, NGC 188, and NGC 6791', *Astronomical Journal* **116**, 789–800.

Larsen, M. F. and Schick, S. (2005), Wide-field Infrared Survey Explorer science payload overview, *in* J. B. Heaney and L. G. Burriesci, eds, 'Cryogenic Optical Systems and Instruments XI', Vol. 5904 of *in 'Proceedings of the Society of Photo-Optical Instrumentation Engineers'*, pp. 166–177.

Latham, D. W., Mathieu, R. D., Milone, A. A. E. and Davis, R. J. (1992), Spectroscopic binaries in the open cluster M67, *in* H. A. McAlister and W. I. Hartkopf, eds, 'IAU Colloq. 135: Complementary Approaches to Double and Multiple Star Research', Vol. 32 of *Astronomical Society of the Pacific Conference Series*, p. 152.

Latham, D. W. and Milone, A. A. E. (1996), Spectroscopic Binaries Among the M67 Blue Stragglers, *in* E. F. Milone and J.-C. Mermilliod, eds, 'The origins, evolution, and destinies of binary stars in clusters', Vol. 90 of *in 'Astronomical Society of the Pacific Conference Series'*, pp. 385–387.

Lauterborn, D. (1970), 'Evolution with mass exchange of case C for a binary system of total mass 7 M sun.', *Astronomy and Astrophysics* **7**, 150–159.

Leiner, E., Mathieu, R. D. and Geller, A. M. (2017), 'On the origin of sub-subgiant stars. II. Binary mass transfer, envelope stripping, and magnetic activity', *Astrophysical Journal* **840**, 67–83.

Leiner, E., Mathieu, R. D., Gosnell, N. M. and Sills, A. (2018), 'Observations of Spin-down in Post-mass-transfer Stars and the Possibility for Blue Straggler Gyrochronology', *Astrophysical Journal Letters* **869**, L29–34.

Leiner, E., Mathieu, R. D., Stello, D., Vanderburg, A. and Sandquist, E. (2016), 'The K2 M67 study: An evolved blue straggler in M67 from K2 mission asteroseismology', *Astrophysical Journal Letters* **832**, L13–L19.

Lejeune, T., Cuisinier, F. and Buser, R. (1997), 'Standard stellar library for evolutionary synthesis. I. Calibration of theoretical spectra', *Astronomy and Astrophysics Supplement Series* **125**, 229–246.

Lejeune, T., Cuisinier, F. and Buser, R. (1998), 'A standard stellar library for evolutionary synthesis. II. The M dwarf extension', *Astronomy and Astrophysics Supplement Series* **130**, 65–75.

Leonard, P. J. T. (1996), 'The implications of the binary properties of the M67 Blue Stragglers', *Astrophysical Journal* **470**, 521–528.

Linsky, J. L. (2017), 'Stellar model chromospheres and spectroscopic diagnostics', *Annual Review of Astronomy and Astrophysics* **55**, 159–211.

Liu, G. Q., Deng, L., Chávez, M., Bertone, E., Davo, A. H. and Mata-Chávez, M. D. (2008), 'A spectroscopic study of the blue stragglers in M67', *Monthly Notices of the Royal Astronomical Society* **390**, 665–674.

Liu, L., Qian, S.-B., Zhu, L.-Y., He, J.-J., Liao, W.-P., Li, L.-J., Zhao, E.-G. and Wang, J.-J. (2011), 'Photometric investigation of three W UMa-type binary stars in the old open cluster NGC 188', *Monthly Notices of the Royal Astronomical Society* **415**, 3006–3012.

Lu, P., Deng, L. C. and Zhang, X. B. (2010), 'Blue straggler formation via close binary mass transfer', *Monthly Notices of the Royal Astronomical Society* **409**, 1013–1021.

Mainzer, A. K., Eisenhardt, P., Wright, E. L., Liu, F.-C., Irace, W., Heinrichsen, I., Cutri, R. and Duval, V. (2005), Preliminary design of the Wide-Field Infrared Survey Explorer (WISE), *in* 'Proceedings of the Society of Photo-Optical Instrumentation Engineers', pp. 262–273.

Marigo, P., Girardi, L., Bressan, A., Groenewegen, M. A. T., Silva, L. and Granato, G. L. (2008), 'Evolution of asymptotic giant branch stars. II. Optical to far-infrared isochrones with improved TP-AGB models', *Astronomy and Astrophysics* **482**, 883–905.

Martin, D. C., Fanson, J., Schiminovich, D., Morrissey, P., Friedman, P. G., Barlow, T. A., Conrow, T., Grange, R., Jelinsky, P. N., Milliard, B., Siegmund, O. H. W., Bianchi, L., Byun, Y.-I., Donas, J., Forster, K., Heckman, T. M., Lee, Y.-W., Madore, B. F., Malina, R. F., Neff, S. G., Rich, R. M., Small, T., Surber, F., Szalay, A. S., Welsh, B. and Wyder, T. K. (2005), 'The Galaxy Evolution Explorer: A space ultraviolet survey mission', *Astrophysical Journal Letters* **619**, L1–L6.

Mason, K. O., Breeveld, A., Hunsberger, S. D., James, C., Kennedy, T. E., Roming, P. W. A. and Stock, J. (2004), Performance of the UV/Optical Telescope (UVOT) on SWIFT, *in* K. A. Flanagan and O. H. W. Siegmund, eds, 'X-Ray and Gamma-Ray Instrumentation for Astronomy XIII', Vol. 5165 of *Proceedings of the Society of Photo-Optical Instrumentation Engineers*, pp. 277–286.

Mathieu, R. D. and Geller, A. M. (2009), 'A binary star fraction of 76 per cent and unusual orbit parameters for the blue stragglers of NGC 188', *Nature* **462**, 1032–1035.

Mathieu, R. D. and Geller, A. M. (2015), *Ecology of Blue Straggler Stars*, Springer Publications.

Mathieu, R. D. and Latham, D. W. (1986), 'The spatial distribution of spectroscopic binaries and blue stragglers in the open cluster M67', *Astronomical Journal* **92**, 1364–1371.

Mathieu, R. D., Latham, D. W. and Griffin, R. F. (1990), 'Orbits of 22 spectroscopic binaries in the open cluster M67', *Astronomical Journal* **100**, 1859–1881.

Mathieu, R. D., Latham, D. W., Griffin, R. F. and Gunn, J. E. (1986), 'Precise radial velocities of late-type stars in the open clusters M11 and M67', *Astronomical Journal* **92**, 1100–1117.

Mathieu, R. D., Van den Berg, M., Torres, G., Latham, D., Verbunt, F. and Stassun, K. (2003), 'Sub-subgiants in the old open cluster M67?', *Astronomical Journal* **125**, 246–259.

Mathys, G. (1991), 'The blue stragglers of M67', *Astronomy and Astrophysics* **245**, 467–484.

Matrozis, E., Abate, C. and Stancliffe, R. J. (2017), 'How much mass and angular momentum can the progenitors of carbon-enriched stars accrete?', *Astronomy and Astrophysics* **606**, A137–147.

McCrea, W. H. (1964), 'Extended main-sequence of some stellar clusters', *Monthly Notices of the Royal Astronomical Society* **128**, 147–154.

Meibom, S., Grundahl, F., Clausen, J. V., Mathieu, R. D., Frandsen, S., Pigulski, A., Narwid, A., Steslicki, M. and Lefever, K. (2009), 'Age and distance for the old open cluster NGC 188 from the eclipsing binary member V 12', *Astronomical Journal* **137**, 5086–5098.

Meynet, G. and Maeder, A. (2000), 'Stellar evolution with rotation. V. Changes in all the outputs of massive star models', *Astronomy and Astrophysics* **361**, 101–120.

Milliman, K. E., Mathieu, R. D. and Schuler, S. C. (2015), 'Barium surface abundances of blue stragglers in the open cluster NGC 6819', *Astronomical Journal* **150**, 84–93.

Milone, A. A. E. (1992), 'The blue stragglers of M67 and other open clusters', *Publications of the Astronomical Society of the Pacific* **104**, 1268–1274.

Milone, A. A. E. and Latham, D. W. (1992), 'The blue straggler f190: A case for mass transfer', *International Astronomical Union* **151**, 475 – 478.

Milone, A. A. E. and Latham, D. W. (1994), 'Radial velocities of blue stragglers. 1: A catalog of candidates in six open clusters', *Astronomical Journal* **108**, 1828–1833.

Milone, A. A. E., Latham, D. W., Mathieu, R. D., Morse, J. A. and Davis, R. J. (1992), Can Evolution in Close Binaries Account for the Blue Stragglers in M67, *in* Y. Kondo, R. Sistero and R. S. Polidan, eds, 'Evolutionary Processes in Interacting Binary Stars', Vol. 151 of *IAU Symposium*, pp. 473–474.

Mochejska, B. J., Stanek, K. Z., Sasselov, D. D., Szentgyorgyi, A. H., Cooper, R. L., Hickox, R. C., Hradecky, V., Marrone, D. P., Winn, J. N. and Schwarzenberg-Czerny, A. (2008), 'Planets in stellar clusters extensive search. V. Search for planets and identification of 18 new variable stars in the old open cluster NGC 188', *Acta Astronomica.* **58**, 263–278.

Mondal, C., Subramaniam, A. and George, K. (2018), 'UVIT imaging of WLM: Demographics of star-forming regions in the nearby dwarf irregular galaxy', *Astronomical Journal* **156**, 109–124.

Montgomery, K. A., Marschall, L. A. and Janes, K. A. (1993), 'CCD photometry of the old open cluster M67', *Astronomical Journal* **106**, 181–219.

Mooley, K. P. and Singh, K. P. (2015), 'Study of X-ray emission from the old open cluster, M67', *Monthly Notices of the Royal Astronomical Society* **452**, 3394–3407.

Morrissey, P., Conrow, T., Barlow, T. A., Small, T., Seibert, M., Wyder, T. K., Budavári, T., Arnouts, S., Friedman, P. G., Forster, K., Martin, D. C., Neff, S. G., Schiminovich, D., Bianchi, L., Donas, J., Heckman, T. M., Lee, Y.-W., Madore, B. F., Milliard, B., Rich, R. M., Szalay, A. S., Welsh, B. Y. and Yi, S. K. (2007), 'The calibration and data products of GALEX', *Astrophysical Journal Supplement* **173**, 682–697.

Naoz, S. and Fabrycky, D. C. (2014), 'Mergers and obliquities in stellar triples', *Astrophysical Journal* **793**, 137–150.

Nissen, P. E., Twarog, B. A. and Crawford, D. L. (1987), 'UvbyH-beta photometry of main-sequence stars in M67', *Astronomical Journal* **93**, 634–646.

Packet, W. (1981), 'On the spin-up of the mass accreting component in a close binary system', *Astronomy and Astrophysics* **102**, 17–19.

Panei, J. A., Althaus, L. G., Chen, X. and Han, Z. (2007), 'Full evolution of low-mass white dwarfs with helium and oxygen cores', *Monthly Notices of the Royal Astronomical Society* **382**, 779–792.

Parsons, S. G., Rebassa-Mansergas, A., Schreiber, M. R., Gänsicke, B. T., Zorotovic, M. and Ren, J. J. (2016), 'The white dwarf binary pathways survey - I. A sample of FGK stars with white dwarf companions', *Monthly Notices of the Royal Astronomical Society* **463**, 2125–2136.

Pasquini, L., Melo, C., Chavero, C., Dravins, D., Ludwig, H.-G., Bonifacio, P. and de La Reza, R. (2011), 'Gravitational redshifts in main-sequence and giant stars', *Astronomy and Astrophysics* **526**, A127–A134.

Peng, Y.-J., Luo, Z.-Q., Zhang, X.-B., Deng, L.-C., Wang, K., Tian, J.-F., Yan, Z.-Z., Pan, Y., Fang, W.-J., Feng, Z.-W., Tang, D.-L., Liu, Q.-L., Sun, J.-J. and Zhou, Q. (2016), 'Photometric solution and period analysis of the contact binary system AH Cnc', *Research in Astronomy and Astrophysics* **16**, 157–163.

Percival, S. M. and Salaris, M. (2003), 'An empirical test of the theoretical population corrections to the red clump absolute magnitude', *Monthly Notices of the Royal Astronomical Society* **343**, 539–546.

Perets, H. B. (2015), *Ecology of Blue Straggler Stars*, Springer Publications.

Perets, H. B. and Fabrycky, D. C. (2009), 'On the triple origin of blue stragglers', *Astrophysical Journal* **697**, 1048–1056.

Pérez Martínez, M. I., Schröder, K.-P. and Cuntz, M. (2011), 'The basal chromospheric Mg II h+k flux of evolved stars: probing the energy dissipation of giant chromospheres', *Monthly Notices of the Royal Astronomical Society* **414**, 418–427.

Pietrinferni, A., Cassisi, S., Salaris, M. and Castelli, F. (2004), 'A large stellar evolution database for population synthesis studies. I. Scaled solar models and isochrones', *Astrophysical Journal* **612**, 168–190.

Piotto, G. (2008), Observational Evidence of Multiple Stellar Populations in Globular Clusters, *in* E. Vesperini, M. Giersz and A. Sills, eds, 'Dynamical Evolution of Dense Stellar Systems', Vol. 246 of *IAU Symposium*, pp. 141–150.

Piotto, G., Bedin, L. R., Anderson, J., King, I. R., Cassisi, S., Milone, A. P., Villanova, S., Pietrinferni, A. and Renzini, A. (2007), 'A Triple Main Sequence in the Globular Cluster NGC 2808', *Astrophysical Journal Letters* **661**, L53–L56.

Piotto, G., Villanova, S., Bedin, L. R., Gratton, R., Cassisi, S., Momany, Y., Recio-Blanco, A., Lucatello, S., Anderson, J., King, I. R., Pietrinferni, A. and Carraro, G. (2005), 'Metallicities on the Double Main Sequence of ω Centauri Imply Large Helium Enhancement', *Astrophysical Journal* **621**, 777–784.

Piskunov, A. E., Schilbach, E., Kharchenko, N. V., Röser, S. and Scholz, R.-D. (2008), 'Tidal radii and masses of open clusters', *Astronomy and Astrophysics* **477**, 165–172.

Platais, I., Kozhurina-Platais, V., Mathieu, R. D., Girard, T. M. and van Altena, W. F. (2003), 'WIYN open cluster study. XVII. Astrometry and membership to V=21 in NGC 188', *Astronomical Journal* **126**, 2922–2935.

Postma, J. E. and Leahy, D. (2017), 'CCDLAB: A graphical user interface FITS image data reducer, viewer, and canadian UVIT data pipeline', *Publications of the Astronomical Society of the Pacific* **129**(11), 115002–115015.

Postma, J., Hutchings, J. B. and Leahy, D. (2011), 'Calibration and performance of the photon-counting detectors for the Ultraviolet Imaging Telescope (UVIT) of the Astrosat observatory', *Publications of the Astronomical Society of the Pacific* **123**, 833–849.

Racine, R. (1968), 'Stars in reflection nebulae', *Astronomical Journal* **73**, 233–245.

Racine, R. and van den Bergh, S. (1970), Reflection Nebulae and Spiral Structure, *in* W. Becker and G. I. Kontopoulos, eds, 'The Spiral Structure of our Galaxy', Vol. 38 of *IAU Symposium*, pp. 219–221.

Reimers, D. (1975), 'Circumstellar absorption lines and mass loss from red giants', *Memoires of the Societe Royale des Sciences de Liege* **8**, 369–382.

Reiners, A. and Giampapa, M. S. (2009), 'The origin of enhanced activity in the Suns of M67', *Astrophysical Journal* **707**, 852–857.

Richer, H. B., Fahlman, G. G., Rosvick, J. and Ibata, R. (1998), 'The white dwarf cooling age of M67', *Astrophysical Journal Letters* **504**, L91–L94.

Roming, P. W. A., Kennedy, T. E., Mason, K. O., Nousek, J. A., Ahr, L., Bingham, R. E., Broos, P. S., Carter, M. J., Hancock, B. K., Huckle, H. E., Hunsberger, S. D., Kawakami, H., Killough, R., Koch, T. S., McLelland, M. K., Smith, K., Smith, P. J., Soto, J. C., Boyd, P. T., Breeveld, A. A., Holland, S. T., Ivanushkina, M., Pryzby, M. S., Still, M. D. and Stock, J. (2005), 'The Swift Ultra-Violet/Optical Telescope', *Space Science Reviews* **120**, 95–142.

Ryan, S. G., Gregory, S. G., Kolb, U., Beers, T. C. and Kajino, T. (2002), 'Rapid rotation of ultra-Li-depleted halo stars and their association with blue stragglers', *Astrophysical Journal* **571**, 501–511.

Salaris, M., Weiss, A. and Percival, S. M. (2004), 'The age of the oldest open clusters', *Astronomy and Astrophysics* **414**, 163–174.

Sánchez-Blázquez, P., Peletier, R. F., Jiménez-Vicente, J., Cardiel, N., Cenarro, A. J., Falcón-Barroso, J., Gorgas, J., Selam, S. and Vazdekis, A. (2006), 'Medium-resolution Isaac Newton Telescope library of empirical spectra', *Monthly Notices of the Royal Astronomical Society* **371**, 703–718.

Sandage, A. (1962), 'Photometric data for the old galactic cluster NGC 188.', *Astrophysical Journal* **135**, 333–348.

Sandage, A. R. (1953), 'The color-magnitude diagram for the globular cluster M 3.', *Astronomical Journal* **58**, 61–75.

Sanders, W. L. (1977), 'Membership of the open cluster M67.', *Astronomy and Astrophysics Supplement Series* **27**, 89–116.

Sandquist, E. L. (2004), 'A high relative precision colour-magnitude diagram of M67', *Monthly Notices of the Royal Astronomical Society* **347**, 101–118.

Sandquist, E. L., Latham, D. W., Shetrone, M. D. and Milone, A. A. E. (2003), 'The blue straggler RS Canum Venaticorum star S1082 in M67: A detailed light curve and the possibility of a triple', *Astronomical Journal* **125**, 810–824.

Sandquist, E. L. and Shetrone, M. D. (2003*a*), 'S986 in M67: A totally eclipsing binary at the cluster turnoff', *Astronomical Journal* **126**, 2954–2962.

Sandquist, E. L. and Shetrone, M. D. (2003*b*), 'Time series photometry of M67: W Ursae Majoris systems, blue stragglers, and related systems', *Astronomical Journal* **125**, 2173–2187.

Sarajedini, A., Brandt, K., Grocholski, A. J. and Tiede, G. P. (2004), 'WIYN open cluster study. XIX. Main-sequence-fitting distances to open clusters using V-K color-magnitude diagrams', *Astronomical Journal* **127**, 991–999.

Sarajedini, A., Dotter, A. and Kirkpatrick, A. (2009), 'Deep 2MASS photometry of M67 and calibration of the main-sequence J - K_S color difference as an age indicator', *Astrophysical Journal* **698**, 1872–1878.

Sarajedini, A., von Hippel, T., Kozhurina-Platais, V. and Demarque, P. (1999), 'WIYN open cluster study. II. UBVRI CCD photometry of the open cluster NGC 188', *AJ* **118**, 2894–2907.

Schaller, G., Schaerer, D., Meynet, G. and Maeder, A. (1992), 'New grids of stellar models from 0.8 to 120 solar masses at Z = 0.020 and Z = 0.001', *Astronomy and Astrophysics Supplement Series* **96**, 269–331.

Shetrone, M. D. and Sandquist, E. L. (2000), 'Spectroscopy of blue stragglers and turnoff stars in M67 (NGC 2682)', *Astronomical Journal* **120**, 1913–1924.

Siegel, M. H., Porterfield, B. L., Linevsky, J. S., Bond, H. E., Holland, S. T., Hoversten, E. A., Berrier, J. L., Breeveld, A. A., Brown, P. J. and Gronwall, C. A. (2014), 'The Swift UVOT stars survey. I. methods and test clusters', *Astronomical Journal* **148**, 131–143.

Siess, L., Dufour, E. and Forestini, M. (2000), 'An internet server for pre-main sequence tracks of low- and intermediate-mass stars', *Astronomy and Astrophysics* **358**, 593–599.

Sills, A. (2015), *Ecology of Blue Straggler Stars*, Springer Publications.

Sills, A., Adams, T. and Davies, M. B. (2005), 'Blue stragglers as stellar collision products: the angular momentum question', *Monthly Notices of the Royal Astronomical Society* **358**, 716–725.

Sills, A., Faber, J. A., Lombardi, Jr., J. C., Rasio, F. A. and Warren, A. R. (2001), 'Evolution of Stellar Collision Products in Globular Clusters. II. Off-Axis Collisions', *Astrophysical Journal* **548**, 323–334.

Sindhu, N., Annapurni, S. and Anu Radha, C. (2015), 'Simulation of old open clusters for UVIT on ASTROSAT', *Research in Astronomy and Astrophysics* **15**, 1647–1670.

Sindhu, N., Subramaniam, A. and Radha, C. A. (2018), 'Ultraviolet stellar population of the old open cluster M67 (NGC 2682)', *Monthly Notices of the Royal Astronomical Society* **481**, 226–243.

Sivarani, T., Bonifacio, P., Molaro, P., Cayrel, R., Spite, M., Spite, F., Plez, B., Andersen, J., Barbuy, B., Beers, T. C., Depagne, E., Hill, V., François, P., Nordström, B. and Primas, F. (2004), 'First stars IV. CS 29497-030: Evidence for operation of the s-process at very low metallicity', *Astronomy and Astrophysics* **413**, 1073–1085.

Skrutskie, M. F., Cutri, R. M., Stiening, R., Weinberg, M. D., Schneider, S., Carpenter, J. M., Beichman, C., Capps, R., Chester, T., Elias, J., Huchra, J., Liebert, J., Lonsdale, C., Monet, D. G., Price, S., Seitzer, P., Jarrett, T., Kirkpatrick, J. D., Gizis, J. E., Howard, E., Evans, T., Fowler, J., Fullmer, L., Hurt, R., Light, R., Kopan, E. L., Marsh, K. A., McCallon, H. L., Tam, R., Van Dyk, S. and Wheelock, S. (2006), 'The Two Micron All Sky Survey (2MASS)', *Astronomical Journal* **131**, 1163–1183.

Spitzer, Jr., L. (1958), 'Disruption of Galactic Clusters.', *Astrophysical Journal* **127**, 17.

Spitzer, Jr., L. and Mathieu, R. D. (1980), 'Random gravitational encounters and the evolution of spherical systems. VIII - Clusters with an initial distribution of binaries', *Astrophysical Journal* **241**, 618–636.

Stecher, T. P., Baker, G. R., Bartoe, D. D., Bauer, F. H., Blum, A., Bohlin, R. C., Butcher, H. R., Chen, P. C., Collins, N. R., Cornett, R. H., Deily, J. J., Greason, M. R., Hennessy, G. S., Hill, J. K., Hill, R. S., Hintzen, P. M., Isensee, J. E., Kenny, P. J., Landsman, W. B., Linard, D. L., Maran, S. P., Neff, S. G., Nichols, G. R., Novello, J., O'Connell, R. W., Offenberg, J. D., Parise, R. A., Pfarr, B. B., Plummer, T. B., Richardson, F. F., Roberts, M. S., Sitko, S. D., Smith, A. M., Stober, A. K., Stolarik, J. D. and Tebay, J. C. (1992), 'The Ultraviolet Imaging Telescope - design and performance', *Astrophysical Journal Letters* **395**, L1–L4.

Stecher, T. P., Cornett, R. H., Greason, M. R., Landsman, W. B., Hill, J. K., Hill, R. S., Bohlin, R. C., Chen, P. C., Collins, N. R., Fanelli, M. N., Hollis, J. I., Neff, S. G., O'Connell, R. W., Offenberg, J. D., Parise, R. A., Parker, J., Roberts, M. S., Smith, A. M. and Waller, W. H. (1997), 'The Ultraviolet Imaging Telescope: Instrument and data characteristics', *Publications of the Astronomical Society of the Pacific* **109**, 584–599.

Stello, D., Vanderburg, A., Casagrande, L., Gilliland, R., Silva Aguirre, V., Sandquist, E., Leiner, E., Mathieu, R. and Soderblom, D. R. (2016), 'The K2 M67 study: Revisiting old friends with K2 reveals oscillating red giants in the open cluster M67', *Astrophysical Journal* **832**, 133.

Stetson, P. B. (1987), 'DAOPHOT - A computer program for crowded-field stellar photometry', *Publications of the Astronomical Society of the Pacific* **99**, 191–222.

Stetson, P. B., McClure, R. D. and VandenBerg, D. A. (2004), 'A star catalog for the open cluster NGC 188', *Publications of the Astronomical Society of the Pacific* **116**, 1012–1030.

Strüder, L., Briel, U., Dennerl, K., Hartmann, R., Kendziorra, E., Meidinger, N., Pfeffermann, E., Reppin, C., Aschenbach, B., Bornemann, W., Bräuninger, H., Burkert, W., Elender, M., Freyberg, M., Haberl, F., Hartner, G., Heuschmann, F., Hippmann, H., Kastelic, E., Kemmer, S., Kettenring, G., Kink, W., Krause, N., Müller, S., Oppitz, A., Pietsch, W., Popp, M., Predehl, P., Read, A., Stephan, K. H., Stötter, D., Trümper, J., Holl, P., Kemmer, J., Soltau, H., Stötter, R., Weber, U., Weichert, U., von Zanthier, C., Carathanassis, D., Lutz, G., Richter, R. H., Solc, P., Böttcher, H., Kuster, M., Staubert, R., Abbey, A., Holland, A., Turner, M., Balasini, M., Bignami, G. F., La Palombara, N., Villa, G., Buttler, W., Gianini, F., Lainé, R., Lumb, D. and Dhez, P. (2001), 'The European Photon Imaging Camera on XMM-Newton: The pn-CCD camera', *Astronomy and Astrophysics* **365**, L18–L26.

Subramaniam, A. (2012), Upcoming Indian facility: UVIT on ASTROSAT, *in* 'Astronomical Society of India Conference Series', pp. 165–167.

Subramaniam, A., Sindhu, N., Tandon, S. N., Kameswara Rao, N., Postma, J., Côté, P., Hutchings, J. B., Ghosh, S. K., George, K., Girish, V., Mohan, R., Murthy, J., Sankarasubramanian, K., Stalin, C. S., Sutaria, F., Mondal, C. and Sahu, S. (2016), 'A hot Companion to a blue Straggler in NGC 188 as revealed by the Ultra-Violet Imaging Telescope (UVIT) on ASTROSAT', *Astrophysical Journal Letters* **833**, L27–L31.

Tandon, S. N., Subramaniam, A., Girish, V., Postma, J., Sankarasubramanian, K., Sriram, S., Stalin, C. S., Mondal, C., Sahu, S., Joseph, P., Hutchings, J., Ghosh, S. K.,

Barve, I. V., George, K., Kamath, P. U., Kathiravan, S., Kumar, A., Lancelot, J. P., Leahy, D., Mahesh, P. K., Mohan, R., Nagabhushana, S., Pati, A. K., Kameswara Rao, N., Sreedhar, Y. H. and Sreekumar, P. (2017), 'In-orbit calibrations of the Ultraviolet Imaging Telescope', *Astronomical Journal* **154**, 128–135.

Taylor, B. J. (2007), 'The benchmark cluster reddening project. II. A reddening value for M67', *Astronomical Journal* **133**, 370–386.

Tian, B., Deng, L., Han, Z. and Zhang, X. B. (2006), 'The blue stragglers formed via mass transfer in old open clusters', *Astronomy and Astrophysics* **455**, 247–254.

Tody, D. (1986), The IRAF Data Reduction and Analysis System, *in* L. Crawford, D, ed., 'Instrumentation in astronomy VI', Vol. 627 of *Proceedings of the Society of Photo-Optical Instrumentation Engineers*, pp. 733–748.

Tremblay, P.-E. and Bergeron, P. (2009), 'Spectroscopic Analysis of DA White Dwarfs: Stark Broadening of Hydrogen Lines Including Nonideal Effects', *Astrophysical Journal* **696**, 1755–1770.

Tremblay, P.-E., Gentile-Fusillo, N., Raddi, R., Jordan, S., Besson, C., Gänsicke, B. T., Parsons, S. G., Koester, D., Marsh, T., Bohlin, R., Kalirai, J. and Deustua, S. (2017), 'The Gaia DR1 mass-radius relation for white dwarfs', *Monthly Notices of the Royal Astronomical Society* **465**, 2849–2861.

Tremblay, P.-E., Ludwig, H.-G., Steffen, M., Bergeron, P. and Freytag, B. (2011), 'Solution to the problem of the surface gravity distribution of cool da white dwarfs from improved 3d model atmospheres', *Astronomy and Astrophysics* **531**, L19.

Turner, M. J. L., Abbey, A., Arnaud, M., Balasini, M., Barbera, M., Belsole, E., Bennie, P. J., Bernard, J. P., Bignami, G. F., Boer, M., Briel, U., Butler, I., Cara, C., Chabaud, C., Cole, R., Collura, A., Conte, M., Cros, A., Denby, M., Dhez, P., Di Coco, G., Dowson, J., Ferrando, P., Ghizzardi, S., Gianotti, F., Goodall, C. V., Gretton, L., Griffiths, R. G., Hainaut, O., Hochedez, J. F., Holland, A. D., Jourdain, E., Kendziorra, E., Lagostina, A., Laine, R., La Palombara, N., Lortholary, M., Lumb, D., Marty, P., Molendi, S., Pigot, C., Poindron, E., Pounds, K. A., Reeves, J. N., Reppin, C., Rothenflug, R., Salvetat, P., Sauvageot, J. L., Schmitt, D., Sembay, S., Short, A. D. T., Spragg, J., Stephen, J., Strüder, L., Tiengo, A., Trifoglio, M., Trümper, J., Vercellone, S., Vigroux, L., Villa, G., Ward, M. J., Whitehead, S. and Zonca, E. (2001), 'The European Photon Imaging Camera on XMM-Newton: The MOS cameras : The MOS cameras', *Astronomy and Astrophysics* **365**, L27–L35.

Twarog, B. A. and Anthony-Twarog, B. J. (1989), 'NGC 188, the age of the galactic disk, and the evolution of the Li abundance', *Astronomical Journal* **97**, 759–770.

Van den Berg, M., Orosz, J., Verbunt, F. and Stassun, K. (2001), 'The blue straggler S 1082: A triple system in the old open cluster M 67', *Astronomy and Astrophysics* **375**, 375–386.

Van den Berg, M., Tagliaferri, G., Belloni, T. and Verbunt, F. (2004), 'A Chandra observation of the old open cluster M 67', *Astronomy and Astrophysics* **418**, 509–523.

van den Bergh, S. (1966), 'A study of reflection nebulae.', *Astronomical Journal* **71**, 990–998.

van den Bergh, S. (1968), 'Associations of Reflection Nebulae and Local Galactic Structure', *Astrophysics Letters.* **2**, 71–75.

VandenBerg, D. A. and Stetson, P. B. (2004), 'On the Old Open Clusters M67 and NGC 188: Convective Core Overshooting, Color-Temperature Relations, Distances, and Ages', *Publications of the Astronomical Society of the Pacific* **116**, 997–1011.

Vats, S., Van den Berg, M. and Wijnands, R. (2018), 'A Chandra X-ray census of the interacting binaries in old open clusters - NGC 188', *Monthly Notices of the Royal Astronomical Society* **481**, 3708–3723.

Weisskopf, M. C., Tananbaum, H. D., Van Speybroeck, L. P. and O'Dell, S. L. (2000), Chandra X-ray Observatory (CXO): overview, *in* 'Proceedings of the Society of Photo-Optical Instrumentation Engineers', pp. 2–16.

Westera, P., Lejeune, T., Buser, R., Cuisinier, F. and Bruzual, G. (2002), 'A standard stellar library for evolutionary synthesis. III. Metallicity calibration', *Astronomy and Astrophysics* **381**, 524–538.

Worthey, G. and Jowett, K. J. (2003), 'The metal abundances of NGC 188 and NGC 6791 from low-resolution spectra', *Publications of the Astronomical Society of the Pacific* **115**, 96–103.

Wright, E. L., Eisenhardt, P. R. M., Mainzer, A. K., Ressler, M. E., Cutri, R. M., Jarrett, T., Kirkpatrick, J. D., Padgett, D., McMillan, R. S., Skrutskie, M., Stanford, S. A., Cohen, M., Walker, R. G., Mather, J. C., Leisawitz, D., Gautier, III, T. N., McLean, I., Benford, D., Lonsdale, C. J., Blain, A., Mendez, B., Irace, W. R., Duval, V., Liu, F., Royer, D., Heinrichsen, I., Howard, J., Shannon, M., Kendall, M., Walsh, A. L., Larsen, M., Cardon, J. G., Schick, S., Schwalm, M., Abid, M., Fabinsky, B., Naes, L. and Tsai, C.-W. (2010), 'The Wide-field Infrared Survey Explorer (WISE): Mission description and initial on-orbit performance', *Astronomical Journal* **140**, 1868–1881.

Yadav, R. K. S., Bedin, L. R., Piotto, G., Anderson, J., Cassisi, S., Villanova, S., Platais, I., Pasquini, L., Momany, Y. and Sagar, R. (2008), 'Ground-based CCD astrometry with

wide-field imagers. II. A star catalog for M 67: WFI@2.2 m MPG/ESO astrometry, FLAMES@VLT radial velocities', *Astronomy and Astrophysics* **484**, 609–620.

Yakut, K., Zima, W., Kalomeni, B., van Winckel, H., Waelkens, C., De Cat, P., Bauwens, E., Vučković, M., Saesen, S., Le Guillou, L., Parmaksızoğlu, M., Uluç, K., Khamitov, I., Raskin, G. and Aerts, C. (2009), 'Close binary and other variable stars in the solar-age Galactic open cluster M 67', *Astronomy and Astrophysics* **503**, 165–176.

Zhang, X. B., Deng, L., Zhou, X. and Xin, Y. (2004), 'Variable stars in the field of the old open cluster NGC 188', *Monthly Notices of the Royal Astronomical Society* **355**, 1369–1377.

Zhao, J. L., Tian, K. P., Pan, R. S., He, Y. P. and Shi, H. M. (1993), 'Study of proper motions in the region of the open cluster M67 and membership of stars', *Astronomy and Astrophysics Supplement Series* **100**, 243–261.

Zhu, L. Y., Qian, S. B., Soonthornthum, B., Liu, L., He, J. J., Liu, N. P., Zhao, E. G., Zhang, J. and Wang, J. J. (2014), 'Three close binaries in different evolutionary stages in the old open cluster NGC 188', *Astronomical Journal* **147**, 42–49.

Zinn, R. (1985), 'The globular cluster system of the galaxy. IV - The halo and disk subsystems', *Astrophysical Journal* **293**, 424–444.

Zombeck, M. V., David, L. P., Harnden, F. R. and Kearns, K. (1995), Orbital performance of the high-resolution imager (HRI) on ROSAT, *in* 'Proceedings of the Society of Photo-Optical Instrumentation Engineers', pp. 304–321.

LIST OF PUBLICATIONS

1. Sindhu, N., Subramaniam, A., and Anu Radha, C. (2015), 'Simulation of old open clusters for UVIT on ASTROSAT', *Research in Astronomy and Astrophysics* **15**, 1647-1670.

2. Subramaniam, A., Sindhu, N., Tandon, S. N., Kameswara Rao, N., Postma, J., Cote, P., Hutchings, J. B., Ghosh, S. K., George, K., Girish, V., Mohan, R., Murthy, J., Sankarasubramanian, K., Stalin, C. S., Sutaria, F., Mondal, C. and Sahu, S. (2016), 'A hot companion to a blue straggler in NGC 188 as revealed by the Ultra-Violet Imaging Telescope on ASTROSAT', *Astrophysical Journal Letters* **833**, L27-L31.

3. Sindhu, N., Subramaniam, A., and Anu Radha, C. (2018), 'Ultraviolet stellar population of the old open cluster M67 (NGC 2682)', *Monthly Notices of Royal Astronomical Society* **481**, 226-243.

4. Sindhu, N., Subramaniam, A., Jadhav, V. V., Chatterjee, S., Geller, A. M., Knigge, C., Leigh, N., Puzia, T. H., Shara, M., and Simunovic, M., (2019), ' UVIT Open Cluster Study. I. Detection of a White Dwarf Companion to a Blue Straggler Star in M67: Evidence of Formation through Mass Transfer ', *The Astrophysical Journal* (accepted)

5. Sindhu, N., Subramaniam, A., Geller, A. M., Jadhav, V. V., Knigge, C., Simunovic, M., Leigh, N., Shara, M., and Puzia, T. H., (2019), 'Detection of a White Dwarf Companions to a Blue Straggler Stars from UVIT Observations of M67 ', *in the Proceedings of the IAU Symposium No. 351, Star Clusters: From the Milky Way to the Early Universe* (accepted)

Appendices

Appendix A

GALEX Photometry of M67

Table A.1 List of M67 members detected by GALEX. Column 1 gives the ID from MMJ93, Column 2 gives the WOCS ID of M67. Column 3 and 4 are V and B-V mag from Montgomery et al. (1993). Column 5 and 6 are GALEX FUV and NUV in AB mag, Corrected for Saturation as Mentioned in the Text. Column 7 are Magnitude from UIT (Landsman et al., 1998). Chandra, ROSAT and XMM -Newton are the X-ray Counterparts given in Column 8, 9 and 10. The Membership and Type/Class taken from the Radial Velocity Membership Study are shown in Column 11 and 12. In the Comments Section, Details Regarding Their UV Properties are Listed

MMJ	WOCS	V	B-V	FUV	NUV	m152	CX	X	NX	Memb.	Type/Class	Comments
Blue Straggler Stars												
6490	1006	10.99	0.11	14.79	13.41	12.1	...	...	...	(BL)M	SB1,RR	
6504	1007	10.94	0.22	17.18	13.92	14.47	...	...	...	BM	SB1,RR,EX Cnc	
6511	1017	10.6	0.34	17.15	13.51	14.32	109	...	...	(S)N	RR	
5191	1020	12.7	0.48	22.67	16.77	...	...	...	...	SM		
6006	1025	12.28	0.39	20.39	15.77	...	...	...	...	BM	SB1,RR	
6510	1026	10.7	0.11	14.73	...	12.06	...	...	...	(BL)M	SB1,RR	
5699	2007	12.26	0.57	20.16	...	...	...	...	...	SM		
6479	2011	11.28	0.13	15.82	13.74	13.15	...	...	...	SM	PV	
...	2013	10.92	0.31	16.89	13.79	14.2	...	...	...	BM	SB1,RR	
6477	2015	12.04	0.6	22.65	16.74	...	...	...	...	SM		
...	2068	12.19	0.55	22.75	16.59	...	...	...	...	BM	SB1	
6501	3005	11.06	0.19	17.02	13.63	14.31	...	...	...	SM	PV	
6047	3009	12.22	0.57	...	16.87	...	...	...	...	SM		
5833	4003	12.78	0.49	21.02	...	...	19	45	20	(BL)M	SB1,EV Cnc,RR,W Uma	
5940	4006	12.26	0.26	18.21	15.03	15.28	...	...	...	(BL)M	SB1,EW Cnc,RR	
5667	5005	12.13	0.46	20.05	...	...	95	...	...	BM	SB1	
5571	9005	12.65	0.52	...	16.76	...	...	...	...	BM	SB1	
Triple Systems												
5451	3012	12.59	0.64	21.19	16.9	...	10	7	8	BM	SB2,PV,RS CVn	FUV bright
5896	7008	12.65	0.57	23.01	17.01	...	36	53	36	BM	SB2,RS CVn	FUV excess and NUV bright
6364	4030	13.41	0.57	23.22	18.02	...	...	...	...	BM		FUV excess
6493	2009	11.25	0.42	17.16	...	15.16	3	4	37	BM	BSS,SB2,ES Cnc, RS CVn	
Yellow Straggler Stars												
6498	1015	10.78	0.94	22.31	17.85	...	47	52	24	BM	SB1	
...	2002	11.52	0.82	18.46	...	15.82	6	10	5	BM	SB1,PV,WD	
6491	2008	11.32	0.61	21.89	...	...	24	37	16	BM	SB1	
...	1112	10.29	0.87	...	16.72	...	...	...	...	SM		
X-ray Sources												
...	1045	9.84	1.36	...	19.62	...	...	19	...	SM	RG	
5821	23015	15.85	1.13	...	23.1	...	61	...	53	U	W Uma,ET Cnc	
5653	12004	13.67	0.56	...	18.23	...	78	...	...	BM	SB1	
5780	14025	14.98	0.78	...	20.31	...	...	28	...	BLM	SB1,HY Cnc	
...	6027	14.58	0.87	...	20.37	...	7	47	17	(BL)	SB1,RR	
6089	6010	12.51	0.6	...	17.04	...	155	...	...	BM	SB2	NUV bright
5671	14007	13.9	0.63	23.34	...	...	48	38	29	BM	SB2,HX CnC	FUV excess
5835	21006	14.97	0.89	...	21.65	...	81	...	...	BM	SB2	
5074	10025	14.47	0.76	...	20.36	...	...	35	73	BU	SB2	
6441	23026	15.81	0.97	...	22.18	...	...	51	25	U	...	
6166	4013	12.73	0.58	23.38	...	...	...	43	...	SM	...	FUV excess
White Dwarfs												
5670	...	18.61	-0.11	16.72	...	13.92	...	...	...	...		
5973	...	19.66	-0.1	18.74	19.01	15.61	...	...	...	...		
6061	...	20.53	-0.14	20.08	20.21	16.5	...	...	...	...		

Sub-Sub Giants												
5542	13008	13.79	1.05	...	20.42	...	1	8	4	BM	SB1,HU Cnc	
5808	15028	13.77	1.01	23.29	19.81	...	...	26	...	BM	SB2,PV	FUV excess
Red Giants with FUV Detections												
...	1036	8.86	1.59	23.18	19.34	...	...	...	...	SM		
6514	1075	8.74	1.67	22.26	19.45	...	...	...	...	SM		
FUV Bright Stars												
5654	2003	12.54	0.59	22.04	...	...	88/10	4 41	64	BM	SB2,PV,RS CVn	
5388	2012	12.67	0.62	19.48	...	...	...	...	...	SM	...	
5741	3001	13.26	0.46	21.48	...	...	...	...	...	BM	SB1	
6076	3015	12.69	0.56	22.71	17.1	...	...	...	...	BM	SB2	NUV bright
5249	3024	13.7	0.56	22.73	18.54	...	...	...	...	SM	...	
6467	5030	13.52	0.54	22.41	18.08	...	...	...	...	BM	SB1	
5969	6006	12.91	0.53	22.59	...	...	...	...	...	SM	...	
5993	6008	12.72	0.68	21.39	18.18	...	49	50	33	BM	SB1,PV	
6027	7009	13.33	0.56	22.48	...	...	16	40	10	(BL)M	SB1,W Uma, AH Cnc,RR	
5825	7010	12.76	0.59	22.4	17.52	...	...	...	...	SM	...	
5603	8004	13.17	0.56	22.26	...	...	...	...	...	SM	...	
5675	11005	12.76	0.56	20.85	...	...	...	...	...	SM	...	
5871	11006	13.33	0.5	21.78	...	...	...	...	...	BU	SB1	
5426	17028	14.14	0.59	22.95	18.86	...	...	...	...	SM	...	
White Dwarf + Main Sequence Candidates												
...	17029	15.74	0.9	23.83	...	...	...	...	...	SM	...	
6452	19032	16.06	1.01	24.23	22.27	...	...	...	...	U	...	
...	19045	15.99	0.63	...	21.6	...	...	...	...	SM	...	
6003	21027	16.41	0.58	...	20.64	...	...	...	...	U	...	
5303	23028	15.5	0.83	23.81	22	...	...	...	...	SM	...	
5771	24022	15.21	0.79	21.15	21.45	...	...	...	...	SM	...	
6448	36035	16.1	0.52	...	20	...	...	...	...	U	...	
6427	...	17.15	1.14	23.8	22.44	...	...	...	...	...	...	
5658	...	16.57	1.16	19.56	...	...	...	...	...	...	...	
6398	...	16.69	0.64	...	21.7	...	...	...	...	...	...	
6409	...	18.54	1.51	...	24.53	...	...	...	...	...	...	
MS stars in the optical CMD with FUV excess												
5992	9007	13.66	0.59	23.07	...	...	...	...	...	SM	...	
...	2044	12.8	0.53	23.19	17.06	...	...	...	...	SM	...	NUV bright
6108	2018	13.21	0.56	23.2	17.87	...	...	...	...	SM	...	
5884	5004	12.73	0.59	23.2	...	...	...	...	...	SM	...	
6205	4023	12.81	0.6	23.25	17.28	...	...	...	...	SM	...	NUV bright
5903	13010	13.71	0.6	23.3	18.47	...	...	...	...	SM	...	
5794	7021	13.7	0.55	23.35	18.45	...	...	...	...	SM	...	
6177	4014	12.65	0.58	23.36	...	...	...	...	...	SM	...	
6019	6014	13.21	0.6	23.37	17.94	...	...	...	...	SM	...	
6018	5008	12.56	0.59	23.41	17.29	...	...	...	...	SM	...	NUV bright
5342	3020	13.27	0.58	23.41	17.86	...	...	...	...	BM	SB1	
...	2041	13.2	0.56	23.48	17.85	...	...	...	...	BM	SB1	
...	10033	13.9	0.64	23.48	18.74	...	...	...	...	SM	PV	
...	4039	13.39	0.56	23.49	17.93	...	...	...	...	BM	SB1	
5586	5009	12.83	0.57	23.53	...	...	...	...	...	SM	...	
5118	3021	12.82	0.52	23.53	17.12	...	...	...	...	SM	...	NUV bright
5248	3023	12.8	0.55	23.56	17.23	...	...	...	...	BM	SB1	NUV bright
5925	7005	12.66	0.6	23.59	...	...	...	...	...	SM	...	
...	5037	12.79	0.58	23.85	17.54	...	...	...	...	BM	SB1,PV	
6218	2026	12.69	0.57	23.86	17.25	...	...	...	...	SM	...	NUV bright
6103	5013	13.08	0.56	23.87	17.63	...	...	...	...	SM	...	
5850	7028	12.78	0.55	23.9	17.54	...	...	...	...	SM	...	
...	4051	12.61	0.59	23.92	17.25	...	...	...	...	BM	SB1	NUV bright
5494	11022	13.59	0.56	23.92	17.67	...	...	...	...	BM	SB1,PV	NUV bright
5926	9010	13.08	0.56	23.93	17.68	...	...	...	...	SM	...	
...	2053	12.75	0.56	23.95	17.28	...	...	...	...	SM	...	NUV bright
...	4044	13.15	0.59	24	17.94	...	...	...	...	SM	...	

NUV Bright Stars												
...	4033	12.71	0.56	24.09	17.2	...	...	...	...	SM	...	
5042	3025	12.86	0.53	24.15	17.23	...	...	...	...	SM	...	
...	4058	12.75	0.55	24.22	17.23	...	...	...	...	SM	...	
...	5035	13.45	0.61	24.46	17.57	...	...	...	...	SM	PV	
5284	4021	12.84	0.52	24.46	17.22	...	...	...	...	SM	...	
6343	2025	12.7	0.56	24.62	17.3	...	...	...	...	SM	...	
5544	3006	12.29	0.68	...	16.49	...	...	...	...	BM	SB2	
...	3107	12.77	0.55	...	17.01	...	...	...	...	SM	...	
...	2029	12.65	0.57	...	17.14	...	...	...	...	SM	...	
...	9065	12.89	...	...	17.16	...	...	...	...	SM	...	
...	4069	12.69	0.55	...	17.16	...	...	...	...	SM	...	
5790	4004	12.53	0.59	...	17.16	...	...	...	...	BM	SB1	
...	3031	12.92	0.54	...	17.17	...	...	...	...	SM	...	
5219	9028	12.8	0.55	...	17.2	...	...	...	...	SM	...	
...	2073	12.58	0.58	...	17.21	...	...	...	...	SM	...	
...	4035	12.86	0.54	...	17.22	...	...	...	...	SM	...	
...	5077	12.88	0.55	...	17.24	...	...	...	...	SM	...	
6224	4015	12.71	0.58	...	17.24	...	...	...	...	SM	...	
...	5051	12.71	0.57	...	17.26	...	...	...	...	SM	...	
...	2030	12.68	0.57	...	17.29	...	...	...	...	SM	...	
...	7044	13.33	0.55	24.2	17.76	...	...	...	...	SM	...	
5478	8007	13.37	0.56	...	17.57	...	...	...	...	BM	SB1	
6176	4016	13.51	0.63	...	17.78	...	...	...	...	BM	SB2,PV	
6175	2016	13.78	0.61	...	17.79	...	...	...	...	BM	SB1,PV	
6125	7015	13.37	0.57	...	17.8	...	...	...	...	SM	...	
5283	8015	13.55	0.57	...	17.87	...	...	...	...	SM	...	
6430	7026	13.46	0.51	...	17.63	...	...	...	...	SM	...	
All the remaining member stars detected by GALEX												
...	7030	13.75	0.61	24.1	18.45	...	...	...	...	SM	...	
5434	6026	13.42	0.54	24.16	18	...	...	...	...	BM	SB1	
...	3049	13.11	0.58	24.25	17.82	...	...	...	...	SM	...	
5312	5025	13.15	0.55	24.31	17.84	...	...	...	...	SM	...	
5041	2031	12.63	0.59	24.31	17.65	...	...	...	...	SM	...	
...	3034	12.69	0.62	24.42	17.52	...	...	...	...	SM	PV	
5314	3018	13.4	0.56	24.59	18.02	...	...	...	...	SM	...	
6009	6017	14	0.62	24.7	18.69	...	...	...	...	BM	SB1	
...	3035	12.71	0.57	...	17.5	...	...	...	...	SM	...	
...	5062	12.76	0.56	...	17.51	...	...	...	...	SM	...	
6077	5015	12.76	0.58	...	17.51	...	...	...	...	SM	...	
5573	12005	12.82	0.57	...	17.51	...	...	...	...	SM	...	
5562	7006	12.81	0.57	...	17.52	...	...	...	...	SM	...	
...	2049	12.67	0.58	...	17.53	...	...	...	...	SM	...	
...	6066	13.01	...	...	17.62	...	...	...	...	SM	...	
5864	7011	12.87	0.6	...	17.64	...	...	...	...	BM	SB2	
...	2070	13.02	...	...	17.64	...	...	...	...	SM	...	
...	2047	12.58	0.61	...	17.65	...	...	...	...	SM	...	
6313	2020	12.79	0.58	...	17.65	...	...	...	...	SM	...	
5335	6022	13.07	0.53	...	17.66	...	...	...	...	SM	...	
...	6075	12.99	0.56	...	17.69	...	...	...	...	BM	SB2	
...	3058	12.6	...	...	17.71	...	...	...	...	SM	...	
5371	6011	12.69	0.63	...	17.73	...	...	...	...	BM	SB1	
...	3061	12.61	0.61	...	17.79	...	...	...	...	SM	...	
6158	3014	12.51	0.66	...	17.8	...	...	...	...	BM	SB1	
5169	7022	13.12	0.54	...	17.81	...	...	...	...	BM	SB1,PV	
...	5069	12.57	0.64	...	17.82	...	...	...	...	SM	...	
6336	6021	13.15	0.57	...	17.86	...	...	...	...	SM	...	
...	5058	13.22	0.58	...	17.88	...	...	...	...	SM	...	
...	6053	13.27	0.57	...	17.89	...	...	...	...	SM	...	
...	5052	13.16	0.58	...	17.91	...	...	...	...	SM	...	
6112	8014	13.34	0.58	...	17.91	...	...	...	...	SM	...	
5061	6023	13.03	0.57	...	17.91	...	...	...	...	SM	...	
...	3032	13.31	0.56	...	17.92	...	...	...	...	SM	...	

...	5049	13.29	0.57	...	17.94	...	...	...	...	BM	SB1	
...	3063	12.58	0.66	...	17.95	...	...	...	...	BM	SB1	
5959	7023	13.19	0.56	...	17.95	...	...	...	...	SM	...	
...	5045	13.2	0.58	...	17.97	...	...	...	...	BM	SB1	
...	3036	13.19	0.57	...	17.97	...	...	...	...	SM	...	
5354	5018	13.48	0.55	...	17.99	...	...	...	...	BM	SB1	
5263	6016	13.29	0.58	...	18	...	...	...	...	BM	SB1	
...	3046	13.24	0.58	...	18.01	...	...	...	...	SM	...	
6213	9022	13.39	0.58	...	18.02	...	...	...	...	BM	SB2	
...	3048	13.21	0.59	...	18.05	...	...	...	...	SM	...	
...	3047	13.24	0.58	...	18.05	...	...	...	...	SM	...	
...	4072	13.2	0.61	...	18.05	...	...	...	...	SM	...	
5277	4031	13.38	0.55	...	18.06	...	...	...	...	SM	...	
...	4045	13.16	0.58	...	18.06	...	...	...	...	SM	...	
...	9044	13.52	0.58	...	18.07	...	...	...	...	SM	...	
6332	5020	13.36	0.58	...	18.07	...	...	...	...	SM	...	
...	7051	13.34	0.58	...	18.1	...	...	...	...	SM	...	
6134	7013	13.38	0.57	...	18.11	...	...	...	...	SM	...	
5900	2027	13.29	0.57	...	18.11	...	...	...	...	SM	...	
5389	4020	13.37	0.55	...	18.11	...	...	...	...	BM	SB1	
6374	5022	13.22	0.6	...	18.14	...	...	...	...	SM	...	
6371	8022	13.41	0.58	...	18.14	...	...	...	...	SM	...	
5183	2032	13.45	0.54	...	18.15	...	...	...	...	BM	SB1	
5546	10007	13.63	0.57	...	18.17	...	...	...	...	SM	...	
5332	7012	13.56	0.55	...	18.18	...	...	...	...	SM	...	
5622	6013	13.26	0.6	...	18.18	...	...	...	...	SM	...	
...	11028	13.34	0.61	...	18.19	...	...	...	...	BM	SB2	
...	5043	13.5	0.56	...	18.22	...	...	...	...	SM	...	
5196	6018	13.6	0.55	...	18.22	...	...	...	...	SM	...	
6127	7020	13.58	0.59	...	18.22	...	...	...	...	SM	...	
...	8052	13.67	0.56	...	18.23	...	...	...	...	SM	...	
5254	13028	13.47	0.56	...	18.24	...	...	...	...	SM	...	
5838	7014	13.31	0.63	...	18.26	...	...	...	...	SM	...	
...	5048	13.55	0.58	...	18.27	...	...	...	...	SM	...	
...	11055	13.62	0.56	...	18.28	...	...	...	...	BM	SB1	
5132	12028	13.41	0.56	...	18.28	...	...	...	...	SM	...	
6109	9023	13.53	0.54	...	18.3	...	...	...	...	SM	...	
...	1046	12.67	0.68	...	18.3	...	...	...	...	SM	...	
...	5034	13.63	0.57	...	18.31	...	...	...	...	SM	PV	
5123	1032	12.65	0.69	...	18.32	...	...	...	...	SM	...	
5301	5017	13.64	0.56	...	18.34	...	...	...	...	SM	...	
...	5031	13.59	0.57	...	18.34	...	...	...	...	SM	...	
6110	8026	13.63	0.66	...	18.35	...	...	...	...	BU	SB1	
...	9035	13.45	0.59	...	18.36	...	...	...	...	SM	PV	
...	5029	13.71	0.57	...	18.38	...	...	...	...	SM	...	
...	4032	13.54	0.59	...	18.39	...	...	...	...	SM	PV	
6058	14010	13.79	0.59	...	18.4	...	...	...	...	SM	...	
...	6043	13.66	0.59	...	18.4	...	...	...	...	SM	...	
...	6040	13.7	0.58	...	18.41	...	...	...	...	SM	...	
...	5040	13.73	0.57	...	18.42	...	...	...	...	SM	...	
5640	7018	13.74	0.57	...	18.43	...	...	...	...	SM	...	
...	6049	13.67	0.58	...	18.44	...	...	...	...	SM	...	
...	12008	13.57	0.59	...	18.44	...	...	...	...	SM	...	
6362	6025	13.7	0.6	...	18.45	...	...	...	...	BU	SB1	
...	4040	13.29	0.61	...	18.46	...	...	...	...	SM	...	
5522	14006	13.9	0.58	...	18.46	...	...	...	...	SM	...	
5413	11009	13.76	0.57	...	18.47	...	...	...	...	SM	...	
...	9030	13.74	0.58	...	18.48	...	...	...	...	SM	...	
...	4034	13.71	0.58	...	18.48	...	...	...	...	BM	SB1	

...	12035	13.68	0.58	...	18.48	...	...	...	...	SM	...	
...	10035	13.79	0.59	...	18.49	...	...	...	...	SM	...	
6107	5012	12.75	0.76	...	18.49	...	...	...	...	SM	...	
5471	10009	13.8	0.59	...	18.49	...	...	...	...	SM	...	
...	11035	13.62	0.6	...	18.5	...	...	...	...	SM	...	
5334	9014	13.49	0.63	...	18.55	...	...	...	...	BM	SB2	
6065	9009	13.76	0.59	...	18.55	...	...	...	...	SM	...	
5408	14011	14.05	0.66	...	18.57	...	...	...	...	BM	SB2	
...	8046	13.86	0.58	...	18.59	...	...	...	...	BM	SB1	
6380	16022	13.83	0.62	...	18.61	...	...	...	...	SM	...	
5932	8013	13.7	0.64	...	18.61	...	...	...	...	BM	SB2	
...	8030	13.78	0.59	...	18.62	...	...	...	...	SM	...	
...	14035	13.84	0.59	...	18.62	...	...	...	...	SM	PV	
5680	6019	13.69	0.55	...	18.64	...	...	...	...	SM	...	
5412	10012	13.89	0.54	...	18.64	...	...	...	...	SM	...	
6060	9012	13.75	0.6	...	18.65	...	...	...	...	BM	SB1	
5189	7019	13.92	0.57	...	18.65	...	...	...	...	SM	...	
5362	4012	12.73	0.74	...	18.66	...	...	...	...	SM	...	
...	2113	12.76	0.74	...	18.69	...	...	...	...	SM	...	
5989	15022	13.94	0.58	...	18.73	...	...	...	...	BLM	SB1	
5601	10011	13.55	0.62	...	18.75	...	...	...	...	SM	...	
5996	4019	12.83	0.78	...	18.8	...	...	...	...	SM	...	
5962	12022	13.86	0.66	...	18.82	...	...	...	...	BM	SB1	
5264	4018	13.64	0.66	...	18.83	...	...	...	...	SM	...	
5182	10022	13.67	0.62	...	18.84	...	...	...	...	SM	...	
6516	1029	10.47	1.12	...	18.84	...	...	...	...	SM	RG	
...	11044	13.89	0.61	...	18.85	...	...	...	...	BM	SB1	
...	2017	12.81	0.75	...	18.93	...	...	...	...	BM	SB1	
6010	12009	14.04	0.62	...	18.93	...	...	...	...	BM	SB2	
5229	11020	14.06	0.58	...	18.94	...	...	...	...	SM	...	
6395	4024	14.04	0.62	...	18.94	...	...	...	...	SM	...	
...	8036	13.97	0.61	...	18.96	...	...	...	...	SM	PV	
6506	2019	10.58	1.1	...	18.96	...	...	...	...	SM	RG	
6267	7017	13.96	0.61	...	18.97	...	...	...	...	SM	...	
6512	1022	10.55	1.1	...	18.97	...	...	...	...	SM	RG	
5776	17007	14.12	0.61	...	18.98	...	...	...	...	BM	SB1	
6494	2010	10.48	1.1	...	18.99	...	...	...	...	SM	RG	
6149	8019	14.05	0.6	...	18.99	...	...	...	...	SM	...	
6237	5032	14.1	0.55	...	19.01	...	...	...	...	SM	...	
5307	7031	14.07	0.6	...	19.01	...	...	...	...	SM	...	
...	9036	14.12	0.61	...	19.02	...	...	...	...	SM	...	
...	6042	13.92	0.63	...	19.03	...	...	...	...	SM	...	
...	8048	14.21	0.59	...	19.03	...	...	...	...	SM	...	
...	15026	14.04	0.59	...	19.03	...	...	...	...	SM	...	
...	3027	14	0.62	...	19.05	...	...	...	...	SM	...	
6104	5024	14.08	0.66	...	19.05	...	...	...	...	SM	...	
6485	1003	10.48	1.11	...	19.05	...	...	...	...	SM	RG	
5567	18005	14.16	0.61	...	19.06	...	...	...	...	SM	...	
6039	8009	13.67	0.66	...	19.08	...	...	...	...	SM	...	
6031	10015	14.11	0.6	...	19.09	...	...	...	...	SM	...	
5181	18022	14.15	0.59	...	19.1	...	...	...	...	SM	...	
5479	12020	14.28	0.59	...	19.11	...	...	...	...	BU	SB1	
5294	13026	14.1	0.6	...	19.13	...	...	...	...	SM	...	
5305	11015	14.09	0.62	...	19.13	...	...	...	...	SM	...	
5656	10014	14.13	0.64	...	19.14	...	...	...	...	SM	PV	
5350	5016	12.78	0.81	...	19.19	...	...	...	...	SM	...	
5203	11021	14.14	0.6	...	19.2	...	...	...	...	SM	...	

6408	4025	12.89	0.82	...	19.21	...	...	...	...	SM	...	
5414	11014	14.05	0.7	...	19.21	...	...	...	...	BM	SB2	
5963	15007	14.22	0.62	...	19.24	...	...	...	...	SM	...	
...	11030	14.18	0.63	...	19.24	...	...	...	...	SM	...	
...	9039	14.17	0.62	...	19.25	...	...	...	...	SM	...	
6405	10030	14.23	0.62	...	19.27	...	...	...	...	SM	...	
6073	15010	14.07	0.64	...	19.28	...	...	...	...	SM	...	
...	9049	14.16	0.62	...	19.29	...	...	...	...	SM	...	
...	7043	14.19	0.63	...	19.31	...	...	...	...	SM	...	
5532	11012	14.2	0.67	...	19.33	...	...	...	...	SM	...	
6254	7016	13.9	0.7	...	19.34	...	...	...	...	BM	SB2	
...	11058	14.2	0.65	...	19.41	...	...	...	...	SM	...	
...	9058	14.21	0.61	...	19.42	...	...	...	...	SM	...	
5338	7025	14.26	0.63	...	19.42	...	...	...	...	SM	...	
6475	1033	11.24	1.1	...	19.44	...	...	...	...	BM	SB1,RG	
6497	2014	10.76	1.13	...	19.46	...	...	...	...	BM	SB1,RG	
...	10036	14.2	0.64	...	19.47	...	...	...	...	SM	PV	
5826	13009	14.17	0.66	...	19.51	...	...	...	...	SM	...	
6347	14020	14.58	0.67	...	19.57	...	...	...	...	BM	SB1	
5704	12012	14.48	0.67	...	19.6	...	...	...	...	SM	...	
6505	1011	11.33	1.07	...	19.63	...	...	...	...	SM	RG	
6306	10018	14.32	0.67	...	19.64	...	...	...	...	BLM	SB1	
6265	9017	14.38	0.66	...	19.65	...	...	...	...	SM	...	
6423	10026	14.12	0.72	...	19.67	...	...	...	...	SM	...	
6499	1005	9.69	1.36	...	19.67	...	...	...	...	BM	SB1,RG	
5663	3019	12.31	0.99	...	19.67	...	...	...	...	SM	RG...	
6500	3011	11.52	1.05	...	19.71	...	...	...	...	SM	RG	
5228	3017	12.93	0.85	...	19.72	...	...	...	...	SM	...	
...	6070	14.36	0.65	...	19.72	...	...	...	...	SM	...	
...	6029	14.05	0.72	...	19.72	...	...	...	...	BM	SB2	
...	1065	10.12	1.3	...	19.72	...	...	...	...	SM	RG	
6241	8025	14.39	0.65	...	19.73	...	...	...	...	SM	...	
...	18028	14.57	0.67	...	19.74	...	...	...	...	SM	...	
6050	5010	12.09	1.01	...	19.78	...	...	...	...	SM	PV,RG	
5444	14023	14.48	0.63	...	19.79	...	...	...	...	BM	SB1	
6082	4027	14.14	0.71	...	19.79	...	...	...	...	SM	...	
...	12025	14.52	0.66	...	19.8	...	...	...	...	SM	...	
6322	6024	14.34	0.68	...	19.81	...	...	...	...	SM	...	
...	11017	14.5	0.66	...	19.81	...	...	...	...	SM	...	
...	11042	14.51	0.66	...	19.82	...	...	...	...	SM	...	
5039	11025	14.42	0.66	...	19.83	...	...	...	...	BM	SB1	
6028	13017	14.44	0.71	...	19.84	...	...	...	...	SM	...	
5541	14017	14.48	0.66	...	19.87	...	...	...	...	SM	...	
5261	9019	14.38	0.71	...	19.88	...	...	...	...	SM	...	
6508	3042	10.93	1.15	...	19.89	...	...	...	...	SM	RG	
6486	2004	10.3	1.26	...	19.91	...	...	...	...	SM	RG	
5744	13021	14.53	0.67	...	19.92	...	...	...	...	SM	...	
6460	7027	14.54	0.68	...	19.92	...	...	...	...	SM	...	
5995	18007	14.49	0.67	...	19.93	...	...	...	...	SM	...	
5855	8008	12.93	0.92	...	19.94	...	...	...	...	SM	PV,RG	
...	8031	14.52	0.66	...	19.96	...	...	...	...	SM	...	
...	11013	14.51	0.67	...	19.99	...	...	...	...	SM	...	
...	9052	14.47	0.67	...	20.02	...	...	...	...	SM	...	
...	7045	14.39	0.69	...	20.03	...	...	...	...	SM	...	
...	13044	14.64	0.69	...	20.03	...	...	...	...	SM	...	
5997	4011	12.23	0.99	...	20.04	...	...	...	...	SM	RG	
6055	17026	14.65	0.75	...	20.06	...	...	...	...	SM	...	
...	8057	14.6	0.69	...	20.07	...	...	...	...	SM	...	

...	3026	12.71	0.91	...	20.09	...	...	...	...	SM	RG	
...	4009	12.42	0.97	...	20.09	...	...	...	...	SM	RG	
...	2052	12.51	0.97	...	20.09	...	...	...	...	SM	RG	
5484	11018	14.58	0.65	...	20.1	...	...	...	...	SM	...	
...	2035	12.54	0.95	...	20.1	...	...	...	...	SM	RG	
5966	13012	14.59	0.68	...	20.14	...	...	...	...	SM	...	
5200	12018	14.54	0.67	...	20.16	...	...	...	...	SM	...	
6443	12026	14.25	0.78	...	20.19	...	...	...	...	SM	...	
6230	11019	14.59	0.72	...	20.2	...	...	...	...	SM	...	
...	4063	12.96	0.91	...	20.22	...	...	...	...	SM	...	
6144	10013	14.31	0.78	...	20.23	...	...	...	...	BM	SB1	
5489	16020	14.7	0.72	...	20.23	...	...	...	...	BM	SB1	
6169	5021	12.91	0.97	...	20.24	...	...	...	...	SM	RG	
...	12030	14.66	0.7	...	20.31	...	...	...	...	SM	...	
...	12031	14.74	0.74	...	20.31	...	...	...	...	SM	PV	
5306	14014	14.65	0.69	...	20.33	...	...	...	...	SM	...	
5469	22022	14.76	0.69	...	20.33	...	...	...	...	SM	...	
...	9034	14.79	0.72	...	20.43	...	...	...	...	SM	...	
...	2046	12.59	0.98	...	20.43	...	...	...	...	SM	RG	
5318	5014	12.86	0.94	...	20.46	...	...	...	...	SM	RG	
...	8032	14.82	0.72	...	20.51	...	...	...	...	SM	...	
...	14030	14.69	0.7	...	20.52	...	...	...	...	SM	...	
6341	9024	14.79	0.71	...	20.56	...	...	...	...	SM	...	
...	15018	14.8	0.72	...	20.59	...	...	...	...	SM	...	
6298	18023	14.71	0.7	...	20.61	...	...	...	...	SM	...	
5346	18013	14.82	0.7	...	20.61	...	...	...	...	SM	...	
6160	13013	14.79	0.75	...	20.61	...	...	...	...	BLM	SB1	
6259	4017	12.92	0.98	...	20.63	...	...	...	...	SM	RG	
5455	18010	14.93	0.71	...	20.67	...	...	...	...	SM	...	
5360	13014	14.79	0.72	...	20.7	...	...	...	...	SM	...	
5376	16018	14.97	0.75	...	20.72	...	...	...	...	SM	...	
...	21022	14.8	0.74	...	20.74	...	...	...	...	BM	SB1	
...	14015	14.6	0.82	...	20.76	...	...	...	...	BM	SB2	
6231	14021	14.5	0.85	...	20.78	...	...	...	...	SM	...	
5424	18012	15.09	0.72	...	20.84	...	...	...	...	SM	...	
5064	19023	14.63	0.81	...	20.85	...	...	...	...	SM	...	
5310	17021	15	0.73	...	20.88	...	...	...	...	SM	...	
5391	16013	15	0.74	...	20.88	...	...	...	...	SM	...	
5578	21008	15.03	0.75	...	20.91	...	...	...	...	SM	...	
...	9041	14.66	0.82	...	20.96	...	...	...	...	SM	...	
...	16036	14.98	0.77	...	21.01	...	...	...	...	BLM	SB1	
...	9037	15.05	0.77	...	21.04	...	...	...	...	SM	...	
5828	23022	14.96	0.76	...	21.07	...	...	...	...	BM	SB1	
5574	18031	15.06	0.77	...	21.12	...	...	...	...	SM	...	
6167	17023	14.62	0.81	...	21.12	...	...	...	...	SM	...	
5730	17020	14.92	0.74	...	21.13	...	...	...	...	SM	...	
...	13030	14.7	0.86	...	21.14	...	...	...	...	BM	SB2	
6459	10027	15.01	0.75	...	21.18	...	...	...	...	SM	...	
5949	19011	15.17	0.81	...	21.18	...	...	...	...	SM	...	
...	13038	15.08	0.77	...	21.19	...	...	...	...	SM	...	
5217	16030	15.09	0.77	...	21.2	...	...	...	...	SM	...	
...	17033	15.04	0.79	...	21.21	...	...	...	...	SM	...	
5340	9016	14.63	0.83	...	21.23	...	...	...	...	BM	SB2	
5297	12016	15.01	0.76	...	21.23	...	...	...	...	SM	...	
6305	14019	15.24	0.84	...	21.25	...	...	...	...	SM	...	
5518	22007	15.11	0.78	...	21.26	...	...	...	...	BM	SB1	
6269	12019	15.06	0.78	...	21.26	...	...	...	...	SM	...	
6388	16031	15.05	0.78	...	21.29	...	...	...	...	SM	...	
5347	19021	15.35	0.83	...	21.3	...	...	...	...	SM	...	

5279	13019	15.11	0.81	...	21.32	...	...	...	...	BM	SB1	
5558	20018	15.22	0.81	...	21.38	...	...	...	...	SM	...	
...	13047	15.25	0.78	...	21.46	...	...	...	...	SM	...	
...	17058	15.13	0.77	...	21.49	...	...	...	...	SM	...	
5526	22013	15.32	0.81	...	21.49	...	...	...	...	SM	...	
...	2083	12.49	...	...	21.53	...	...	...	...	SM	...	
...	16038	15.28	0.83	...	21.54	...	...	...	...	SM	...	
5282	21028	15.3	0.82	...	21.57	...	...	...	...	SM	...	
...	12032	15.01	0.8	...	21.58	...	...	...	...	BLM	SB1	
6321	20020	15.22	0.81	...	21.63	...	...	...	...	SM	...	
6340	10024	15.26	0.8	...	21.63	...	...	...	...	BLM	SB1	
...	21035	15.16	0.82	...	21.63	...	...	...	...	SM	...	
5948	22008	15.24	0.79	...	21.72	...	...	...	...	SM	...	
6008	19013	15.16	0.83	...	21.73	...	...	...	...	SM	SB1	
5964	16009	14.98	0.88	...	21.87	...	...	...	...	SM	...	
6139	19018	15.32	0.78	...	21.97	...	...	...	...	SM	...	
5090	24023	15.42	0.83	...	21.98	...	...	...	...	SM	...	
6161	19017	15.29	0.83	...	21.99	...	...	...	...	SM	...	
5186	21021	15.35	0.8	...	22.03	...	...	...	...	SM	...	
5060	12024	15.44	0.84	...	22.11	...	...	...	...	SM	...	
5563	24005	15.38	0.85	...	22.21	...	...	...	...	SM	...	
5904	20009	15.51	0.87	...	22.22	...	...	...	...	SM	...	
5800	21009	15.56	0.9	...	22.23	...	...	...	...	SM	...	
6303	21018	15.53	0.89	...	22.24	...	...	...	...	SM	...	
5623	18016	15.92	0.94	...	22.26	...	...	...	...	SM	...	
6048	21012	15.47	0.97	...	22.38	...	...	...	...	SM	...	
...	28035	15.74	0.93	...	22.45	...	...	...	...	SM	PV	
...	16032	15.69	1.04	...	22.49	...	...	...	...	SM	...	
5841	23013	15.47	0.86	...	22.5	...	...	...	...	SM	...	
...	25046	15.65	0.88	...	22.55	...	...	...	...	SM	...	
5047	18025	15.65	0.86	...	22.64	...	...	...	...	U	...	
...	16029	15.73	0.85	...	22.64	...	...	...	...	BLM	SB1	
5116	...	15.73	0.85	...	22.65	...	...	...	...	...	...	
5320	16027	15.81	0.88	...	22.68	...	...	...	...	SM	...	
6102	27010	15.72	0.92	...	22.69	...	...	...	...	SM	...	
...	23038	16.21	1.01	...	22.74	...	...	...	...	SM	...	
5470	17016	15.77	0.9	...	22.75	...	...	...	...	U	...	
...	24038	16.27	1.07	...	22.81	...	...	...	...	SM	...	
5467	26023	15.79	0.88	...	22.88	...	...	...	...	SM	...	
5129	...	15.73	0.89	...	22.96	...	...	...	...	...	...	
5956	26013	15.8	0.91	...	23.07	...	...	...	...	SM	...	
5386	23017	15.77	0.93	...	23.15	...	...	...	...	U	...	
6379	...	16.51	1.08	...	23.21	...	...	...	...	...	...	
...	18048	16.24	...	...	23.25	...	...	...	...	SM	...	
...	21040	16.12	0.96	...	23.56	...	...	...	...	SM	...	
5233	26021	16.2	1	...	23.58	...	...	...	...	SM	...	
5862	26026	16.18	1	...	23.59	...	...	...	...	SM	...	
...	22044	16.01	0.98	...	23.66	...	...	...	...	SM	...	
5502	25026	16.12	0.92	...	23.78	...	...	...	...	SM	...	
...	27047	16.43	0.99	...	23.84	...	...	...	...	SM	...	
5533	25020	15.98	0.99	...	23.87	...	...	...	...	U	...	
...	18041	15.94	1.13	...	23.93	...	...	...	...	SM	...	
6078	...	16.67	1.1	...	23.93	...	...	...	...	...	...	
...	25036	16.21	1.02	...	24.17	...	...	...	...	SM	...	
5149	27021	16.48	1.06	...	24.21	...	...	...	...	SM	...	
6021	25017	16.52	1.1	...	24.28	...	...	...	...	U	...	
...	17034	16.15	0.92	...	24.32	...	...	...	...	SM	...	
6211	27020	16.02	1.15	...	24.34	...	...	...	...	SM	...	
5160	27026	16.37	1.04	...	24.46	...	...	...	...	SM	...	
5052	19034	16.2	0.98	...	24.82	...	...	...	...	SM	...	